白山における甚の助谷巨大地すべり
突発災害の前兆現象および運動予測

平成15年度～17年度科学研究費補助金(基盤研究(B)(2))
(研究課題番号:15310127)

研究成果報告書

平成18年3月

研究代表者　　汪　発武
(京都大学防災研究所)

平成 15 年度～17 年度科学研究費補助金（基盤研究（B）（２））研究成果報告書

1. 研究課題番号　（15310127）

2. 研究課題　白山における甚の助谷巨大地すべり突発災害の前兆現象および運動予測

3. 研究代表者　汪　発武（京都大学防災研究所・助手）

4. 研究分担者　松本樹典（金沢大学大学院自然科学研究科・教授）
宮島昌克（金沢大学大学院自然科学研究科・教授）
桝谷　浩（金沢大学大学院自然科学研究科・教授）
蔡　　飛（群馬大学工学部・助手）
王　功輝（京都大学防災研究所・助手）
佐々恭二（京都大学防災研究所・教授）

5. 研究協力者　奥野岳志（金沢大学大学院自然科学研究科・大学院生）
（現在：新潟県上越地域振興局新井砂防事務所・砂防担当）
Ogbonnaya IGWE　（京都大学大学院理学研究科・大学院生）
Jozef JURKO　（京都大学大学院理学研究科・大学院生）
齊藤龍太（京都大学大学院理学研究科・大学院生）
南谷太一（京都大学大学院理学研究科・大学院生）

6. 交付決定額（配分額）

平成１５年度	５，９００千円
平成１６年度	４，１００千円
平成１７年度	２，４００千円
総　　計	１２，４００千円

7. 研究発表

(1) 論文発表

Wang, F.W., K. Sassa (2006): Initiation and traveling mechanisms of the May 2004 landslide−debris flow at Bettou-dani of the Jinnosuke-dani landslide, Haku-san Mountain, Japan. Soils and Foundations (in press).

Wang, F.W., T. Okuno, T. Matsumoto (2006): Deformation characteristics and influential factors for the giant Jinnosuke-dani landslide in the Haku-san Mountain area, Japan. Landslides: Journal of the International Consortium on Landslides (in revising).

Boldini D., F.W. Wang, K. Sassa, P. Tommasi (2006): Application of large-scale ring-shear tests to

the analysis of December 2002 tsunamogenic landslides at Stromboli volcano (Italy). Geotechnique (submitted).

Igwe, G., K. Sassa, F.W. Wang (2006): The influence of grading on the shear behavior of loose sands in stress-controlled ring shear tests. Landslides: Journal of the International Consortium on Landslides (in press) .

Igwe, G., K. Sassa, H. Fukuoka, F.W. Wang (2006): The undrained response of sands with different gradations in a stress-controlled ring shear tests. Canadian Geotechnical Journal (submitted).

宮島昌克, 奥野洋平, 北浦　勝 (2006): 白山における地震時の斜面崩壊危険性の評価. 日本海域研究, 37, 15-21.

Wang, F.W., T. Matsumoto, Y. Tanaka (2005): Two recent flowslides in Yamashina area, Kanazawa City, Japan. Landslides: Journal of the International Consortium on Landslides. 2(3):229-234.

Wang, F.W. (2005): Fluidization mechanisms and motion simulation on flowslides triggered by earthquake and rainfall. Chinese Journal of Rock Mechanics and Engineering. 24(10)1654-1661.

Sassa, K., H. Fukuoka, F.W. Wang, G. Wang (2005): Dynamic properties of earthquake-induced large-scale rapid landslides within past landslide masses. Landslides: Journal of the International Consortium on Landslides, 2(2): 125-134.

田中康博, 汪发武, 中村佳代, 松本樹典 (2005): 金沢市山科町における長雨を誘因とする流動性地すべりの特徴と運動機構. 日本地すべり学会誌, 42(2) 34-43.

Wang, F.W., Y. Tanaka, K. Nakamura. 2005. Fluidization mechanisms of the Tsukidate flowslide triggered by earthquake and the Yamashina flowslides induced by rainfall. Proc. 16th ICSMGE, Osaka, 2607-2610.

Boldini, D., F.W. Wang, K. Sassa, P. Tommasi (2005): Mechanism of landslide causing the December 2002 tsunami at Stromboli volcano (Italy). In Landslides: Risk Analysis and Sustainable Disaster Management (K. Sassa, H. Fukuoka, F.W. Wang, G. Wang Eds.), Springer, 173-180.

Sassa, K., H. Fukuoka, F.W. Wang, G. Wang (2005): Dynamic properties of earthquake-induced large-scale rapid landslides within past landslide masses. Landslides: Journal of the International Consortium on Landslides, 2(2): 125-134.

Wang, F.W., Wang, G., Sassa, K., Takeuchi, A., Araiba, K., Zhang, Y., Peng, X (2005): Displacement monitoring and physical exploration on the Shuping Landslide reactivated by impoundment of the Three Gorge Reservoir, China. In: Landslides - Risk Analysis and Sustainable Disaster Management (ed. Sassa K, Fukuoka H, Wang G, Wang F), Springer Verlag, pp.313-319, 2005.

Igwe, O., Sassa, K., Fukuoka, H. and Wang, F.W. (2005): Threshold pore pressure: a new perspective on the mechanisms of flowslides. Proc. of 11th International Conference and Field Trips on Landslides, Norway, September, 2005, pp.165-171.

汪　発武, 佐々恭二, 松本樹典, 奥野岳志(2004): 粒子破砕を考慮した地すべりの流動化メ

カニズムと運動範囲予測. 地すべり学会誌, 40 (5), pp. 17-28.

Fukuoka, H., Wang, G., Sassa, K., Wang, F.W., and Matsumoto, T. (2004): Earthquake-induced rapid long-traveling flow phenomenon: May 2003 Tsukidate landslide in Japan. Landslides: Journal of the International Consortium on Landslides. 1(2):151-155.

Sassa, K., Wang, G., Fukuoka, H., Wang, F.W., Ochiai, T., Sugiyama, M., and Sekiguchi, T. (2004): Landslide risk evaluation and hazard zoning for rapid and long-travel landslides in urban development areas. Landslides: Journal of the International Consortium on Landslides, Vol. 1, No. 3, pp. 221-235.

Wang, F.W., T. Matsumoto and K. Sassa (2004): Deforming mechanism and influential factors of giant Jinnosuke-dani landslide, Japan. 京都大学防災研究所年報，47-B, 883-891.

汪　発武, 奥野岳志, 松本樹典. 2004. 地盤材料の破砕性と高速土砂流動　－実験結果に基づいた運動予測－ 都市域斜面防災の新世紀～地震豪雨時の高速長距離土砂流動現象の解明(APERIF)公開シンポジウム論文集, Vol.1, 273-290.

Okuno, T., F.W. Wang, T. Matsumoto. 2004. The deforming characters of the giant Jinnosuke-dani landslide in Haku-san mountainous area, Japan, Proceedings of the 9th International Symposium on Landslides, Landslides: Evaluation and Stabilization, June 28 to July 2, 2004, Rio de Janeiro, Vol.2, 1279-1295.

Wang, F.W., T. Okuno, T. Matsumoto. 2004. Deformation style and influential factors of the giant Jinnosuke-dani landslide in Japan. 15th Southeast Asian Geotechnical Society Conference, 22 -26 November 2004, Bangkok, Thailand, Vol.1, 399-404.

Wang, F.W., K. Nakamura, T. Matsumoto, Y. Tanaka. 2004. Fluidization and motion mechanisms of the Tsukidate flowslide triggered by Sanriku-Minami earthquake in Japan. Proceedings of 15th Southeast Asian Geotechnical Society Conference, 22 -26 November 2004, Bangkok, Thailand, Vol.1, 899-904.

Tanaka, Y., F.W. Wang, K. Nakamura, T. Matsumoto. 2004. Sliding mechanism of the Yamashina flowslide triggered by continual rainfall in Kanazawa City, Japan. Proceedings of 15th Southeast Asian Geotechnical Society Conference, 22 -26 November 2004, Bangkok, Thailand, Vol.1, 331-336.

奥野岳志・汪　発武・松本樹典 (2004): 白山における巨大甚之助谷地すべりの運動様式及び影響素因. 地すべり学会誌（地すべりの運動機構特集）, Vol.41, No.1, pp.57-64.

Wang, F.W., Y.M. Zhang, Z.T. Huo, T. Matsumoto, B.L. Huang (2004): The July 14, 2003 Qianjiangping Landslide, Three Gorges Reservoir, China. Landslides: Journal of the International Consortium on Landslides, Vo.1, No.2, pp.157-162.

F.W. Wang, T. Okuno (2004): Deforming mechanism of the giant Jinnosuke-dani landslide in Haku-san mountainous area, Japan. Chinese Journal of Geological Hazards and Environment Preservation, Vol.15, No.3, pp.48-54.

F.W. Wang, K. Sassa, H. Fukuoka, G. Wang (2004): Prediction of Landslides: Occurrence Time and Passing Area, Proc. of the 2nd International Symposium on Mitigation of Geo-hazards in

Areas around Japan Sea. Kanazawa, Japan. 13pp.

汪　発武・佐々恭二 (2004): 地すべり運動シミュレーションとハザードマップ. 日本地すべり学会関西支部シンポジウム「GIS と地すべりハザードマップ」論文集, pp.61-79.

Zhang, Y.M., X.M. Peng, F.W. Wang, Z.T. Huo, B.L. Huang (2004): Current status and challenge of landslide monitoring in Three-gorge reservoir area, China. リアルタイム災害情報検知とその利用に関するシンポジウム論文集, 土木学会, pp.165-170.

Wang, F.W., K. Sassa (2003): A general mechanism of long-runout landslides induced by earthquake and rainfall in crushable soils. Proceedings of International Symposium on Fast Slope Movements: Prediction and Prevention for Risk Mitigation, 11-13 May 2003, Naples, Italy. 531-536.

Wang, F.W., T. Matsumoto, K. Sassa (2003): Effects of grain crushing properties on rapid landslides, -from experimental study to motion simulation. Proc. Int'l Conf. Fast slope movements: Prediction and prevention for risk mitigation, pp.523-530.

Wang, F.W., K. Sassa (2003): A general mechanism of long-runout landslides induced by earthquake and rainfall in crushable soils. Proc. Int'l Conf. Fast slope movements: Prediction and prevention for risk mitigation, pp.531-536.

⑵ 口頭発表

汪　発武, 高田　渉, 松本樹典 (2004): 崩壊誘起土石流の数値実験及び別当崩れを対象とした事例研究. 第 39 回地盤工学会研究発表会平成 16 年度発表講演集, pp.2127-2128.

田中康博, 汪　発武, 中村佳代, 松本樹典(2004）: 第三紀泥岩層で発生した金沢市山科地すべりの長距離運動機構. 第 39 回地盤工学会研究発表会平成 16 年度発表講演集, pp.2147-2148.

中村佳代, 汪 発武, 松本樹典, 田中康博 (2004): 三軸圧密非排水せん断試験結果に基づく築館地すべりの流動化機構の考察. 第 39 回地盤工学会研究発表会平成 16 年度発表講演集, pp. 2083-2084.

上月真人, 汪　発武, 松本樹典 (2004): 数値解析による斜面アンカー工の最適設計法の検討と山科地すべりへの事例解析. 第 39 回地盤工学会研究発表会平成 16 年度発表講演集, pp.2191-2192.

奥野岳志, 汪　発武, 松本樹典 (2004): 白山甚之助谷地すべりの変形メカニズム及び運動範囲の予測. 第 39 回地盤工学会研究発表会平成 16 年度発表講演集, pp.2131-2132.

田中康博, 汪　発武, 松本樹典, 水道信二, 縄　大輔(2004): 金沢市山科町における第三紀泥岩層中で発生した流動化地すべりの特徴及び長距離運動機構. 第 43 回日本地すべり学会研究発表会講演集, pp.65-68.

Wang, F.W., T. Matsumoto, T. Okuno (2004): Influential factors of the giant Jinnosuke-dani landslide. 第 43 回日本地すべり学会研究発表会講演集, Vol.1, 329-332.

汪　発武, 松本樹典, 田中康博, 藤森　学, 佐々恭二. 2003. 三陸南地震による築館地すべりの運動シミュレーション. 第 42 回日本地すべり学会研究発表会講演集, Vol.1,

239-242.

Wang, F.W., T. Matsumoto, K. Sassa (2003): Effects of permeability o rainfall-induced flowslides in laboratory flume tests. 第 42 回日本地すべり学会研究発表会講演集, Vol.1, 257-260.

8. 研究実績の概要

白山は標高 2,000 メートルを超える急峻な活火山である。山頂周辺は溶岩・火砕流などの火山噴出物に覆われ，なだらかな斜面となっている。山頂周辺では，冬季の積雪量は 10mにまで達する。そのため，融雪期には，甚の助谷及び別当谷においては，白山から流下する融雪水が深く山体を刻み，斜面崩壊，及びそれの崩積物による土石流災害がしばしば発生している。明治時代から砂防工事が始まり，これまでに 100 基を超える砂防ダムが建設されている。甚の助谷と別当谷に挟まれている「甚の助谷巨大地すべり」は，これらの砂防ダムを乗せたまま，年間 10－40cm の速度で移動していることが，国土交通省の GPS 観測データから明らかになっている。甚の助谷を起源とする手取川の中流部では，貯水量が１億トンを超す手取川ダムが 1980 年に完成し，広大なダム湖を形成している。手取川の下流域では，金沢市，松任市，小松市の人口密集地が分布しているため，豪雨・地震による甚の助谷地すべりの大崩壊をきっかけにした大規模土石流がダム湖を直撃した時の被害予測が重大な問題になっている。

しかし，今のところ，甚の助谷地すべりの破壊運動メカニズムは解明されていないため，甚の助谷及び別当谷での砂防工事手法は明治時代以来経験的なものにとどまっている。甚の助谷地すべりの上部ブロックにおいて集水井，排水トンネルが施工されているが，これらの構造物は施工後に地すべり運動によって，かなり破壊されている。すなわち，排水工のみでは，地すべり運動を抑止できないことが明らかである。したがって，有効な地すべり防災対策を施すには，まず地すべりの発生・運動機構を明かにすることが，不可欠である。

本研究の目的は，地形学，地質学，岩盤力学，地盤工学の多角的な視点から，甚の助谷巨大地すべりの発生・運動メカニズムを解明するとともに，甚の助谷地すべりの豪雨・地震による突発災害の前兆現象を把握し，地すべりによる土石流の運動範囲予測を行うことである。具体的に，下記のことを目的とした。

（１）地質調査及び地形測量によって，上部ブロックと下部ブロックの異なる移動挙動を解明する；

（２）地すべりの安定性に影響する地下水，地震，すべり層の強度低下などの素因を定量的に評価し，巨大地すべりの前兆現象を把握する；

（３）岩盤力学，土質力学及び地すべり運動学の解析に基づいて，地すべりの運動範囲を予測し，ハザードマップを作成する。

平成１５年度から１７年度までの各年度に得た成果は以下の通りである。

（平成１５年度）

（１） 甚之助谷地すべりは中生代ジュラ紀から白亜紀前期で堆積した手取層群の砂岩・頁岩の互層において発生している。当地すべりは上部ブロックと下部ブロックに分けられ，上

部ブロックは年間 80 mm ～ 170 mm の速度で活発に変位しているのに対して，下部ブロックはほとんど安定している。また，上部ブロック全体の動きの方向は手取層群の傾斜方向と一致しており，谷側の斜面部分では谷向きの変位成分も観測されている。孔内傾斜計の観測結果より，場所によって，風化の進行の差が大きいことが分かった。

（２） 地すべりの運動誘因に関しては，孔内伸縮計観測結果と孔内水位変化の比較より，斜面変位はある臨界水位を超える地下水位の上昇量とほぼ比例関係にあることが分かった。この結果は当地すべり対策工の設計に重要な情報を与える。

（３） 別当谷では，砂岩層が節理によって極度に破砕され，頁岩層は粘土化された上，常に飽和状態であることが観察された。そこで採取した頁岩試料の物理特性及びせん断抵抗などのパラメータを求めた。今後，されにリングせん断試験機を用いて，クリープ試験及び長距離せん断試験を予定している。

（４） 現地調査，変形観測データ，及び土質試験結果に基づいて，当地すべりの運動様式を解明するための数値解析を行った。風化による砂岩・頁岩の変形特性の劣化を想定して解析を行った結果，観測データとほぼ一致している変形傾向が見られた。今後，さらに地下水位の影響も考慮して，突発災害の前兆現象を抽出する予定である。

（平成１６年度）

（１） 甚の助谷地すべりの中央尾根ブロックの地下水位変動による変形挙動を再現するためのリングせん断試験を行なって，地下水変動による斜面変位の再現試験を行なった。

（２） 大規模地すべりが発生した場合を想定した運動予測に関して，まず基礎となる地すべり運動範囲予測プログラムの開発・改良を行ない，その妥当性を検証した。

（３） 1934 年に発生した別当崩れ及び平成 16 年度に発生した土石流災害に対する逆算から求めた運動中の力学パラメータを甚之助谷地すべりに適用し，運動範囲予測を行った結果，地すべり土塊は下流に建設された手取川ダム貯水池に突入することとなり，十分な警戒が必要であることを示唆した。

（平成１７年度）

今年度は２００４年５月に別当谷で発生した地すべり－土石流を中心に，調査・研究を実施し、以下の結論を得た。

（１）別当谷の渓流堆積物は，上流から下流にかけて粒子破砕し易さが減少する傾向が見られ，これは渓床堆積物の非排水挙動に影響を及ぼした；

（２）発生域の調査からは，集中的に流出していた地下水は斜面崩壊を誘起し，さらにその後の流動化にも影響を及ぼした；

（３）リングせん断試験機を用いた地下水の上昇による斜面崩壊の再現試験では，源頭部土試料は自然排水状態でも，せん断抵抗の急激な低下が見られ，地すべり発生後の高速運動の原因となっていることが認識される；

（４）源頭部の崩壊土砂が渓床堆積物に衝撃載荷によって，ほぼ液状化している試験結果から，地すべり土塊が別当谷の中に滑り込んだ直後，土石流を誘起したことと推定される；

（5）液状化して土石流になった崩壊土砂が別当谷の中に運動している時に，渓床堆積物に衝撃を与えながら，進行している流下過程の再現試験は，土石流進行中の斜面勾配の変化（緩くなること）によって，流動過程における見かけの摩擦係数の増大傾向が見られた；

（6）土石流運動の最終段階の再現試験では，せん断中に発揮している見かけの摩擦角度は斜面勾配とほぼ等しくなり，土石流の停止過程を示唆した。また，渓床堆積物に実施した残留せん断強度は減少傾向が見られ，粒度分級の変化によるものと認められる。

また，平成 17 年度では，イタリアのストロムボリ火山地すべり，及び中国三峡貯水池地域の地すべりに対する調査研究も実施した。

Wang, F. W., T. Okuno, T. Matsumoto
(2006)

Deformation characteristics and influential factors for the giant Jinnosuke-dani landslide in the Haku-san Mountain area, Japan

Landslides: Journal of the International Consortium on Landslides (in Press)

Deformation characteristics and influential factors for the giant Jinnosuke-dani landslide in the Haku-san Mountain area, Japan

Fawu Wang
Research Centre on Landslides, Disaster Prevention Research Institute, Kyoto University
Gokasho, Uji, Kyoto 611-0011, Japan
Tel.: +81-774-38-4114; fax: +81-774-38-4300
E-mail: wangfw@landslide.dpri.kyoto-u.ac.jp

T. Okuno[1, 2], T. Matsumoto[1]
[1] Division of Civil and Environmental Engineering, Graduate School of Natural Science and Technology, Kanazawa University

Kakuma-machi, Kanazawa, Ishikawa 920-1192, Japan

Tel: +81-76-234-4625; Fax: +81-76-234-4632
E-mail address: matsumot@t.kanazawa-u.ac.jp

[2] Arai Sabo Agency, Jyoetsu Regional Development Bureau, Niigata Prefecture, Japan

Abstract: The Jinnosuke-dani landslide is a giant landslide 2,000 m long and 500 m wide in the Haku-san Mountain area, Japan. It was also the first landslide to be designated as a "Landslide Prevention Area" according to the "Japan Landslide Prevention Law". This landslide consists of alternating layers of sandstone and shale in the Tedori Formation, which was deposited from the Jurassic period to the Early Cretaceous. Based on deformation monitoring results for more than 7 years, the landslide is divided into upper and lower blocks. The upper block has moved at a speed of 80 to 170 mm/year, while the lower block has moved more slowly (3 to 15 mm/year). Monitoring data show that the variation of the groundwater level has a great influence on the landslide movement. The deteriorating effect of the weathering of the alternating layers of sandstone and shale on the landslide deformation has been confirmed by borehole exploration and monitoring.

KEYWORDS: Jinnosuke-dani landslide, Japan, weathering; rockslide; reversal of topography; groundwater; deformation; monitoring

1. Introduction

Haku-san Mountain, an active volcano with summit elevation of 2,703 m, is located at the boundary between Ishikawa Prefecture and Gifu Prefecture in the Hokuriku district, Japan (Fig. 1). The studying area, Jinnosuke-dani area, is the source area of the Tedori-gawa River, which is the largest river in Ishikawa Prefecture. The Tedori-gawa River is about 72 km long from its source to its estuary.

According to historical records, many landslides have occurred in the studying area; most of them transformed into rapid debris flows and caused human casualties and economic losses in the down-stream area. In 1934, a debris flow that was initiated by a landslide in the Bettou-dani near the Jinnosuke-dani landslide reached the Japan Sea and caused great losses (Note: "Dani" means valley in Japanese). For more than 100 years, slope disaster-prevention measures have been conducted in this area by the central and local governments. Resulting from these efforts, the frequency of occurrence of landslides in this area has decreased markedly. However, a few giant landslides, such as the Jinnosuke-dani landslide, are still active.

Generally, “Jinnosuke-dani landslide” refers to the larger area of the “Landslide Prevention Area” designated by the central government in 1962 according to the “Landslides Prevention Law” (as shown with the dotted red line area in Fig. 2). It is located on the southwest slope of Haku-san Mountain. In the designated prevention area, many types of slope-failure phenomena, such as subsidence ponds, rockfalls, toppling, and even debris flows, can be observed. Table 1 describes related events concerning the landslide phenomena and prevention work in the Haku-san Mountain area, especially for the Jinnosuke-dani landslide. In this paper, we refer to the central ridge part of the large landslide prevention area as the “Jinnosuke-dani landslide”; although it is formally called the “Central Ridge Block of the general Jinnosuke-dani landslide” (Here, “General Jinnosuke-dani land-slide” was used to mean the large general landslide area, and “Jinnosuke-dani landslide” to represent the central ridge part of the general landslide).

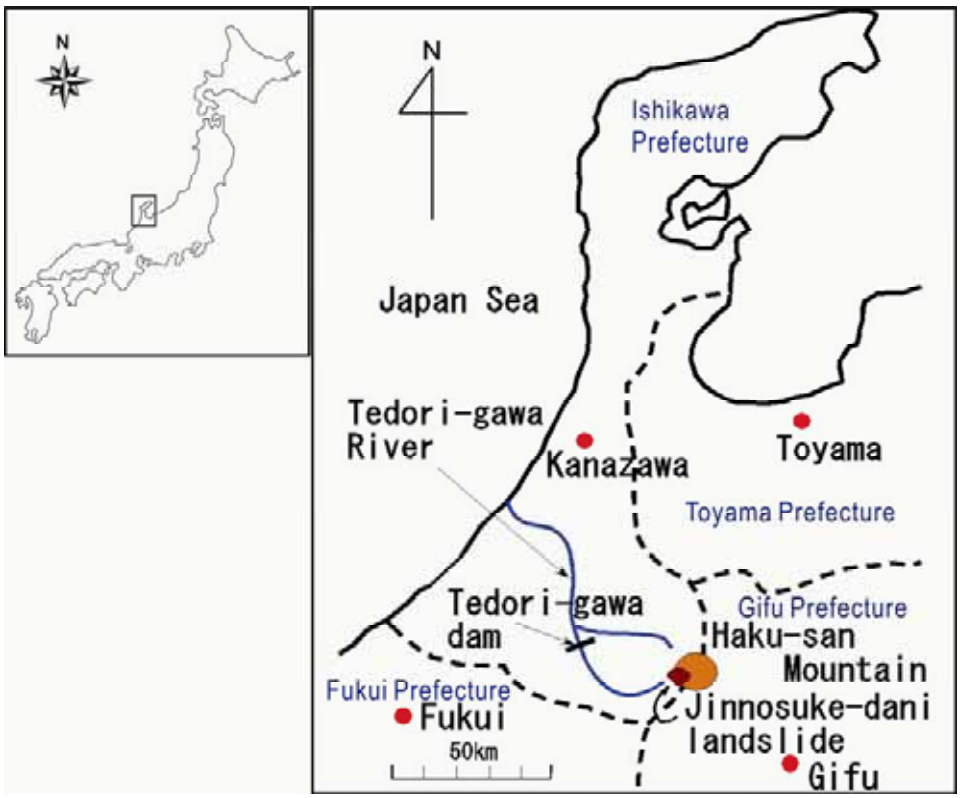

Fig. 1 Location of the Jinnosuke-dani landslide in Haku-san Mountain area, Hokuriku district, Japan

The Jinnosuke-dani landslide is about 2,000 m long and 500 m wide, and is sandwiched between the Bettou-dani valley on its right side and the Jinnosuke-dani valley and Yanagi-dani valley on its left side. Around the Jinnosuke-dani landslide, there are also several active sliding blocks that show high activity in the monitoring data. In the valleys of Jinnosuke-dani valley, Yanagi-dani valley, and Bettou-dani valley, more than 80 debris-retention dams (DRD) have been constructed to prevent debris-flow disasters. The Jinnosuke-dani landslide is the most actively moving landslide with a displacement velocity of about 10 cm/year, and some of the DRDs in the valleys have also moved with the landslide. In 1980, Tedori-gawa Dam, a rockfill gravity dam, was constructed at the upper-middle part of the Tedori-gawa River. The distance from the landslide to the Tedori-gawa reservoir is about 20 km (see Fig. 1). There is a high risk of the Jinnosuke-dani landslide traveling to the reservoir. In the slight case of the dam being damaged by a seiche caused by a potential rapid landslide, the possibility of flooding would put the 1,200 people of the downstream area in danger.

Fig. 2 Aero-photograph of the "Landslide Prevention Area" of the Jinnosuke-dani landslide (Photo Courtesy of Kanazawa Office of River and National Highway, MLIT)

To achieve an understanding of the landslide mechanism and to provide disaster warning and prevention, deformation monitoring has been conducted on the Jinnosuke-dani landslide by the Ministry of Land Infrastructure and Transport of the central government of Japan. Based on the results of monitoring, countermeasure works have been carried out and improved continually (Isobe 1996). This paper aims to analyze the deforming character of the Jinnosuke-dani landslide based on the results of monitoring, and to clarify the factors that influence landslide deformation.

Table 1 Chronology of disaster and prevention events associated with Haku-san Mountain area

706	Eruption in Haku-san Volcano
1042	Eruption in Haku-san Volcano
1554	Eruption in Haku-san Volcano
1579	Eruption in Haku-san Volcano
1659	The latest eruption in Haku-san volcano
Under the jurisdiction of Ishikawa Prefecture	
1891	Triggered by Nouo earthquake, slope failure occurred in Jinnosuke-dani valley.
1896	Large scale avalanche triggered by intense rainfall.
1911	Ishikawa Prefecture started the field investigation on slope instability
1912	Reforestation was begun at Jinnosuke-dani valley and Yanagi-dani valley.
Under the national jurisdiction	
1927	Changed to be a national government run project, and the full-dress Sabo works were started with the establishment of the Haku-san Sabo Work belonging to the Niigata Civil Engineering Branch Office of Home Affairs Ministry. From 1927 to 1939, the first step-check-dams were originally constructed in Yanagi-dani valley and Jinnosuke-dani valley to control the slope failure.
1934	Lots of Large scale avalanches were triggered by heavy rainfall in Bettou-dani valley and nearby area and became to debris flow. Houses of 172 families and also the Haku-san Sabo Work were destroyed (The main scarp and sliding surface of the landslide occurred in that time is also visible in the Bettou-dani valley).
1937	The construction of the check-dam grouping Bettou-dani valley was started.
1944	Because of the World War II, the construction of the check-dam was ceased.
1957	No.5 check dam in Jinnosuke-dani valley displaced obviously. The investigation on the Jinnosuke-dani landslide was initialized in national level.
1961	The countermeasure work on the Jinnosuke-dani landslide was started.
	Because of North Bino earthquake, landslides in small scale occurred in the Haku-san area.
1962	The Jinnosuke-dani landslide was designated as “Landslide Prevention Area” by central government.
1973	The countermeasure work plan for the Jinnosuke-dani landslide was finished temporarily.
1980	The Tedori-gawa dam was completed.
1982	Because obvious displacement appeared in the Jinnosuke-dani landslide, anew countermeasure work plan for the Jinnosuke-dani landslide was started.
1990	Hillside reforestation was started in Bettou-dani valley.
1999	A small scale landslide was induced by heavy rainfall in Bettou-dani valley, and a landslide dam was temporarily formed.
2001	A landslide with 20,000m^3 in volume occurred in the left bank of Bettou-dani valley.

2004	After a 216 mm precipitation in two days, a landslide with 176,000m^3 in volume occurred in the left bank of Bettou-dani valley and became to debris flow. The sliding distance of the debris flow front exceeded 2,000 m.

2. General conditions of the Jinnosuke-dani landslide

2.1 Climatic conditions and topographic features

The Hokuriku district of Japan is characterized by heavy precipitation and the Tedori-gawa River has a steep gradient. In winter, due to the strong influence of monsoons from Siberia, there is heavy snowfall in this area. The accumulative winter snowfall may exceed 12 m in the Haku-san Mountain area. In the other seasons, half of the days are rainy. For this reason, local annual average precipitation is 3,295 mm, about twice the national average of 1,700 mm (Fig. 3).

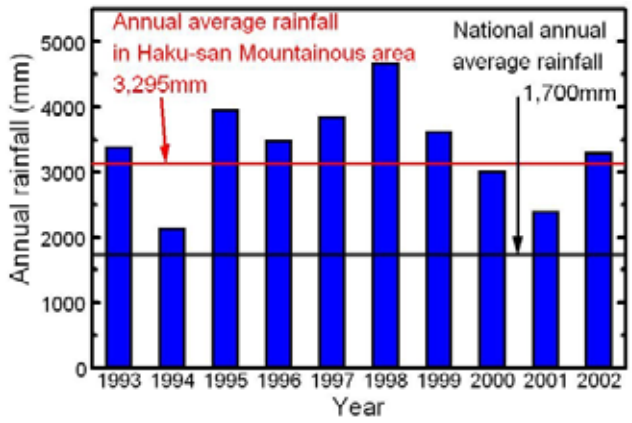

Fig. 3 Annual rainfall in Haku-san Mountain area from 1993 to 2002

The Tedori-gawa River is one of the steepest rivers in the world (Fig. 4). Its gradient is 1:70, while, for example, the gradient of the upper Colorado River (USA) is 1:1700. In Japan, steep rivers al-ways have serious debris-flow problems. For example, the Gamahara torrent debris flow occurred in December of 1996 in Hime-gawa river system in Nagano Prefecture (Sassa et al. 1997); a rapid landslide – debris flow occurred in July of 1997 in Izumi city of Kagoshima Prefecture (Sassa et al. 1998), and a slide-triggered debris flow occurred in July of 2003 in Minamata City, Kumamoto Prefecture (Sassa et al. 2004). Also, in the Gamahara debris flow case, workers constructing debris retention dams were killed by debris flow. This phenomenon caused great social and legal problems. In the case of Jinnosuke-dani case, the steep river beds supply high gravity potential for the displaced debris after slope failure. The steepness is also the major reason for the long-traveling debris flow that occurred in 1934 in the Bettou-dani valley and reached the Japan Sea after traveling for 72 km. At this event, a village was completely destroyed by the debris flow.

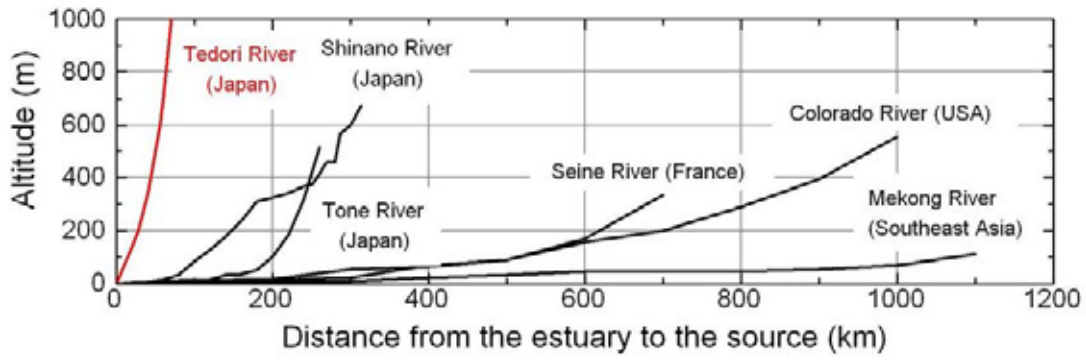

Fig. 4 The longitudinal torrent bed-slope of the Tedori-gawa River comparing with some famous rivers in the world

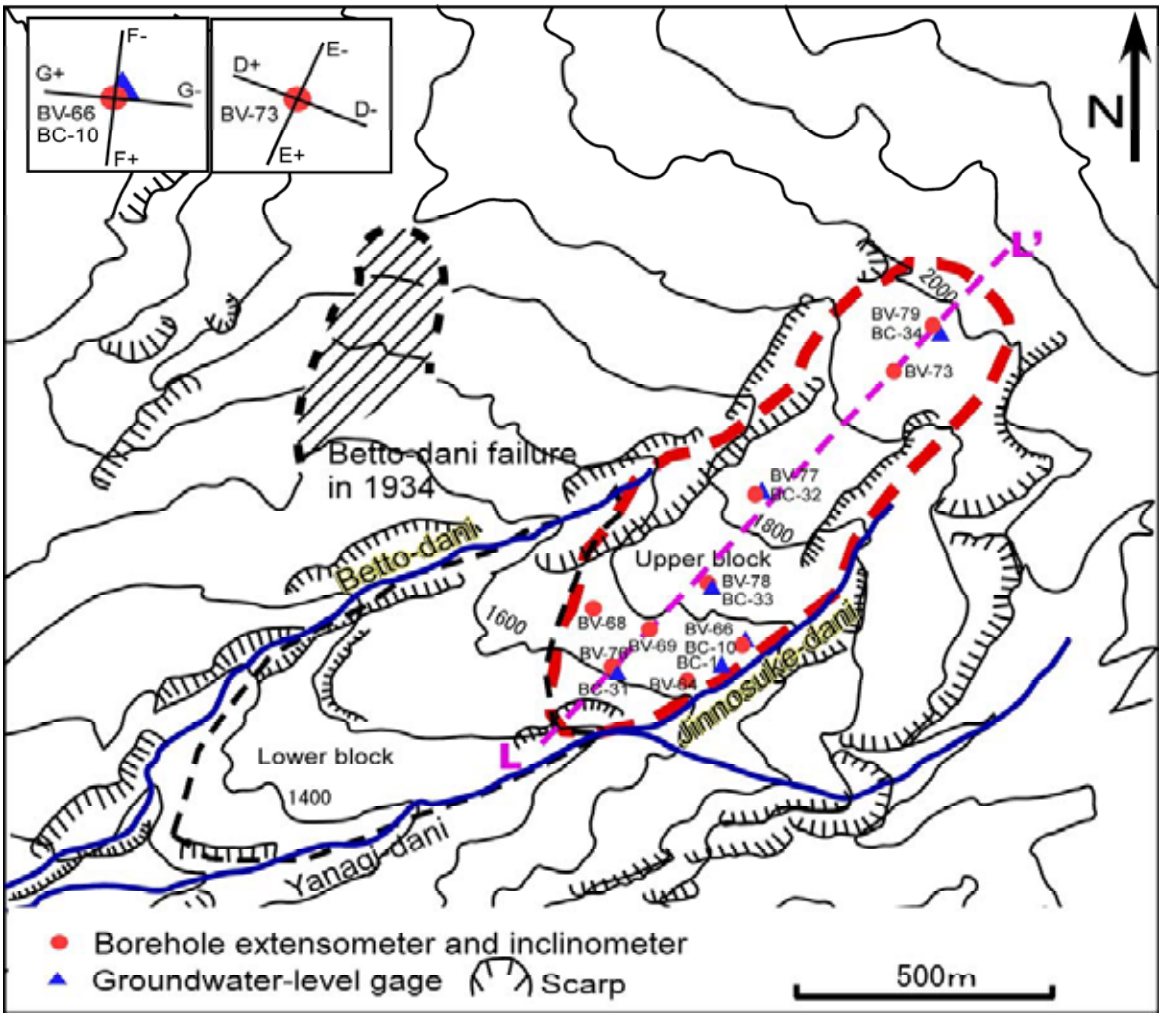

Fig. 5 Geomorphological map of the Jinnosuke-dani landslide area, together with the locations of the monitoring devices (After Kanazawa Work Office, Ministry of Land, Infrastructure and Transport of Japan, 2002)

Fig. 5 is a contour map of the Jinnosuke-dani landslide and the nearby area of the designated "Landslide Prevention Area". Because of the large scale of the landslide, the crack distribution was not shown in this map. According to slope-surface-displacement monitoring, the upper part is active, while the lower part is almost stable. Because the central ridge is continued and the boundary between the active part and stable part is not clear, we divided the landslide into two blocks: an upper block and a lower block. Locations of some measurement devices in the upper block are also shown in this figure. The elevation of the landslide ranges from 1,200 m to 2,100 m. The average slope angle for the upper block and lower blocks is 22 and 20 degrees, respectively.

2.2 Geological and hydro-geological conditions

The basal bedrock in the Haku-san Mountain area is the lower Paleozoic Hida gneiss. As a part of the 1:50,000 geological map of Haku-san Mountain area, a geological map of the Jinnosuke-dani landslide and nearby area was completed by Kaseno (2001). From the Jurassic to Early Cretaceous periods, the Haku-san Mountain area was a lake near the sea. The series of lacustrine sediments de-posited in that period is called the Tedori Formation deposits. The deposits are sedimentary strata consisting of shale, sandstone, and conglomerate layers that have undergone hydrothermal alteration during the mountain-building process of Haku-san Mountain. General descriptions of the geology can be found in Kaseno (1993).

Fig. 6(a) is a DEM model for a large area around the Haku-san mountain area. The model is built on the elevation data with contour difference of 50 m. The image of lava deposit distribution around the summit of

Haku-san (vent of the Haku-san volcano) is visible. Fig. 6(b) is the geological map of the corresponding area to Fig. 6(a). The Nohi Rhyolite of the Cretaceous period is distributed at the upper right corner in the figure and the alternating layers of sand-stone and shale of the Tedori Formation are distributed below and to the left. Both units form the bedrock of the Haku-san Mountain area. Volcanic lava deposits, which erupted 100,000 and 10,000 years ago, overlie the strata of the Tedori Formation and the Nohi Rhyolite. Fig. 6(c) shows an estimated longitudinal section of the Z-Z' section (shown in Fig. 6(b)). The deposition subsequence of the strata and volcanic deposit is clear. The Jinnosuke-dani landslide area is indicated in the dotted line box. At the northwest corner of the dotted line area, the disconnection of H2 old volcanic deposit can be observed. The reason for this phenomenon maybe caused by erosion and land-slide, and this will be discussed in details later.

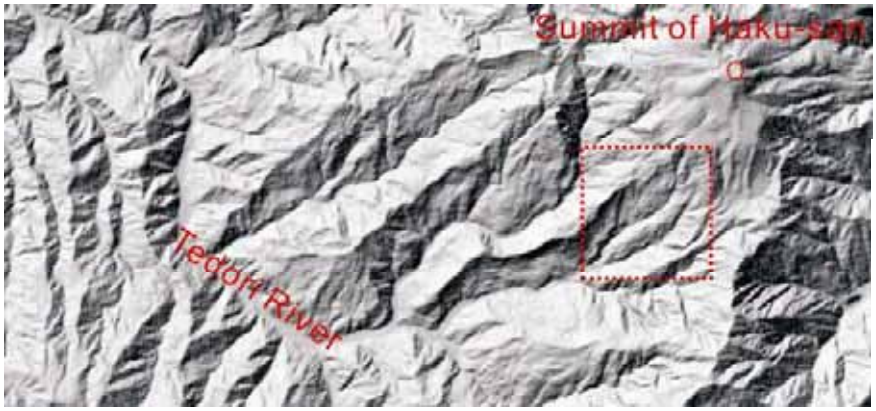

(a)

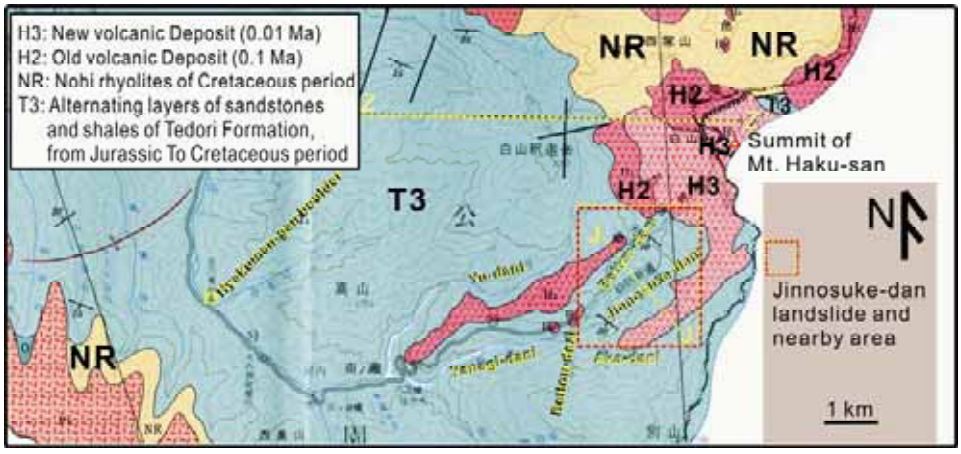

(b)

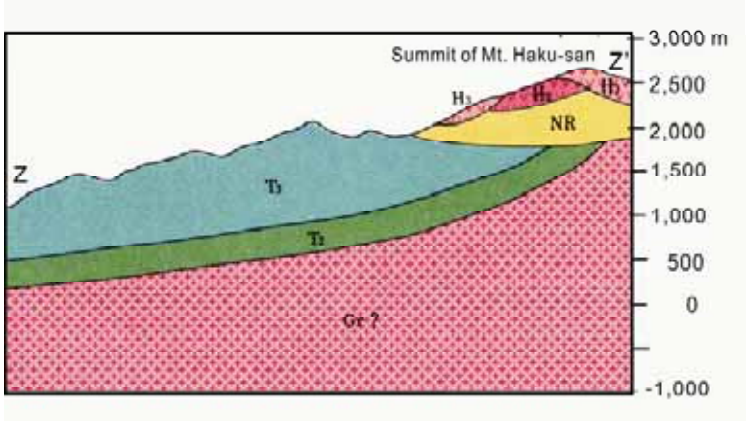

(c)

Fig. 6 Topography and geological condition of the Haku-san and nearby area. (a) DEM model, (2) Geological map (after Kaseno, 1993), (3) Longitudinal section of Z-Z' in (b) (after Kaseno, 1993).

Fig.7 shows the detailed geological condition for the studying area. It is clear that all of the lava depositions came from the summit of the Haku-san Mountain as the vent of Haku-san volcano. In the southwest part, many landslides occurred in the Tedori Formation. Contrasting to this phenomenon, there are few landslides in the volcanic deposit (lava deposit) area. This difference may be due to the erosion-resistant difference of the two types of strata, which means that the lava deposition has high erosion resistant comparing with sandstone and shale of the Tedori Formation. In the dotted line box area, besides the Jinnosuke-dani landslide, there are other five landslide blocks, and for some landslides, the main scarps are outcropped.

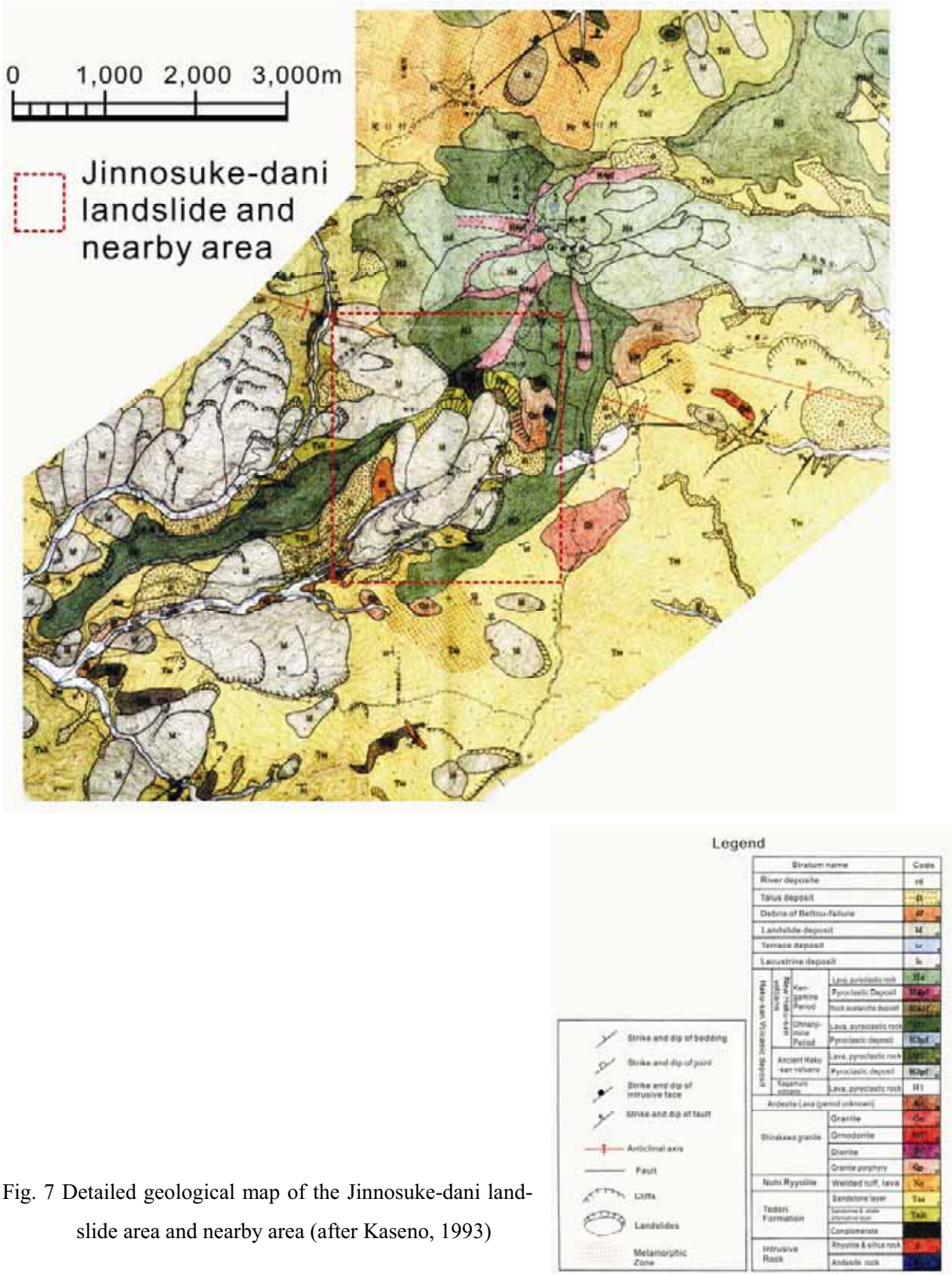

Fig. 7 Detailed geological map of the Jinnosuke-dani landslide area and nearby area (after Kaseno, 1993)

In the topography-forming process, during a volcanic eruption, lava will generally be deposited in valleys with a relative low elevation, rather than on mountain ridges. As shown in this area, lava de-posits are more difficult to be eroded than sandstone and shale. Looking at the geological map of this area, it is notable that the lava deposits are located on the mountain ridge around the Jinnosuke-dani landslide. The reason is, after a long period of eruption of the Haku-san volcano, due to the physical weathering and surface erosion in the Tedori Formation deposits that made up the former mountain ridge, this ridge became lower than the former valleys that were filled by lava. Fig. 8 shows a schematic diagram of the topography-changing process, which is called "reversal of topography" at the J-J' section crossing the Jinnosuke-dani landslide and valleys at both sides (see Fig. 6(b)). In this topography-changing process, the former ridge that overlay the Jinnosuke-dani landslide was eroded away (Fig. 8b). The possible eroded thickness at the ridge of this area is estimated about 100 m in recent 0.01 Ma period (The elevation decrease caused by landsliding should also be considered for an exact estimation). Mechanically, this erosion was an unloading process of the alternating layers of sandstone and shale in the Tedori Formation. This unloading process resulted in deterioration of the strength and deformation-resisting properties of these sandstones and shales. Moreover, the intensive progressive erosion in the valleys at both sides have caused the landslide to evolve in its current location.

Many joints and small faults have also developed in the Tedori Formation (Okuno et al. 2004). Fig. 9 is a rose diagram showing the strike direction of the strata and discontinuities. The average strike direction of the strata was N54W, the average dip direction was S36W, and the dip angle was 40 to 45 degrees. Most discontinuities developed perpendicular to the strike direction of the Tedori Formation strata, and the strike direction of the discontinuities mainly ranged from N11E to N56E. This direction is parallel to the Bettou-dani, suggesting that valley erosion was influenced by joint systems.

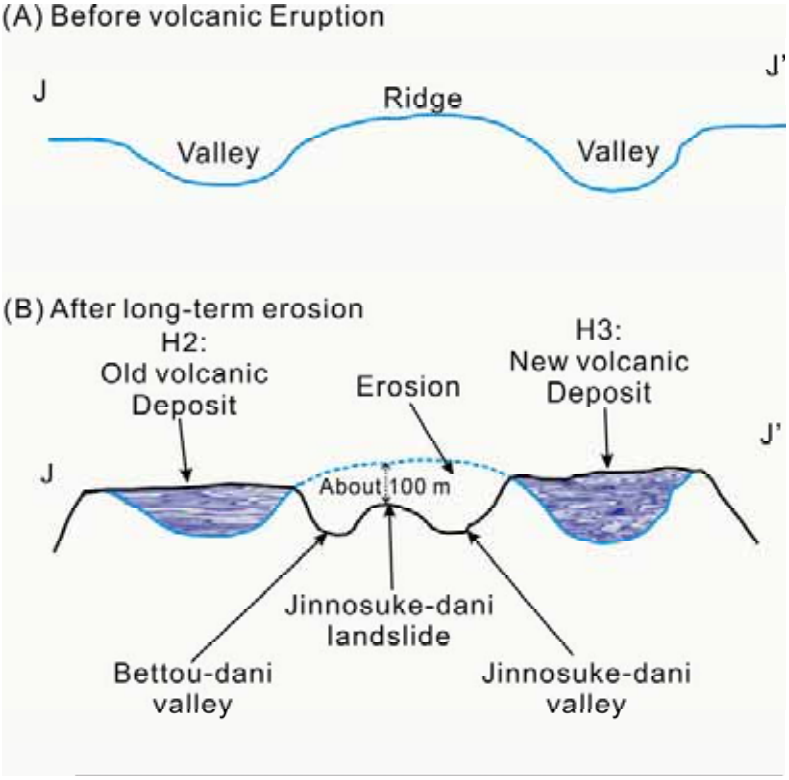

Fig. 8 Schematic diagram showing reversal process of topography in the Jinnosuke-dani landslide area

Fig. 10 shows a geological columnar section obtained from outcrop observations and measurements in the Bettou-dani valley. Soil sampling was carried out near an elevation of 1,780 m. Four-teen probable sliding surfaces were detected in the strata in the 23.1-m-thick section. Even in the dry season, water oozed from the probable sliding surface, where the low permeability stopped ground-water flow and change the flow along the shale layer. As shown in the photograph of Fig. 10, the sliding surface probably developed

in the thin shale existing between two sandstone layers. Shear-box tests were performed on disturbed soil samples that were taken from a general argillaceous probable sliding surface outcropped in Bettou-dani valley. From the shear tests, an effective internal friction angle of 26.3 degrees for the residual state was obtained.

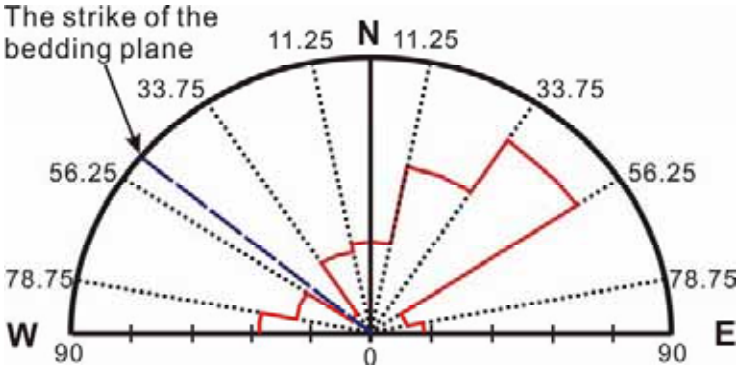

Fig. 9 Rose diagram of the strike directions of the Tedori formation strata and the discontinuities

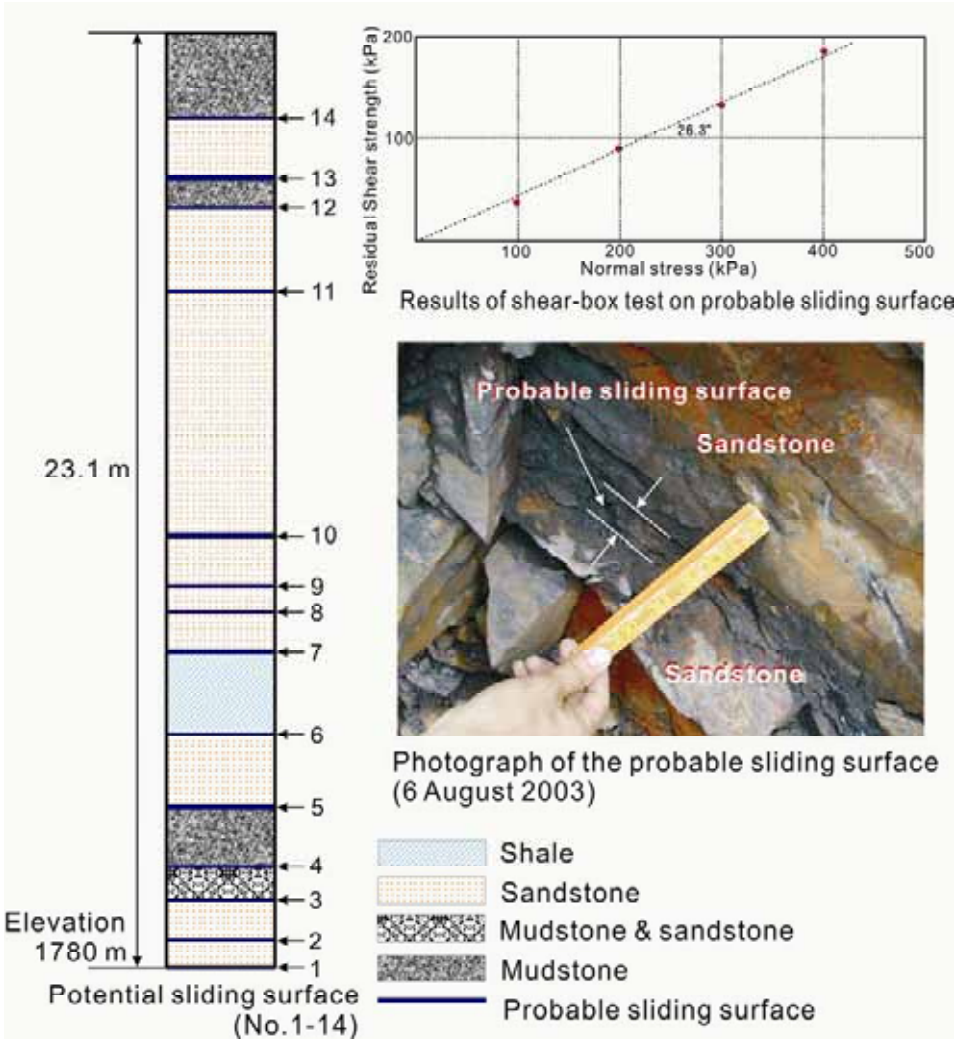

Fig. 10 Geological columnar section of the Tedori formation obtained from outcrop observation at the Bettou-dani valley, photograph of the probable sliding surface examination, and results of shear box tests on the soil from the probable sliding surface

Fig. 11 shows the grain size distribution of the argillaceous shale. The fines content of the sample, including silt and clay, was 58%, the plasticity index was 8.3, the liquid limit was 20.1%, and the liquidity index was 0.99. This soil from the probable sliding surface was classified as “clay with low liquid limit”. Because the sandstone is highly jointed and this area is subject to heavy rainfall and snowfall, it may be conservative to assume that the shale in the alternating layers is always in a fully saturated condition, which is dangerous in regard to stability of the slope.

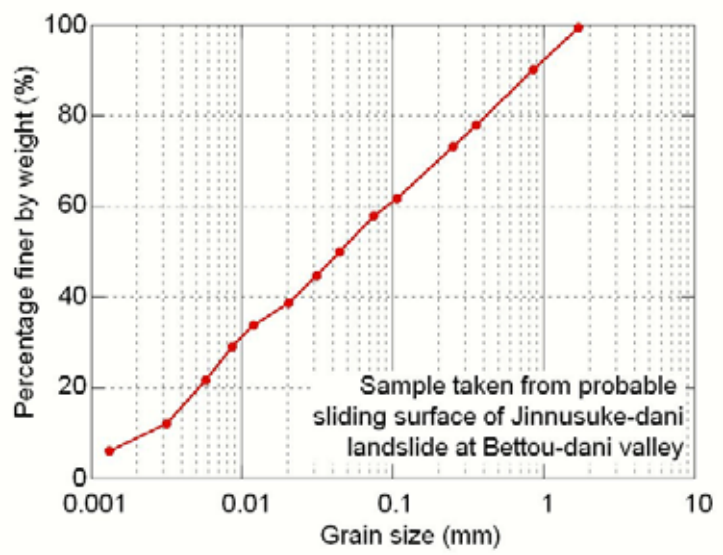

Fig. 11 Grain size distribution of the soil sample taken from the probable sliding surface of Jinnosuke-dani landslide at Bettou-dani valley

3. Deformation character of the Jinnosuke-dani landslide

To understand the deformation character of the Jinnosuke-dani landslide for the purpose of land-slide prevention and early warning, especially concerning the safety of the Tedori-gawa Dam and reservoir, deformation monitoring of the landslide has been conducted by slope surface-displacement monitoring and borehole monitoring. This monitoring was carried out by the Ministry of Land, Infrastructure and Transport of Japan beginning in the 1980s (Kanazawa Work Office, Ministry of Land Infrastructure and Transport of Japan 2002). The following shows the details of the measurement principles and some results of monitoring.

3.1 Slope surface-displacement monitoring

The Electronic Distance Measuring (EDM) method and Global Positioning System (GPS) monitoring method have been used at this site to monitor slope displacements. Fig. 12 shows the initial locations of the monitoring points in the designated “Landslide Prevention Area” and the displacement vectors of the slope surface from 1994 to 2001. There are 9 survey points (A1 to A9) in the lower block of the landslide and 12 survey points (B1 to B12) in the upper block. Six points (C1 to C6) were located outside of the Jinnosuke-dani landslide. The monitored results show that the upper block displaced quite actively; the cumulative displacements of survey points B5 and B11 exceeded 1,100 mm in the 7 years. The main features of the monitoring results in the upper block are: (1) The points at the central part almost moved along the downslope direction; (2) The points near valleys had a component to the valley side, besides along the downslope direction. However, the lower block has been relatively stable. While, C1, C2, C3 and C4 which located on different landslide blocks also indicated the motion of the corresponding blocks. The boundary between the upper block and the lower block is not clear at the slope surface. So, the landslide is divided to blocks just according to the surface displacement. The average movement direction of the upper block of the Jinnosuke-dani landslide is S36W. This direction of movement corresponds well with the dip direction of the Tedori Formation.

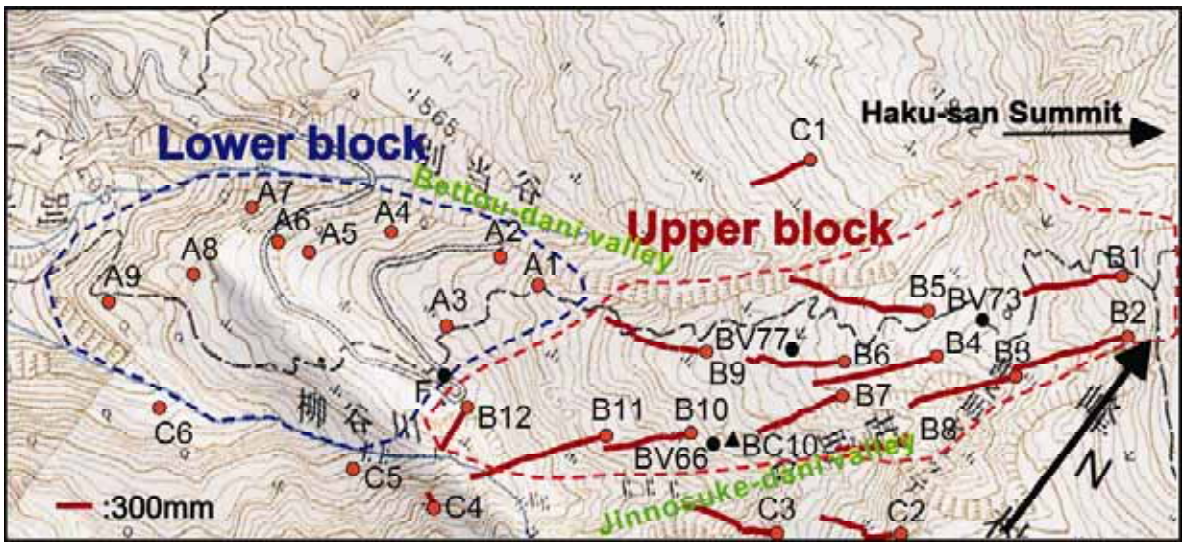

Fig. 12 Cumulative displacements of the landslide from 1994 to 2001

Fig. 13 shows the time series of cumulative displacements for points B1 to B12 and C1 to C3. The displacement rates for all of the monitoring points were almost constant during the 7-year period. The displacement rate at point B5 at Bettou-dani side was 170 mm/year, and that of point B11 at Jinnosuke-dani side was 165 mm/year. They are the fastest points and obviously have a component directing to the valley sides (Fig. 12). The monitoring points near the central line were displaced 130 mm/year, almost at the same rate as at the valley sides. According to the displacement-rate distribution, it can be concluded that the dip-slope structure and the erosion in both side valleys are the two main factors causing the landslide displacement. From this viewpoint, debris-retention dams constructed in the side valleys are very important countermeasure works for landslide stabilization in the long run, by protecting against toe erosion at the valleys in both sides.

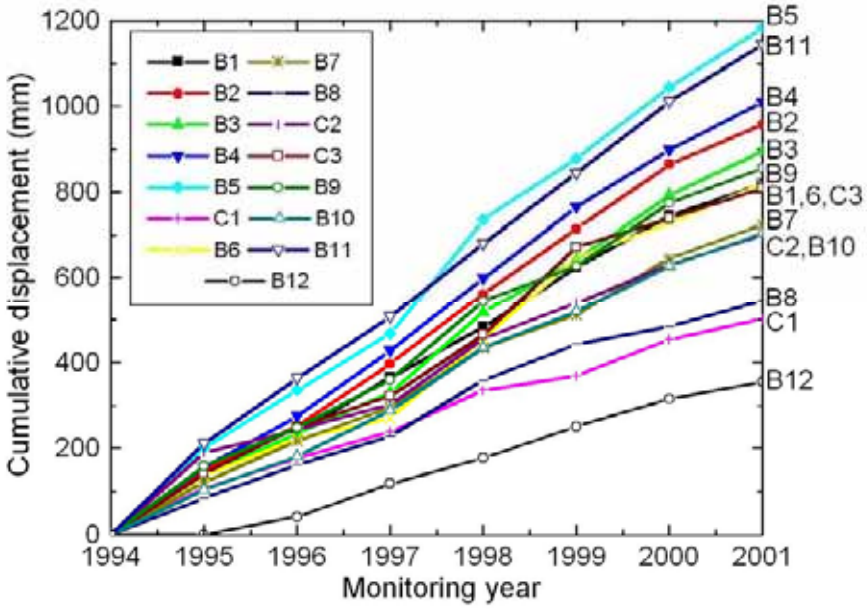

Fig. 13 Time series of cumulative displacements of survey points B1-B12 and C1-C3 from 1994 to 2001 (Measurement at point B12 started from 1995)

As a special case, point B12 in the lowest part of the upper block displaced in a direction different from the other points in the upper block (see Fig. 12). The displacement at point B12 turned left about 50 degrees from the central line. From this result, it can be estimated that the motion of the upper block is hindered by the lower block.

3.2 Borehole-inclinometer monitoring results

Borehole-inclinometer monitoring was used to determine the depth of the sliding surface and the direction of movement of the landslide blocks. By comparing the measured results at different times, the deformation rates at different depths can also be evaluated.

Fig. 14 shows the monitored results of inclinometer BV73 located in the upper part of the upper block near the central line (see Fig. 5 and 11). Figs. 14a and 14b are the results in the D-direction (perpendicular to the downslope direction) and E-direction (downslope direction), respectively. The monitoring began on October 23, 1997. Two results monitored on October 27, 2000, and August 6, 2001, are plotted to show the deformation velocity. Sliding occurred in two directions: one is down-ward along the slope, and the other is toward the Jinnosuke-dani. The maximum depth of the sliding surface is at about 38 m at this position. In addition, three shallow sliding surfaces exist at depths of 8 m, 13 m, and 20 m. The sliding surfaces were estimated to correspond to the argillaceous shale layers based on the boring logs, and the parts between the sliding surfaces to correspond to the sand-stone layers. Relatively smaller deformation was also observed in the sandstone layers.

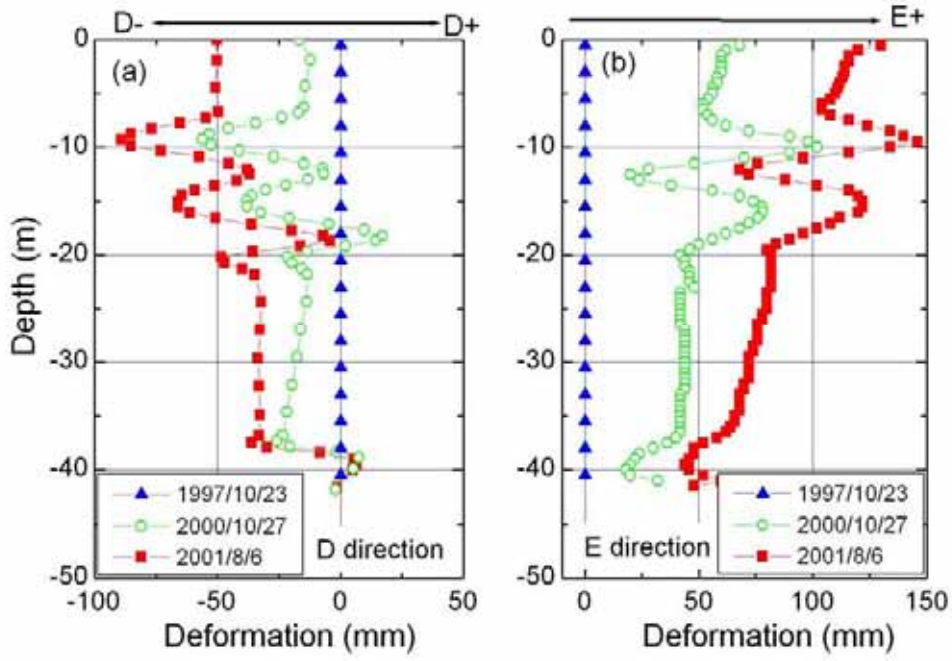

Fig. 14 Monitored results of borehole inclinometer at point BV73

Fig. 15 shows the monitored results of inclinometer BV77 located below BV73. The two components similar to BV73 were shown. The monitoring began on November 13, 2001, and two results monitored on August 6, 2002 and August 23, 2003, respectively were shown. From Fig. 15(a), it is clear that the main sliding surface is located at about 128 m deep. At depth of 108 m, 102 m, 75 m, relative sliding between the two adjacent layers occurred obviously, and it indicated that the sand-stone and shale structure should not be disturbed so much at this position.

Fig. 16 shows the monitored results of inclinometer BV66 located in the lower part of the upper block near the Jinnosuke-dani (see Fig. 5 and 12). Figs. 16a and 16b show the monitored results in the F-direction (dip direction) and G-direction (strike direction), respectively. The monitoring began on November 12,

1989. Results obtained on August 2, 2000, and August 3, 2001, are plotted in Figs. 16(a), and (b). The main sliding direction is in the direction of dip. Except an obvious displacement occurred at 60-65 m, there was no obvious sliding surface in the sliding mass shallower than 60 m, which nearly at the same elevation of the adjacent valley bottom at this position, and the slope here deformed as a homogenous plastic sliding mass similar to that of a homogenous soil mass. It is estimated that the deformation properties of the sandstone and shale layers became uniform because of long-term weathering.

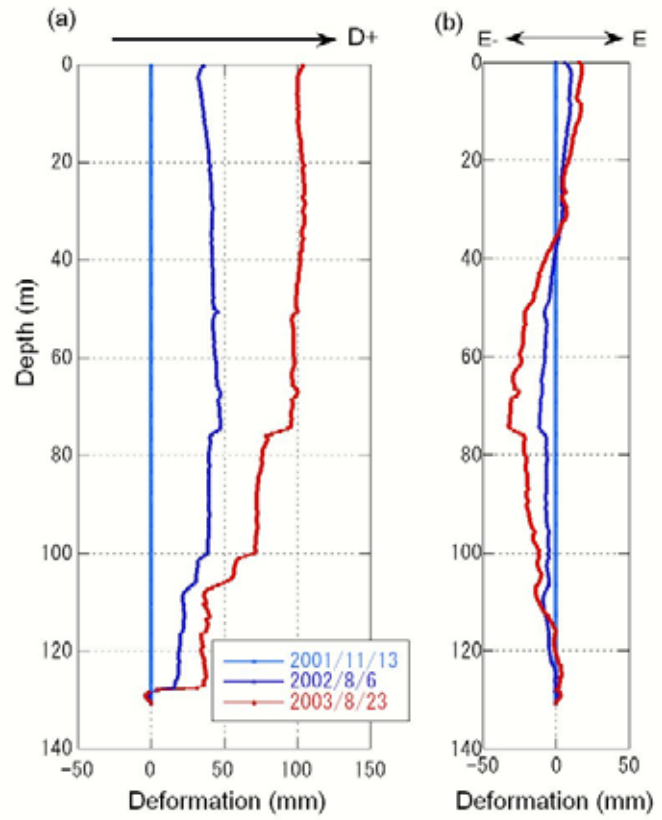

Fig. 15 Monitored results of borehole inclinometer at point BV77

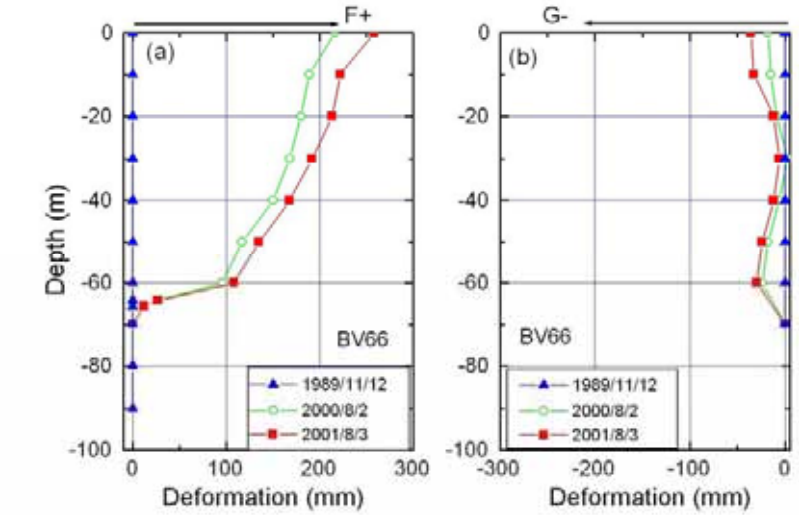

Fig. 16 Monitored results of borehole inclinometer at point BV66

Comparing the monitored results of boreholes BV73 and BV66, it is estimated that the weathering degree of the sandstone in the Tedori Formation may control the deformation style of the landslide, and the weathering degree varies from place to place, and the weathering degree at valley side is relatively higher than the other locations. The sandstone at the valley side near BV66 is weathered more heavily than the upper part near BV73. Fig. 17 summarizes the influence of physical weathering on the deformation style by means of three simplified models, which represent deformation styles in the sandstone for three different weathering degrees compared to that of the shale layer. Fig. 17(b) corresponds to the situation at BV73, and Fig. 17(c) to that at BV66. As the weathering degree in-creases, the deterioration in the deformation property of the sandstone layers increases, and the difference in deformation between sandstone and shale become indistinguishable at BV66.

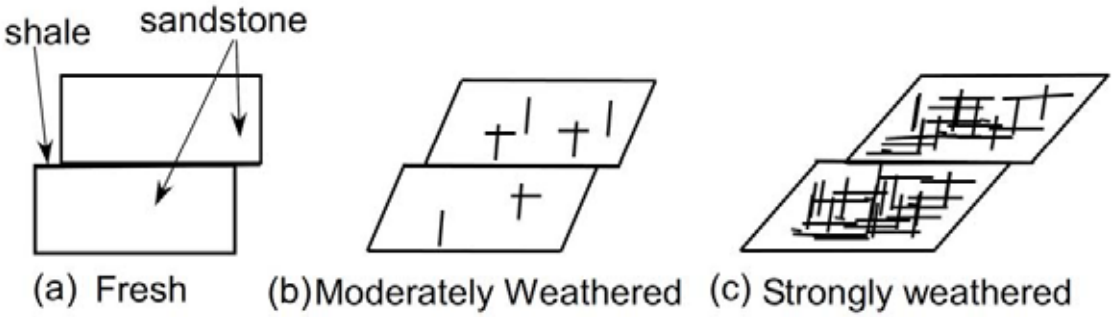

Fig. 17 Deformation model of the alternative layers of sandstone and shale at different weathering degrees

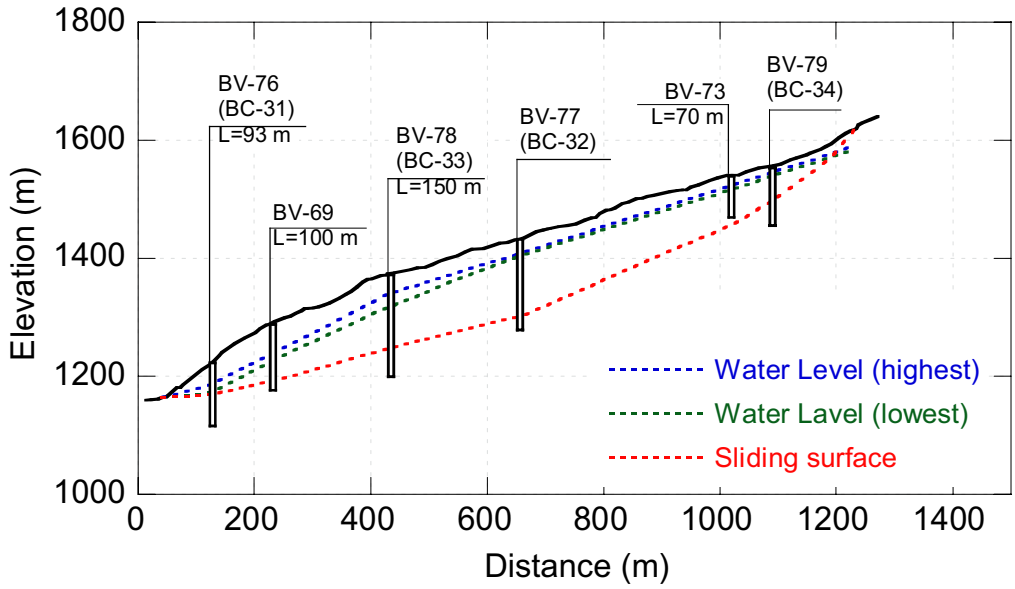

Fig. 18 Longitudinal section (L-L') of the upper part of the Jinnosuke-dani landslide

The effect of physical weathering on the slope structure, as well as the forming of the landslide body, is supported by the longitudinal section of the upper part of the Jinnosuke-dani landslide (Except BV73, which was finished in the early period when the information of potential sliding mass thickness was very limited) (Fig. 18). This section is based on monitoring and exploration data in boreholes up to the end of 2004 by the Kanazawa Work Office, Ministry of Land Infrastructure and Transport, Japan. The geometry of the longitudinal section is very similar to that of a homogenous soil slope, and the dip-slope structure of the original slope is not obvious in the section.

3.3 Borehole-extensometer and groundwater-level monitoring

Seven borehole extensometers with super-invar wire were installed in boreholes to monitor the relative deformation between the slope surface and the base rupture of the landslide. One end of the wire was fixed at the base layer of a borehole, and the other end was connected to a rotating disk on the slope surface. By monitoring the rotation of the disk, the extension or compression between the slope surface and the other end (generally, the bottom of the borehole) was measured.

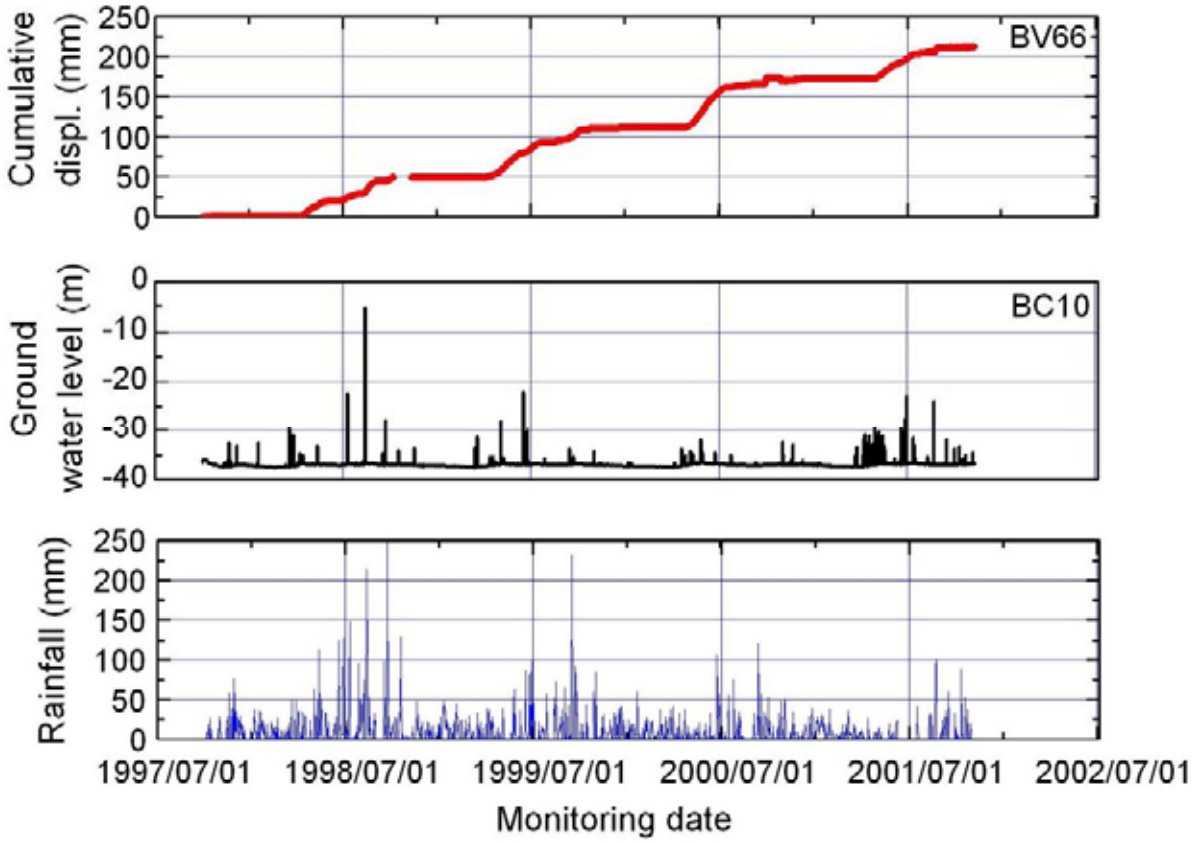

Fig. 19 Monitored results of borehole extensometer at BV66, ground water level at BC10 and rainfall in the Haku-san Mountain area

Piezometers of pore-water pressure transducer style were installed in the boreholes to monitor changes in groundwater level. Because the boreholes used for the groundwater-level monitoring were the same or adjacent to those for extensometers or inclinometers, the effects of groundwater-level change on landslide deformation could be determined. In Fig. 19, the annual change of ground-water level (for 2004) is shown. Fig. 20 shows a comparison of the monitored results of the bore-hole extensometer located at point BV66, the groundwater-level change at the nearby borehole (BC10), and the rainfall data monitored at an elevation of 470 m at Haku-san Mountain. Because groundwater level was monitored by pore-water pressure transducers, although some fluctuations were recorded, the total tendency of the groundwater level changes can be observed. The vertical grid lines in these figures indicate July of each year, the rainy season in this area. As a fact, snowmelt occurs until the end of May each year. On the whole, the groundwater level rose around July each year as a result of rainfall and snowmelt. Corresponding to the increasing groundwater level, the landslide movement entered an active state. When the groundwater returned to its normal level, movement stopped. Thus, it is considered that high groundwater level was a triggering factor for landslide displacement.

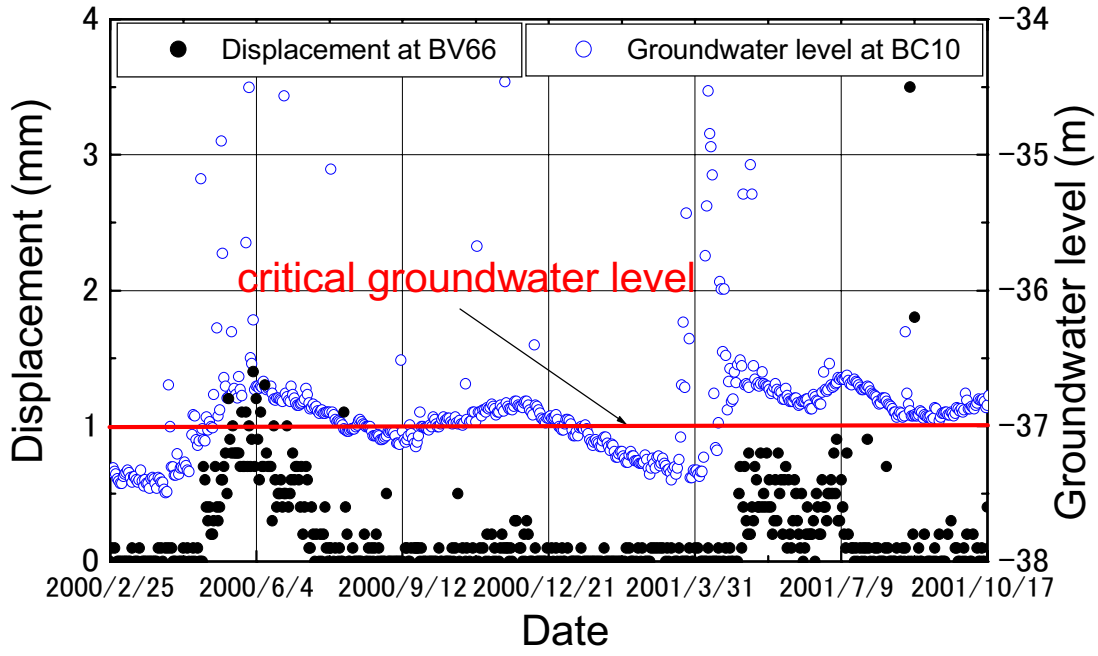

Fig. 20 Relationship between displacements measured at BV66 and groundwater level at BC10 indicating a critical groundwater level existing

Fig. 20 shows the relationship between displacement measured at BV66 and the groundwater level at BC10 from January 1, 2000, to November 18, 2001. The groundwater level started to rise in April and remained at a high level until the end of July, and it rose again at the end of October due to autumnal rain. Responding to the increased groundwater level, the landslide movement became active. In one cycle with a period of one year, the landslide movement accelerated from April to July, and then became dormant in winter. It was observed that the displacement started to increase when the groundwater level exceeded a depth of 37 m, which can be noted as the "critical groundwater level" at this position. When the groundwater level exceeded this critical level, displacement increased. The larger the height of the groundwater level over the critical level, the greater the landslide displacement. On the other hand, when the groundwater level became lower than this critical level, the landslide displacement stopped.

4. Conclusions

The giant Jinnosuke-dani landslide occurred in the Tedori Formation consisting of alternating layers of sandstone and shale. By topographical and geological analyses and deformation monitoring, especially based on the surface displacement monitoring results, the Jinnosuke-dani landslide is divided into two blocks. The upper block moves at an average velocity of 130 mm/year, while the lower block is relatively stable.

In the 7-year monitoring period, a critical groundwater level acted as a triggering factor for land-slide movement. This suggests that drainage at the landslide site will be an effective countermeasure for slope stability, and dewatering could reduce the potential for future movement.

Field monitoring supported our conclusions that physical weathering, including erosion that caused reversal of topography, was a fundamental influential factor for deformation of the alternating layers of sandstone and shale. This weathering may cause deterioration of the strength of these rocks and sub-sequent deformation of the rockmass, and result in the weakening of the effect of the dip-structure. Especially at the lower part of the upper block near the valley side, weathering caused this landslide in a rockmass to deform in a manner similar to a slide in a homogenous soil mass.

Acknowledgments

This study was funded by a scientific research grant (No. 15310127) from the MEXT of Japan, a joint research project (No. 16G-03) of the Disaster Prevention Research Institute, Kyoto University, and the International Programme on Landslides (IPL M102) of the International Consortium on Landslides (ICL). The authors are grateful for the data supplement from Kanazawa Office of Rivers and National Highways, Ministry of Land Infrastructure and Transport, Japan.

REFERENCES

Isobe A (1996) Current situation of countermeasure work in Jinnosuke-dani landslide. Foundation Engineering and Equipment, 24(6): 88-94 (in Japanese)

Kanazawa Work Office, Ministry of Land, Infrastructure and Transport of Japan (2002) Investigation Work Report of the Jinnosuke-dani Landslide (in Japanese). 140p

Kaseno Y (1993) Geological Mapping of Ishikawa Geology Bulletin (in Japanese)

Kaseno Y (2001) Supplement of Geological mapping of Ishikawa Geology Bulletin (in Japanese)

Okuno T, FW Wang, and T Matsumoto (2004) The deforming characters of the Jinnosuke-dani landslide in Haku-san Mountainous area, Japan. In: WA Lacerda, M Ehrlich, SAB Fontoura, and ASF Aayao (eds) Proceedings, 9th International Symposium on Landslides, Rio de Janeiro, Brazil, Vol. 2. AA Balkema, Rotterdam. pp 1279-1284

Sassa K, H Fukuoka, FW Wang (1997) Possible mechanism of the debris flow: Gamahara Torrent debris flow on 6 December 1996, Japan. Landslides News, 10:6-9

Sassa K, H Fukuoka, FW Wang (1998) A rapid landslide-debris flow at Izumi city, Kagoshima, Japan, 1997. Landslides News, 11:2-6

Sassa K, Fukuoka H, Wang G, Ishikawa N (2004) Undrained dynamic-loading ring-shear apparatus and its application to landslide dynamics. Landslides 1(1):7-20

Wang, F. W., K. Sassa
(2006)

Initiation and traveling mechanisms of the May 2004 landslide － debris flow at Bettou-dani of the Jinnosuke-dani landslide, Haku-san Mountain, Japan

Soils and Foundations (in Press)

Initiation and traveling mechanisms of the May 2004 landslide – debris flow at Bettou-dani of the Jinnosuke-dani landslide, Haku-san Mountain, Japan

Fawu Wang and Kyoji Sassa
Research Centre on Landslides, Disaster Prevention Research Institute, Kyoto University
Gokasho, Uji, Kyoto 611-0011, Japan.
Tel: +81-774-38-4114, Fax: +81-774-38-4300
E-mail: wangfw@landslide.dpri.kyoto-u.ac.jp

Abstract
In May 2004, a landslide occurred at the right flank of the Jinnosuke-dani landslide; this slide was transformed into a debris flow after fluidization. By analysis of the monitored video images of the debris flow, field investigation of the source area of the landslide, and a series of simulation tests with a ring-shear apparatus on the initiation of the rainfall-induced landslide and its traveling process, the initiation and traveling mechanisms of the debris flow traveling in the valley were investigated. It is shown that concentrated groundwater flow was the main reason for the landslide initiation, and a rapid decrease of the mobilized shear resistance even under naturally drained condition caused the rapid landslide motion. During the debris motion in the valley, high potential for grain-crushing of deposits in upstream and lower potential for the downstream deposits controlled the traveling and stopping process. Different grain-crushing potential of the valley deposit played an important role in the debris flow traveling and stopping processes.
Key words: landslide, fluidization, groundwater, grain-crushing, ring-shear test

1. Introduction
Haku-san Mountain is located at the boundary between Ishikawa Prefecture and Gifu Prefecture in Hokuriku district, Japan (Fig. 1). It is an active volcano with a summit 2,703 m in elevation, and the whole mountain is a national park. This park is famous for its beautiful scenery and about 50,000 mountain climbers visit here in the period from 15 May to 15 October every year. Tedori River, the largest river in Ishikawa Prefecture, originates in this area. The Jinnosuke-dani landslide (Fig. 2) is a giant landslide located on the southwestern slope of Haku-san Mountain ("dani" means valley or torrent in Japanese.). It was also the first landslide designated as a "Landslide prevention area" by the "Japanese Landslide Prevention Law" in 1958. Landslides frequently occur in this area, and commonly trigger debris flows that travel long distances and damage properties in the downstream valley of the Tedori River. In the photograph of Fig. 2, the areas not covered by vegetation are local slope failures. For example, at the left side of the photograph, the main scarp and sliding surface of the Bettou-dani failure, which occurred in 1934, is visible. In that event, a debris flow initiated by a landslide reached the Japan Sea after traveling for 72 km. The upper part of the central ridge sandwiched by the Bettou-dani at the left side and the Jinnosuke-dani at the right side is an active landslide, according to data obtained by monitoring, and is called the "Central Ridge Block" of the Jinnosuke-dani landslide. The width and length of this block are 500 m and 2,000 m, respectively. In recent decades, accompanying the deformation of the Central Ridge Block, local landslides with different volumes occurred at both boundary valleys of the Central Ridge Block and caused damage, although many countermeasure works have been conducted in this area for more than 50 years. In May 2004, a landslide occurred at the upper part of the Bettou-dani from the Central Ridge Block. This landslide was transferred into a debris flow that traveled more than 2 km after it slid into the Bettou-dani. A suspension bridge was completely destroyed, and a local road with a simple bridge utilized for debris-retention dam construction at the middle of Bettou-dani was heavily damaged. Fortunately, nobody was injured because there were not many mountain climbers passing through the valley when the landslide – debris flow occurred. However, the risk for further landslide and debris flow activity still exists. This paper attempts to clarify the initiation and traveling mechanisms of the landslide – debris flow, aiming to supply insight for future landslide disaster prevention in this area.

2. General conditions of the Jinnosuke-dani landslide on Haku-san Mountain

The Haku-san Mountain area is characterized by heavy precipitation and the Tedori River is characterized by its steep gradient (Wang et al., 2004; Okuno et al., 2004). In winter, due to the strong influence of monsoons from Siberia, the accumulative snowfall may exceed 12 m in the Haku-san Mountain area. In the other seasons, half of the days are rainy. For this reason, local annual average precipitation is 3,295 mm, about two times the national average of 1,700 mm for Japan. In this area, snowmelt generally begins in the middle of March and finishes at the end of May. In May 2004 when the landslide occurred, snow melting was on-going, and the accumulative rainfall for three days before the landslide occurred was 216 mm (Fig. 3). It is also reasonable to think that the effective water that infiltrated into the slope was more than this value. Because the movement was recorded by a monitor video camera of the Kanazawa Office of Rivers and National Highways, Ministry of Land Infrastructure and Transport, Japan (KORNH- MLIT) (2004b), the actual failure time was also exactly recorded.

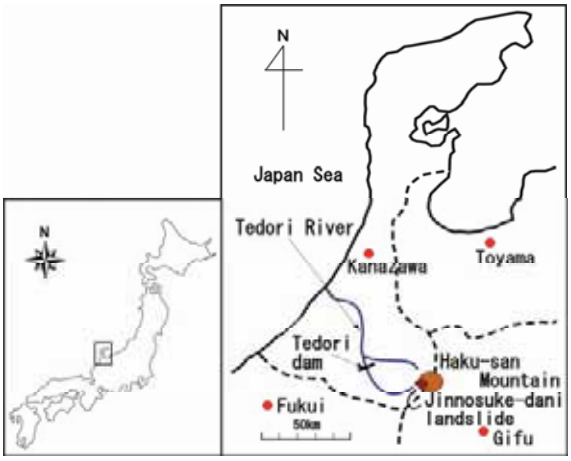

Fig. 1 Location map of the Jinnosuke-dani landslide

Fig. 2 Aerial photograph of the "Landslide Prevention Area" of the Jinnosuke-dani landslide (Photo Courtesy of Kanazawa Office of Rivers and National Highways, MLIT)

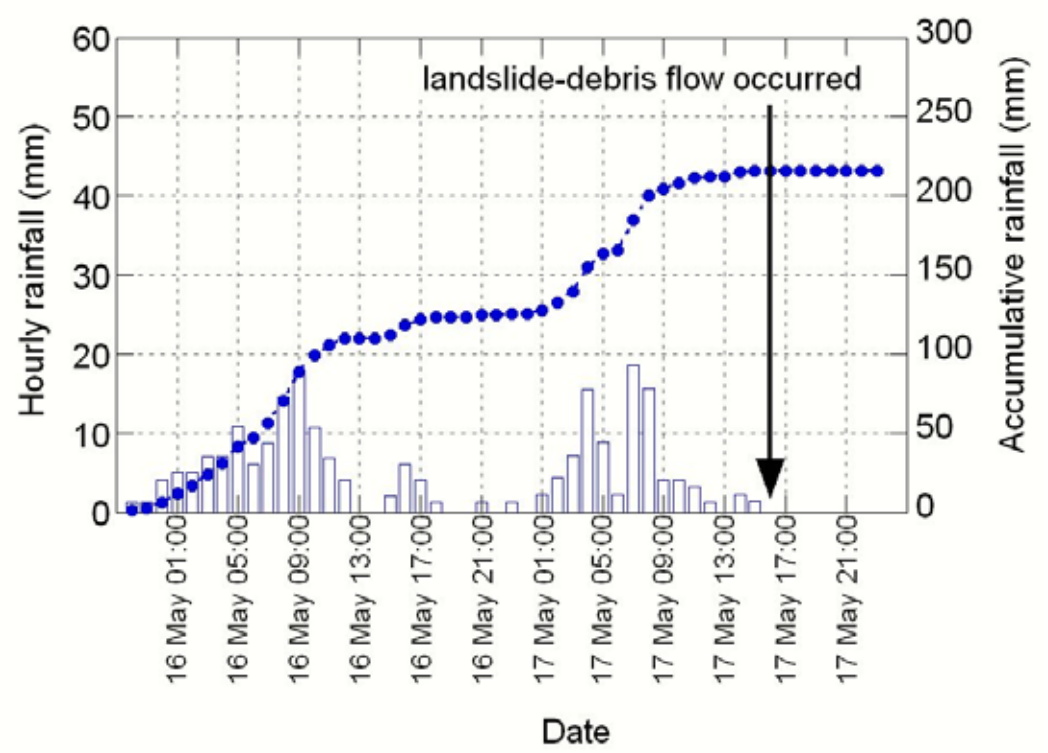

Fig. 3 Hourly rainfall before the landslide – debris flow occurred (The rainfall gauge was located at the central ridge block of Jinnosuke-dani landslide, and was measured by Kanazawa Office of Rivers and National Highways, MLIT)

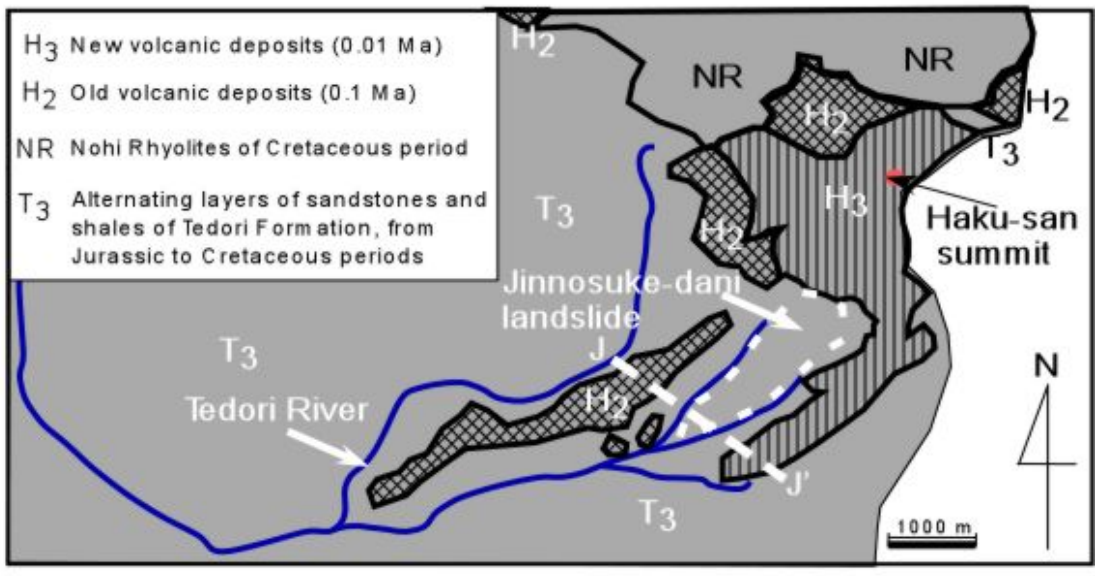

Fig. 4 Geological map of the area adjacent to the Jinnosuke-dani landslide (modified from Kaseno, 2003)

As a part of the 1:50,000 geological map of the Haku-san mountainous area, a geological map of the Jinnosuke-dani landslide and the nearby area was completed by Kaseno (2001). The basal bedrock in the Haku-san mountainous area is Lower Paleozoic Hida gneiss. Overlying this gneiss are Jurassic to Early Cretaceous sediments, consisting of shale, sandstone and conglomerate, and lacustrine sediments known as the Tedori Formation. General descriptions of the geology can be found in Kaseno (1993). Fig. 4 shows the distribution of strata in this area. Alternating layers of sandstone and shale of the Tedori Formation are

distributed at the left side of the figure, and the Cretaceous Nohi rhyolites are distributed at the right side. Both form the bedrock of this area. Volcanic deposits, which erupted 100,000 years ago and 10,000 years ago, overlie the strata of the Tedori Formation and the Nohi Rhyolites.

3. The May 2004 landslide − debris flow

As mentioned earlier, the landslide occurred on 17 May 2004 after continuous intense rainfall for two days. The elevation of the source area of the landslide was about 1,900 m, and the elevation of the toe part of the deposit of the debris flow caused by the landslide was about 1,200 m. Fig. 5 shows two aerial photographs taken before the event ((a): in the fall of 2003), and after the event ((b): on 24 May 2004, 7 days after the landslide − debris flow), and the trace of the debris flow with elevations at some key points (c). As shown in Fig. 5a, the source area is a steep cliff and there was not any vegetation on the lower segment of the landslide; however, at the upper part, the slope is relatively gentle and is covered by vegetation. For mountain climbers, after leaving Bettou Deai, which has facilities such as parking areas, rest rooms, simple restaurants, and a bus stop, most of the climbers have to cross the suspension bridge and access the Central Ridge Block of the Jinnosuke-dani landslide to get to the summit of Haku-san Mountain. At the middle of the Bettou-dani, an access road for construction of debris-retention dams crosses the valley and enters the Central Ridge Block. As shown in Fig. 5b, both the roads and the bridge were badly damaged when the debris flow hit them. The entire flowing process of the debris flow was recorded by a video camera, which was set at an elevation of about 1,860 m by the KORNH-MLIT (2004a). By means of the recorded video, it is estimated that the velocity of the debris flow may have reached a maximum of 20 m/sec. As shown in Fig. 5c, the distance between the source area and the toe of the deposits of the debris flow was 700 m, and the horizontal distance that the debris flow traveled was about 2,000 m. Based on these data, the apparent friction angle of the debris flow is estimated to be 19.3 degrees.

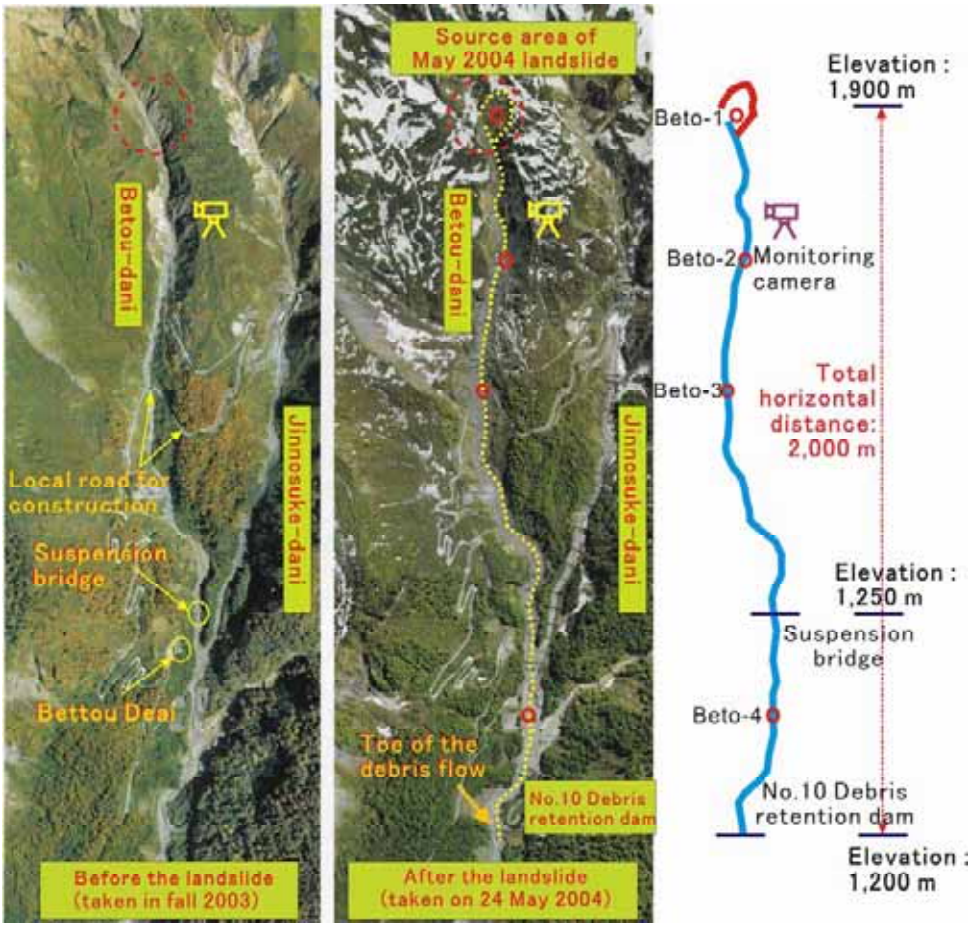

Fig. 5 The May 2004 landslide – debris flow, which occurred in the Bettou-dani from the Central Ridge Block of the Jinnosuke-dani landslide. (a) aerial photograph taken before the slope failure (in the fall of 2003); (b) aerial photograph after the landslide (taken on 24 May 2004); (c) trace of the debris flow (Photos courtesy of the Kanazawa Office of Rivers and National Highways, MLIT)

Fig. 6 shows the situation when the suspension bridge was completely destroyed. Large boulders 3-4 m in diameter were transported and deposited near the bridge site. Some thin debris was deposited on the top of the left pillar of the bridge, about 10 meters above the valley bottom. This shows that even near the terminus of the debris flow, the sliding potential was high and powerful.

Fig. 6 The suspension bridge that was completely destroyed by the May 2004 debris flow in the Bettou-dani (Photo courtesy of the Kanazawa Office of Rivers and National Highways, MLIT)

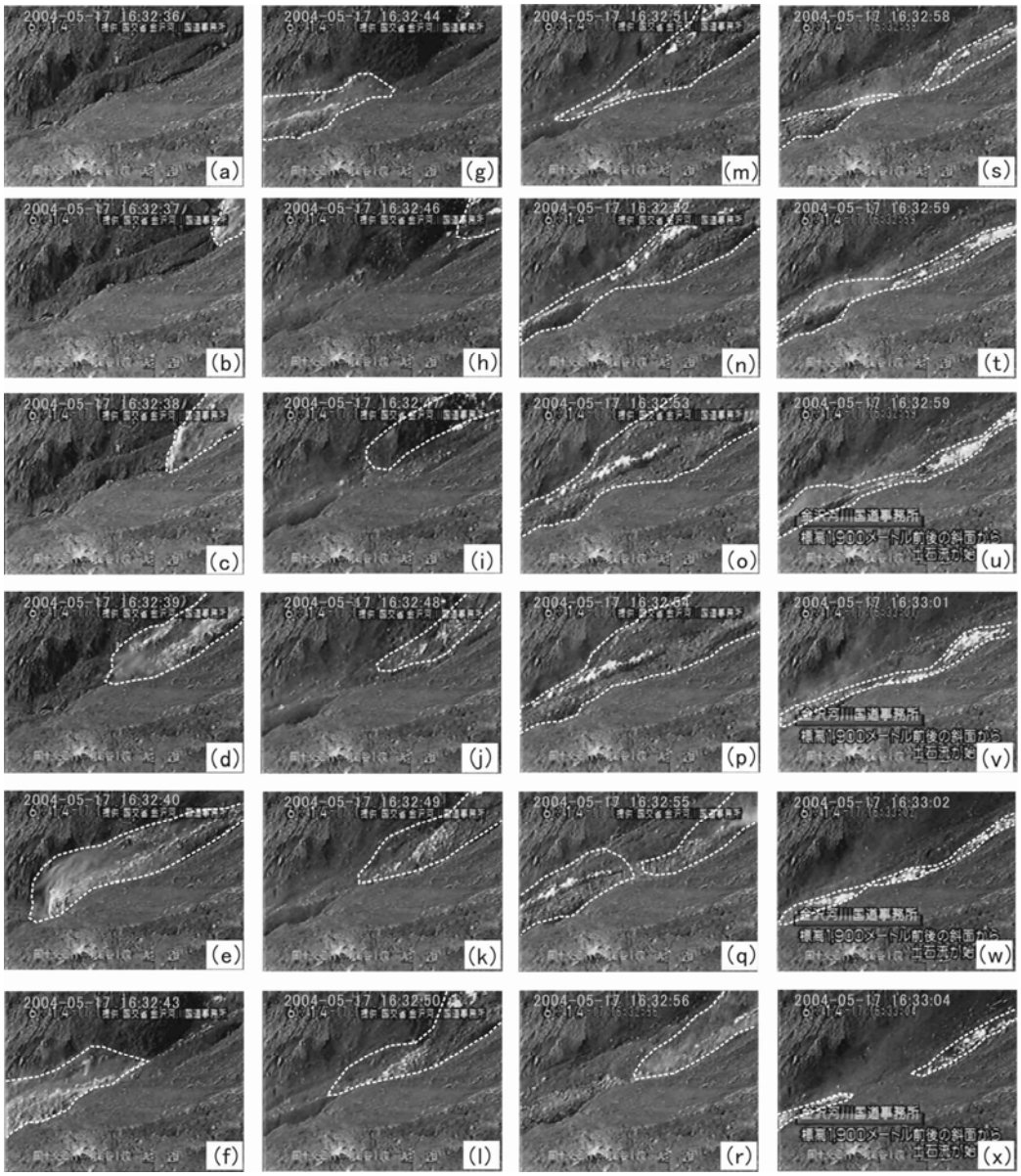

Fig. 7 Continuous images of the May 2004 debris flow in the Bettou-dani (Video courtesy of the Kanazawa Office of Rivers and National Highways, MLIT). Sliding mass is shown in white dotted lines.

Fig. 7 shows a series of continuous images taken from the monitoring video of KORNH-MLIT. The location of the video camera was about 250 m downstream from the source area of the landslide. The time in seconds is shown at the top of each image. Fig. 7a shows the situation just before the debris flow arrived. The white color in the images is snow. The debris flow passed through the video from 16:32:37 to 16:33:16 hrs; thus, the entire process continued for only 40 seconds. By analysis of the video images shown in Fig. 7, the debris flow can be divided into four separate waves. The first wave was from (b) to (h), which continued for 9 seconds; the second wave was from (h) to (m), which continued for 6 seconds; the third wave was from (m) to (r), which continued for 6 seconds; and the fourth wave was from (r) to (x), which continued for 9 seconds. It is obvious that all of the debris included snow. As compared to Fig. 7a, muddy fog can be recognized in Figs. 7d and 7e in the front of the first wave, and 7r, 7s and 7t in the front of the fourth wave, indicating rapid motion during downstream travel.

Fig. 8 shows the situation at the source area of the landslide. The average slope angle was about 28 degrees. The average thickness of the sliding mass was estimated as 30 m by KORNH-MLIT (2004b). In this figure, L1, L2, and L3 show the rear boundaries of the different sliding blocks, which moved for a limited distance; however, most of these blocks did not move far, but just rested on the slope. At the middle block, between L1 and L3, most of the debris material slid out of the source area, entered into the Bettou-dani, and joined the debris flow. Also, at the lower part of L2, most of the debris slid out into the valley. A common phenomenon at the source areas of these sliding blocks is that concentrated groundwater flow exited at W1, W2, and W3 at relatively high positions. This fact ensured that the debris, especially in the potential sliding zone, was fully saturated and that high water pressure was supplied to the back of the debris to make the slope unstable. The groundwater exiting at a high position at the head of the debris was a great triggering factor for the landslide which fluidized into a debris flow. Contrary to the case for the fluidized blocks, the groundwater exits at Block L3 were relatively low, and this may be the reason for the short sliding distance of this large block.

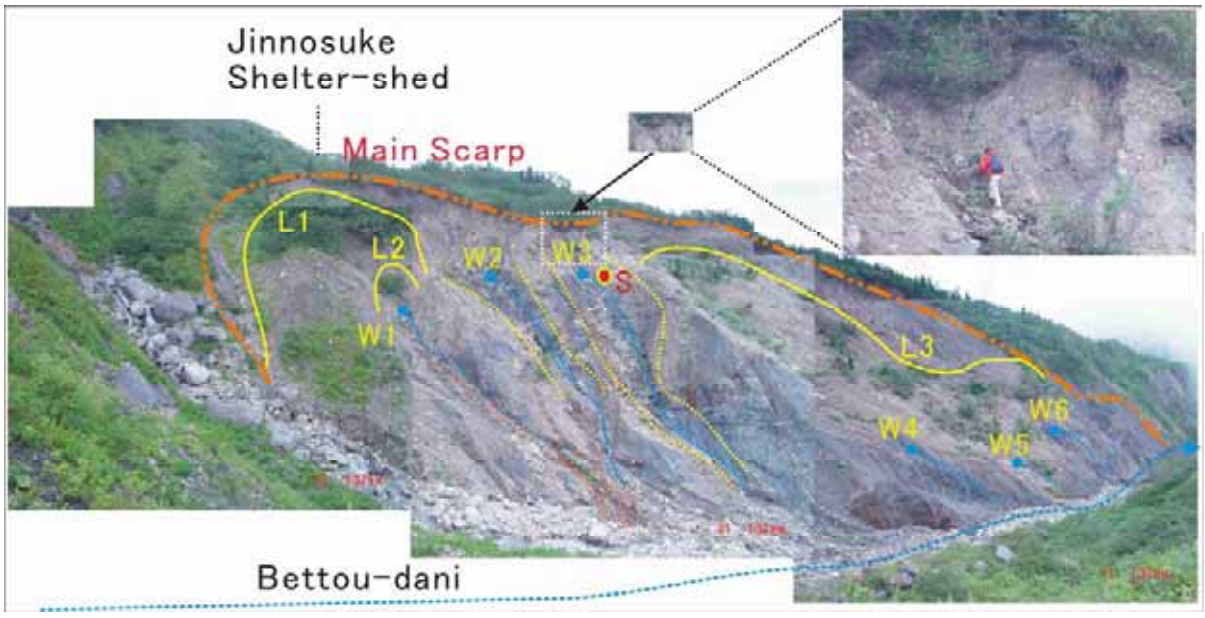

Fig. 8 Source area of the May 2004 landslide – debris flow in the Bettou-dani
Blue points represent the groundwater exits. Solid lines are the rear boundaries of the sliding blocks (Photo taken by FW Wang on 11 September 2005)

To investigate the initiation and traveling mechanism of the landslide – debris flow, soil samples were obtained at the source area and along the travel path in the valley of the Bettou-dani. Soil sample Beto-1 was taken from point "S" (Figs. 8 and 5b) at the source area. This sample was subjected to the ring-shear test, simulating a rainfall-induced landslide, to investigate the initiation mechanism of the landslide. Soil samples Beto-2, Beto-3, and Beto-4 were taken along the traveling path of the debris flow, and were subjected to ring-shear tests that simulated dynamic loading of the landslide mass on the valley deposits

and the dynamic loading of the debris flow on the valley deposits to investigate the traveling mechanism of the debris flow traveling down the valley.

In the soil sampling, coarse grains larger than 20 mm were excluded. Fig. 9 shows the grain-size distribution of the four soil samples. Sample Beto-1 is the finest sample among them, and all of the samples show a similar gradation. For sample Beto-2, 3, 4, Beto-3 has the least amount of fines. The grain-size distribution of the samples may indicate the potential of the water transport in the valley, i.e., upstream of the Beto-3 sample site, the fine part dominates because of the supply of the weathered material; while the downstream part is rich in fines, because of their transport by water. The average grain-sizes of the soil samples were 2.7 mm, 6.0 mm, 4.8 mm, 6.0 mm, while the uniformity coefficient was 20.9, 25.7, 7.6, and 34.7, respectively. The specific gravity of the samples was 2.71.

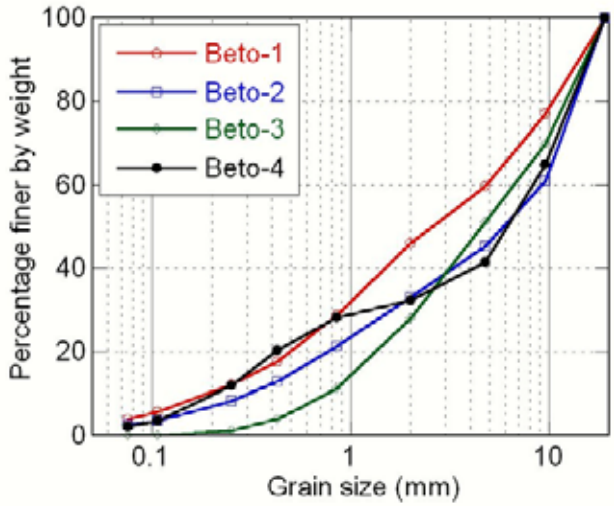

Fig. 9 Grain-size distribution of soil samples

4. Grain-crushing susceptibility of the valley deposits in different parts of the Bettou-dani

It is believed that the difference in grain-crushing susceptibility should cause the difference in the traveling process of the landslide – debris flow. To confirm this concept, drained ring-shear tests were conducted under the same test conditions on all the samples. The test conditions were: consolidate the sample at 300 kPa normal stress, and shear it under constant speed of 10.0 mm/sec until the shear displacement reaches 6.4 m. For comparison, Toyoura silica sand which is known as a standard sandy soil that is difficult to crush, was also sheared under the same test conditions.

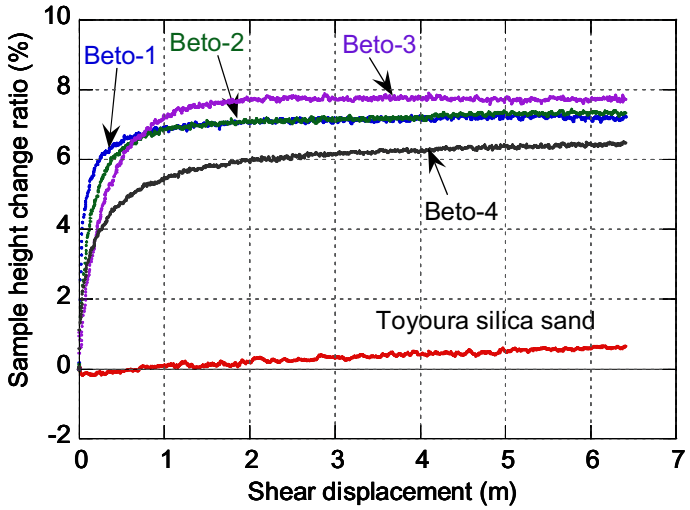

Fig. 10 Sample-height change with shear displacement during constant-shear-speed drained ring-shear tests on samples Beto-1, Beto-2, Beto-3, Beto-4, and Toyoura silica sand. Normal stress = 300 kPa, Shear velocity = 10.0 mm/sec.

Fig. 10 shows sample-height change during the drained ring-shear tests. Soil with high grain-crushing susceptibility generally has large sample-height change (contraction) during drained shear. The sample-height changes that occurred in the samples taken from Bettou-dani were quite a bit larger than that of Toyoura silica sand. Among the samples taken from Bettou-dani, Beto-4 has the smallest sample-height change during shearing, showing a relatively lower grain-crushing susceptibility.

Figs. 11a and b show the grain-size distribution of the tested samples before and after shearing, and the grain-crushing percentage B_p of all samples (Marsal, 1967), respectively. B_p is the summation of the difference of grain-size distribution at each sieve size of the sample before and after drained shear (taken from shear zone), and it indicates the grain-crushing susceptibility of the soil. It is obvious that grain-crushing susceptibility becomes lower from the upstream part to the downstream part of the Bettou-dani.

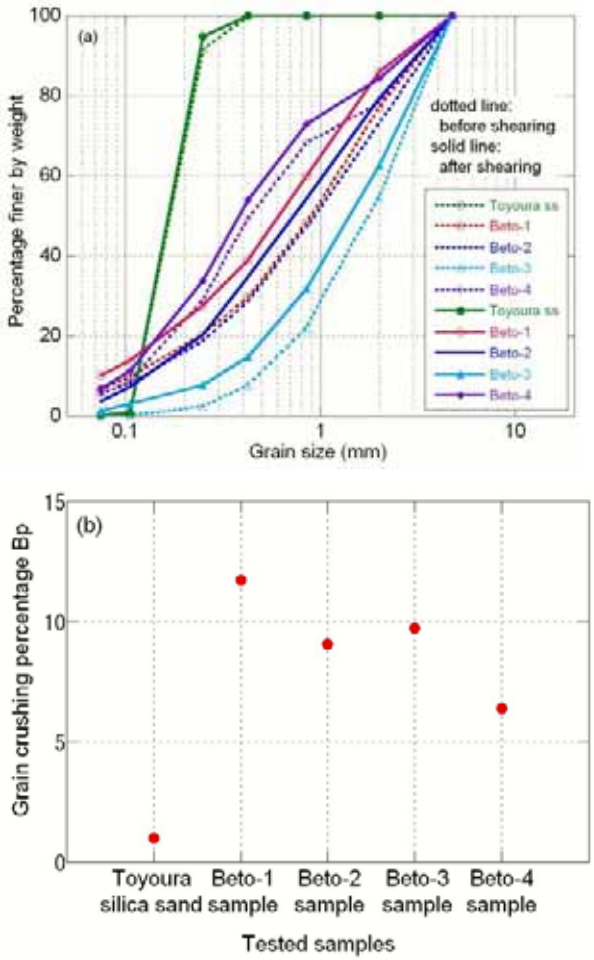

Fig. 11 Grain crushing occurred in the drained constant-shear-speed ring-shear tests on samples Beto-1, Beto-2, Beto-3, Beto-4, and Toyoura silica sand
(a) Grain-size distribution of the tested samples before and after shearing; (b) Marsal's grain crushing susceptibility B_p (Marsal, 1967).

5. Ring-shear tests on soil samples taken from the source area

Ring-shear tests were conducted using ring-shear apparatus DPRI-5, which was developed by Sassa in 1996 (Sassa et al, 2003). The diameters of the outer ring and inner ring are 180 mm and 120 mm, respectively. The sample, after placement in the shear box, had a donut shape with a width of 30 mm. To avoid possible grain-size effects on the shearing behavior, only grains with diameter smaller than 4.75 mm were included in the tested samples.

The purpose of this test is to simulate the initiation of the landslide by water pressure. The initial slope condition was simplified as being 30 m in thickness and 28 degrees in slope angle. The landslide was triggered in the ideal slope by rainfall and snowmelt water. The initial normal stress and shear stress acting

on the sliding surface were 420 kPa and 224 kPa, respectively. Pore-water pressure acting on the element increased as the result of rainfall and snowmelt. The test was conducted under the following procedure:

(1) Saturate the soil sample to a high degree of saturation with carbon dioxide and de-aired water; it was confirmed that the B_D value reached 0.96, showing a high degree of saturation.
(2) Consolidate the sample under normal stress of 420 kPa;
(3) Apply the initial shear stress of 224 kPa gradually at 41.7 Pa/sec to avoid pore-water pressure generation;
(4) Increase the pore-water pressure gradually at a rate of 0.5 Pa/sec until failure occurs;
(5) Measure the residual friction angle of the soil with constant shear speed, while increasing the normal stress gradually from a low stress level (about 90 kPa) to a high stress level (about 400 kPa).

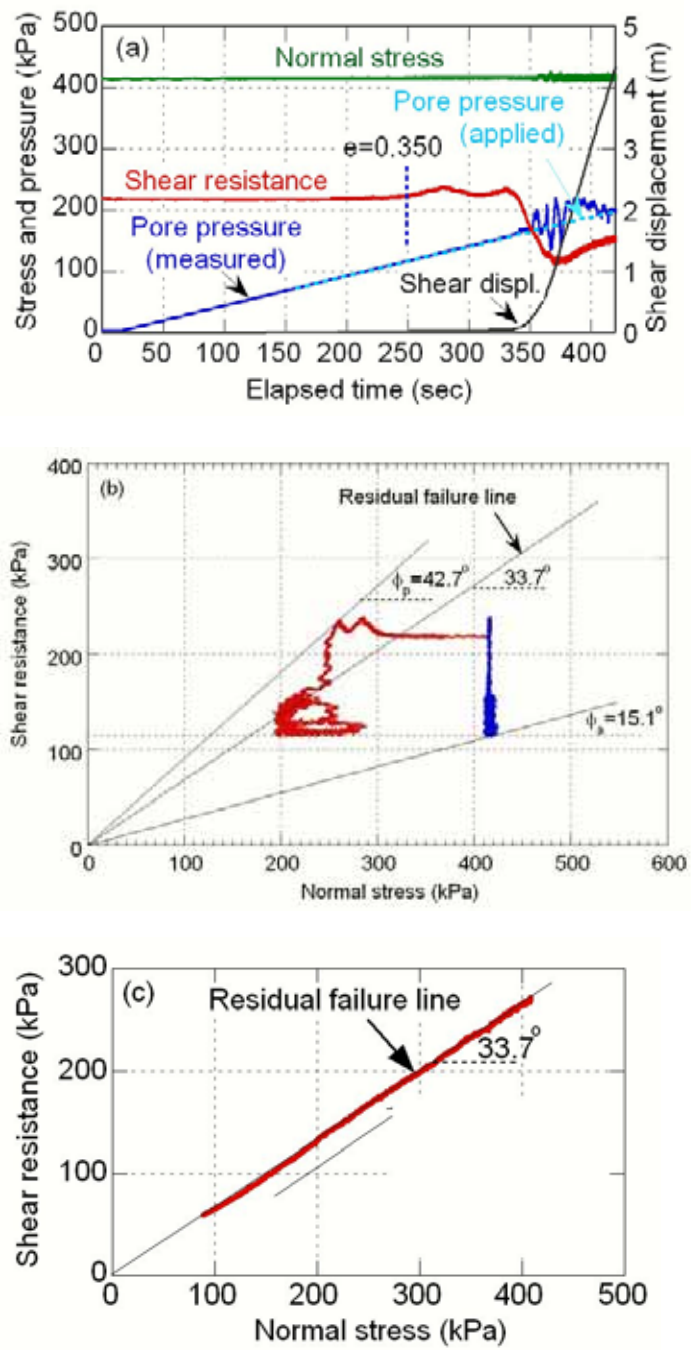

Fig. 12 Simulation test results of landslide initiation triggered by rainfall under naturally drained condition. B_D = 0.96, Pore water pressure increasing rate = 0.5 kPa/sec.
(a) Time-series data; (b) Stress paths; (c) Residual friction angle of the tested soil sample from the source area.

Figs. 12a, b, and c present the test results. Fig. 12a shows the time-series data for the whole test series. From the beginning to nearly 200 sec, the normal stress and shear resistance were kept constant, while the pore pressure was increased gradually. From 200 sec to 330 sec, small displacement occurred, and the shear resistance mobilized a little bit higher, although the shear stress was kept constant. This may have been caused by the adjustment of the soil grains along the shear surface. After 330 sec, rapid failure occurred, which can be confirmed by the acceleration of the shear displacement. Corresponding to the rapidly increasing shear displacement, the shear resistance decreased rapidly to about 110 kPa. At that point, the apparent friction angle became 15.1 degrees, which is shown by the total stress path and effective stress path in Fig. 12b. The residual friction angle of the soil was measured at 33.7 degrees, which is shown in Fig. 12c. Thus, it is possible that the slope can remain stable at its initial slope angle of 30 degrees, if there is no increase in pore-water pressure at the sliding surface. In addition, from Fig. 12b, it can be seen that the peak friction angle of the soil at initial failure is much higher than 33.7 degrees.

The test results show that the slope failure was triggered by increase in pore-water pressure caused by heavy rainfall and snowmelt. In addition, after the slope failure, because of a rapid decrease in shear resistance, the displaced sliding mass moved downward to the Bettou-dani with increasing acceleration. This is a possible mechanism of the initiation in the source area of the May 2004 Bettou-dani landslide.

6. Ring-shear tests on soil samples taken from the landslide travel path in the Bettou-dani

To simulate the landslide motion in the Bettou-dani, three other samples (Beto-2, Beto-3, Beto-4) were used in ring-shear tests to show the fluidization process of the landslide (see Fig. 5b). Beto-2 was taken near the uppermost debris-retention dam in the Bettou-dani; Beto-3 was taken near the destroyed bridge; and Beto-4 was taken below the suspension bridge and near the toe of deposit of the debris flow.

Fig. 13 is a model proposed by Sassa et al. (1997) to simulate the undrained-loading behavior of valley deposits by a rapidly sliding mass. At the Bettou-dani, the sliding mass moved down the slope (I), and applied a load to the valley deposits at the foot of the slope (II). Because a surface-water stream or subsurface flow existed and some of the deposits were saturated, the valley deposit was sheared by undrained loading and transported downstream together with the sliding mass (III) (Sassa et al, 2004). The test results shown in Fig. 12 indicate that the landslide occurred at slope (I).

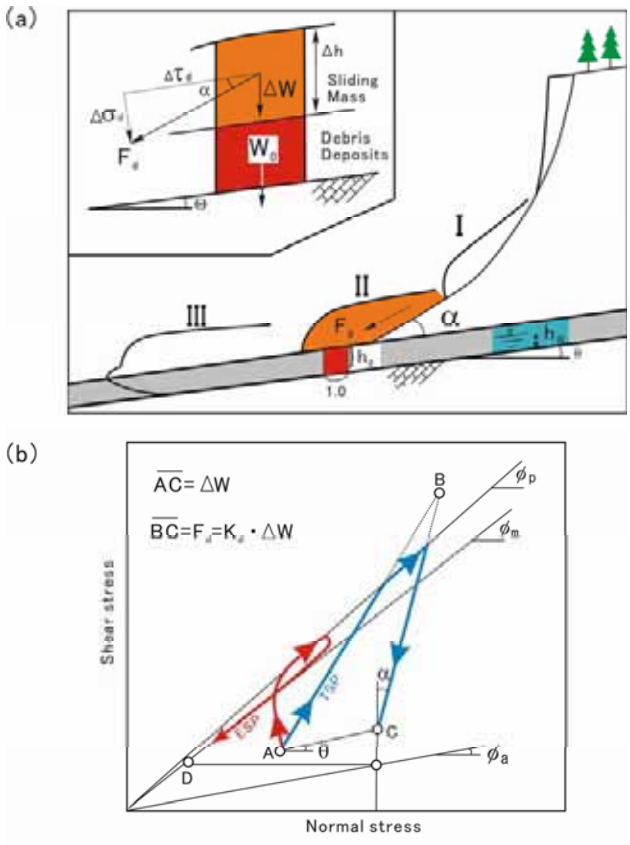

Fig. 13 Model for undrained loading of saturated deposits by a displaced sliding mass (Sassa et al., 1997)

To simulate the succeeding process, sample Beto-2 was used to simulate the situation at slope (II), while samples Beto-3 and Beto-4 were used to simulate the behavior at slope (III), and the local slope angles of the valley at the sampling points (Beto-3 and Beto-4) were considered.

In Fig. 13, the valley deposit has a thickness of h_0, an initial slope angle of the valley θ, and groundwater thickness on the sliding surface h_w. The undrained loading from a rapidly moving displaced landslide has a thickness of Δh, an intrusion angle of α, and a dynamic (impact) coefficient of K_d. Based on Sassa et al. (1997) and Sassa et al. (2004), it is reasonable for K_d to take a value of unity. Then, the increment of normal stress and shear stress from the rapidly sliding mass to the deposits can be determined. The initial conditions for the three sampling points, which were employed in the ring-shear tests, are summarized in Table 1.

Table 1 Initial condition for undrained loading on the valley deposits from a rapid sliding mass, Bettou-dani landslide

	θ (deg.)	h_0 (m)	h_w (m)	α (deg.)	Δh (m)
Beto-2	18	5	3	10	30
Beto-3	18	5	3	0	20
Beto-4	5	5	3	0	5

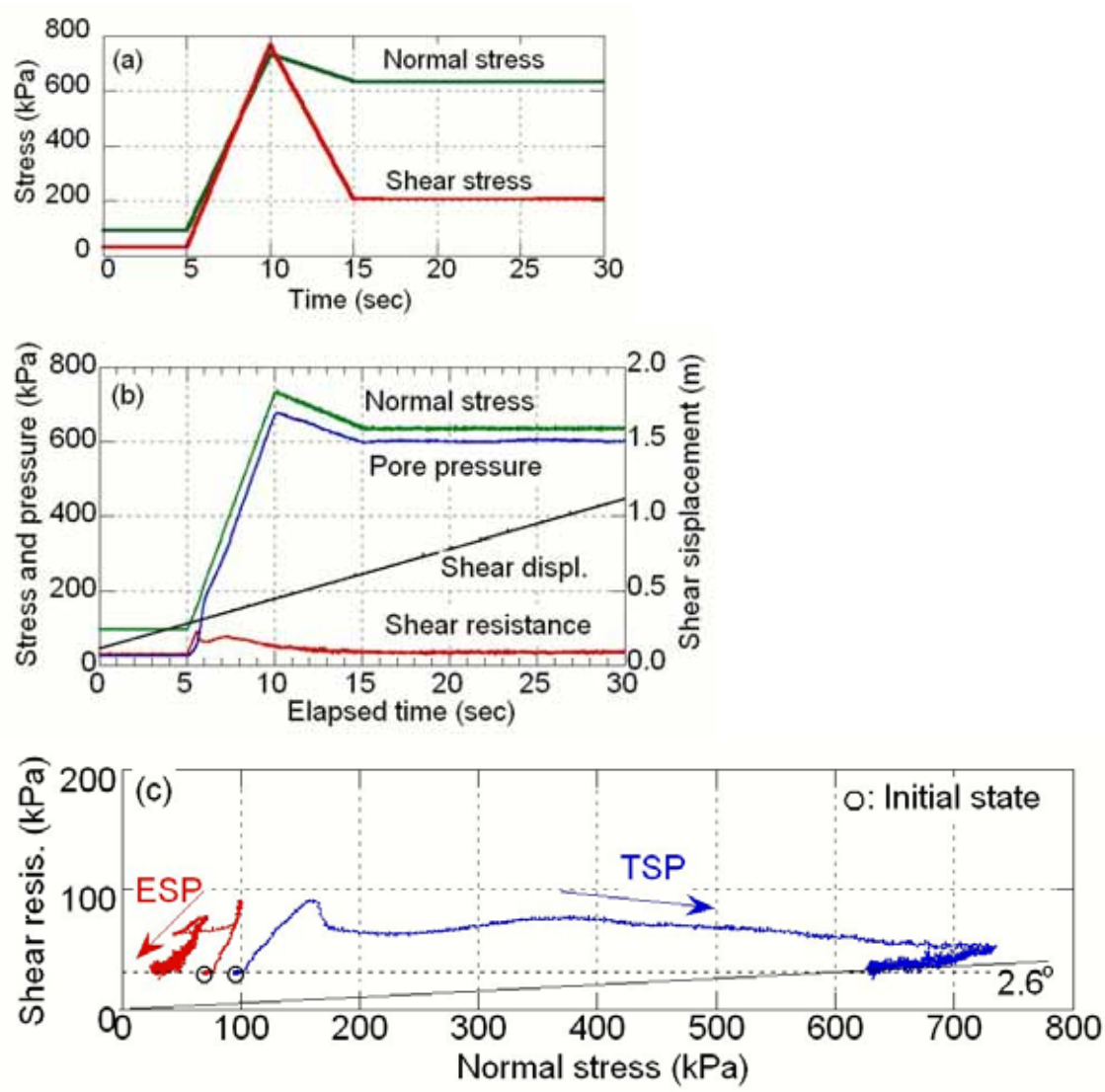

Fig. 14 Simulation test results on sample Beto-2. (a) Applied-stress signals (normal-stress and shear-stress increments); (b) Time-series data; (c) Stress paths. $B_D = 0.96$.

Fig. 14 shows the results of the simulation test on slope (II) using sample Beto-2. Fig. 14a shows the input stress signals of normal stress and shear stress before (0-5 sec), during (5-15 sec), and after the dynamic impact process (15-30 sec).

As can be seen in the time-series data (Fig. 14b), pore-water pressure was generated at the same rate as the applied normal stress, and failure occurred as soon as the loading was applied. Shear resistance reached its peak strength at 7 sec, and arrived at its steady-state strength at 15 sec. As shown by the stress paths (Fig. 14c), the apparent friction angle is only 2.6 degrees, showing a high mobility of the valley deposit after the dynamic loading. All of the series test results show that the valley deposits fluidized after the dynamic loading of the rapidly moving displaced sliding mass in an undrained condition.

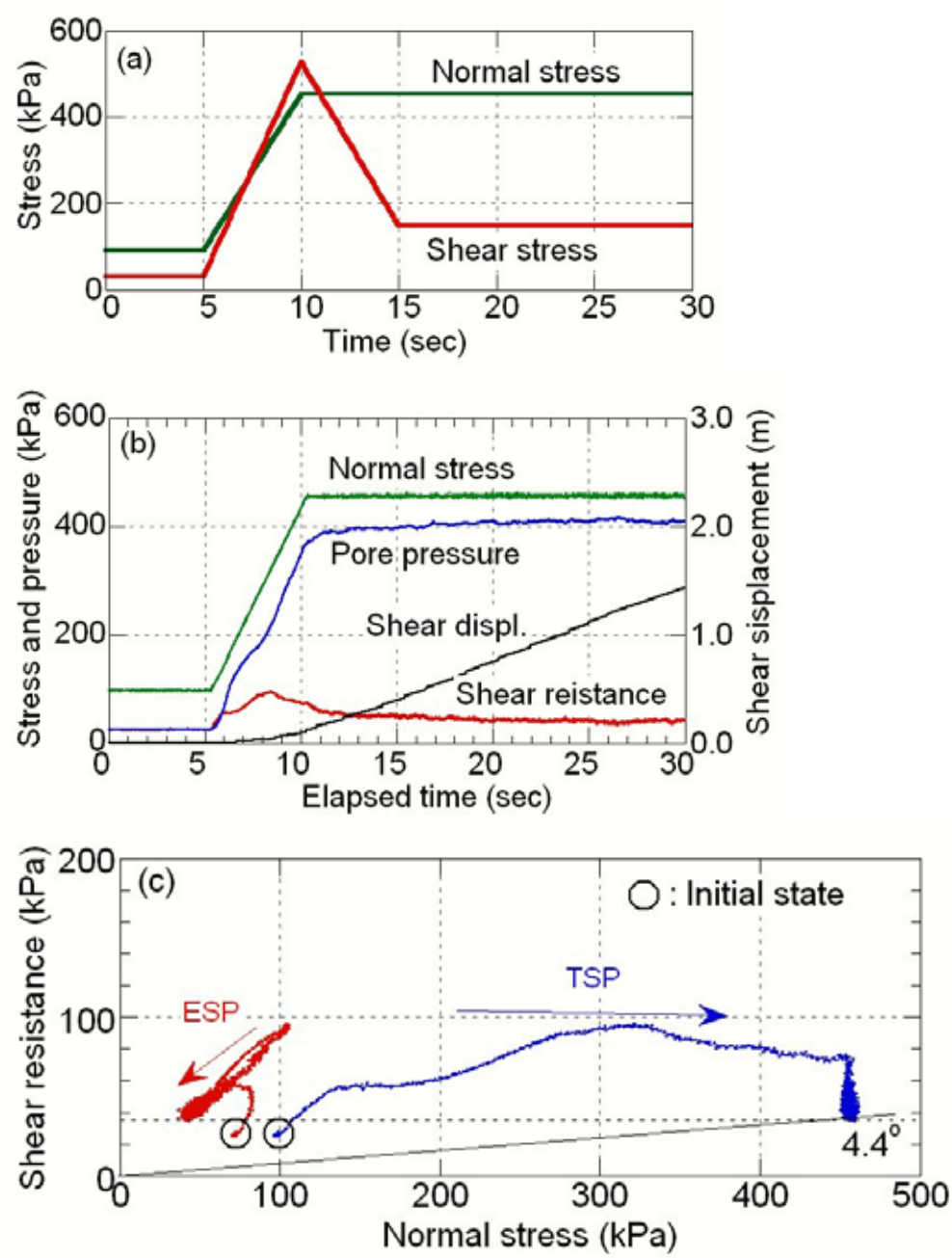

Fig. 15 Simulation test results on sample Beto-3. (a) Applied-stress signals (normal stress and shear stress increments); (b) Time-series data; (c) Stress paths. $B_D = 0.99$.

Fig. 15 shows the results of the simulation test on sample Beto-3 at slope (III). The intrusion angle was assumed to be zero because the displaced sliding mass came from the upper part of the same valley with the same slope angle. Fluidization also occurred, and the apparent friction angle mobilized at the steady state

came to 4.4 degrees, slightly higher than that of the Beto-2 sample.

Fig. 16 shows the simulation-test results on sample Beto-4, taken near the toe of the deposits. The apparent friction angle of Beto-4 was 5.0 degrees, the same value as the slope angle of the Bettou-dani at this part. For this reason, the shear displacement generated in this test was only 38 mm when the loading was completed.

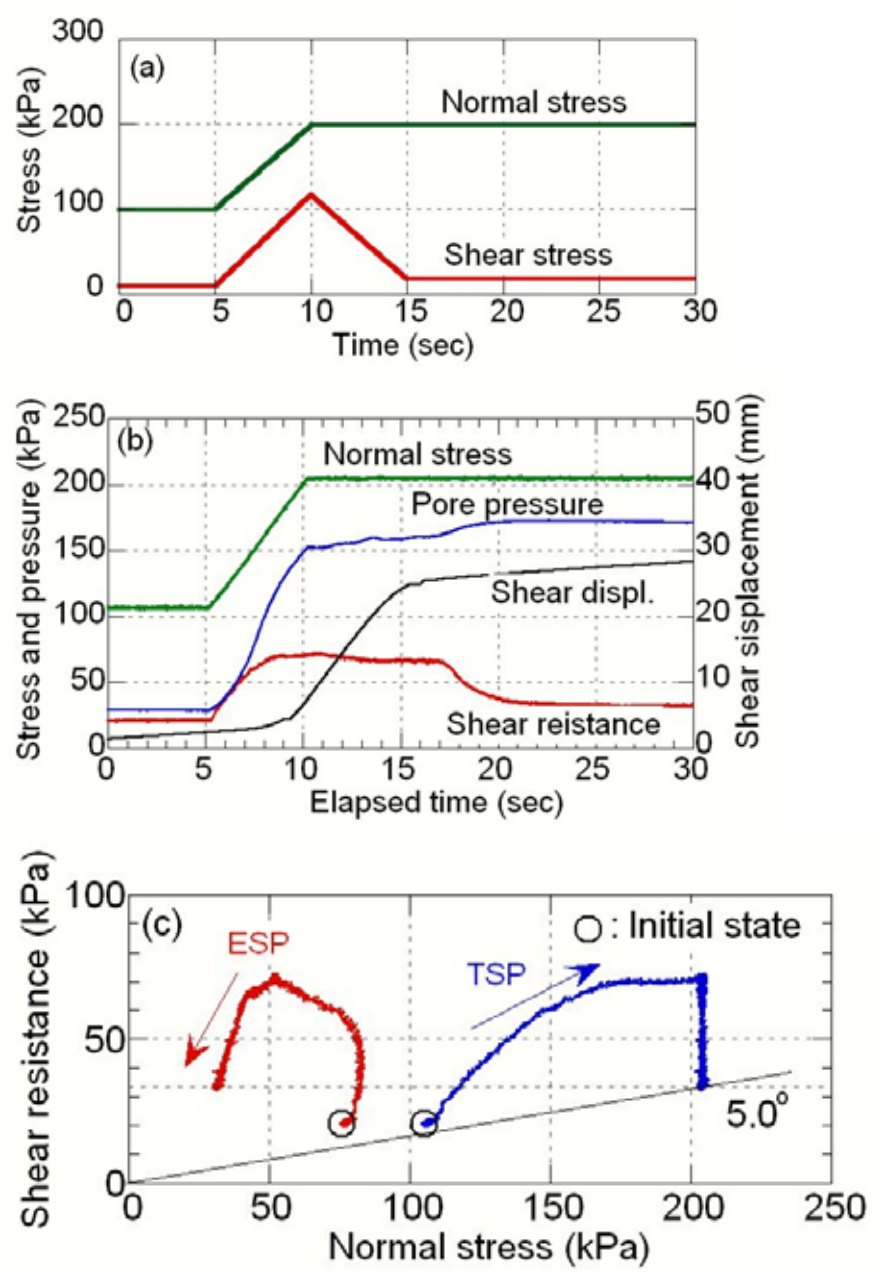

Fig. 16 Simulation test results on sample Beto-4. (a) Applied-stress signals (normal stress and shear stress increments); (b) Time-series data; (c) Stress paths. $B_D = 0.95$.

As a summary of the above dynamic tests, the shear resistance at steady state under the undrained condition, the minimum apparent friction angle, and the residual friction angle of the three soil samples taken from the Bettou-dani are presented in Table 2. Because all of the possible grain-crushing should have been completed when the shearing reached the steady state, the shear resistances at the steady state were almost the same. When the normal stress became smaller, the apparent friction angle became larger; and when it was larger than the slope angle, the debris flow should have decelerated and finally came to a stop.

From the above simulation tests that reproduced rapid loading on valley deposits, the impact process, the traveling process, and stopping process of the debris flow that occurred in May 2004 were well reproduced

in the laboratory.

Table 2 Summary of ring-shear test results on sample Beto-2, 3, and 4

Sample	Shear resistance at steady state under the undrained condition (kPa)	Total normal stress (kPa)	The minimum apparent friction angle (degrees)
Beto-2	About 35	620	2.6
Beto-3	About 35	460	4.4
Beto-4	About 35	205	5.0

7. Conclusions

The May 2004 landslide – debris flow that occurred in the Bettou-dani of the Jinnosuke-dani landslide, Haku-san Mountain, showed a fluidization process from landslide to debris flow. By analysis of the monitored video images of the debris flow, field investigation of the source area of the landslide, and laboratory ring-shear tests that simulated the rainfall triggering mechanism and the fluidization mechanism during the process of downstream travel, the followings were concluded:

(1) Concentrated groundwater flows were a main triggering factor for the landslide initiation by increasing water pressure in the slope;

(2) In the ring-shear simulation test of the landslide initiation, it was shown that even under naturally drained conditions, the mobilized shear resistance of the weathered soil in the source area showed a rapid decrease after landslide initiation, and this should be the instinctive factor for rapid landslide motion after its initiation;

(3) In the ring-shear simulation test of dynamic loading on the valley deposits, it was shown that high potential for grain-crushing of upstream deposits and lower potential of the downstream deposits controlled the traveling and stopping process of the debris flow;

(4) The shear resistance at steady state under undrained conditions is the same for the soil samples taken from different parts of the valley (Sample Beto-2, 3, 4). A possible reason is that although the initial grain gradations of these samples differ, the soil at the shear zone would become the same when the shearing process reached the steady state, when all of the possible grain-crushing is completed.

Acknowledgments

Deep thanks are given to the Kanazawa Office of Rivers and National Highways, MLIT, for cooperation in the field work and as a source of information on the May 2004 landslide － debris flow. Financial supports by research grants (No. 15310127, Representative: F.W. Wang) from the Ministry of Education, Culture, Sports, Science, and Technology of Japan (MEXT), and 16G-03 Joint Research Programme of Disaster Prevention Research Institute (DPRI), Kyoto University are highly appreciated. Dr. Huabin Wang, Mr. Ryuta Saito, Mr. Jozef Jurko, and Mr. Taichi Minamitani of the Research Centre on Landslides (RCL), Disaster Prevention Research Institute, Kyoto University, joined the sampling and field investigation.

References

Kanazawa Office of Rivers and National Highways, Ministry of Land, Infrastructure and Transport of Japan (2004a): http://210.131.8.12/~kanazawa /mb5_kouhou/press/news.html.

Kanazawa Office of Rivers and National Highways, Ministry of Land, Infrastructure and Transport of Japan (2004b) Debris flow occurred on 17 May 2004 in Bettou-dani, *Newsletter Sabo Hakusan*, Vol. 6: 1-4 (in Japanese).

Kaseno, Y. (1993): *Geological Mapping of Ishikawa Geology Bulletin* (in Japanese).

Kaseno, Y. (2001): *Supplement of Geological mapping of Ishikawa Geology Bulletin* (in Japanese).

Marsal, R. J. (1967) Large scale testing of rockfill materials, *ASCE Journal of Soil Mechanics and Foundations Division*, 93(SM2), 27-43.

Okuno, T., Wang, F.W., Matsumoto, T. (2004): The deforming characters of the Jinnosuke-dani landslide in Haku-san mountainous area, Japan, in *Landslides: Evaluation & Stabilization* (Lacerda, W., Ehrlich,

M., Fontoura S., Sayao, A. eds)*, Proc. IX International Symposium on Landslides*, Rio de Janeiro, Vol. 2, 1279-1285.

Sassa K., Fukuoka H., Wang F.W. (1997): Mechanism and risk assessment of landslide-triggered-debris flows: Lesson from the 1996.12.6 Otari debris flow disaster, Nagano, Japan. In: *Landslide Risk Assessment* (Cruden D. M., Fell R. eds.), Proc. of the International Workshop on Landslide Risk Assessment. Honolulu, 19-21 February, 347-356.

Sassa K., Wang G., Fukuoka H. (2003): Performing undrained shear tests on saturated sands in a new intelligent type of ring-shear apparatus, *Geotechnical Testing Journal*, ASTM, 26(3): 257-265.

Sassa K., Fukuoka H., Wang G., Ishikawa N. (2004): Undrained dynamic-loading ring-shear apparatus and its application to landslide dynamics, *Landslides: Journal of the International Consortium on Landslides*, 1(1): 7-19.

Wang F.W., Okuno T., Matsumoto T. (2004): Deformation style and influential factors of the giant Jinnosuke-dani landslide in Japan, *Proceedings of the Fifteenth Southeast Asian Geotechnical Conference*, Vol.1: 399-404.

汪　発武・佐々恭二
(2004)

地すべり運動シミュレーションとハザードマップ

日本地すべり学会関西支部シンポジウム「GIS と地すべりハザードマップ」論文集, pp. 61-79.

地すべり運動シミュレーションとハザードマップ

金沢大学大学院自然科学研究科　汪　発武
京都大学防災研究所・斜面災害研究センター　佐々恭二

1. はじめに

流動性地すべりのような高速土砂流動現象は運動速度が速く，移動距離が大きいため，大きな災害をもたらすことが多い。特に近年地震及び豪雨などによって，土砂災害がしばしば引き起こされている。例えば，2003 年 7 月 20 日に熊本県水俣市で発生した斜面崩壊－土石流災害，2003 年 5 月 26 日に三陸南地震による築館地すべり，2002 年 11 月 8 日及び 2003 年 12 月 31 日に降雨・融雪による金沢市山科地すべり等，その流動距離の大きさが注目される。急速に進んでいる都市化によって，流動化地すべりによる被害の拡大が予想される。斜面災害を有効に防ぐために，危険斜面崩壊後の運動予測が重要であることが認識されている。これまでに，地すべり運動予測に関する研究が幾つかの成果が挙げられている。例えば，Hungr (1995)がすべり土塊のレオロジー特性を考慮できるように，運動方程式のラグランジュ解に基づいた運動予測法を提案した。Miao et al.(2001)はすべり土塊の変形パラメータを利用したブロック法を提案した。しかし，これらの予測法は二次元的なものであり，実務への応用までは至っていない。Sassa(1988)は三次元的地形データを用いた「地すべり運動モデル」を提案した。汪他（2004）はこの「地すべり運動モデル」に，「すべり面の見かけの摩擦係数変化モデル」を加えた。さらに，佐々恭二を代表とする文部科学省・科学技術振興調整費「地震豪雨時の高速長距離土砂流動現象の解明」（APERIF プロジェクト，平成 13 年～15 年度）の一環として，実務向けに「地すべり運動シミュレーション」システムを改良した。ここで，本シミュレーションシステムの基本的原理である「地すべり運動モデル」と「すべり面の見かけの摩擦係数変化モデル」を紹介すると共に，事例研究を通して，本シミュレーションの有効性を説明する。

近年，GIS(Geographic Information System，地理情報システム)は地形，地質，植生，人工活動などの空間情報を便利に取り扱えるため，それを利用した斜面危険性評価に関する研究も盛んに行ってきている。本論文では，GIS を用いた流動性地すべりの発生可能性を判断し，潜在地すべりの影響範囲を GIS 上で表示することによって，流動性地すべりに関するハザードマップ作成の考え方について示す。

2. 地すべり運動シミュレーション

2－1　シミュレーションの原理

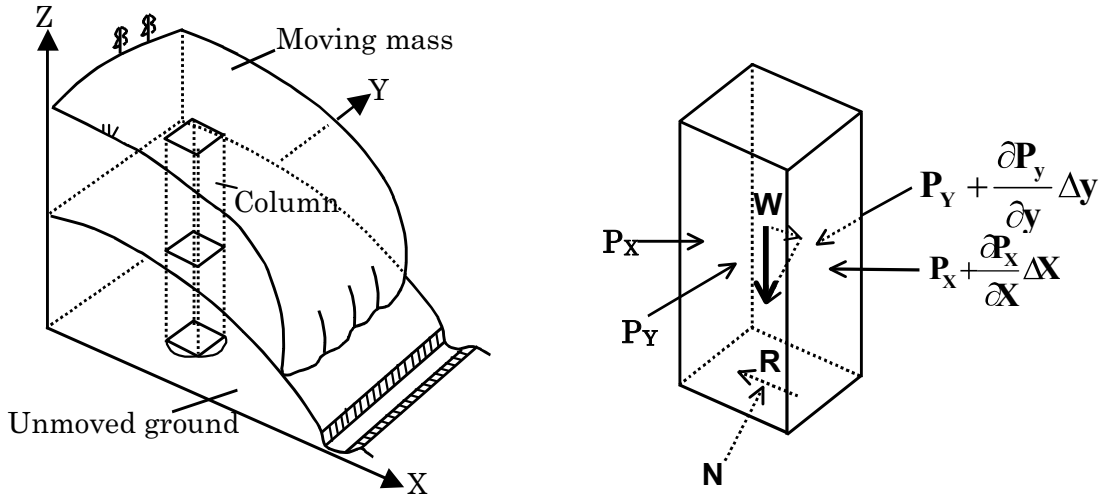

(a) 地すべり運動モデル　　(b)すべり土塊コラムに作用する力

図－1　地すべり運動モデル（Sassa，1988 より）

図－1 は Sassa（1988）によって提案された地すべり運動モデルであり，すべり土塊が安定している斜面を下っている様子を示している。運動域の平面座標系を x－y 座標系とし，そして，メッシュ分割を行う。任意のメッシュにあるすべり土塊のコラムを対象に，x，y 方向の運動方程式を立てられる。このコラムに作用する力は重力 W，すべり面による支持力 N，摩擦力 R，隣土塊からの側面土圧力 P_x，P_y である。そして，想定したすべり土塊の総体積が変わらないの仮定に基づいて，質量保存則により，運動域全体の連続方程式が求められる。式（1）と（2）はそれぞれ x，y 方向の運動方程式であり，式（3）は連続方程式である。運動方程式から x，y 方向の土塊の流量である M，N を求め，それを連続方程式に代入することによって，任意時間におけるすべり土塊の厚さ h を求める。これらの方程式を差分することによって，時間ステップごとの各メッシュにあるすべり土塊の厚さ h が計算され，運動土塊の通過した範囲は地すべりの影響範囲とし，運動停止状態での堆積範囲はこの地すべりの到達範囲を意味している。

$$\frac{\partial M}{\partial t}+\frac{\partial}{\partial x}(uM)+\frac{\partial}{\partial y}(vM)=gh\frac{\tan\alpha}{q+1}-Kgh\frac{\partial h}{\partial x}-\frac{g}{(q+1)^{1/2}}\cdot\frac{u}{(u^2+v^2+w^2)^{1/2}}\{h_c(q+1)+h\tan\phi_a\} \quad (1)$$

$$\frac{\partial N}{\partial t}+\frac{\partial}{\partial x}(uN)+\frac{\partial}{\partial y}(vN)=gh\frac{\tan\beta}{q+1}-Kgh\frac{\partial h}{\partial y}-\frac{g}{(q+1)^{1/2}}\cdot\frac{v}{(u^2+v^2+w^2)^{1/2}}\{h_c(q+1)+h\tan\phi_a\} \quad (2)$$

$$\frac{\partial h}{\partial t}+\frac{\partial M}{\partial x}+\frac{\partial N}{\partial y}=0 \quad (3)$$

ただし，h：すべり土塊の厚さ；K：水平土圧係数；M,N：x, y 方向における単位幅流量（$M=uh,N=vh$）；u,v はそれぞれ x,y 方向の流速；$\tan\phi_a$：すべり面見かけの摩擦係数；h_c：粘着

力項($c = \rho g h_c$のように定義される。長距離運動地すべりでは，ゼロとされる。ρはすべり土塊の密度，gは重力加速度，cは粘着力)；$\tan\alpha$，$\tan\beta$：x-z 平面及びy-z 平面におけるすべり面の傾斜；$q = \tan^2\alpha + \tan^2\beta$；$w = -(u\tan\alpha + v\tan\beta)$.

上述したモデルの中にせん断抵抗の項には，見かけの摩擦係数$\tan\phi_a$が含まれている。プログラミングする際に，すべり面の摩擦係数$\tan\phi_{a1}$とすべり土塊中の摩擦係数$\tan\phi_{a2}$を区別して使っている。ゆえに，すべり土塊がすべり面を沿って運動するときに，すべり面の摩擦係数$\tan\phi_{a1}$が使われているのに対し，谷を流下する運動土塊の一部が尾根をオーバーフローする場合などすべり土塊の内部でせん断が生じる場合は，すべり土塊の摩擦係数$\tan\phi_{a2}$を使う。すべり面の見かけの摩擦係数$\tan\phi_{a1}$に関して，長距離非排水リングせん断試験結果から得られた知見に基づいて，モデル化を行った。典型的な例として，Okada et al. (2000)によって行った非排水リングせん断試験の結果を取上げる（図―2)。試験は完全飽和した大阪層群の砂質土を用いて，異なる初期圧密応力で圧密してから，それぞれ非排水せん断試験を行った。圧密後の供試体の間隙比をほぼ一定になるように揃えた。長距離せん断後，定常状態に達した時のせん断抵抗は供試体が受けた初期圧密応力と関係なく，一定値となった。この結果をすべり面のせん断抵抗の変化に適用すると，長距離運動地すべりのすべり面の定常状態でのせん断抵抗はすべり土塊の厚さと関係なく，一定値である

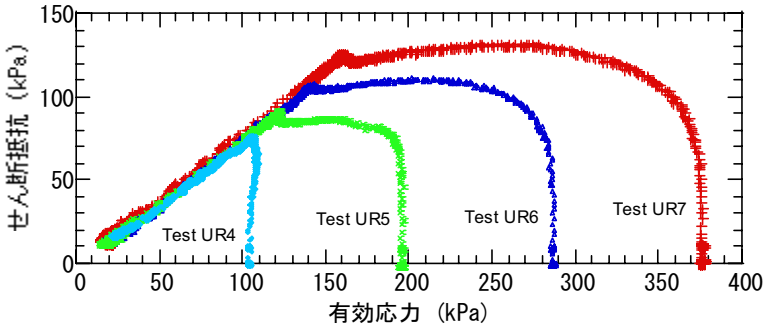

図―2　大阪層群の砂質土の異なる初期有効応力での非排水リングせん断試験における有効応力経路（圧密後の間隙比は0.71に揃えた）（Okada et al. 2000）

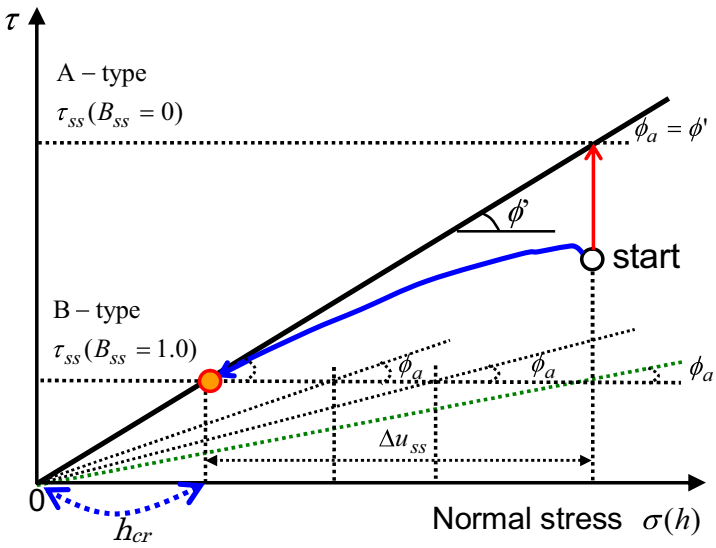

図―3　すべり面の見かけの摩擦係数変化モデル（汪他，2004）

ことを示唆している。すなわち，材料毎にそれ以下の圧力では粒子破砕が進行しない一定応力が存在することを示している。このような試験結果に基づいて，汪他（2004）は図―3 に示すような「すべり面の見かけの摩擦係数変化モデル」を提案した。

図―3 に示す「すべり面の見かけの摩擦係数変化モデル」は応力径路で表わされている。初期安定している斜面が何かの誘因（例えば，地震，降雨）で破壊したとする。破壊後の挙動として，完全排水と完全非排水の極端な 2 ケース（A-type と B-type）を示している。地すべり運動過程において，完全排水状態の場合（A-type）は，応力径路は初期応力状態から，有効応力が変化せず，せん断応力だけ増加し，破壊線まで到達する。すべり面の見かけの摩擦角度はすべり面土の有効内部摩擦角と等しく，すべり土塊は長距離運動をしない。一方，地すべり運動過程において，すべり面が完全非排水状態の場合（B-type）は，過剰間隙水圧の上昇（蓄積）によって，有効応力が減少し，小さいせん断抵抗で運動が続ける。長距離運動することによって，すべり面が定常状態に到達し，せん断抵抗が一定値である「定常状態のせん断抵抗」になる。さらに，地すべり構造が図―4 に示す「すべり面（せん断ゾーン)」と「地すべり土塊」の二層構造に簡略化できるので，すべり面が定常状態に達した後，すべり面のせん断抵抗が変わらなくなり，「地すべり土塊」の厚さだけが変化する。「地すべり土塊」の厚さが地すべり運動過程において変化することが一般的に認められている。「すべり土塊」の厚さの変化によって，見かけの摩擦角が変化するが，ある臨界厚さ h_{cr} 以下になると，見かけの摩擦角が土の内部摩擦角と等しくなる。図―5 は「すべり土塊」厚さの変化によるすべり面「見かけの摩擦係数」の変化を示している。

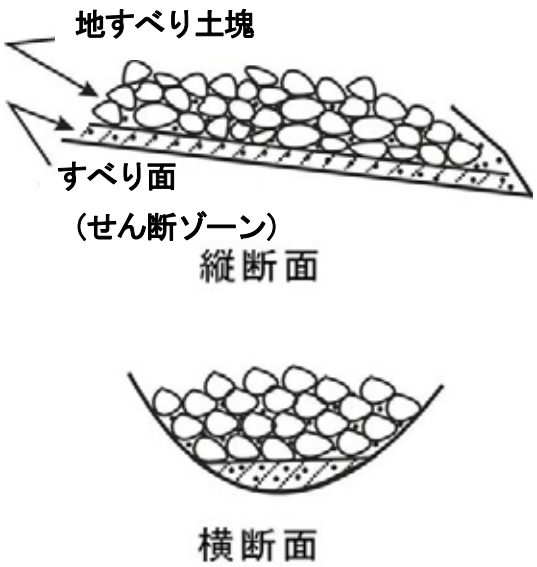

図―4　地すべりの 2 層構造

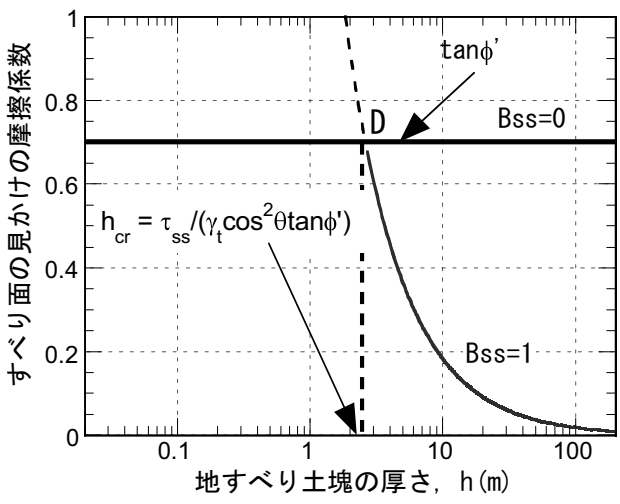

図―5　すべり土塊厚さの変化によるすべり面の見かけの摩擦係数の変化

実際の斜面での地すべり運動は以上に示した二つのケースの中間にあると思われる。その非排水の程度は「過剰間隙水圧蓄積率」B_{ss} で表わさ

れ，斜面の地形，飽和条件，土質条件などの排水に影響する素因を総合的に考慮した上で決まる。完全排水の場合は，$B_{ss}=0$ とし，完全非排水の場合，$B_{ss}=1.0$ とする。

2−2　理想斜面における地すべり運動シミュレーションの確認

地すべりの運動方程式より，地すべり運動に影響を与える因子として，以下のパラメータがある。

1)　すべり面で発揮される有効内部摩擦角ϕ'_1（地すべり運動開始後，粘着力は無視できる）
2)　すべり面で発揮される定常状態でのせん断抵抗τ_{ss}
3)　運動中の土塊内部で発揮される水平土圧係数K
4)　運動土塊の単位体積重量γ_t
5)　運動土塊内部で発揮される内部摩擦角(ϕ_{a2})と粘着力(c_{a2})
6)　運動域での過剰間隙水圧の蓄積率B_{ss}

以上の因子の中で，(1) と (2) のすべり面の内部摩擦角と定常状態でのせん断抵抗，及び (6) の運動域での過剰間隙水圧の蓄積率が「すべり面見かけの摩擦係数」の計算に必要となっているので，地すべりの運動距離に大きな影響を与えている。なお，(1) と (2) はリングせん断試験によって，求めることができる。運動過程における土塊間の水平土圧係数は土塊内部で発揮される内部摩擦角と間隙水圧から推定され，すべり土塊のやわらかさの程度を表わす指標であり，運動方向の直行方向の広がりに影響を与える。

以上の地すべり運動モデルの有効性の検証するために，図−6 に示す単純な仮想斜面の運動を例として取上げる。すべり面の形状は楕円とし，斜面方向に長軸を置き，それに直交する斜面の平行方向（水平方向）に短軸を置く。また，長軸と短軸の寸法を変えて，異なる体積の運動土塊のシミュレーションを行った。

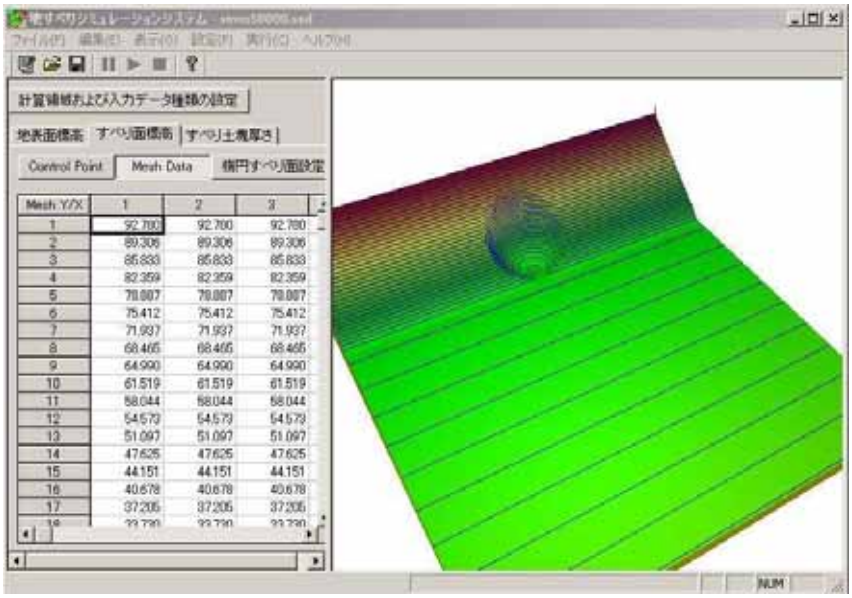

図−6　地すべりシミュレーションのメイン画面

図−6 はシミュレーションのメイン実行画面で，右部分の画像はすべり面の状況を示している。図−7 はすべり面及びすべり土塊のパラメータの設定画面である。図−8 は計算過程の一部を抽出して計算時間順で表わしている。

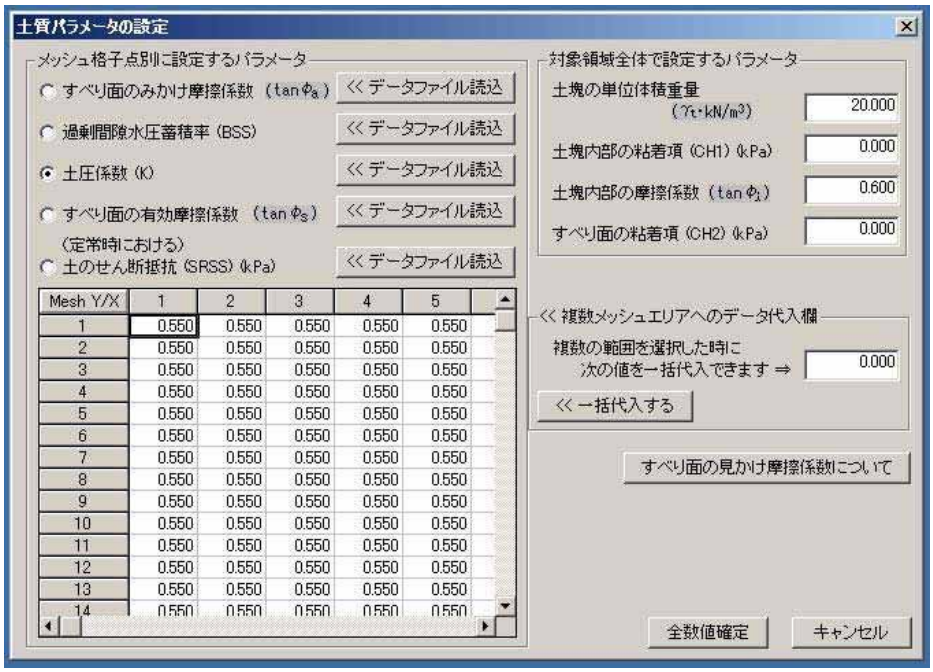

図−7　地すべりシミュレーションのパラメータ設定画面

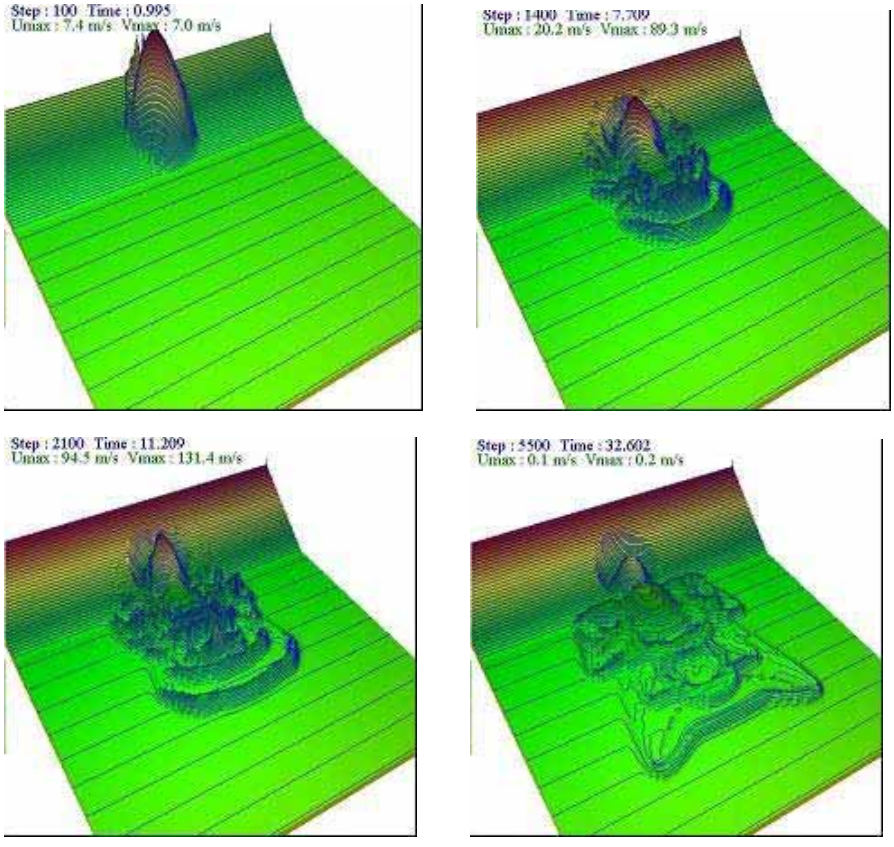

図−8　仮想斜面（体積＝5000 m^3）でのシミュレーション結果（t = 1.0 sec, t =7．7 sec, t = 11.2 sec, t = 32.6 sec）

図－9 はシミュレーションの結果に基づいて求めた平均の見かけの摩擦係数（$\tan\phi_a$：地すべり発生時頂点からすべり土塊の末端までの水平距離 L と鉛直距離 H の比で，H/L で表わされる）とすべり土塊の体積の関係を示している。これらの結果より，見かけの摩擦係数はすべり土塊体積の増加にしたがって，減少している傾向が確認でき，この結果は奥田（1984）に示した統計の結果とほぼ合致している。

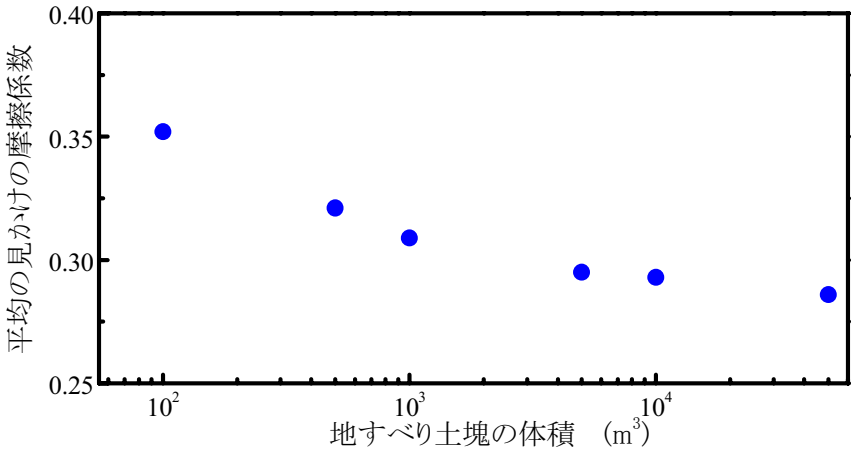

図－9　シミュレーションから得た見かけの摩擦係数とすべり土塊体積の関係

2－3　事例研究

開発した地すべり運動シミュレーションのソフト（RAPID/LS と名づけている）を用いて，幾つかの発生した地すべり事例に適用し，さらに地すべり発生危険性のある地すべり運動の予測を試みた。

発生した地すべりの事例研究に関して，以下の地すべりを取上げた。

(a) 2003 年 5 月地震による築館地すべり（Tsukidate landslide）；

(b) 2002 年 11 月連続降雨による山科地すべり（Yamashina landslide）；

(c) 1934 年 7 月集中降雨による白山別当崩れ（Bettou failure）

地すべり運動予測の対象として，白山地域にある現在でも活動している甚之助谷地すべり（Jinnosuke-dani landslide）を取上げた。

以上の地すべりの場所を図－10 に示している。

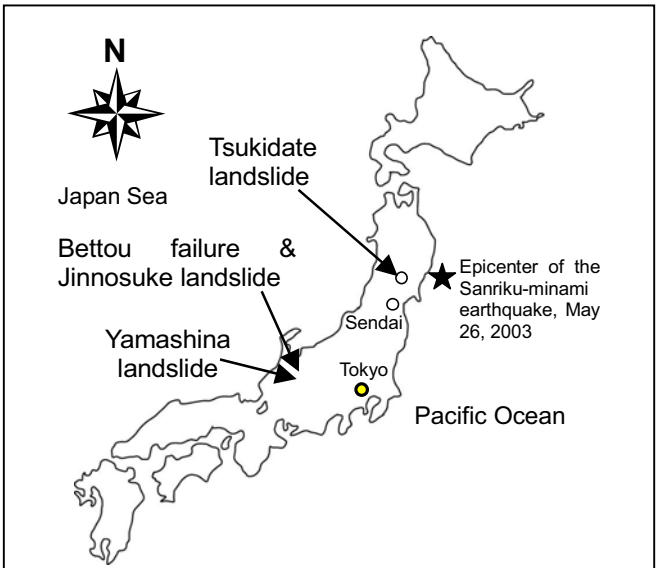

図－10　事例研究の対象である地すべりの位置

2−3−1　地震による築館地すべりのシミュレーション

図−11　三陸南地震による築館地すべり（読売新聞ホームページより，2003 年 5 月 27 日撮影したものに加筆）

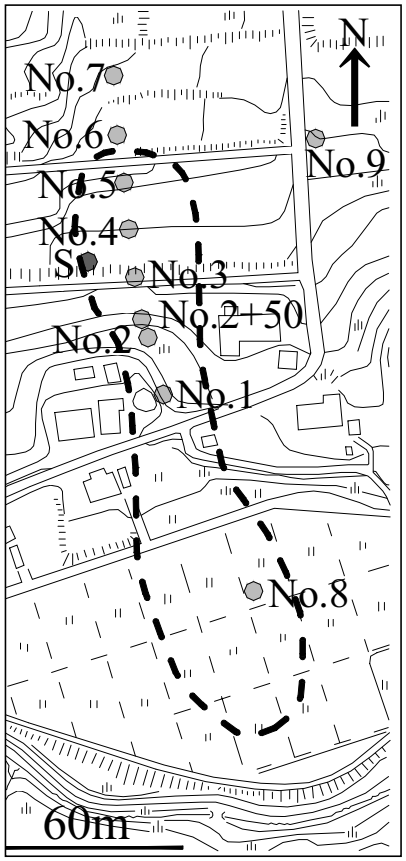

図−12　築館地すべりの平面図

2003 年 5 月 26 日 18 時 24 分ころ，東北地方の宮城沖で，マグニチュード 7.0，震源深さが約 71km の三陸南地震が発生した。この地震によって，岩手県から宮城県にかけて震度 6 弱が観測され，築館町で長距離高速運動地すべりが誘起された（図−11，読売新聞，2003）。

築館地すべりは築館町役場より西 750m の館下地区に位置しており，昭和 45 年に宅地造成した際の火山性堆積物（火砕流堆積物）の盛土地盤で発生した（国土地理院，2003）。築館地すべりは，ほぼ南方向へ運動した。先端の移動距離は約 130m で，源頭部の最大幅は約 40m であった（図−12）。竹は運動土砂と一緒に，立ったままで水田の上に堆積した。また，池の崩壊による水溜まりの確認もできた。現地調査・実験および室内実験の結果より，火山性堆積物材料の盛土は，透水性が低く，かつ地表から数メートル下では，ほぼ完全飽和していたことが推定される。また，低い貫入抵抗値から，せん断強度が非常に低かったことも推定される。したがって，地すべりはゆるく詰められた盛土部分の中で発生したと考えられる。

計算に当たって，地形データとして，すべり面の標高とすべり始める時のすべり土塊の厚さが必要である。宮城県土木部砂防水資源課から提供された地すべりが発生する前の 1:2,500 の地形図，

地すべり発生直後に京都大学防災研究所斜面災害研究センターによって測量された中央縦断面図（Fukuoka et al., 2004），および簡易貫入試験の結果に基づいて，すべり面の標高とすべり土塊の初期厚さを推測した。図－13 は発生域の中央縦断面に沿う地すべり発生前後の地形，推定すべり面の形状を表している。この図から，中央断面でのすべり面標高とすべり土塊の初期厚さを決定した。

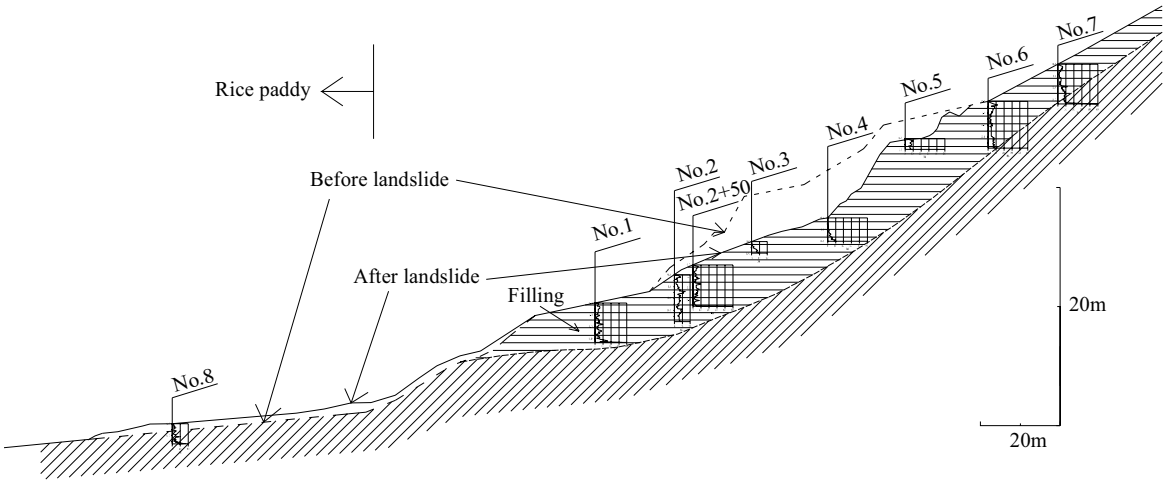

図－13　推定された地すべりの中央縦断面

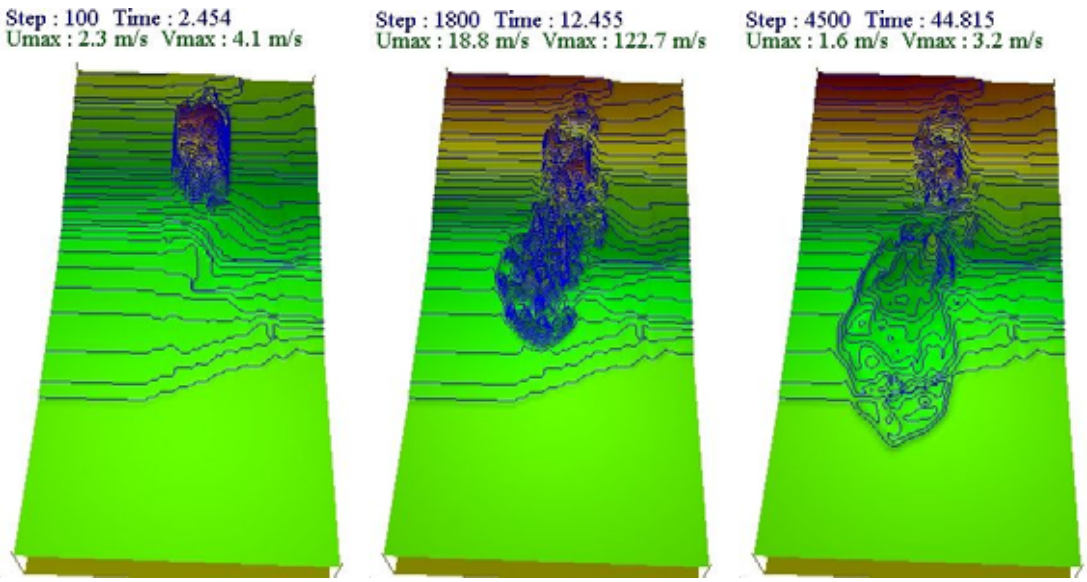

図－14　築館地すべりの運動シミュレーション結果（左から右への経過時間は 2.5sec, 12.5sec, 44.8 sec である）（すべり土塊 5 倍拡大表示；等高線間隔：1 m；計算範囲：116 m×226 m）

土質力学的なパラメータとしては，すべり面土の性質とすべり土塊の性質が必要である。今回のシミュレーションでは，地すべりの堆積範囲を実際堆積範囲と一致させるように，土質力学的パラ

メータを逆算した。すべり面の定常状態でのせん断強度を 3.5kPa，有効内部摩擦角が 25 度にした。そして，すべり土塊も同じ盛土と推定したため，同じく有効内部摩擦角を 25 度にした。また，すべった直後の写真からすべり土塊内部が飽和されていたと推定し，過剰間隙水圧の蓄積率 B_{ss} を 1.0 に設定した。

図－14 は築館地すべりの運動シミュレーションにおける地すべり発生直後（2.5 sec），途中(12.5 sec)，および最終ほぼ停止状態(44.8 sec)の結果を示す。堆積土塊の分布はおおむね実際の状況と対応していることが確認できる。

2－3－2　連続降雨による山科地すべりのシミュレーション

2002 年 11 月 8 日に，石川県金沢市山科町で，源頭部の幅約 60m，長さ 100m，滑落崖の高さ約 10m，移動距離約 200m の流動性の山科地すべりが発生した（図－15）。この地すべりの誘因は発生前 13 日間の連続降雨であると考えられる。この地すべりによって源頭部でりんご畑が崩壊し，末端付近で林道が抉られ，破壊された。地すべり発生後，地すべりによる土石流被害を防ぐための砂防堰堤が末端部に建設された。その後も滑落崖での崩壊の拡大が続き，2003 年 12 月 31 日には，再び流動化地すべりが発生した。

図－15　金沢市山科町で発生した流動性地すべり（2002 年 11 月 8 日発生）（石川県県央農林総合事務所　提供）

地すべり地周辺の地質は第三紀中新世の泥岩層（犀川層）である。紺野（1993），柳沢（1999）によれば，本層は大桑層に不整合に覆われ，下荒屋凝灰岩層を整合に覆う。また，山科地すべり地の東部では高位の段丘堆積物が犀川層を不整合に覆う。犀川層の岩相は塊状無層理の泥岩であり，層厚は約 200 m である（田中他，2004）。地すべり地周辺は小起伏山地で，斜面は比較的緩やかに傾斜する。地すべりが発生する前は沢地形であり，斜面勾配は約 13° であった。地すべり発生後は

源頭部の両脇から湧水が見られ，小沢を形成している。山科地すべり周辺の植生はほとんどが竹林であるが，地すべり地の源頭部にはりんご畑が広がる。このりんご畑は過去の農地造成により造られた平地上にある。

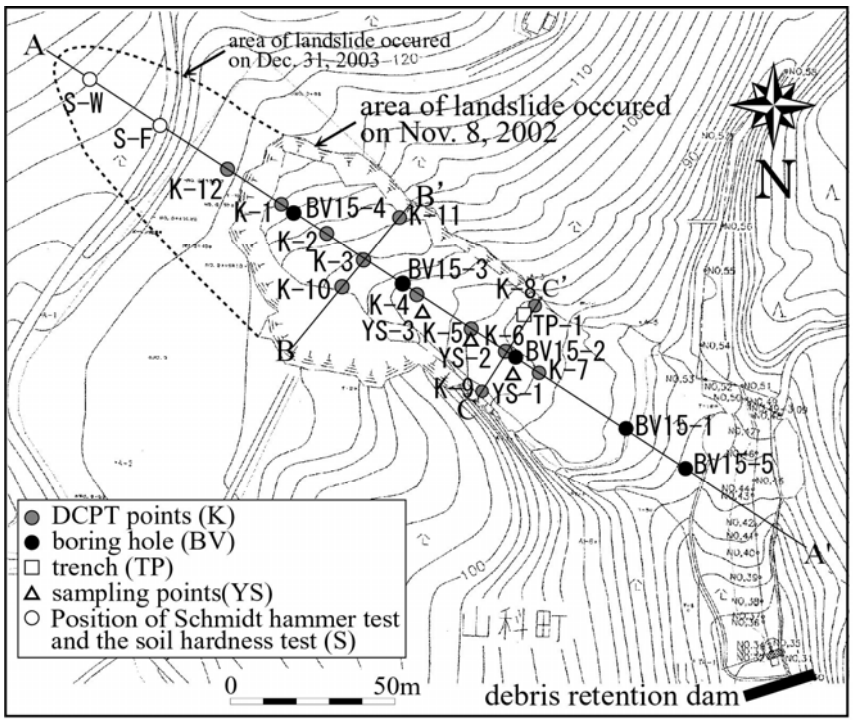

図－16　山科地すべりの平面図

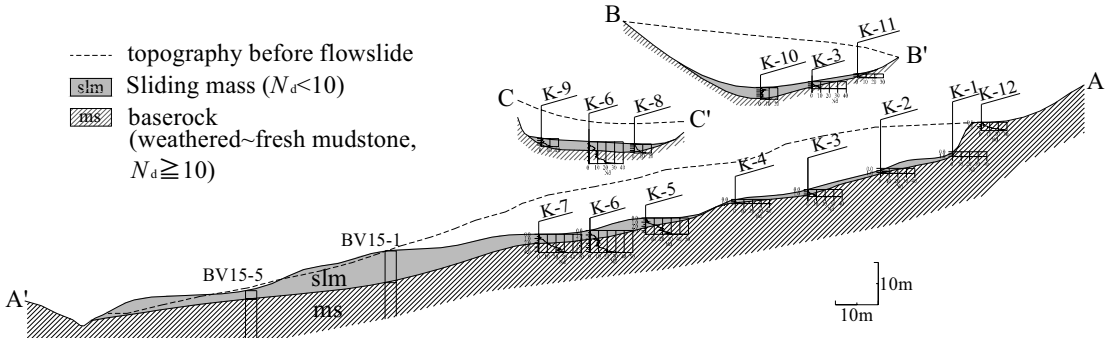

図－17　山科地すべりの中央縦断面図

図－16 は，地すべり地内で行った調査位置図である。調査内容は，すべり面の位置を調べる目的で，地表踏査，簡易動的コーン貫入試験（以下 DCPT ; K-1～K-12），ボーリング調査（BV15-1～5，石川県実施）を行った。また，地すべり土塊の特徴を把握する目的でトレンチ調査（TP-1），試料採取（YS-1～YS-3）を行った。DCPT，ボーリング調査及びトレンチ調査結果から地質断面図（図－17）を推定した。頭部でのすべり面は新鮮な泥岩であるのに対し，中部～末端でのすべり面は粘土化した強風化泥岩である。したがって風化層と新鮮層の間で発生した地すべりは，一旦強風化泥

岩分布域を高速運動したが，斜面末端の竹林の分布する緩傾斜の地域で停止した。

シミュレーションを行った範囲は地すべり運動全体を把握できるように東西方向に 240 m（60 メッシュ），南北方向 252 m（63 メッシュ）とした。図－18 は運動シミュレーションを行った範囲と地すべり地周辺の植生状況などを示している。運動シミュレーションに用いた土質パラメータは，実際の堆積範囲に一致するように逆算法で定めた（表－１）。すべり面での定常状態でのせん断抵抗を竹林部とその他で分けた理由は，地すべり現場では，竹林が明らかにすべり土塊を塞き止める役割を果たしており，その部分のせん断抵抗を高くすることが妥当であると考えたからである。発生直後の崩壊土砂は，完全に飽和しており，水溜りも多数見られたので，過剰間隙水圧蓄積率 は 0.99 とした。

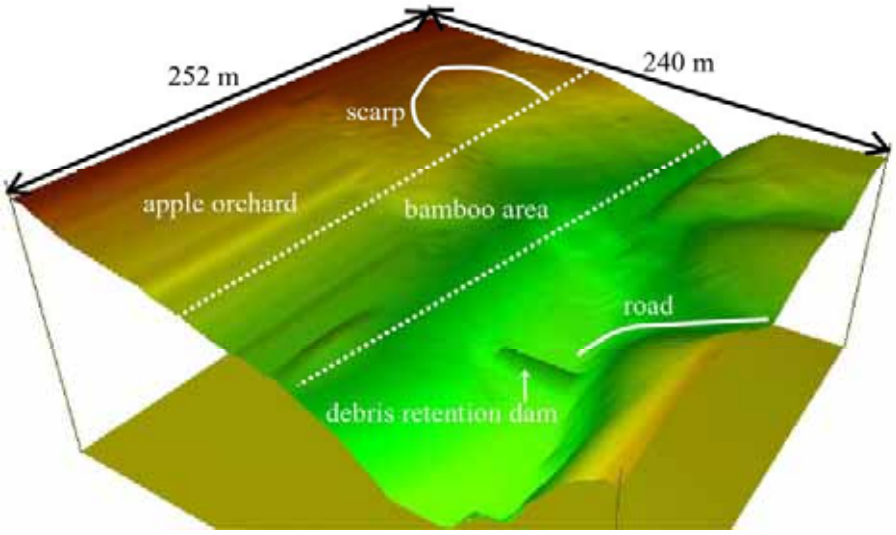

図－18　山科地すべりのシミュレーション範囲

表－１　山科地すべりの運動シミュレーションに用いた土質パラメータ

すべり土塊の単位体積重量, γ_t (kN/m^3)	15.0
すべり土塊の内部摩擦角, ϕ_{a2} (deg.)	0
すべり土塊の粘着力, c_{a2} (kPa)	40
すべり土塊の水平土圧係数, K	0.6
すべり面土の定常状態でのせん断抵抗	
竹林域, τ_{ss}-1 (kPa)	50
その他の地域, τ_{ss}-2 (kPa)	10
すべり面土の有効内部摩擦角, ϕ' (deg.)	35
過剰間隙水圧蓄積率, B_{ss}	0.99

図－19 に t = 0，9.8，19.5，32.3 sec の運動シミュレーション結果を示す。運動土塊の動きを明確に示すように，運動土塊の厚さを計算値の 3 倍にして表示した。シミュレーションによって求めら

れた速度は東西方向の最大速度 U_{max} と南北方向の最大速度 V_{max} を示す。これらの速度は地すべり土塊のメッシュ間の移動速度である。地すべり土塊の最大移動速度は竹林到達前後で最も大きく 10.9 m/s であった。

飽和している強風化泥岩の定常状態のせん断抵抗を 10 kPa，竹林でのせん断抵抗を 50 kPa を与えることにより，ほぼ実際に発生した流動状況が再現できた。

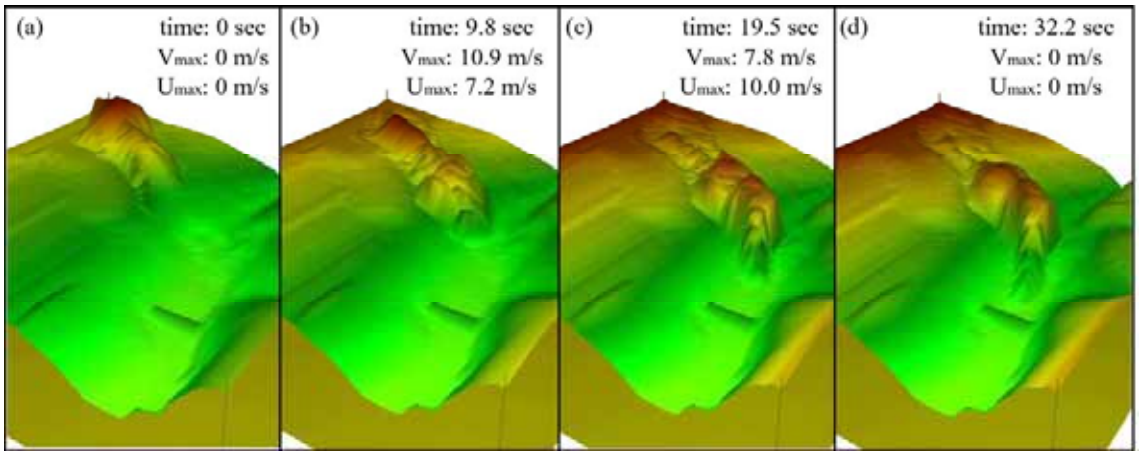

図－19　山科地すべりのシミュレーション結果（計算範囲：240 m×252 m）

2－3－3　集中降雨による白山地域における別当崩れのシミュレーション

図－20　白山地域における別当崩れと甚之助谷地すべり

白山南西斜面（図－20）にある別当崩れは，1934 年 7 月 11 日，3 日間で 500 mm の豪雨によって発生した。崩壊した約 1 千万 m^3 の土砂は手取川の堆積物を巻き込みながら土石流となって，約 4 km 下流の市ノ瀬村落を埋没させた。その後も手取川を流下経路として甚大な被害を及ぼし，ついには，約 70 km 下流の日本海に到達した。この土石流によって死者 112 名，倒壊家屋 240 棟という甚大な被害をもたらした。

表－２　別当崩れの運動シミュレーションより求めた土質パラメータ

過剰間隙水圧蓄積率：B_{ss}		0.95
水平土圧係数：K		0.65
定常状態のせん断抵抗：τ_{ss} (kPa)	崩壊地	200
	河床	8
	その他の部分	50
すべり面の有効内部摩擦係数：tanϕ'		0.7
すべり土塊の単位体積重量：γ (kN/m^3)		20
すべり土塊の内部摩擦係数 tanϕ_{2a}		0.65
すべり面及びすべり土塊の粘着力（kPa）		0

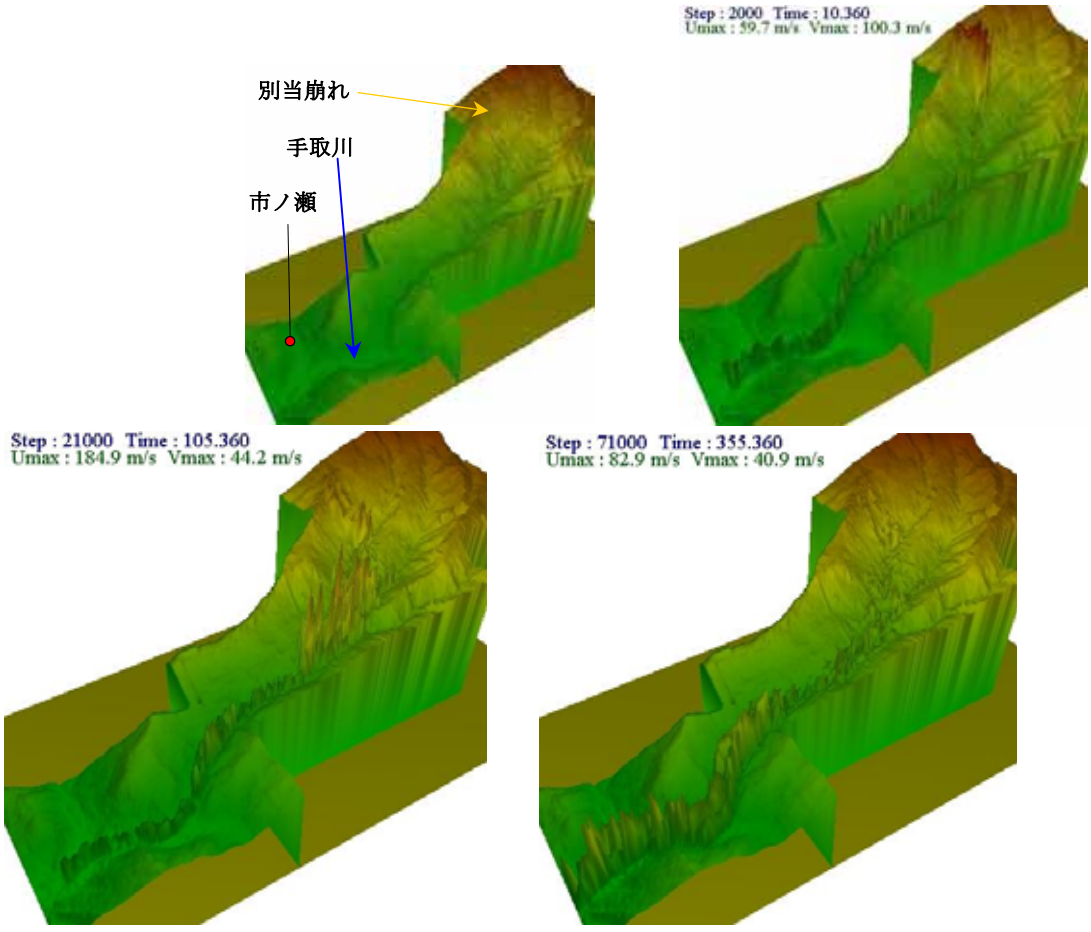

図－21　別当崩れのシミュレーション結果（すべり土塊厚さを 10 倍で表示）

運動シミュレーションには，崩壊前の地表面標高，すべり面の標高，崩壊土砂とすべり面及び流下経路の土質パラメーターが必要である。崩壊前の地表面は現地形図を基に復元し，すべり面標高は別当崩れ上部の露出しているすべり面と層理面の関係から推定した。土質パラメータは運動シミュレーションより逆算する（表―2）。運動シミュレーションは，縦 3.25 km×横 5.825 km（130×233 mesh，mesh size: 25 m×25 m）の範囲で実施し，別当崩れと市ノ瀬集落間 4 km の土石流の運動を再現した。この運動シミュレーションには，崩壊土砂の衝撃による河床堆積物の流動化過程を考慮するために，河床堆積物を設置した。

図―21 は別当崩れの運動シミュレーションの結果である。崩壊土砂が別当谷，手取川を流下し，更に下流の市ノ瀬を通過した。流下途中ですべり土塊の一部の堆積が見られたが，河床堆積物を巻き込むことにより，すべり土塊の体積が減少することなく流下していく現象が再現できた。

2―3―4　白山地域における甚之助谷地すべりの運動シミュレーション

甚之助谷地すべりは手取川の源流である白山に位置しており，別当崩れのすぐ隣である。手取川中流部には貯水量約 2 億 m^3 のロックフィル形式の手取川ダム（高さ 153 m，幅 420 m）が 1980 年に建設された。大規模な地すべり土塊が貯水池に流れ込んだ場合，越流によるダム崩壊の危険性が懸念される。当地域の豊富な降水量及び手取川の急峻な河床勾配によって，地すべりは土石流に転換することが多い。国土交通省は 1980 年代から行っている甚之助谷地すべりの調査及び観測結果によると（国土交通省金沢工事事務所，2002），排水などの対策工事を行っているにも関わらず，甚之助谷地すべりは現在でも活発的な動きを示している。

甚之助谷地すべりは図―20 の写真中央に位置しており，長さ約 2,000 m，幅約 500 m で，海抜 1,200 m～2,100 m の間に分布している。右岸側は別当谷であり，1934 年に発生した別当崩れの滑落崖が残されている。左岸側には甚之助谷（上流）と柳谷（下流）が存在している。土石流を防ぐために，1927 年から現在までに，別当谷に約 30 基，甚之助谷と柳谷に約 50 基の砂防ダムが建設されている。

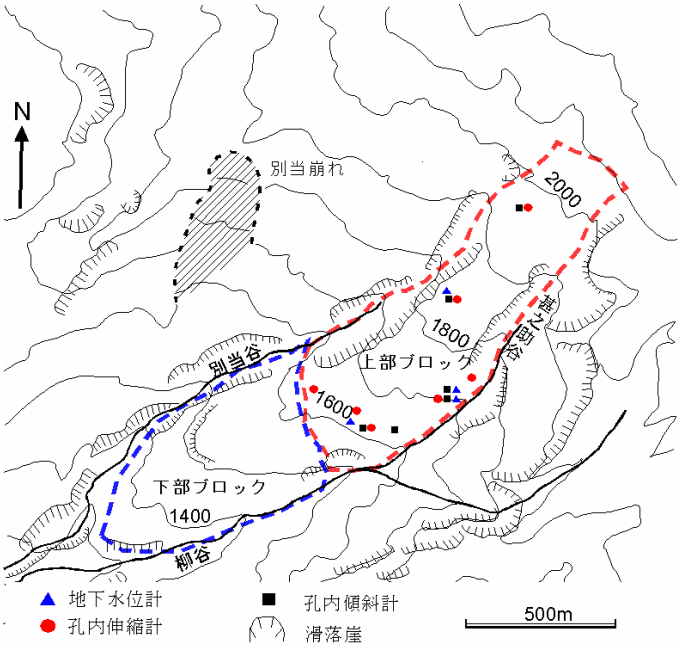

図―22　甚之助谷地すべりの平面図

図―22 は甚之助谷地すべりとその周辺の地形図を示している。“大規模中間尾根ブロック”と呼ばれている（国土交

通省，2002）上部ブロックの平均勾配は約 25° であり，下部ブロックの平均勾配は約 20° である。図－22 には国土交通省によって上部ブロック内に設置されている観測機器の位置も示している。地下水位計 4 箇所，孔内傾斜計 6 箇所，孔内伸縮計 7 箇所の観測が行われている（2003 年 11 月現在）。

地すべりとその周辺の 1：100,000 地質図によれば，白山の基盤岩は古生代の飛騨片麻岩であり，その上にジュラ紀～白亜紀前期の湖成堆積層である手取層群の頁岩・砂岩互層及びレキ岩が広く分布している（紺野，1993）。

図－23 は地すべり防止区域内の観測点の分布と，1994 年から 2001 年まで 7 年間の地表面変位観測結果をベクトルで示したものである。この観測結果によれば，上部ブロックは非常に活発に変位しており，7 年間に約 1,180 mm の累積最大変位が B5 と B11 観測点で生じている。上部ブロックの年平均移動量は 80 mm～170 mm である（奥野他，2004）。

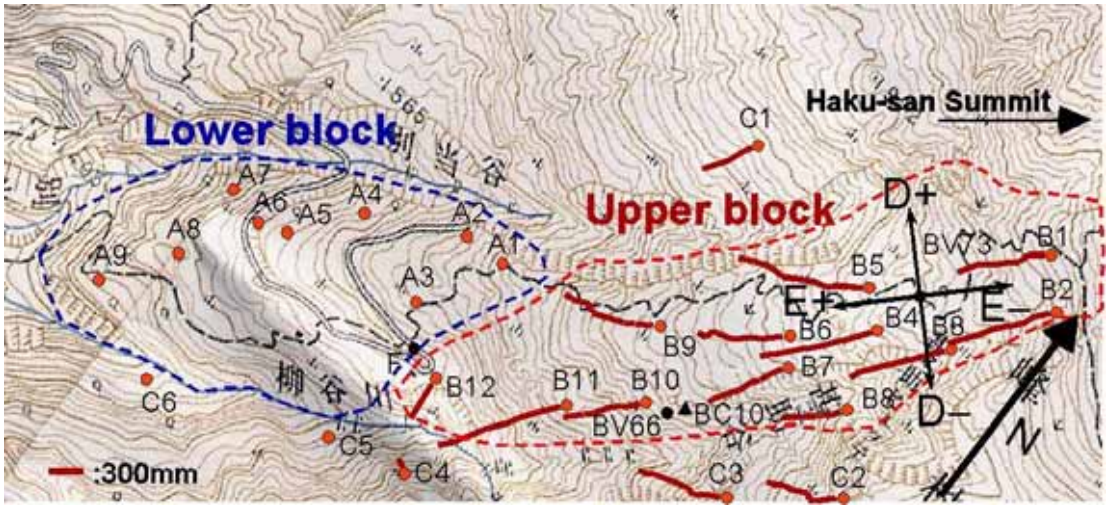

図－23　1994 年から 2001 年までの甚之助谷地すべりにおける累積地表面変位量

この 7 年間での変位観測結果から，甚之助谷地すべり地域で排水工などの対策工が行っているにも関わらず，地すべりが変位し続けていることが分かる。地すべりの規模から見ると，対策工の規模もさらに拡張する必要がある。地すべりが発生した場合の運動予測は非常に重要である。そこで，先に行った別当崩れの運動シミュレーションから求めた土質パラメータを用いて，甚之助谷地すべりへ適用し，運動範囲を予測するためのシミュレーションを行った。因みに，当地域の深いボーリングが限られているため，潜在すべり面を推定するには地表踏査と変位観測の結果も考慮に入れた。

図－24 は甚之助谷地すべりに関する運動予測を行った結果である。土質力学的なパラメータは前述した別当崩れの運動から逆算した結果を参照した。なお，甚之助谷地すべりのすべり土塊厚さが非常に大きいため，見かけの摩擦係数を計算する時に，別当崩れのパラメータをそのまま代入すると，見かけの摩擦係数は非常に小さくなり，運動速度が非常に大きくなる。甚之助谷地すべりの深度ははるかに大きいため，硬い岩盤と考えて，すべり面の定常状態でのせん断抵抗は別当崩れの二倍にした。また，甚之助谷地すべりの両サイドにある別当谷，甚之助谷，柳谷はほぼ常時水が流れ

ているので，過剰間隙水圧蓄積率も 0.95 にした。結果としては，別当崩れのシミュレーション結果と比べると分かるように，甚之助谷地すべりの運動土塊の体積が大きいため，運動速度はさらに大きくなっている。地すべりが破壊してから，崩壊土砂が別当谷と甚之助谷の両方に突入し，下部ブロックの両側を通過し，その末端で合流する。その後，手取川を下って行く。市ノ瀬を通過した時点でも，運動速度がまた速い。このような予測結果から，崩壊した土砂が手取川ダム貯水池に入り込み，それによる波がダムに衝撃を与えることが推定される。さらに，それによる洪水災害，あるいは土石流災害への拡大も懸念される。今回の予測計算には，推定している素因が非常に多いので，予測の精度を向上するためには，甚之助谷地すべりに関する詳細な調査研究が必要である。

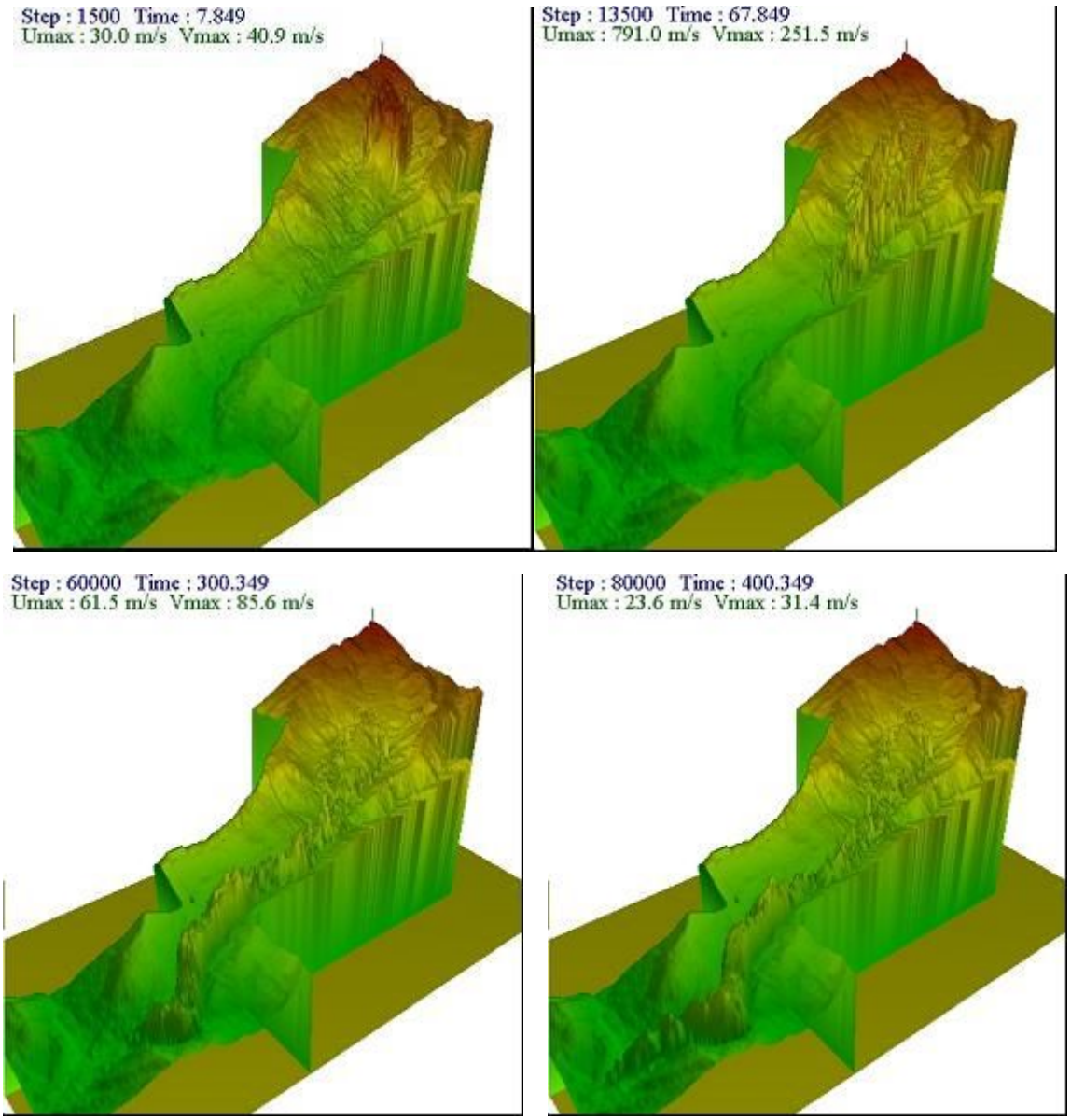

図－24　甚之助谷地すべりのシミュレーション結果(すべり土塊を 10 倍拡大表示)(t＝7.8 sec, t＝67.8 sec, t＝300.3 sec, t＝400.3 sec)

3. GIS を用いた流動性地すべりの危険性予測

GIS は地形データ，地質，植生，土質試験結果などのデータを容易に統合できるため，地すべり危険地域の判定に重要なツールになっていくには間違いがない。いままでに，GIS を用いた斜面災害の危険性判定の研究例が幾つかが公表されている。例えば， Ayalew et al. (2004)は新潟県阿賀野川角田地区において，岩盤の性質，斜面勾配及び傾斜方向，海抜，道路及び断層構造などを重ね合わせることによって，地すべり発生危険性を表わす危険性分布図を作成した。

GIS を用いた流動性地すべりの危険性予測に関しては，二つの内容を考えている。まず，どこで流動性地すべりが発生しやすいに関しては，いままでの研究成果を利用し，それに流動性地すべりの発生しやすい素因を取り入れることによって，流動性地すべりの発生しやすいの程度を判断できる。近年発生した流動性地すべりの事例から見ると，盛土及び土地造成などの行為は流動性地すべり発生に大きな影響を与えている。また，このような判断に基づいて，流動性地すべりが発生可能な箇所に対して，詳細な調査及び土質試験を行ない，地すべり運動シミュレーションを行う。最終的に GIS を用いて，地すべり運動シミュレーションによる危険地域の予測結果をプロットすることによって，流動性地すべりの危険予測図を作成できる。

4. 終わりに

地すべりなどの斜面災害に関する研究は単なる安定性評価では社会のニーズに満足できない状況になってきた。GIS を利用した斜面危険性評価も一層地すべりなどの影響範囲まで発展させる必要なある。本論文はその基本となっている地すべり運動範囲予測のツールの開発について，その理論的背景，検証計算，事例研究，及び運動予測を説明した。詳細な地形測量，現場の地質調査，及び土質試験を行った上での地すべり運動シミュレーションは十分な有効性が示されている。その結果をさらに GIS 技術に適用することによって，流動性地すべりのハザードマップの作成ができる。なお，現地から採取した土のリングせん断試験結果から推定した土質定数を用いた運動予測も実施しており，その結果は国際ジャーナル「Landslides」に掲載予定である。

謝辞：本論文に関する事例研究を行う際に，一部の現場調査及びシミュレーション実施に参加して頂いた金沢大学大学院自然科学研究科の松本樹典教授，山上尚幸技官，大学院生の奥野岳志君，田中康博君，卒業生の中村佳代さん及び高田渉君に感謝します。

参考文献

Ayalew, L, Yamagishi, H., Ugawa, N. (2004): Landslide susceptibility mapping using GIS-based weighted linear combination, the base in Tsugawa area of Agano River, Niigata Prefecture, Japan. Landslides, Vol.1, No.1, pp.73-82.

Fukuoka, H. Wang, G.H., Sassa, K. Wang, F.W., Matsumoto, T. (2004): Earthquake-induced rapid long-traveling flow phenomenon: the case of May 2003 Tsukidate landslide in Japan. Landslides, Vol.1, No.2, in press.

http://www.yomiuri.co.jp/national/news/20030527it04.htm (読売新聞, 2003)

Hungr, O. (1995): A model for the runout analysis of rapid flow slides, debris flows, and avalanches. Canadian Geotechnical Journal, Vol.32, pp.610-625.

紺野義夫（1993）：新版石川県地質図（10 万分の 1）・石川県地質誌．北陸地質研究所，321pp.

紺野義夫（2001）：石川県地質誌・補遺，北陸地質研究所，194p.

国土地理院（2003）：2003 年 5 月 26 日宮城県沖の地震に伴う崩壊等地形変動調査について．http://www.gsi.go.jp/WNEW/PRESS-RELEASE/2003/0612.htm.

国土交通省金沢工事事務所（2002）：平成 13 年度甚之助谷地すべり調査作業報告書，139p.

Miao, T.D., Liu, Z.Y, Niu, Y.H, and Ma, C.W. (2001): A sliding block model for the runout prediction of high-speed landslides. Canadian Geotechnical Journal, Vol.38, pp.217-226.

宮城県土木部砂防水資源課(2003)：H15.5.26「三陸南地震」による築館町館下被災状況.

Okada, Y., Sassa, K., and Fukuoka, H. (2000): Liquefaction and the steady state of weathered granite sands obtained by undrained ring shear tests: A fundamental study on the mechanism of liquidized landslides. Journal of Natural Disaster Science, Vol.22, No.2, pp.75-85.

奥田節夫(1984) :歴史記録から見た大崩壊の土石堆積状態の特性．京都大学防災研究所年報，Vol.27, B-1, pp. 353-368.

奥野岳志・汪発武・松本樹典（2004）：白山における巨大甚之助谷地すべりの運動様式及びその影響素因．地すべり，Vol.41，No.1，印刷中.

Sassa, K. (1988): Geotechnical model for the motion of landslides. Proc. 5th Inter'l Symp. on Landslides, Vol.1, pp.37-56.

田中康博・汪発武・中村佳代・松本樹典（2004）：金沢市山科町における長雨を誘因とする流動化地すべりの特徴と運動機構．地すべり，投稿中.

汪発武・佐々恭二・松本樹典・奥野岳志（2004）：粒子破砕を考慮した地すべりの流動化メカニズムと運動範囲予測．地すべり，Vol.40，No.5，pp.377-388.

柳沢幸夫（1999）：金沢市南部地域に分布する中新統の珪藻化石層序．地質調査所月報，Vol.50, No.1, pp. 49-65.

Boldini D., F.W. Wang, K. Sassa, P. Tommasi
(2006)

Application of large-scale ring-shear tests to the analysis of December 2002 tsunamogenic landslides at Stromboli volcano (Italy)

Geotechnique (submitted)

Application of large-scale ring-shear tests to the analysis of December 2002 tsunamogenic landslides at Stromboli volcano (Italy)

Daniela Boldini[1], Fawu Wang[2], Kyoji Sassa[3], Paolo Tommasi[4]

[1] Lecturer, Department of Chemical, Mining and Environmental Engineering, University of Bologna, viale Risorgimento 2, 40136 Bologna, Italy; e-mail: daniela.boldini@unibo.it
[2] Assistant Professor, Research Centre on Landslides, Disaster Prevention Research Institute, Kyoto University, Gokasho, Uji, Kyoto 611-011, Japan; e-mail: wangfw@landslide.dpri.kyoto-u.ac.jp
[3] Professor, Research Centre on Landslides, Disaster Prevention Research Institute, Kyoto University, Gokasho, Uji, Kyoto 611-011, Japan; e-mail: sassa@scl.kyoto-u.ac.jp
[4] Researcher, Institute for Geo-Engineering and Environmental Geology, National Research Council, c/o Faculty of Engineering, via Eudossiana 18, 00184 Rome, Italy; e-mail: paolo.tommasi@uniroma1.it

Abstract: The island of Stromboli (Southern Italy) is a large volcanic edifice 4,000 m high, which rises for about 900 m above the sea level. Most of the NW flank of Stromboli volcano is formed by a wide depression called Sciara del Fuoco, which is filled mostly by irregular alternations of layers of volcanoclastic materials. Between 29th and 30th December 2002, the NW flank of Stromboli volcano (Sciara del Fuoco) was involved in submarine and subaerial destructive landslides that caused two tsunami waves with a maximum run-up of 10 m. In this paper, a joint research between the National Research Council (Italy) and the Disaster Prevention Research Institute of Kyoto University (Japan) is presented. Tests were performed with the large-scale ring-shear apparatus at the Disaster Prevention Research Institute in order to investigate the mechanism governing the relatively slow deformation phase that preceded the landslide initiation and the subsequent triggering of the rapid submarine landslide that provoked the first tsunami. Since drainage conditions for the submarine slide were not known, tests were performed with both opened and closed drainages at the specimen top and the shear behaviour was analysed in terms of shear strength, pore-water pressure generation and grain crushing. Experimental results indicate that fully or partial liquefaction can be invoked to explain the submarine failure and the subsequent long run-out (more than 1,000 m) of the failed materials.

Key words: Landslide, tsunami, volcanoclastic material, ring-shear tests, liquefaction, Stromboli volcano, grain crushing

INTRODUCTION

The Stromboli volcano, located in the homonymous island (Southern Italy), spreads its products over the NW flank called Sciara del Fuoco (fire stream). The Sciara del Fuoco is formed by a more than 200-m thick deposit consisting of irregular alternations of volcanoclastic layers with minor layers of primary products (i.e., pyroclastites and lava flows).

Between December 29th and 30th 2002, the thrust exerted by the magma intruded during a major eruption, triggered a sequence of large-scale instability phenomena on the Sciara del Fuoco culminating in a submarine and two subaerial destructive landslides. Landslides involved about 20 millions m3 of slope materials and produced two series of tsunami waves, which run up the inhabited coasts of the Stromboli island for a maximum height of 10 m, damaged shoreline facilities of the facing Panarea Island (20 km far) and were felt on the northern coast of Sicily (60 km far).

The Italian Department of Civil Defence has promoted a research programme on the effects of the eruption, including the reconstruction of instability mechanisms of landslides. In the framework of this programme, a joint research between the National Research Council (Italy) and the Disaster Prevention Research Institute (DPRI) of Kyoto University (Japan) was conducted as a part of the UNITWIN Cooperation Programme by UNESCO, Kyoto University, and the International Consortium on Landslides (ICL) “Landslide Risk Mitigation for Society and the

Environment". The joint research aimed at:

- characterizing the mechanical behaviour of the volcanoclastic materials in the conditions that were possibly developed during the landslide processes;
- refining and supporting with experimental evidences the mechanisms of landslide initiation and propagation that had been suggested on the basis of post-failure observations and surveys (Tommasi et al. 2005a).

Modelling the progressive passage from pre-failure deformations to failure initiation and early landslide propagation requires formulating an extremely complex constitutive model for stress-strain analysis. Experimental activity can contribute to clarify some unresolved aspects of the particular mechanical behaviour of volcanoclastic material and therefore to set up a reliable model.

This paper refers to tests performed with the large-scale ring-shear apparatus at DPRI, Kyoto University, in order to investigate mechanism governing the relatively slow deformation phase that preceded landslide initiation and the subsequent triggering of the rapid submarine landslide. Different drainage conditions were adopted in order to investigate the influence of the displacement rate on excess pore-water pressure generation and strength reduction during the shearing process.

SCIARA DEL FUOCO MORPHOLOGY AND INSTABILITY PHENOMENA

The island of Stromboli is the subaerial portion of a 4,000 m high volcanic edifice that rises for about 900 m above the sea level. The Sciara del Fuoco, hereafter called SdF or simply Sciara, is a scree slope, which collects the products of the persistent volcanic activity and drives them to the sea (Fig. 1). Actually, the Sciara is a depression originated by the last lateral collapse occurred after 5.6±3.3 kyears b.p. (Tibaldi 2001), that is filled by a more than 200 m thick alternation of overlapping thick layers of loose volcanoclastic materials with minor layers of primary products (i.e. pyroclastites and lava flows).

Fig. 1 View of the Sciara del Fuoco before the 2002 landslides from the sea

Volcanoclastic materials result from continuous sliding of primary products and their incessant redistribution over the slope by sheet slides and subsequent grain flows so as to produce a series of irregular, mostly reverse-graded grain-supported layers (Fig. 2).

THE DECEMBER 2002 TSUNAMOGENIC LANDSLIDES

Detailed description of the instability events and their links with volcanic activity is reported in the paper by Tommasi et al. (2005a). The eruption started in the early evening of December 28th when lava poured from the NE crater and rapidly reached the shoreline. Due to the adverse meteorological conditions and continuous steam emission from the craters, the first photographs were taken by helicopter in the early morning of December 30th.

They revealed that a relatively deep-seated landslide had occurred in the preceding hours (α in Fig. 3). The movement, which is indicated as α slide, had produced a significant displacement in the upper half of the slope with intense deformations, but did not evolve into a destructive landslide. Post-slide morphological reconstruction and pre-failure helicopter photographs of the lower part of the slope indicated that α slide had a limited extension to the submarine slope.

Fig. 2 View of the Sciara foot after the 2002 landslides and detail of the volcanoclastic deposit (in the foreground the front of a major lava flow of the 1985 eruption)

In the early morning of December 30th, the slope was relentlessly deforming and the α slide body was fragmenting into several "blocks". The larger block (which would have collapsed afterwards producing the second tsunamogenic landslide β) extended from 450-500 m a.s.l, down to the shoreline (Fig. 3).

In the late morning two series of tsunami waves propagated from the SdF and hit the inhabited coastal areas of the island with a maximum run-up of more than 10 metres (Tinti et al. 2005). The initial wave receding at Sciara del Fuoco suggests that the first tsunami wave was generated by a submarine slide, hereafter called Ω slide (Figs. 3 and 4). The Ω slide was followed by a second tsunamogenic landslide β detached from the disarranged subaerial slope. This interpretation is supported by amplitude of near-field waves recorded in physical models performed by Watts (2000).

LITHOLOGICAL AND PHYSICAL PROPERTIES OF THE VOLCANOCLASTIC MATERIAL

Volcanoclastic layers represent the most abundant and weakest component of the Sciara deposit and extend with continuity over extremely large areas (up to some 10^5 m^2). Observations of the deposition process on the Sciara slope before and after the 2002 events indicate that lithology, grain size and structure of volcanoclastic materials remain virtually unaltered in the course of time. Therefore, these levels of loose granular materials are likely to exist also at depth and can represent preferable initiation paths for slip surfaces.

Continuous falls of products ejected by the explosions inhibit the access to a large area around the craters. At lower elevations, incessant rock falls and small debris avalanches resulting from the shallow failures of the slope materials make large part of the Sciara slope not accessible excepting for few minutes at some

selected sites. In these conditions in situ borehole investigations cannot be carried out and samples of volcanoclastic materials for geotechnical characterization can only be taken from the surface layers. However, since the deposition process is repetitive, they can be considered as being representative of the material at depth.

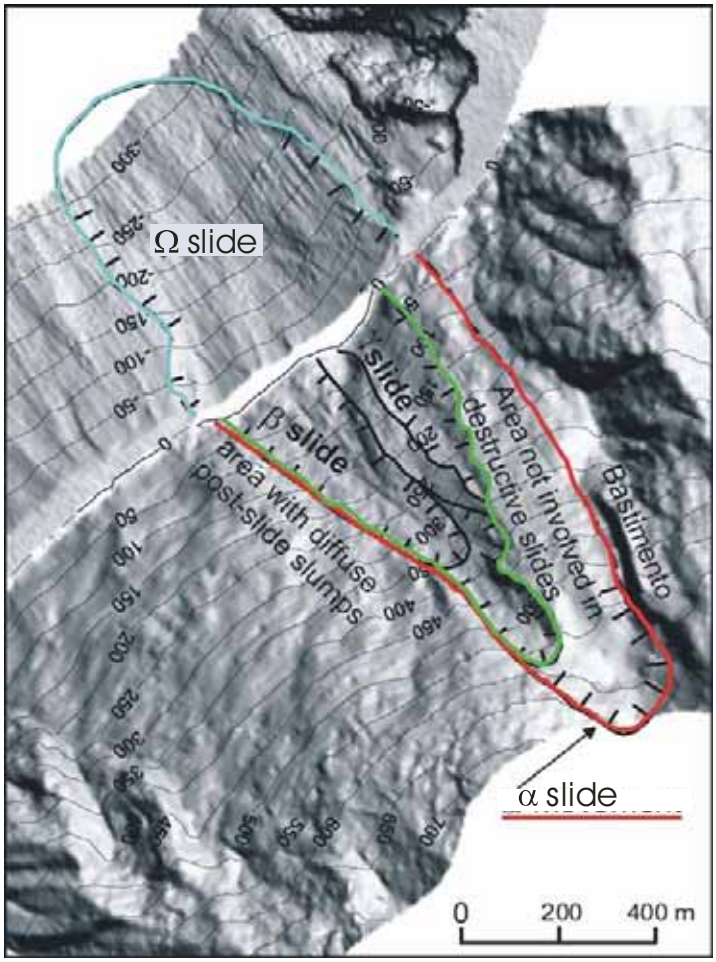

Fig. 3 Limits of the major instability phenomena occurred on December 30th 2002 (from Tommasi et al. 2005b)

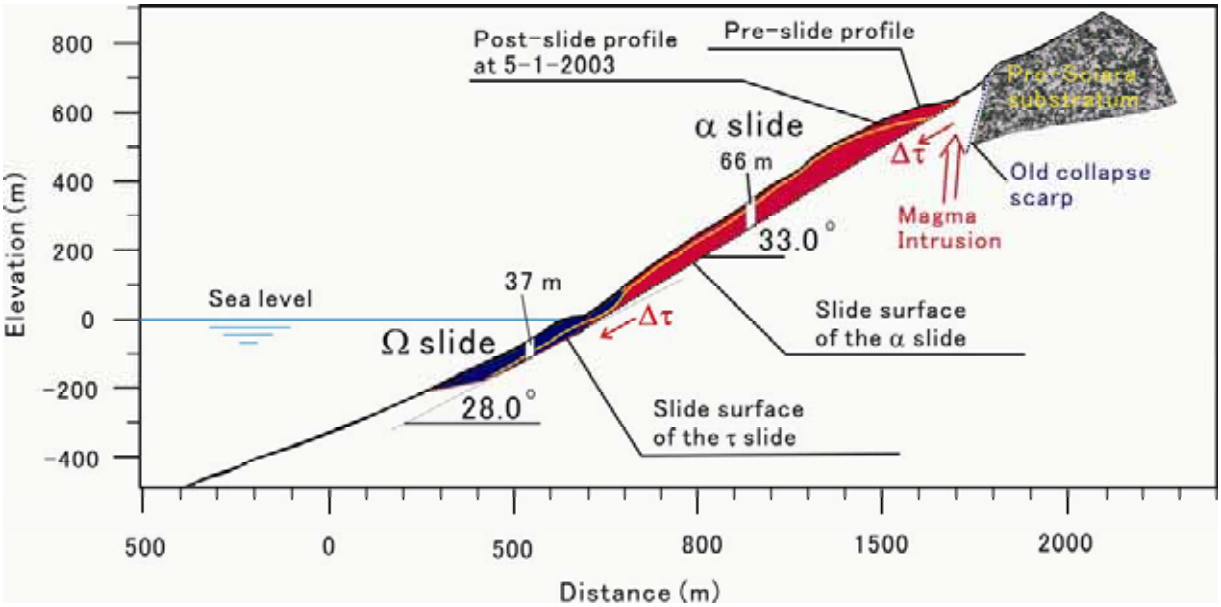

Fig. 4 Profile of the Sciara del Fuoco slope. Slip surfaces reconstructed by comparison of pre- and post-slide morphology are shown

Suitable sampling sites are all endangered by rockfalls and slides. Minimum duration of sampling operations and transfers from access points to sampling sites and vice versa is obtained when sampling is conducted at the near-toe part of the slope. Further reduction of the probability of being hit by sliding/falling materials was assured by carrying out sampling during the wet season in the early morning when water content in the shallow layers is higher. Under these conditions, increased soil suction prevents skin slides and subsequent spreading of debris downslope.

The volcanoclastic material is mainly composed by gravelly and sandy layers (box in Fig. 2), which in the sampling area, have angular to subangular clasts with high surface roughness and low sphericity. Rounding, smoothness and sphericity progressively increase proceeding downslope, due to grain sliding and rolling (Kokelaar and Romagnoli 1995).

Recently, bottom samples were collected on the seafloor of the south-eastern part of the submerged Sciara slope, which was not involved in the 2002 slide events and therefore can be considered as being representative of the pre-slide conditions. Rounding and sphericity of the grains were found to be similar to those of the subaerial materials used for experimental investigations. This result justifies the use of subaerial samples for analysing the shear behaviour of the submerged slope material.

Fig. 5 Macrophotograph of black (on the left) and reddish (on the right) scoriae.

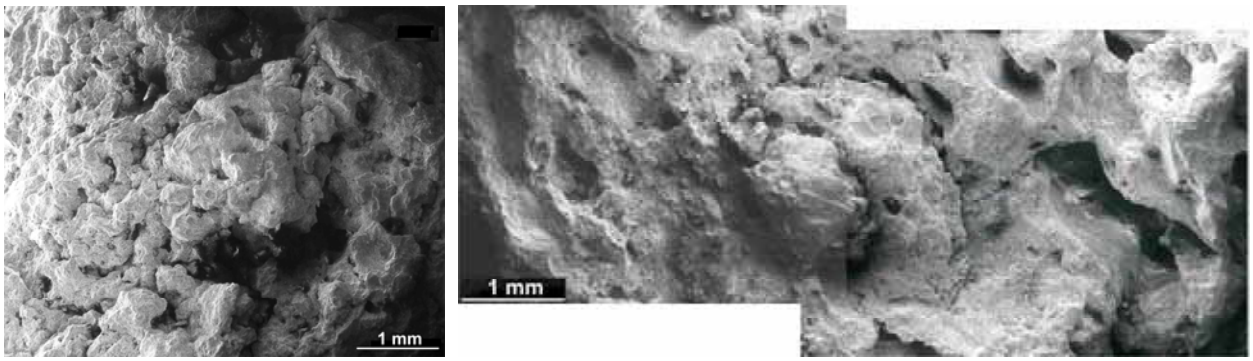

Fig. 6 SEM microphotographs of black (on the left) and reddish (on the right) scoriae.

Physical and mechanical properties of grains were determined by Tommasi et al. (2005b). The most abundant are black and reddish scoriae that, at the scanning electron microscope, appear to be formed by small lumps (mostly vitric) ranging in size from few tenths of millimetres to few millimetres, which are welded together as to form a continuous frame (Figs. 5 and 6). Pores are extremely diffuse and generally do not exceed few tenths of millimetre in size, even though larger pores (up to 2-3 mm) are observed (Figs. 5 and 6). Black and reddish scoriae result from the disruption of the outer parts of brecciated lava flows (aa-type), spatters and agglutinates. Less frequent are grey fragments of aphanitic lava with low-porosity coming from the core of lava flows.

Mean values of dry density measured on the different grain size classes with a mercury pycnometer were 2.34, 2.30 and 2.37 Mg/m^3 for the scoriaceous (black and reddish) and grey, respectively. The mean value of the density of the whole set of samples is 2.34 Mg/m^3 with a standard deviation of 0.04 Mg/m^3. Solid matrix density determined with a helium picnometer on powders of a representative sample of the aggregate is on average of 2.90 Mg/m^3 yielding a mean value of the total porosity of the grains equal to 19.2%, that is almost completely connected.

Grain strength estimated through point load tests on larger clasts revealed to be low and strongly dependent on grain porosity. For grain porosity of 20% (i.e., the average value of the sample), the strength index $I_{S,50}$ is equal to 0.9 which according to the correlation suggested by ISRM (1985) yields a uniaxial compressive strength σ_c of 21 MPa. The multiplying factor suggested by ISRM (σ_c=22$I_{S,50}$), derived from tests on hard rock materials, could be too high for this type of soft rocks and in turn actual uniaxial strength of the clasts would be significantly lower than 21 MPa. On the basis of tests conducted on biohermal lime materials, which present some textural analogies with the volcanoclastic grains (i.e. large pores diffused throughout the material), Smith (1997) proposed a multiplying factor of 14.3. This factor reduces the σ_c of the Stromboli volcanoclastic grains, pointing out the potential high attitude of grains to crushing even under low contact stresses.

The grain size distribution of a typical layer of the volcanoclastic deposit is shown in Fig. 7. In order to assure a convenient ratio between the maximum grain size and the sample height in the ring-shear apparatus, tests were performed on the fractions passing the 8 mm sieve. The corresponding grain size distribution (Fig.7) was obtained by shifting the in-situ curve parallel to the grain size axis according to Fumagalli (1969). The tested material can be classified as sand with gravel.

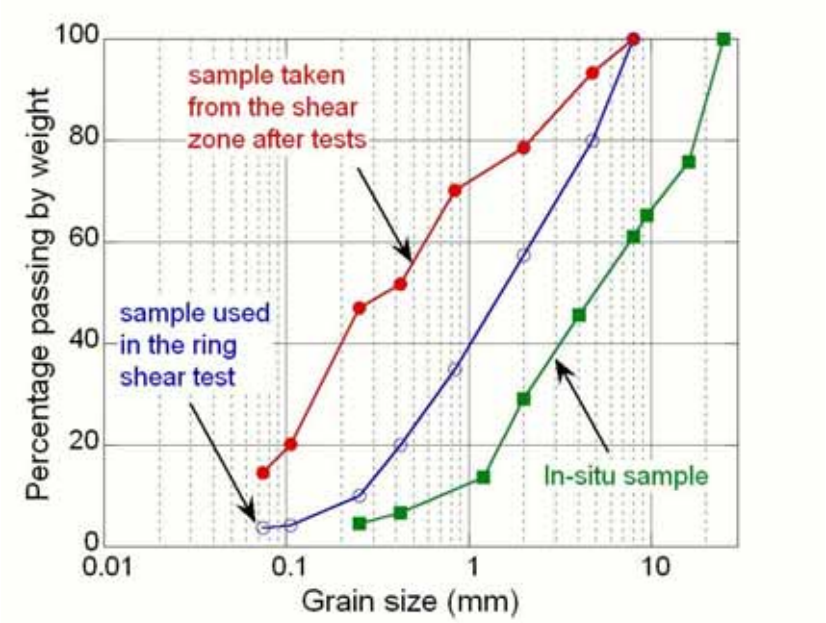

Fig. 7 Particle size distribution curves of in situ material and tested material before and after the tests

The minimum and maximum void ratios of the tested material were calculated from densities measured in laboratory through the ASTM standard procedure leading to values of e_{max} and e_{min} equal to 0.72 and 0.41 respectively.

In situ void ratio was calculated from dry density determined on the surface material by driving a large thin walled sampler into the soil. In fact, the standard sand replacement method provided unreliable values due to the instability of the rim of the cavity to be replaced by sand. The calculated value of the in situ void ratio (e_0= 1.18) was much higher than the maximum void ratio determined in the laboratory on the tested material. This difference is due to the higher percentage of the coarser fraction and to the lower sorting of the layers where in situ measurement was possible.

AIM OF EXPERIMENTAL ACTIVITY

For the comprehension of the shear behaviour of volcanoclastic materials in the phase of initiation of landslides and during the runout of the submarine slide, a series of shear tests were performed with the

ring-shear apparatus DPRI-6 developed at the DPRI of Kyoto University (Sassa 1997). Methodology followed for shear testing with this new apparatus and the recent results obtained from simulation of shear processes occurred in various landslide phenomena (e.g. Otari debris flow disaster and earthquake-induced-landslides in the upper slope of the Nikawa area) were reported by Sassa (1996) and Sassa et al. (1997, 2003 and 2004a).

This large-scale ring-shear apparatus is characterised by an inner diameter of 250 mm, an outer diameter of 350 mm and a maximum height of the sample of 150 mm and, thus, is suitable for testing coarse-grained volcanoclastic material. The DPRI-6 ring-shear apparatus allows performing tests in both drained and undrained conditions thanks to a water-leakage tightness system formed by O-rings on the upper loading platen and bonding rubber edges on the two confining rings of the lower rotary pair (Sassa et al. 2004b). Pore-water pressure is measured by two transducers located 2 mm above the shear surface.

The sample was placed into the shear box by the dry pluviation method (see e.g. Ishihara 1985). In order to avoid segregation phenomena during the infilling, the whole sample was initially subdivided into eight smaller parts which were subsequently deposited in the apparatus in different layers without tamping. The void ratio expected at the depth where the shear surface is supposed to have developed was obtained by applying the in situ state of stress during the consolidation phase. Lower values of void ratio due to overconsolidation are likely to be excluded. In fact after each erosional phase of the Sciara slope, the continuous deposition of new material rapidly re-establishes a state of normal consolidation.

Based on the reconstructed succession of the events on 29 and 30 December 2002, a testing programme was defined at DPRI in order to reproduce conditions existing at the moment of the initiation and propagation of the different landslides that succeeded since the beginning of the eruption as follows.

1) magma intrudes into the slope from the feeding system of the volcano and exerts a thrust on the dry soil mass which is involved in a huge movement (α slide);
2) the southern part of the α slide (β slide) detaches from the main slide body and start sliding at a higher displacement rate;
3) the movement of β slide produces the undrained or partially drained loading of the fully-saturated submarine deposit which finally results in a rapid submarine Ω slide;
4) While the α slide mainly involved the dry subaerial slope, the rapid failure of the submarine slide was reasonably triggered by a significant rise of excess pore-water pressure in the submerged slope.

RESULTS OF RING-SHEAR TESTS

The subaerial landslide (α slide)

Since most of the slip surface of the α slide developed inside the subaerial flank of the volcanic edifice, the test was conducted in dry conditions. The material was subjected to an initial state of stress reproducing in situ stress conditions at the base of the α slide body. The slip surface was estimated to be located at an average depth of 66 m with an average dip of 33° (Fig. 4). By assuming a dry unit weight γ_d= 13 kN/m^3 (equal to that obtained from in situ measurements), the sample was anisotropically consolidated at a normal stress of 600 kPa and at a shear stress of 390 kPa. At the end of consolidation, the dry unit weight reached the value of 17.3 kN/m^3.

In order to simplify the testing procedure and the interpretation of test results, it was assumed that the dip of the shear surface of the landslides did not vary significantly throughout the slope. Therefore only additional shear stress was applied after consolidation by increasing the shear torque with a loading rate of 204 Pa/s (0.12 kgf/cm^2/min).

Time-histories of normal stress and shear resistance for the test are plotted in Fig. 8a and 8b. Shear resistance increases linearly according to the linear increasing of applied torque up to a peak value corresponding to an instantaneous friction angle of 40° (with two short hold-ups). After peak shear resistance, the shear strength decreases down to a value corresponding to an instantaneous friction angle of 34°, which maintains constant for the remaining part of the test. Due to the torque-controlled procedure, the drop of shear resistance after peak is accompanied by a sudden increase of the shear displacement rate.

Both peak and residual friction angles resulted to be higher than the average slope angle (33°) of the α slip surface and that of the subaerial slope. This is an indirect evidence that an external load, such that applied by the intruded magma, was necessary to initiate the α slide. Without a magmatic intrusion the subaerial slope would have been stable with the slope geometry existing in December 2002.

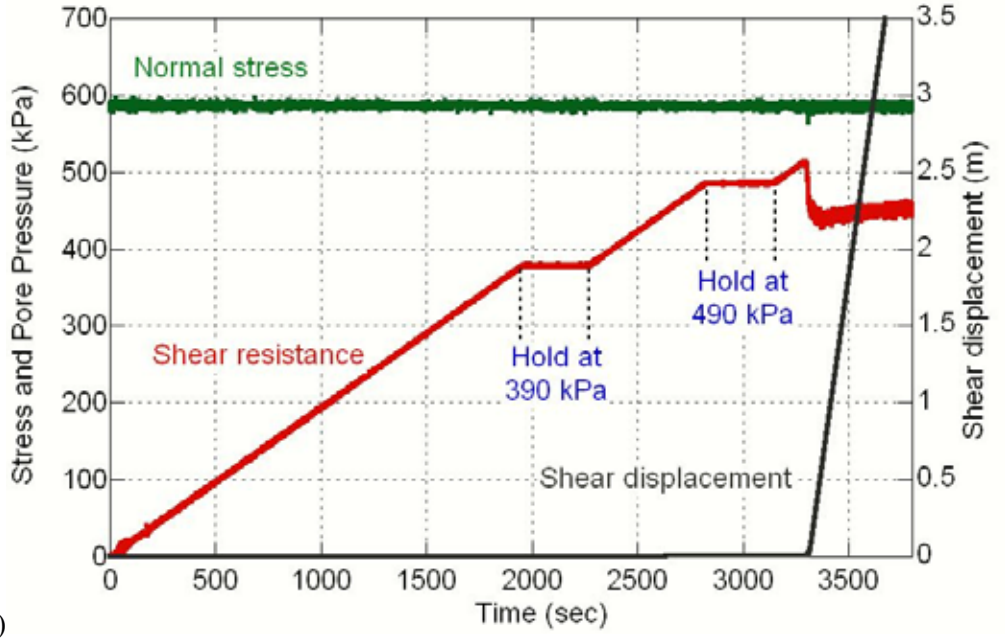

(a)

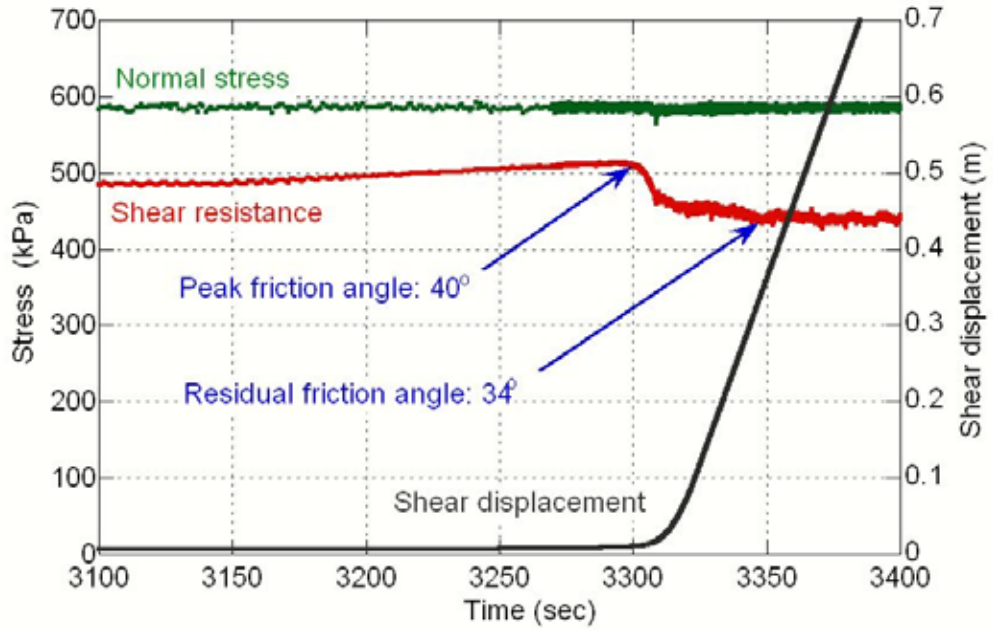

(b)

Fig. 8 Time histories of total normal stress, shear resistance and shear displacements recorded during a dry ring shear test: a) data of the whole test; b) detail of the near-failure stage

The submarine τ slide

The second set of tests was conducted in fully-saturated conditions, as those existing in the submarine slope before and during the Ω slide. Full saturation was obtained by supplying the sample with a CO_2 flux followed by a de-aired water flux for a time (generally more than 12 hours) sufficient to obtain a B_D value (Skempton's pore pressure parameter B in direct shear condition, Sassa 1988) higher than 0.95.

Since the loading rate and the related drainage conditions of Ω slide were uncertain, two different types of torque-controlled tests were performed: undrained shear tests and shear tests with open drainages from the sample top through the upper loading platen. In the latter procedure drainage is not prevented and excess pore-water pressure can generate depending on material behaviour and loading rate (these conditions are referred to as naturally drained conditions (Sassa et al. 2004a).

In both cases, samples were first consolidated at an anisotropic state of stress corresponding to that acting along the τ slip surface, characterized by average depth and dip of 37 m and 28°, respectively. Therefore a normal stress of 230 kPa and a shear stress of 122 kPa were applied under drained condition. At the end of the consolidation phase, dry unit weight ranged between 16.6 and 17.2 kN/m^3. In the further more

shearing process simulating the shear loading from α slide, shear torque was loaded at a rate of 55 Pa/s.

Undrained shear tests

Results of the undrained torque-controlled test are reported in Figs. 9a, 9b and 10. Figures 9a and 9b show the time-histories of total normal stress, shear resistance, pore-water pressure and shear displacement in the whole test and details of the near-failure stage, whilst the effective and total stress paths are plotted in Fig. 10. During the first stages of the undrained shearing, excess pore-water pressure generated as shear stress increased, producing a decrease of the effective normal stress (Fig. 10).

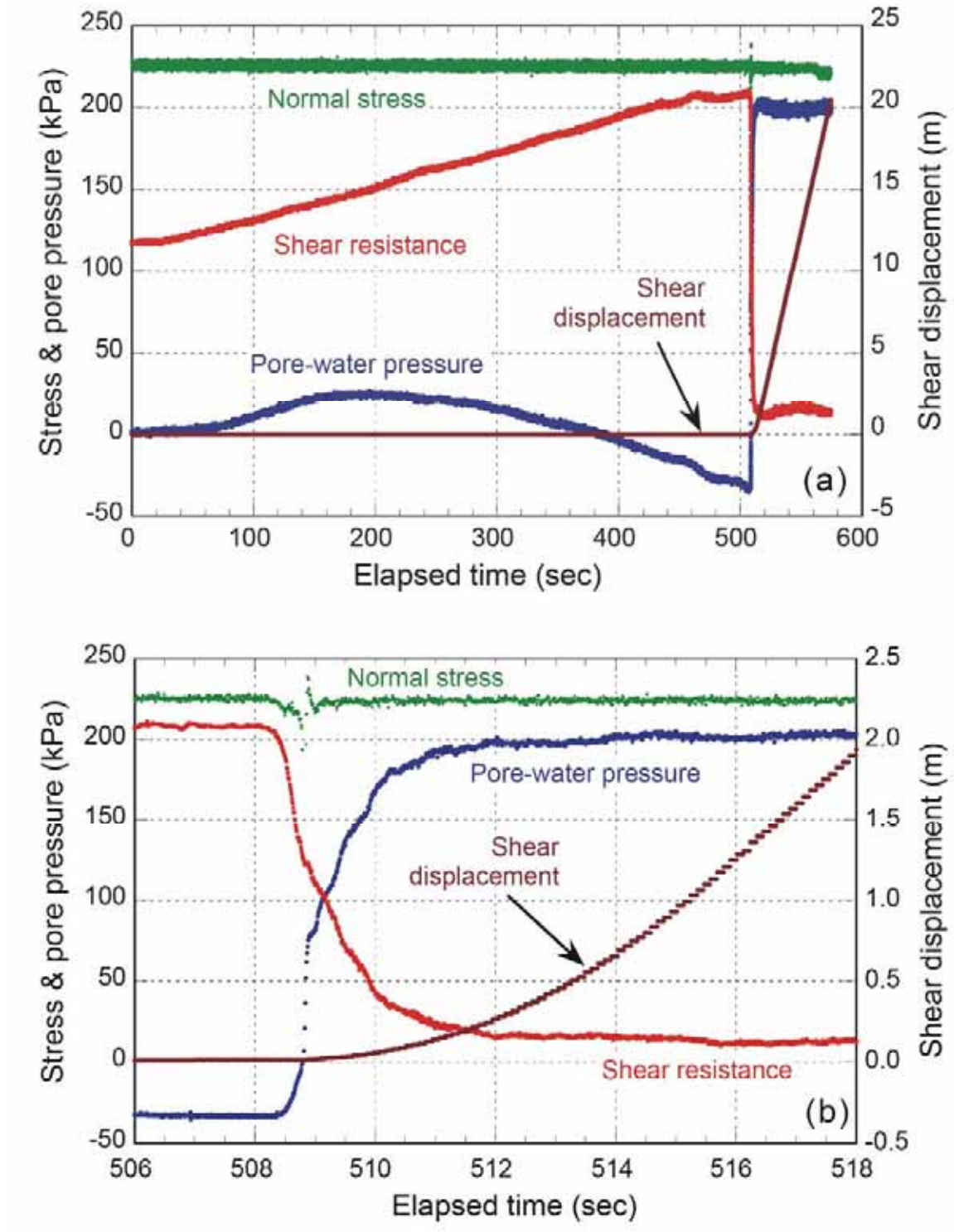

Fig. 9 Time-histories of total normal stress, shear resistance, pore-water pressure and shear displacement recorded during the undrained ring shear test: a) data of the whole test; b) detail of the near-failure stage

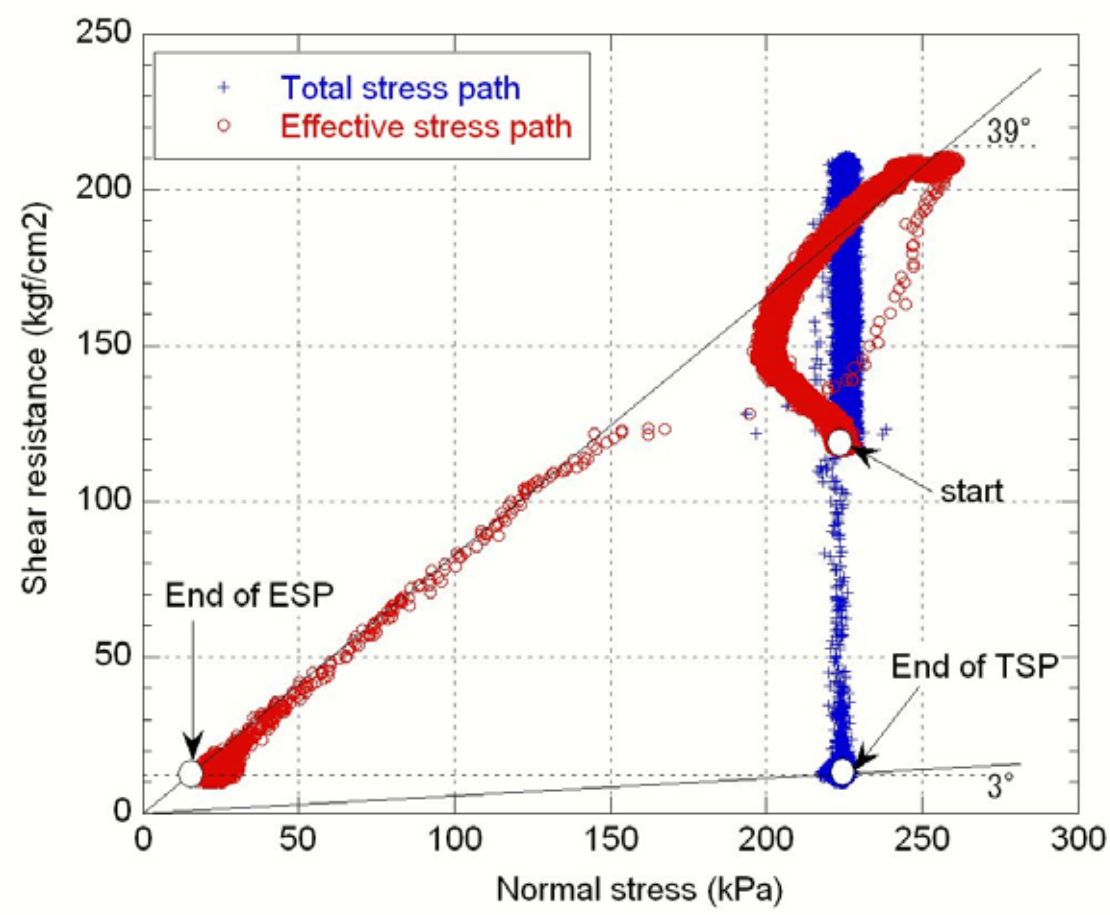

Fig. 10 Effective and total stress paths during the undrained ring shear test

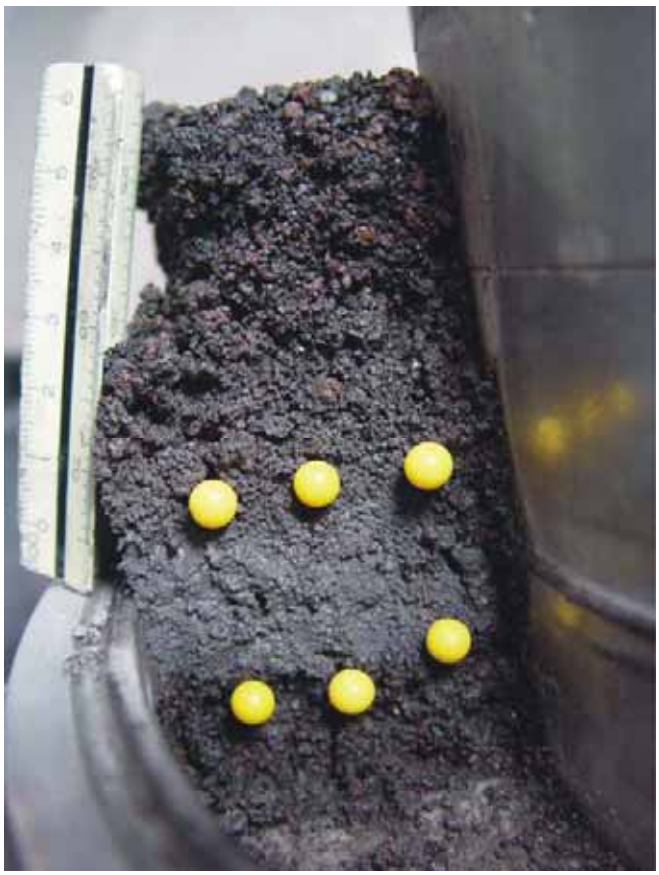
Fig. 11 View of the shear zone after the test

This behaviour inverted when pore-water pressure reached about 25 kPa; from this point material dilation induced a progressive decrease of pore-water pressure down to negative values, producing a progressive increase of the effective normal stresses (Fig.9a). When negative pore-water pressure reached about 45 kPa, the volcanoclastic material experienced liquefaction: pore-water pressure rose up to values higher than 200 kPa, shear resistance abruptly decreased down to few kilopascals and correspondingly the shear displacement rate increased significantly (Fig. 9b).

The apparent friction angle at the final stage, given by the arctangent of the ratio between the mobilised shear resistance and the total normal stress, is about 3°, showing a high mobility of the material under undrained shearing in the liquefied state.

The angularness and surface roughness, typical of the volcanic grains, are responsible of the dilatant behaviour which induced negative excess pore-water pressures up to -30 kPa high. Dilatant behaviour was also recorded by other authors (e.g., Castro 1969) in the initial stage of triaxial tests on medium-dense sands, which display a strain-softening behaviour after dilation takes place, without being affected by liquefaction. Liquefaction of medium-dense to dense sands were already observed in ring-shear tests performed in undrained conditions at DPRI by Sassa (1996) and Wang and Sassa (2002), who demonstrated that, irrespective of the initial void ratio of the soil, liquefaction can be triggered if the following two conditions are verified:

1) the shear stress has to be great enough to initiate failure of the soil;
2) soil grains have to crush during-shearing under the applied normal stress.

Since grain crushing results in volume reduction, excess pore-water pressure generates. Furthermore, the reduction of grain size within the shear zone decreases permeability and in turn the velocity of excess pore-water pressure dissipation.

Grains of the Stromboli volcanoclastic deposit revealed to be highly crushable under the applied testing conditions. Grain crushing induced by the shearing process is apparent both in the photograph of the material forming the shear zone (Fig. 11) and in its grain size distribution (Fig. 7).

Shear tests with open drainages

The second set of tests was conducted with the drainages open at the specimen top. Time-histories of the total normal stress, shear resistance and shear displacement of a typical test are plotted in Fig. 12.

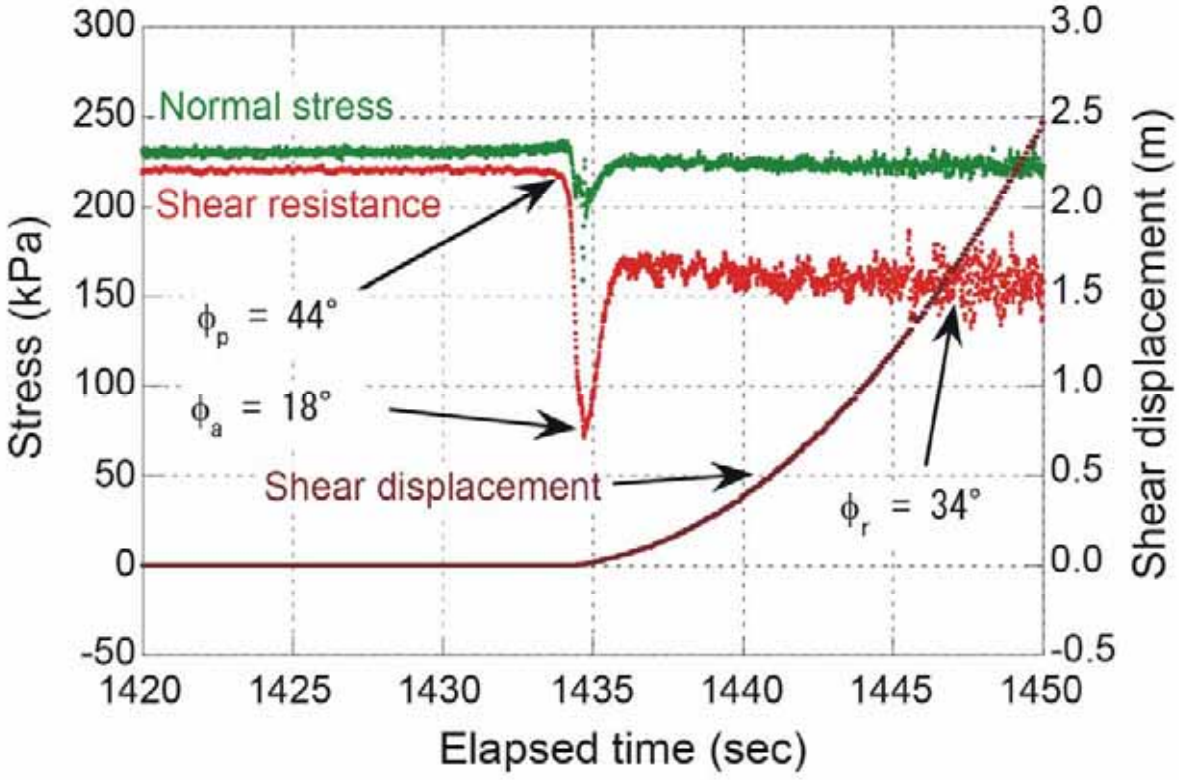

Fig. 12 Time-histories of total normal stress, shear resistance and shear displacement recorded during the ring shear test with open drainages

The shear resistance increased gradually up to the maximum value, corresponding to a peak friction angle of about 44°. The linear increase of shear resistance with the increase of the applied shear stress indirectly indicates that drained conditions can be reasonably assumed for this first part of the test. After peak the shear resistance suddenly dropped for some seconds, as a result of shear failure and increasing of shear displacements, and thereafter increased up to around 34°. In fact, grain crushing rate is the greatest immediately after failure and decreases as shear displacement proceeds, while pore pressure dissipation rate is function of pore pressure difference between the shear zone and the sample top.

The drop of the shear resistance below the dynamic residual friction angle (a minimum apparent friction angle of 18° was reached) is likely to be a consequence of local excess pore-water pressure within the shear zone, which can build-up due to the high crushability of the Stromboli volcanoclastic material. Since the rate of grain crushing, and in turn the rate of pore-water pressure generation, decreased as shear displacement proceeded, excess pore-water pressure decayed soon and the shear resistance was progressively recovered up to a value corresponding to an apparent friction angle of about 34° (Fig. 12).

Peak friction angle measured in this test (44°) are higher than those determined through the test in dry conditions (40°). That result is accounted for by the higher normal stress applied in the test on dry materials in conjunction with the typical non-linear strength envelope of granular materials (Marsal 1973; Indraratna et al. 1993; Tommasi et al. 2005b) and in particular for those with crushable grains.

Conclusions

The normally consolidated Stromboli volcanoclastic material displays a high peak friction angle at failure and is highly dilatant in the initial shearing stage, as a consequence of the angularness and surface roughness of grains. Such a behaviour support the hypothesis that an additional thrust by magma intruded in the upper part of the slope was necessary for the initiation of the deep seated instability, which was instrumental in the further evolution of the slope.

Results of the undrained ring-shear test indicate that, if undrained condition was established in the submerged slope, liquefaction can be invoked to explain the submarine failure and the subsequent long run-out of the marine landslide (greater than 1000 m).

The test performed with open drainage, however, provided experimental evidence that a significant drop-down of shear resistance would have been sufficient to lead the slope to failure even during not fully undrained shearing.

The two experimental conditions could be related to different deformation processes occurred in the submarine slope immediately before failure.

Failure could have occurred simply when shear stress reached a threshold value at which grain crushing significantly occurred and local excess pore-water pressure may have generated. This mechanism seems to correspond to the conditions existing in the test with open drainages.

Alternatively a sharp increase in shear displacement rate at the base of the sliding mass could have been produced during fragmentation of the original subaerial sliding mass (Tommasi et al. 2005a) or could have resulted from local sudden failures of more resistant/rigid parts of the slope. This second mechanism should have induced a much more rapid increase of excess pore-water pressures, compared to time required for their dissipation, and therefore could be better represented by the fully undrained testing conditions.

At present no indication exists about the loading rate at the stage preceding the submarine Ω slide. Assuming that the loading rate adopted in the fully saturated tests is comparable to that of the actual shear process, the values of the apparent friction angles determined in the undrained tests (3°) and in tests with open drainages (18°) are respectively the lower and upper bound of the shear strength mobilised after failure at the base of the submarine slide body.

Acknowledgements

Financial support of National Research Council within the research program “Short-term mobility” to visit the Research Centre on Landslides of Disaster Prevention Research Institute, Kyoto University was greatly appreciated by the first author. The UNITWIN Cooperation Programme by UNESCO- Kyoto University-ICL “Landslide Risk Mitigation for Society and the Environment” enabled this international joint research cooperation. Financial support to research activity in Italy by Italian Department for Civil Defence is greatly acknowledged. Mr. K. Kondo gave a valuable help in apparatus maintenance. Prof. Tatiana Rotonda had a major role in the physical characterization of the material. Mr. R. D’Inverno and Eng. F. Cignitti prepared

samples for ring-shear tests. Mr. M. Zaia (Zazà) largely contributed to the access to sampling sites and sampling operations.

References

Boldini D, Wang FW, Sassa K, Tommasi P (2005) Mechanism of landslide causing the December 2002 tsunami at Stromboli volcano (Italy). In Sassa K, Fukuoka H, Wang FW, Wang G (eds) Landslide: Risk Analysis and Sustainable Disaster Management, 173-180

Castro G (1969) Liquefaction of sands. Ph.D. thesis, Harvard University, Cambridge, Massachusetts

Fumagalli E (1969) Tests on cohesionless materials for rockfill dams. Journal of Soil Mechanics and Foundation Engineering Division (ASCE). 95, SMI: 313-330.

Indraratna B, Wijewardena LSS, Balasubramaniam AS (1993) Large-scale triaxial testing of greywacke rockfill. Géotechnique, 43(1), 37-51.

Ishihara K (1985) Stability of Natural Deposits During Earthquakes, Theme Lecture, Proceeding of the XI ICSMFE, Vol. 2, pp. 321-376.

ISRM (1985) Suggested Method for determining point load strength, International Journal of Rock Mechanics, Mining Sciences and Geomechanical Abstracts, 22, 51-60

Kokelaar P, Romagnoli C (1995) Sector collapse, sedimentation and clast population evolution at an active island-arc volcano: Stromboli, Italy. Bulletin of Volcanology 57: 240-262

Marsal RJ (1973) Mechanical properties of rockfill. In Embankment-Dam Engineering. Casagrande volume, 109-200, John Wiley & Sons, New York.

Sassa K (1988) Geotechnical model for the motion of landslides. Special Lecture of the 5th International Symposium on Landslides, "Landslides", Vol. 1, Rotterdam: Balkema, pp.37-55

Sassa K (1996) Prediction of earthquake induced landslides. In: Proceedings of 7th International Symposium on Landslides. A.A. Balkema. Trondheim, 17–21 June, Vol. 1, pp. 115–132

Sassa K (1997) A new intelligent type dynamic loading ring-shear apparatus. Landslide News, No.10, pp.33

Sassa K, Fukuoka H, Wang FW (1997) Mechanism and risk assessment of landslide-triggered-debris flows: lesson from the 1996.12.6 Otari debris flow disaster, Nagano, Japan. In: Cruden DM, Fell R (eds) Landslide Risk Assessment, Proceedings of the International Workshop on Landslide Risk Assessment. Honolulu, February 2003, A.A. Balkema, pp. 347-356

Sassa K, Wang G, Fukuoka H (2003) Performing undrained shear tests on saturated sands in a new intelligent type of ring-shear apparatus. Geotechnical Test J 26(3):257–265

Sassa K, Wang G, Fukuoka H, Wang FW, Ochiai T, Sugiyama M, Sekiguchi T (2004a) Landslide risk evaluation and hazard mapping for rapid and long-travel landslides in urban development area. Landslides 1(3):221-235

Sassa K, Fukuoka H, Wang G, Ishikawa H (2004b) Undrained dynamic-loading ring-shear apparatus and its application to landslide dynamics. Landslides 1(1):9–17

Smith HJ (1997) The point load test for weak rock in dredging applications. International Journal of Rock Mechanics & Mining Sciences, 34: 3-4, Paper 295.

Tibaldi A (2001) Multiple sector collapses at Stromboli volcano, Italy: how they work. Bulletin of Volcanology 63:112-125

Tinti S, Manucci A, Pagnoni G, Armigliato A, Zaniboni F (2005) The 30 December 2002 landslide-induced tsunami in Stromboli: sequence of the events reconstructed from the eyewitness accounts. Natural Hazards and Earth System Sciences, 5:763-775

Tommasi P, Baldi P, Chiocci FL, Coltelli M, Marsella M, Pompilio M, Romagnoli C (2005a) The landslide sequence induced by the 2002 eruption at Stromboli volcano. In Landslide: Risk Analysis and Sustainable Disaster Management (Sassa K, Fukuoka H, Wang FW, Wang G, eds.), pp. 251-258

Tommasi P, Boldini D, Rotonda T (2005b) Preliminary characterization of the volcanoclastic material involved in the 2002 landslides at Stromboli. In: Bilsel & Nalbantoğlu (eds), Proceedings of the International Conference on Problematic Soils GEOPROB 2005, Vol. 3, Famagusta: pp. 1093-1101

Wang G, Sassa K (2002) Post-failure mobility of saturated sands in undrained load-controlled ring-shear tests. Canadian Geotechnical Journal 39: 821-837

Watts P (2000) Tsunami features of solid block underwater landslides. Journal of Waterway, ports, Coastal and ocean engineering, 126 (3): 144-151

Wang, F. W., T. Matsumoto, Y. Tanaka
(2005)

Two recent flowslides in Yamashina area, Kanazawa City, Japan

Landslides: Journal of the International Consortium on Landslides. 2(3):229-234.

Original Article

Landslides (2005) 2: 229–234
DOI: 10.1007/s10346-005-0060-6
Received: 1 February 2005
Accepted: 5 May 2005
Published online: 16 July 2005

Fa-Wu Wang · Tatsunori Matsumoto · Yasuhiro Tanaka

Two recent flowslides in Yamashina area, Kanazawa City, Japan

Abstract Due to a continual rainfall, a flowslide occurred in Yamashina area, Kanazawa City, Japan on November 8, 2002 in the Tertiary mudstone area. The sliding mass was fully fluidized during the motion and moved downward the slope for a long distance. On December 31, 2003, slope failure was triggered by intensive rainfall and snowmelt water at the same site again, and resulted in the second occurrence of flowslide. The total displacement of the slope was recorded with an extensometer. Through field investigation, the difference of the sliding mechanism between the two flowslides was examined.

Introduction

Two flowslides occurred in Yamashina area, which is the mountain side area of Kanazawa City, Ishikawa Prefecture, Japan in 2002 and 2003, respectively. Figure 1 shows the location of the flowslides. Kanazawa City is characterized by high annual precipitation which exceeds 4,500 mm. In this area, averagely in a year, half of the days are rainy or snowy days. The stratum around the Yamashina area consists of massive mudstone of Saikawa formation in Miocene epoch, Tertiary period (Kaseno 1993). The Saikawa formation is overlaid by Onma formation unconformably, and it covers Shimoaraya formation conformably. In the eastern part of this area, highmoor terrace deposit covers the Saikawa formation unconformably. The Saikawa formation is a no-bedding massive mudstone with a layer thickness of about 200 m (Kaseno 1993; Yanagisawa 1999). Generally, in the Tertiary strata area, landslide motion is characterized by repeated reactivation with small sliding distance, and these landslides have been specially named as "Tertiary landslides" (Shuzui 2001). However, in the Saikawa formation mudstone area, both of the two flowslides moved with high velocity and long travel-distance. The difference of the triggering factor is that, the first flowslide was triggered by a thirteen-day continual rainfall in November 2002, and the second flowslide was triggered by an intensive rainfall after a heavy snowfall at the end of 2003.

Outline of the first flowslide

Figure 2 shows the first flowslide which occurred on November 8, 2002. The width and length of the source area were about 60 m and 100 m, respectively. The height of the main scarp was about 10 m, and the moving distance of the main sliding mass was more than 100 m. Fresh weathered mudstone was outcropped because most of the displaced sliding mass moved out of the source area. In this event, an apple yard in the source head area was damaged, and a local road near the flowslide toe was cut. The bamboo grove on the slope was completely destroyed. To prevent further debris flow hazard, a debris retention dam was built in front of the toe part of the debris deposits after the occurrence of the flowslide.

Fig. 1 Location of the Yamashina flowslides in Kanazawa City

It is believed that the trigger for this flowslide was a thirteen-day continual rainfall. Figure 3 presents daily precipitation in October and November in 2002, when the flowslide was triggered. The maximum daily precipitation of 79.0 mm occurred on November 4. However, it is not so high comparing to the historical maximum value. For example, a daily precipitation of 187.5 mm occurred on June 25, 1996, and a daily precipitation of 172.0 mm occurred on September 10, 2000 were monitored, and no displacement was observed at least in the apple yard during the two extreme rainfall events. The accumulated rainfall for the thirteen days before the first occurrence of flowslide was 377.0 mm. Such a high continual rainfall had not been observed for the recent ten years. It seems that the rainfall intensity coincided well with the infiltration velocity of the rainwater into the weathered mudstone, so that the rainwater could be absorbed by the weathered mudstone effectively, and resulted in the slope failure.

Exploration results on the sliding mass and sliding surface of the first flowslide

Figure 4a is the plan and Fig. 4b is a birds-eye view of the Yamashina slope after the first flowsliding. The apple yard was relatively flat. It was formed artificially by slope-cutting and refills for agriculture purpose. The refills were refilled in front of the apple yard, which formed the main sliding mass in the first flowslide. From the plan and bird-view, it is seen that the displaced sliding mass slid down along the slope, and then turned right when it joined the valley in front of the failed slope. This phenomenon shows the fluidization behavior of this flowslide.

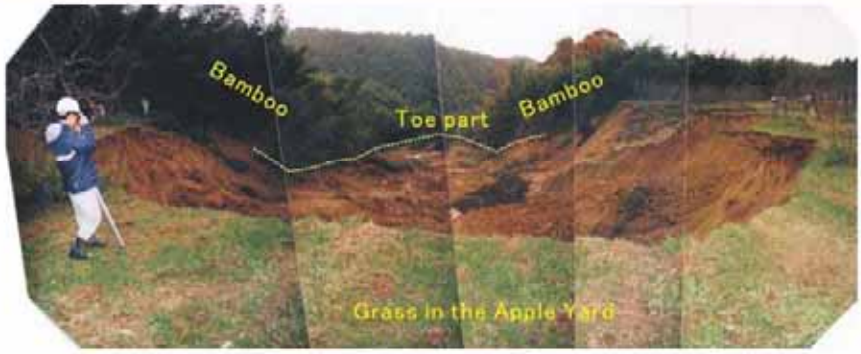

Fig. 2 Photograph of the first flowslide occurred on November 8, 2002 in Yamashina area (photo courtesy of Agriculture and Forestry Central Administration office, Ishikawa prefecture)

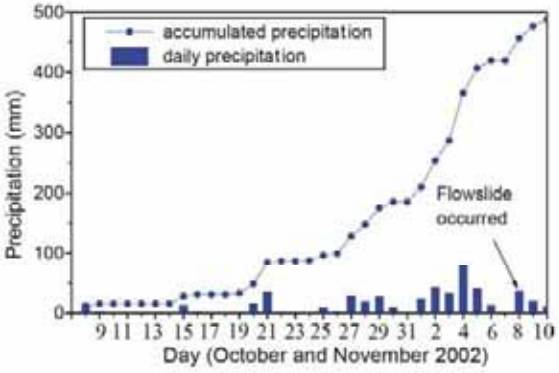

Fig. 3 Daily precipitation data in October and November 2002 (monitored by the Japan Meteorological Agency in Kanazawa City 2002)

Field investigations including portable dynamic cone penetration tests (DCPT, notated as "K" in Fig. 4a) and boreholes (notated as "BV" in Fig. 4a) were carried out to investigate the sliding surface. The original DCPT was developed in response to the need for a simple and rapid device for the characterization of the subgrade soil by Scale (1956) in Australia. It uses a 5 kg hammer to penetrate a cone into the ground from 50 cm height. The stiffness of the underground soil can be evaluated by the blows of the hammer during a 10 cm penetration of the cone. For the purpose of easy comparison, the blows were corrected to N_d, which means deduced N value. The N value is the blow number for standard penetration test (SPT), which is a well-established and unsophisticated method, which was developed in the United States around 1925. In this study, DCPT tests were conducted six months after the flowslide, because the sliding mass was too soft and weak at the moment after the flowslide. The borehole exploration was conducted by the Ishikawa Prefectural Government. Besides of that, trench excavation to discover the sliding deposit structure, was performed by ourselves.

Figure 5 is the central longitudinal section of the landslide area after the first flowslide (Fig. 5a) and the DCPT test results (Fig. 5b). From direct observation of the outcrop of sliding surface, results of DCPT tests, and borehole explorations, it is certain that the sliding surface of this flowslide is the weathered mudstone stratum surface. It dipped down the slope, and its massive structure made its permeability very low. Comparing with the former slope surface line, it is easy to understand that most of the sliding mass moved out of the source area. In this section, the apparent friction angle, which can be measured as the angle of inclination from the top point at the source area to the toe, was about 12 degrees. Considering the landslide turned right, and moved another 50 m, the actual apparent friction angle must be smaller than this value. The small apparent friction angle represented a high mobility of this flowslide.

In addition, the N_d values of the DCPT points at the source area (K-1, K-2, K-3, K-4, K-10, K-11) are almost smaller than 10 (Fig. 5b). The debris was very thin in this part. The N_d values became greater near C-C' section where the debris became thicker. It is estimated that the penetration resistance must have recovered in the six months period after the occurrence of the first flowslide. The results of those penetration tests show that the shear resistance of the debris mass was very small when in a saturated condition, which can be formed in the weathered mudstone debris laying over the massive mudstone during the thirteen-day rainfall. It can also be estimated that during the motion, all of the displaced debris was in a saturated situation and fluidized.

Figure 6 shows a photograph in the trench. In it, corroded tree-roots and apples were found at the right upper side, and fresh weathered mudstone was observed at the left lower side. Although the trench was excavated about six months after the occurrence of the flowslide, it was also very soft and weak. However, when the depth reached 1.2 m, it became much harder. At the nearby DCPT point K-8, N_d values were smaller than 10 before the depth reached 1.7 m (Fig. 5b). Thereafter, N_d values increased rapidly, and it became impossible to penetrate any more after the depth reached 1.9 m.

Outline of the second flowslide in Yamashina area

The second flowslide occurred on December 31, 2003. During the period between the first flowslide and the second flowslide, many cracks were observed behind the main scarp of the first flowslide. Especially in November 2003 and later, those cracks extended obviously. Mainly based on the deformation phenomenon that occurred at the apple yard and the road behind the main scarp of the first time flowslide, warning was announced by the local government, and traffic across the main scarp was prohibited.

For failure time forecasting, an extensometer was set at the right side of the main scarp on December 24 which crossed a main crack with 100 mm width at the apple yard (see Fig. 4). Figure 7 shows the meteorological data including snowfall, rainfall and temperature (Fig. 7a) and the monitored displacement results (Fig. 7b). The meteorological data was monitored by the Kanazawa Local Meteorological Observatory which is located at the seaward side of Kanazawa City,

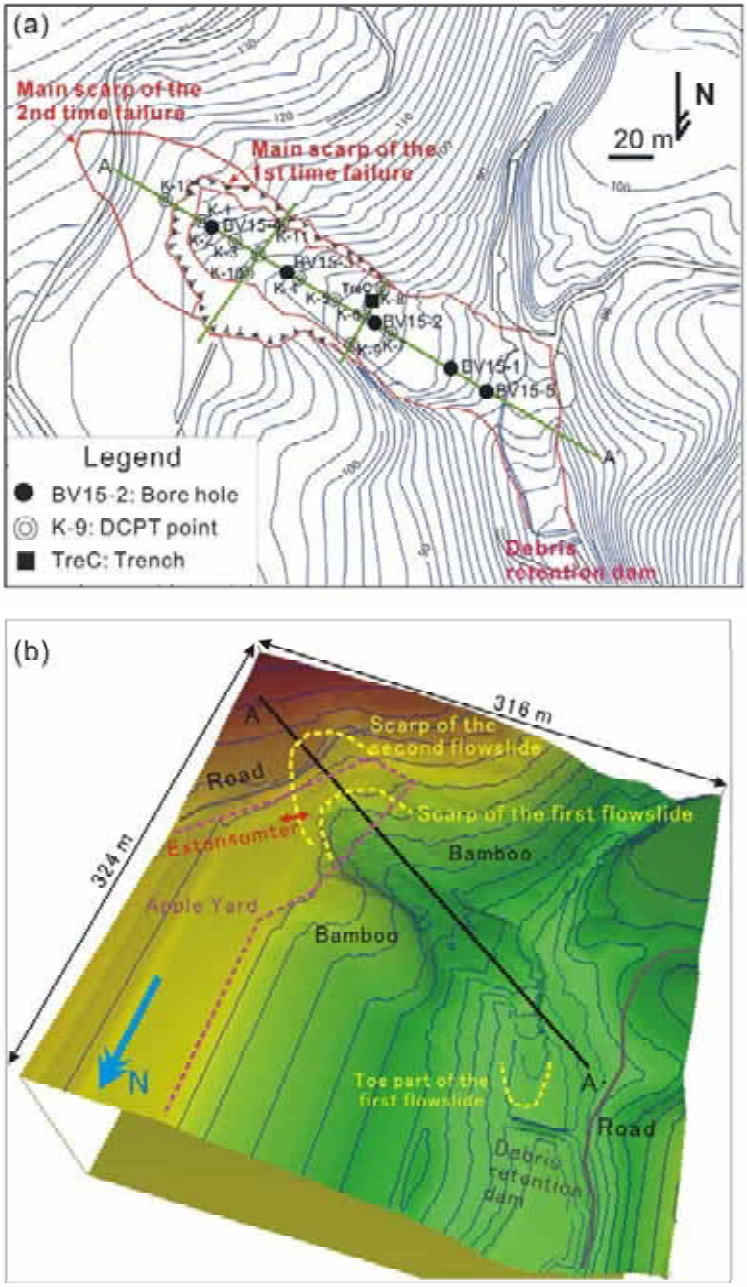

Fig. 4 **a** Plan and **b** birds-eye view of the first flowslide in Yamashina area

about 10 km north from the landslide site. There is a tendency for the precipitation and snowfall to be higher at the mountain side than that at the seaside in Kanazawa City, so these data was presented here just for reference. A rainfall event from 26 to 27 December caused a small displacement. After the heavy snow on 27 December, the displacement ceased temporally. On 29 December, because of the temperature rising, the snow began to melt. Accompanying the snowmelt, a rainfall event on December 29 accelerated slope deformation. However, the displacement velocity was very small from midnight of 30 until the morning of 31 December. Another rainfall event on December 31 triggered the flowslide. The failure time was recorded as 14:30 on December 31, 2003. The main scarp of the second landslide was enlarged 70 m backward from the main scarp of the first flowslide (See Fig. 4a and b). From the monitored results, it is found that the displacement behavior

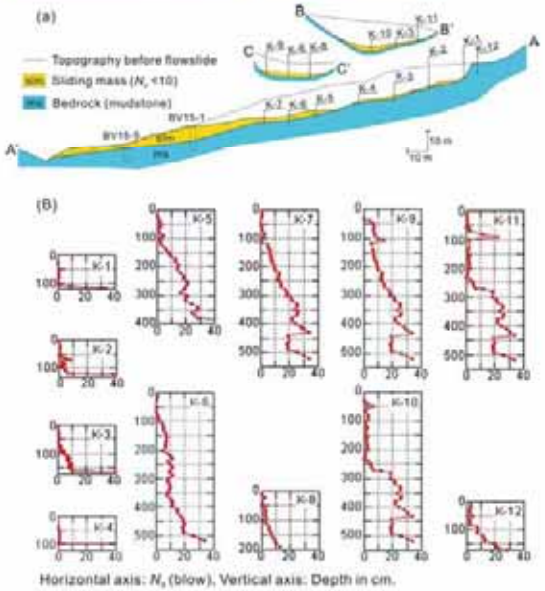

Fig. 5 **a** The geological longitudinal section. **b** The exploration result with portable cone tests (DCPT) of the first flowslide in Yamashina area

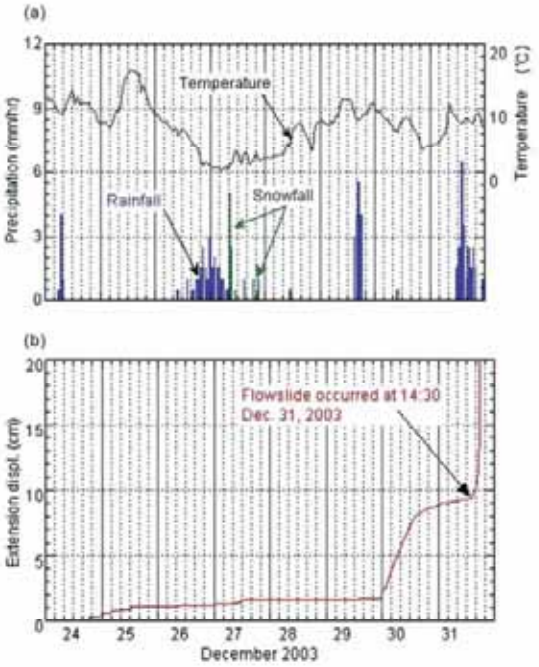

Fig. 7 **a** Meteorological data. **b** Monitored displacement by extensometer across the crack at the right side of the main scarp

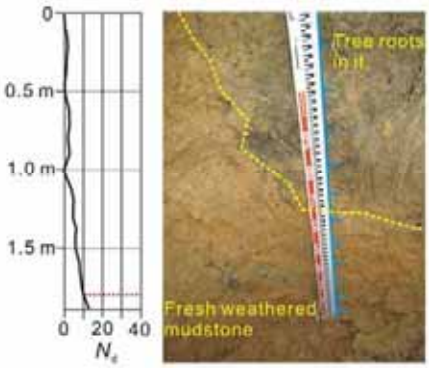

Fig. 6 Trench excavation after the first flowslide near K-8 point

Fig. 8 Air photo of the second flowslide occurred on December 31, 2003 (taken with remote-controlled camera in balloon, photo courtesy of Agriculture and Forestry Central Administration Office, Ishikawa Prefecture). (**A**) The grass previously distributed in the apple yard behind the main scarp of the first flowslide. It moved for 200 m as a whole block. (**B**) Deposit of the first flowslide. It bulged up because of the pushing by the second flowslide

of the landslide was controlled directly by the rainfall and snowmelt. Considering the failed part was subjected to stress release after the first flowslide, and there were many cracks developed in it, the precipitation and snowmelt controlling process on the landslide movement is easily understood. However, it brings a challenge for landslide researchers how to predict the displacement with the monitored results.

Figure 8 is an air-photo of the second flowslide taken by remote-controlled balloon, showing the debris with trees and grass on the surface moved for a long distance. It also pushed the deposits of the first flowslide, and made it bulged. A local road was damaged at the main scarp of the flowslide. The moving distance of the trees was about 200 m. Figure 9a shows the main scarp with a height of about 15 m at the time of the second flowslide. The displaced soil mass at this time was estimated to be about 50,000 m³. The blue sheets left on the main scarp were used to protect water infiltration through the crack into the slope. The weathered mudstone with yellow color was observed. Figure 9b shows the edge of the sliding mass of the second flowslide. At the toe part is the grass which previously existed

Fig. 9 Photographs showing the details of the second flowslide in Yamashina area. **a** The main scarp of the second flowslide (taken on January 1, 2004). **b** The toe part of the second flowslide. Part A shows the standing trees and bamboos; Part B shows the grass ground moved as a whole block; Part C shows the deposits of the first flowslide was pushed and bulged up. **c** The fresh mudstone outcropped as a sliding surface after the second flowslide

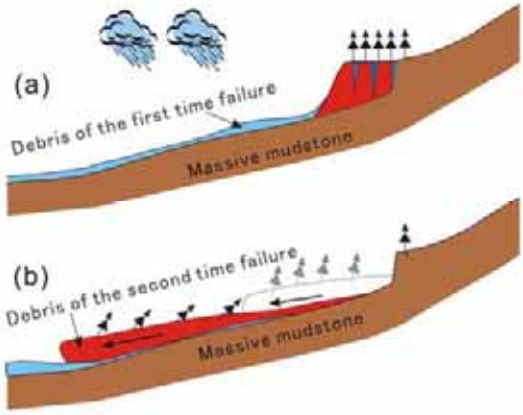

Fig. 10 A possible mechanism of the second flowslide. **a** In the period of rainfall and snowmelt, debris of the first flowslide was saturated, and the cracks behind the main scarp were filled with water. **b** Debris of the second flowslide moved rapidly on the saturated debris of the first flowslide with small shear resistance

behind the main scarp of the first flowslide, and following it are the standing trees and bamboos. It shows that the landslide moved as a mass for such a long distance. In front of the grass, the debris deposits of the first flowslide were pushed and bulged. As can be confirmed in Fig. 9c, the fresh mudstone is a grey color. Obviously, the displaced debris slid along the stratum surface of the massive mudstone with very small resistance, because there are almost no scratches that can be observed on the sliding surface.

Figure 10 is a possible sliding mechanism of the second flowslide. After the snowmelt from December 27 and the heavy rainfall from the morning of 31 December, the debris deposits of the first flowslide were in a fully saturated state especially at the source area, because the precipitation was so heavy and the debris layer of the first flowslide overlaying on the massive mudstone with low permeability was not so thick. At the same period, the cracks in the main scarp of the first flowslide were filled with water. It can be estimated that the slope destabilization was triggered by water pressure in the cracks and the increase of soil mass weight caused by the rainwater infiltration (Fig. 10a). After the slope failure, the displaced sliding mass loaded on the saturated debris layer of the first flowslide, and formed an undrained loading. In this process, the shear resistance at the sliding surface must be very small, because of the low permeability of the weathered mudstone debris. This can explain the phenomenon on the second flowslide where the sliding mass with grass moved a very long distance (see Fig. 9b), while some sliding mass with big trees just fell down in front of the main scarp (see Fig. 9a).

Concluding remarks

Two recent flowslides occurring in the mudstone area in Yamashina area, Kanazawa City were reported. Through field investigation on the two flowslides in Yamashina area, the following scenario was clarified. For the first flowslide, continual rainfall saturated the weathered mudstone at the slope surface, and finally caused destabilization of the slope. During the motion of the displaced debris mass, because of the low permeability and high water content at the surface soil, the sliding mass almost fluidized and all of the sliding mass moved down with a very low shear resistance. For the second occurrence, snowmelt and two periods of intense rainfall made the debris deposits of the first flowslide fully saturated, and the water pressure at the cracks in the back of the main scarp companying with the weight increasing of the slope body caused the second slope destabilization. The quick undrained loading on the fully saturated debris of the first time flowslide resulted in the second flowslide.

Acknowledgements

The authors thank Naoyuki Yamakami for his assistance in the set-up of the extensometer. The DCPT tests were conducted with the participation of the students of Department of Civil Engineering, Kanazawa University when the first author worked there. Agriculture and Forestry Central Administration Office of Ishikawa Prefecture supplied the plan and borehole data in this area after the first occurrence of the flowslide. Their help is deeply appreciated. We thank Dr. Heather Viles for comments on an earlier draft of the paper.

References

Japan Meteorological Agency (2002) http://www.data.kishou.go.jp
Kaseno Y (1993) Geology of Ishikawa-ken, Japan (with Geological Maps). Hokuriku Geology Institute (in Japanese)
Scale AJ (1956) Simple methods of flexible pavement design using cone penetrometers. Proc. 2nd Australian-New Zealand Conference on Soil Mechanics and Foundation Engineering, pp 73
Shuzui H (2001) Process of slip-surface development and formation of slip-surface clay in landslides in Tertiary volcanic rocks, Japan. Engn Geol 61(4):199–219
Yanagisawa Y (1999) Diatom bio-stratigraphy of the Miocene sequence in the southern Kanazawa area, Ishikawa Prefecture, Central Japan. Bull Jpn Geol Surv (in Japanese) 50(1):49–65

F.-W. Wang (✉)
Research Centre on Landslides, Disaster Prevention Research Institute, Kyoto University,
Uji, 611-0011 Kyoto, Japan
e-mail: wangfw@landslide.dpri.kyoto-u.ac.jp
Tel.: +81-774-38-4114
Fax: +81-774-38-4300

T. Matsumoto · Y. Tanaka
Graduate School of Natural Science, Kanazawa University,
Kodatsuno 2-40-20,
920-8667 Kanazawa, Japan

奥野岳志・汪　発武・松本樹典
(2004)

白山における巨大甚之助谷地すべりの運動様式及び影響素因

地すべり学会誌（地すべりの運動機構特集）, Vol.41, No.1, pp.57-64.

報告 Technical report

■白山における巨大甚之助谷地すべりの運動様式及びその影響素因

The deforming style and influencing factors of the Giant Jinnosuke-dani landslide in Haku-san mountainous area

金沢大学大学院自然科学研究科／奥野岳志
Graduate School of Natural Science & Technology, Kanazawa University／Takeshi OKUNO

金沢大学工学部土木建設工学科／松本樹典
Department of Civil Engineering, Kanazawa University／Tatsunori MATSUMOTO

金沢大学工学部土木建設工学科／汪　発武
Department of Civil Engineering, Kanazawa University／Fawu WANG

キーワード：変形観測，地下水位変動，運動メカニズム，風化，地すべり
Key words : ceformation monitoring, groundwater level, deforming mechanism, weathering, landslide

1．はじめに

石川県と岐阜県の県境に位置している白山は標高2,703mの活火山である。この地域は，急峻な地形，多雨・多雪の気象状況及び軟弱な砂岩・頁岩互層からなる地質状況を有しているため，古くから地すべり・土石流災害が多発している。その中でも，規模の最も大きい甚之助谷地すべりが白山の南西斜面に位置し，現在でも活発に変位している（図－1）。

甚之助谷地すべりを含む白山の南西斜面では，中生代ジュラ紀から白亜紀前期の手取層群の厚い湖成堆積層が広く分布しているが，このような地層の中で形成された地すべりの運動様式は未解明な点が多い。

甚之助谷地すべりの両側にある谷では，頻繁に小規模崩壊が発生し，谷底に多くの崩積物が堆積しているため，土石流が周期的に引起こされている。土石流災害を防ぐために，明治時代から両側の谷に砂防ダムの建設が開始され，現在まで80基以上もの砂防ダムが建設されている。しかし，砂防ダムを含めて地すべりが下方へと変位していることが最近の観測結果から明らかになっている。

甚之助谷地すべりは手取川の源流に位置している。手取川中流部には貯水量約２億m³のロックフィル形式の手取川ダム（高さ153m，幅420m）が1980年に建設された。多量の地すべり土塊が貯水池に流れ込んだ場合，越流によるダム崩壊の危険性が懸念される。

国土交通省は1980年代から，甚之助谷地すべりの調査及び観測を開始した（国土交通省金沢工事事務所，2002a）。本報告はその調査・観測結果及び著者らが行った調査・観察・土質試験に基づいて，甚之助谷地すべりの運動様式及び影響素因を考察するものである。

図－1　甚之助谷地すべりの位置

2．甚之助谷周辺の気象状況と地形特徴

この地域では，冬にはシベリアからのモンスーンの強い影響を受けて，多くの降雪に見舞われている。特に，白山山頂部では累積降雪量が12mにも及ぶ。一方，その他の季節では約２日に１回の割合で降雨がある。図－２

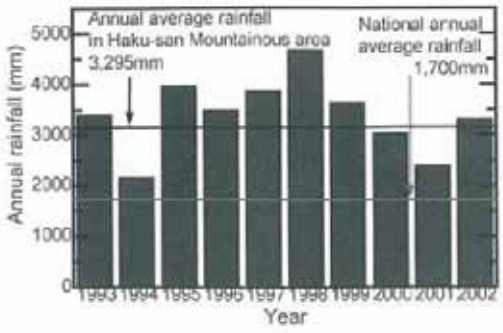

図－2　1993年から2002年までの白山地域における年間降水量

は1993年から2002年までの白山地域における年間降雨量を示している。年平均降雨量が3,295mmにも達し，国内の年平均降雨量1,700mmの約２倍である。

甚之助谷地すべり周辺にも幾つかの崩壊ブロックが分布しており，それらを含めて，1962年に「地すべり防止区域」に指定された（図－３）。防止区域内では多くの斜面崩壊現象が発生しており，植生で覆われていない斜面は全て過去に斜面崩壊が発生した斜面，あるいは現在でも崩落現象が起こっている斜面である。本報告の対象となる甚之助谷地すべりは写真中央に位置しており，長さ約2,000m，幅約500mで，海抜1,200m～2,100mの間に分布している。右岸側は別当谷であり，1934年に発生した別当崩れの滑落崖が残されている。左岸側には甚之助谷（上流）と柳谷（下流）が存在している。土石流を防ぐために，1927年から現在までに，別当谷に約30基，甚之助谷と柳谷に約50基の砂防ダムが建設されている。

図－３　甚之助谷地すべりの航空写真
（国土交通省の航空写真に加筆）

図－４　甚之助谷地すべりとその周辺の地形図及び観測機器の位置

図－４は甚之助谷地すべりとその周辺の地形図を示している。“大規模中間尾根ブロック”と呼ばれている（国土交通省，2002a）上部ブロックの平均勾配は約25°であり，下部ブロックの平均勾配は約20°である。図－４には国土交通省によって上部ブロック内に設置されている観測機器の位置も示している。地下水位計４箇所，孔内傾斜計６箇所，孔内伸縮計７箇所の観測が行われている（2003年11月現在）。

３．地質状況

この地域での地質調査は1996年から1998年にかけて行われ，調査結果は紺野（2001）によって総括された。地すべりとその周辺の1：100,000地質図によれば，白山の基盤岩は古生代の飛騨片麻岩であり，その上にジュラ紀～白亜紀前期の調成堆積層である手取層群の頁岩・砂岩互層及びレキ岩が広く分布している（紺野，1993）。手取層群の上を白亜紀の濃飛流紋岩，そして，第四紀の古白山火山噴出物（10万年前），新白山火山噴出物（１万年前）が覆っている（図－５）。もともと，溶岩は尾根部に比べ谷部により厚く堆積していたと推測される。厚い溶岩で覆われていた谷部が風化と表面浸食に耐え，現在の高い地形となり，尾根であった甚之助谷地すべりのところが浸食と風化作用を受けて，低い地形となっている（図－６，図－５に示すJ－J'断面）。このような現象は“地形の逆転”と呼ばれている（千木良，1998）。風化作用によって，斜面を構成する地層のせん断強度特性及び変形特性が劣化していくことがHoek et al.(1995)の計測によって明らかになっている。

手取層群の柱状図を図－７に示す（松川，2002）。手取層群は石徹白亜層群（Itoshiro subgroup）と赤岩亜

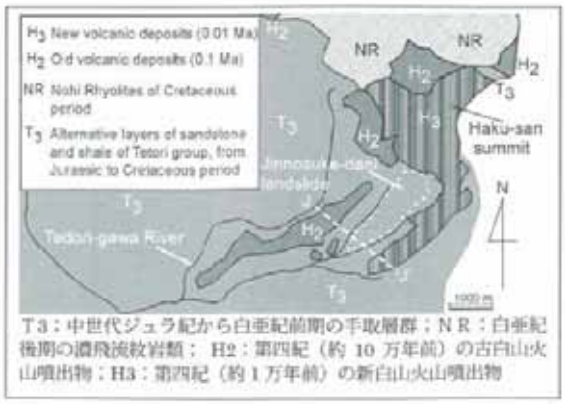

T３：中世代ジュラ紀から白亜紀前期の手取層群；ＮＲ：白亜紀後期の濃飛流紋岩類；Ｈ2：第四紀（約 10 万年前）の古白山火山噴出物；Ｈ3：第四紀（約１万年前）の新白山火山噴出物

図－５　地すべりとその周辺の地質図（紺野（1993）に加筆）

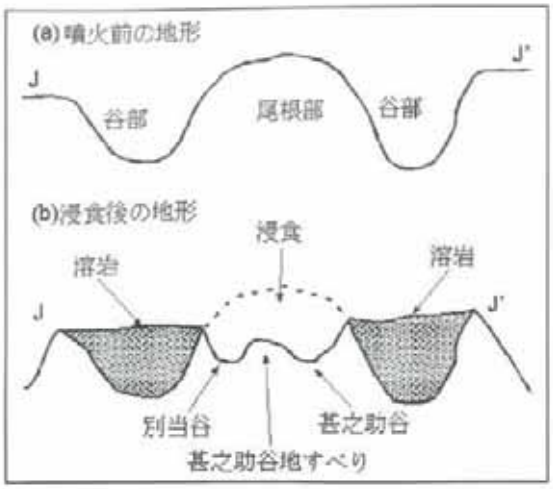

図－6　甚之助谷地すべりにおける“地形の逆転”模式図

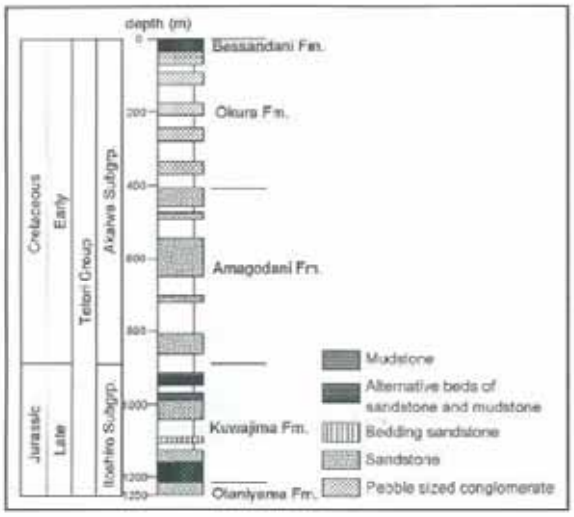

図－7　別当谷周辺で計測された手取層群の柱状図
（松川，2002）

層群（Akaiwa subgroup）からなる。大谷山層と桑島層に区分される石徹白亜層群に主に砂岩・頁岩互層からなっており，赤岩亜層群は主に砂岩から成立っている。桑島層は含雲母黒色頁岩及び砂質頁岩と，細・中・粗粒の砂岩との互層からなり，層厚10cm～10mで繰返し，頁岩及び砂質頁岩が優勢である。

国土交通省金沢工事事務所（2002b）が2001年に海抜1,830mで実施したボーリング調査の結果によれば，深さ130mのコアも片状を呈する砂岩と頁岩起源のレキ混じ粘土であった。

2003年8月に別当谷の露頭で手取層群の層理面及びその中に分布している節理の現地調査を行った。平均的な層理面の走向と節理の走向分布をローズダイヤグラムで図－8に示している。節理走向の多くは層理面の走向方向とほぼ直交している。図－9はシュミットネットに層

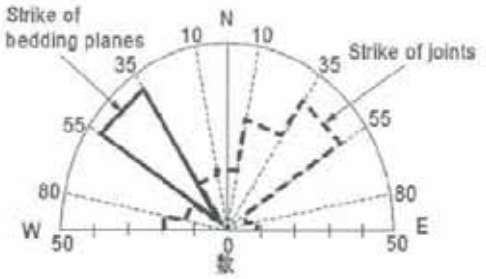

図－8　別当谷での層理面の走向と節理の走向の計測結果

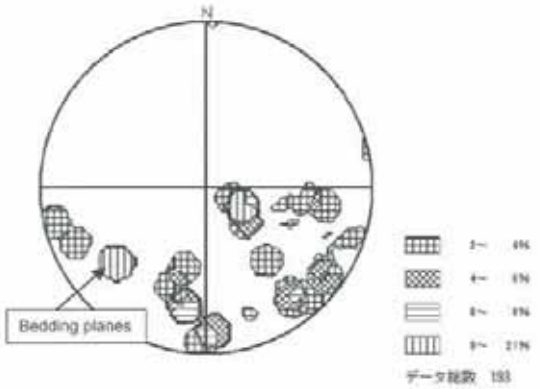

図－9　手取層群の層理面及びその中で発達している節理傾斜方向と傾斜角のシュミットネット下半球投影

理面と節理の傾斜方向及び傾斜角度を投影したものである。層理面の平均傾斜方向はS36°W，傾斜角度は40°である。節理の走向は別当谷とほぼ平行であることから，谷の応力解放によって谷側斜面での節理が発達したものと考えられる。

4．白山における斜面崩壊に関連する歴史

表－1は706年から現在までの甚之助谷地すべり周辺における災害と砂防に関連する歴史である（白山砂防直轄70周年記念事業実行委員会，1999）。白山の噴火は700年代初めから1600年代中ごろまで頻繁に生じており，最後の噴火活動は1659年に発生した（玉井，1958）。706年，1042年及び1554年から1659年までの三回の活動期が見られ，その点から，噴火は100年～150年の活動期間を経て，約300年の休止期間へと続く。この傾向から推測すると，現在，白山は休止期の終わりにあたる。次の活動期に予想される新たな火山活動による溶岩流，火砕流及び地震活動は白山地域の地すべりの安定性に影響すると懸念される（守屋，1984）。

これまでに，甚之助谷地域で発生した斜面崩壊の中で最も被害が大きかったのは1934年の別当崩れである（図－3参照）。集中豪雨（3日間での降雨量は約500mm）によって，斜面崩壊が引起こされた。崩壊土砂は，土石流に発展し，手取川に沿って，日本海まで流下した。この土石流災害によって，112名の命が失われ，172戸の家屋が倒壊し，市ノ瀬村落が完全に壊滅した。

5．甚之助谷地すべりの運動様式

1980年代初期から，地質マッピング，地盤測量，地下水位及び地すべりの変位量観測が継続されている。

光波測距儀（EDM）を用いた光波辺長測量観測とGPS観測が地すべり変位観測に利用され，EDM観測は年一回の割合で行われている。図－10は地すべり防止区域内の観測点の分布と，1994年から2001年まで７年間の地表面変位観測結果をベクトルで示したものである。この観測結果によれば，上部ブロックは非常に活発に変位しており，７年間に約1,180mmの累積最大変位がB５とB11観測点で生じている。上部ブロックの年平均移動量は80mm～170mmである。平均移動方向はS36°Wであり，手取層群の傾斜方向とほぼ一致している。この結果によって，甚之助谷地すべりの上部ブロックの運動は手取層群の流れ盤構造の影響を受けていることが分かる。また，谷側の斜面部分は谷地形の影響を受けて，谷方向の変位成分も呈している。

上部ブロックの活発な変位に対して，下部ブロックの尾根方向が手取層群の傾斜方向と約30°ずれているため，活発な動きがなく，ほぼ安定している。

上部ブロックの先端部分にあるB12観測点の運動方向は上部ブロックの他の観測点とは異なっており，約50°近く南方向へ偏っている。図－11はB12点近くにある工事道路の擁壁（図－10のF点）の破壊状況である。上部ブロックが擁壁を甚之助谷側へ押出して，最大開口幅が10cmになっていることが確認できる。

図－12は上部ブロックにある各観測点の累積変位量と観測経過時間の関係を示している。変位速度はこの７年間にほぼ変わっていない。別当谷側にあるB５観測点と甚之助谷側にあるB11観測点は最も速く変位しており，

表－１　白山地域における災害と砂防の歴史
（白山砂防直轄70周年記念事業実行委員会，1999）

706年	白山噴火	
1042年	白山噴火	
1554年	白山噴火	
1579年	白山噴火	
1659年	白山の最も新しい噴火	
1891年	濃尾地震により甚之助谷に崩壊発生	石川県施行
1896年	同地区での集中豪雨により大崩壊が発生	
1911年	石川県により調査着手	
1912年	甚之助谷，柳谷における山腹工の施工開始	
1927年	国の直轄事業に移管され，本格的な砂防事業が開始されるとともに内務省新潟土木出張所白山砂防工場が設置された。1927年から1939年に渡り，柳谷，甚之助谷の荒廃渓流を治める工法として渓流で初めて階段状に砂防ダムを施工した。	国直轄
1934年	未曾有の豪雨により手取川で大出水，別当谷で大崩壊が発生し，山津波を起こし，流出耕地2,808町歩，流出家屋172戸の被害が生じた。この被害により白山砂防工場が流出し，現場事務系が一時閉鎖となった。このため白山砂防工場を金沢市野町に設置した。	
1937年	別当谷砂防ダム群工事開始	
1944年	第２次世界大戦により砂防工事が一時閉鎖となった。	
1957年	甚之助谷第５号ダムの移動が激しくなってきたため，国直轄で甚之助谷地すべり調査を開始した。	
1961年	甚之助谷地すべり対策事業に国直轄で着手した。	
1962年	北美濃地震が発生し，白山山麓に大被害を及ぼした。甚之助谷地すべりが地すべり防止区域に指定される。	
1973年	甚之助谷地すべり対策事業が完成された。	
1980年	手取川ダム完成	
1982年	侵食にたい変化が見られてきたため，甚之助谷地すべり対策事業を再開した。	
1990年	別当谷山腹工工事開始	
1999年	大雨によって別当谷では，斜面崩壊が発生し，天然ダムが形成された。	
2001年	推定崩壊土砂量20,000m³の斜面崩壊が別当谷左岸で発生した。	

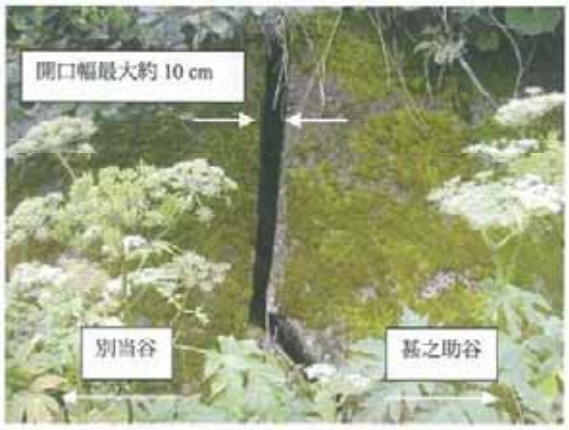

図－11　上部ブロックと下部ブロックの境界（図－10，F点）における擁壁のクラック（2003年９月３日著者撮影）

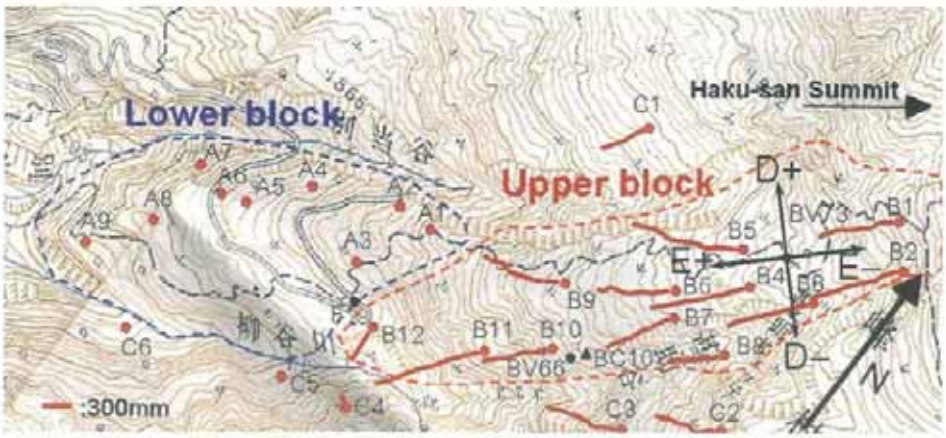

図－10　1994年から2001年までの甚之助谷地すべりにおける累積地表面変位量

中央線付近の観測点はほぼ同速度で動いている。

谷に建設されている砂防ダムは，上流からの崩壊土砂を止めるとともに，谷底の浸食も食い止めている。この意味で砂防ダム群は甚之助谷地すべりの局所変形を抑制する役割も果たしていると言える。

孔内傾斜計観測は地すべりブロックのすべり面深さ，移動方向及び変形速度を求めるのに利用される。図－13は上部ブロックに位置する孔内傾斜計BV73（図－10参照，D－は甚之助谷方向，E＋は斜面下方）の観測結果を示している。測定は1997年10月23日に開始され，図－13には2000年10月27日と2001年８月６日の観測結果を示している。斜面下方への傾斜成分と甚之助谷側への傾斜成分の両成分を有する。すなわち，地すべりの変動は地層層理面の傾斜方向と谷地形の両方の影響を受けていることが推察される。また，BV73観測点におけるすべり面は三つ存在していることが確認でき，最大深さは約38mである。

2003年８月に実施した別当谷での露頭調査と試料採取によれば，頁岩の粘土化現象が顕著である。調査した厚さ23.1mの露頭では，粘土化している14の弱面（潜在すべり面）が検出された（図－14）。これらの弱面は非常に薄く，ほとんど砂岩層とその下に分布している頁岩層・泥岩層の間に形成され，常に水に満たされている状態である。図－15に粘土化した頁岩層の粒度分布の一例を示している。液性限界は20.1%であり，低液性限界粘土と分類される。この粘土試料の自然含水比は20.0%であり，ほぼ液性限界に達している。また，この粘土の撹乱試料を用いて，一面せん断試験を行った結果，残留内部摩擦角度が26.3°であった（図－16）。

以上のことより，甚之助谷地すべりの運動様式は以下のようにまとめられる：(1)飽和状態にある粘土化した多

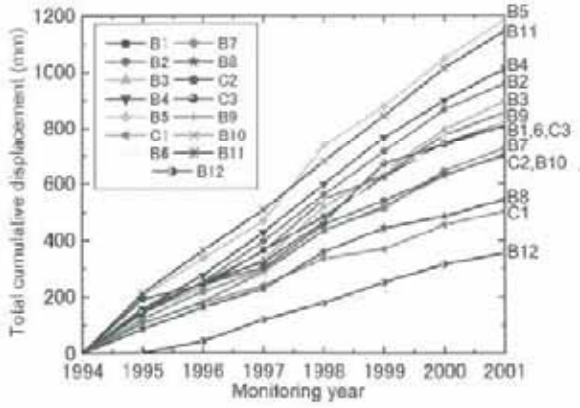

図－12　上部ブロックにおける1994年から2001年の累積移動変位量（B1－B12，C1－C3）

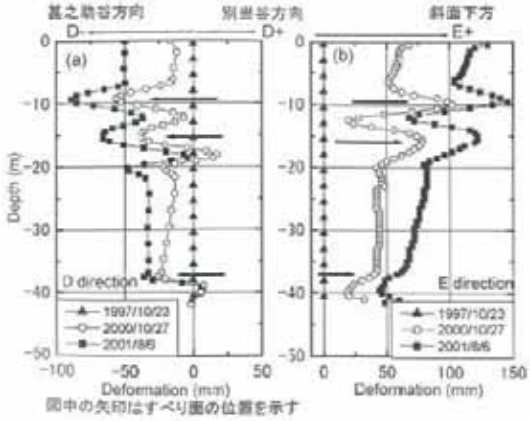

図－13　BV73観測点における孔内傾斜計の観測結果（1997年10月23日観測開始）

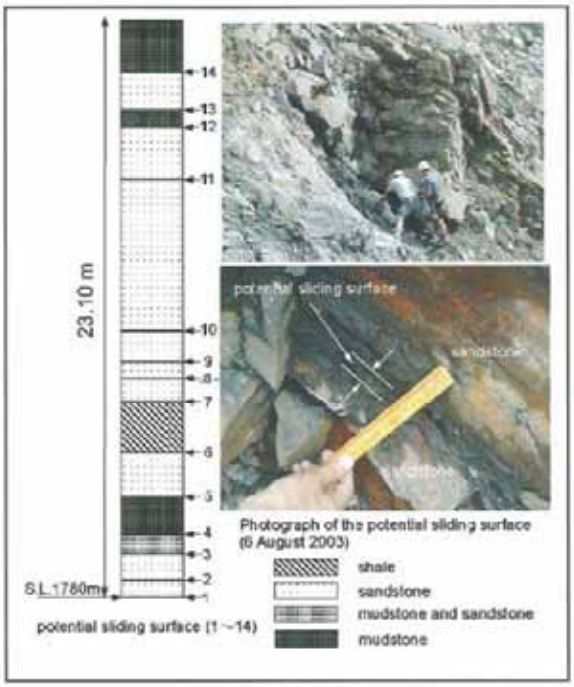

図－14　別当谷の露頭観察による潜在すべり面の調査結果（左），試料採取（右上）および観察写真（右下）

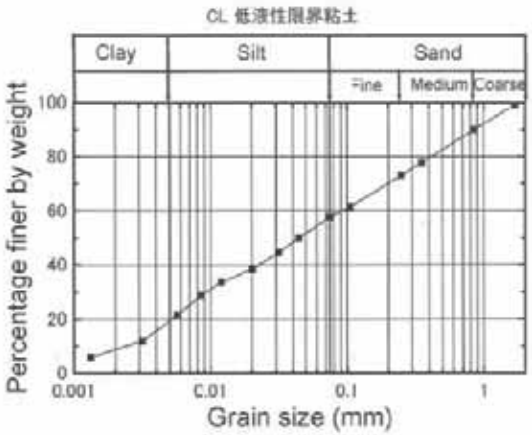

図－15　粘土化している頁岩層の粒度分布

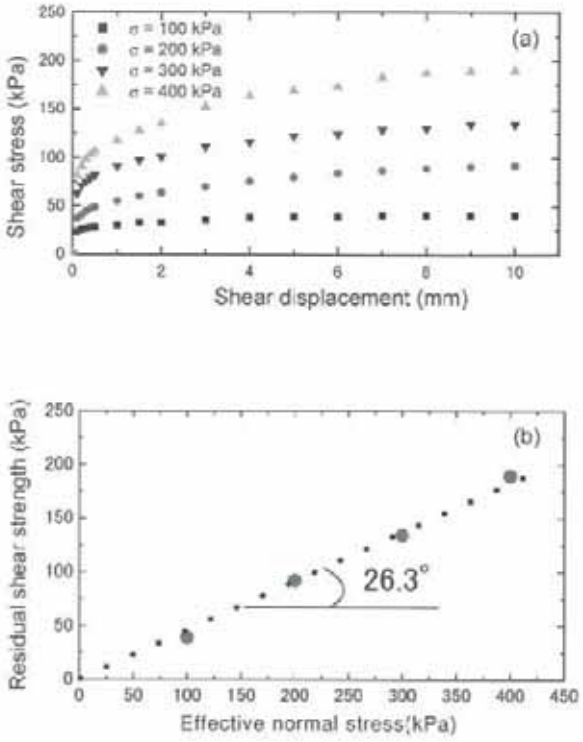

図－16　粘土化した頁岩層の撹乱試料を用いた一面せん断試験結果
(a)　せん断応力とせん断変位の関係
(b)　残留せん断強度と有効垂直応力の関係

数の弱面が存在している；(2)変位主方向が層理面の傾斜方向と一致している；(3)局部的には，谷地形の影響を受けている。

6．地下水変動による地すべり移動量への影響

孔内伸縮計は地すべり変形を観測するためにボーリング孔内に設置されている。ワイヤーの一端は観測孔の底部に固定され，他端は地上の回転盤に連結されている。孔内伸縮計の近くに，地下水位計が設置されている。図－17はBV66観測点（図－10を参照）における孔内伸縮計で観測された累積移動量，BC10観測点（図－10を参照）の地下水位，及び地すべり地で計測された降雨量の関係を示している。時間軸のグリッド線はこの地域の梅雨の季節にあたる毎年７月を示している。地下水位は融雪と降雨によって，４月から上昇し始め，７月ごろにピークに達する。地下水位の上昇に伴って，地すべりの運動が活発な時期に入る。地下水位が通常のレベルに落着く時，地すべり運動はほぼ休止する。

図－17の中から2000年２月25日から2001年10月17日までの地すべりの日移動量と地下水位の関係を図－18に示す。地下水位は４月から上昇し始め，７月下旬まで高いレベルを保っている。秋雨によって10月下旬より地下水位は再び上昇し，それに伴い，変位が発生する。地下水位が37mの臨界水位を超えると，地すべり変位が生じる。１年を通して，地すべり運動は４月中旬から加速し，７月にピークとなり，９月以降はほぼ安定している。11月ごろの秋雨時期では，水位上昇量が少ないため，地表変位はそれほど大きくない。図－19に2000年２月25日から2000年９月12日までの地すべり移動量増分と地下水位増分（地下水位37m以上）の相関関係を示す。地すべり移動量の増分と地下水位増分には相関関係が見られる。このことから地下水位が臨界地下水位以上に上昇すると地すべり移動量が増加し始める。この計測結果より，臨界水位を超える地下水位が地すべり運動の最も敏感かつ大

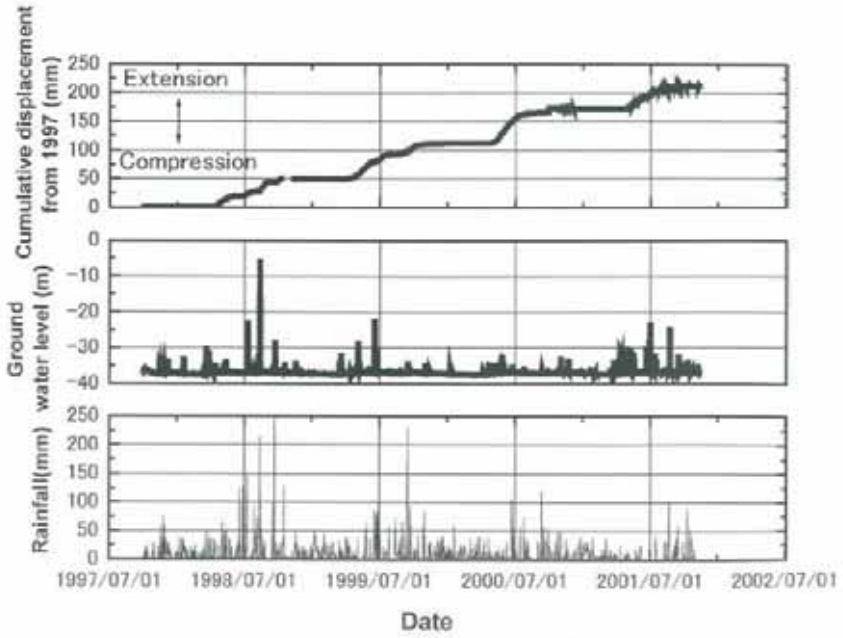

図－17　BV66観測点の孔内伸縮計，BC10観測点の地下水位および降雨の観測結果

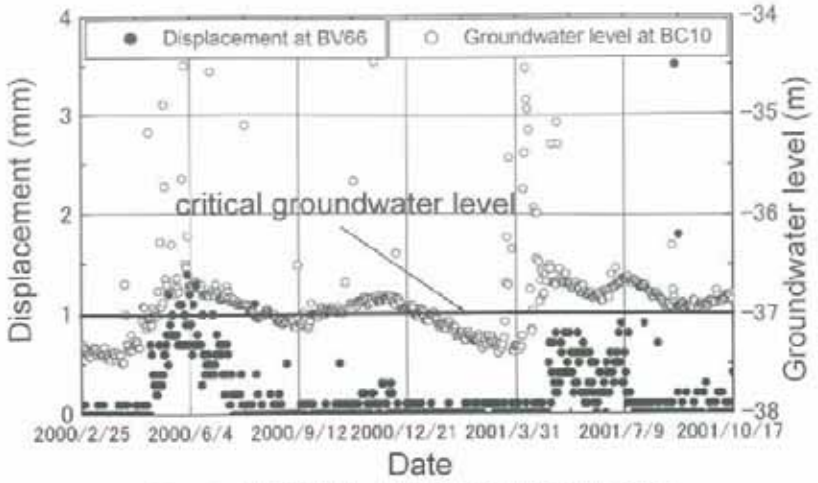

図－18　甚之助谷地すべりの日移動量と地下水位の関係

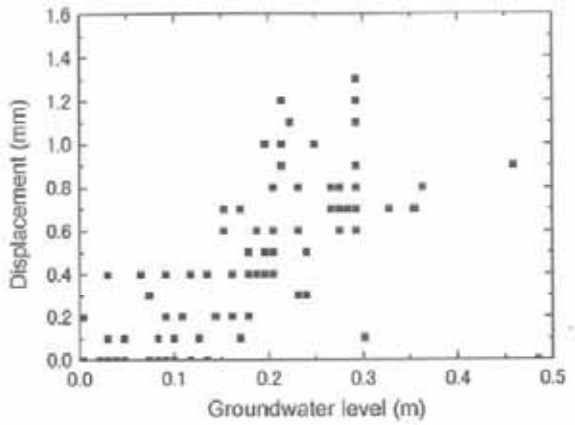

図－19　移動量増分と37mからの地下水位上昇量の相関関係

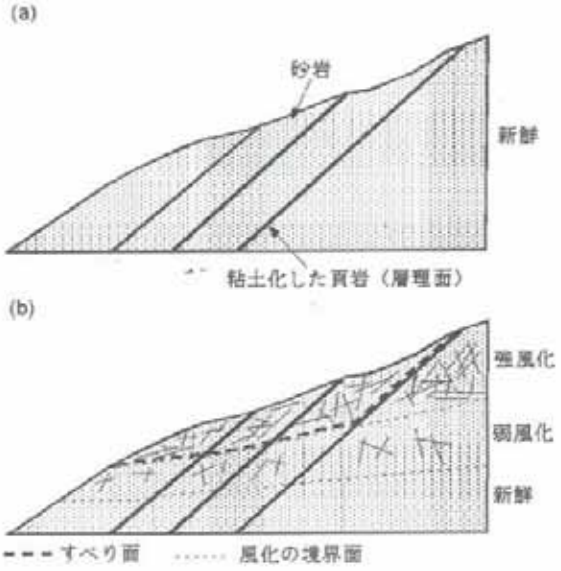

図－20　斜面崩壊の模式図
(a)　新鮮岩の場合
(b)　風化した場合

きな誘因であると判断できる。この結果に基づく排水工の設置は地すべり変位の抑制にはより大きな効果が期待できる。

7．考察と結論

甚之助谷地すべりは手取層群の流れ盤構造の上で発生している巨大地すべりである。その運動様式は複雑であり，影響素因も多様である。しかし，以下の三つの角度が興味深い。手取層群の平均傾斜角度が40°であり，弱層である粘土化した頁岩層の内部摩擦角は26.3°，上部ブロックの平均勾配は25°である。流れ盤構造といいながら，粘土化した頁岩層（層理面）の傾斜が斜面表面傾斜より大きい場合，頁岩層に沿ってすべることが不可能である（図－20a）。ただし，もし砂岩層が強風化され，地層の完全性が失われた場合には，すべり面が粘土化した頁岩層を追跡しながら，風化した砂岩を通過する複合的なすべり面の形成が可能になる（図－20b）。甚之助谷地すべりでは，砂岩・頁岩互層において深さ130mまでの風化がボーリング調査によって確認されている。別当谷斜壁で見られる甚之助谷地すべりの内部構造の調査解析より，このような複合すべり面の存在が確認されている（藤井・堀，2003）。図－20bのようになった場合，すべり面のせん断抵抗が粘土化した頁岩層（残留内部摩擦角が26.3°）と風化した砂岩層のせん断抵抗に支配される。地下水位変動に対して地すべり変位が敏感に反応していることから，排水工を中心とした対策を一層強化する必要があると考えられる。

以上の観測データ解析及び考察より，以下の結論が導かれる。

(1)　甚之助谷地すべりは２つのブロックに分けられる。上部ブロックは年間80mm－170mmの速度で変位しており，下部ブロックはほとんど安定している。上部ブ

ロック全体の変位方向は手取層群の傾斜方向に影響されており，局部的には両側の谷地形の影響を受けて谷側へも変位している。

(2) 臨界地下水位を超える地下水位変動が地すべり変位に対する大きな誘因である。

(3) 手取層群の高い透水係数を持つ破砕された砂岩層と頁岩・泥岩層の互層構造は風化作用を受けやすいことが地すべり変動の基本的素因である。

(4) 対策の一つとして，排水工が非常に有効である。

謝辞

本研究は文部科学省による研究補助金（No. 15310127 代表者：汪　発武）を受けた。国土交通省北陸地方整備局金沢河川国道事務所に観測資料を提供して頂いた。現地調査において，金沢大学大学院生の臼中康博君，学部生の上月真人君と高田渉君の協力を得た。記して，感謝の意を表する。

参考文献

千木良雅弘（1998）：災害地質学入門，近未来社，206p.

藤井幸泰・堀伸三郎（2003）：別当谷斜樋で見られる白山甚之助谷地すべりの内部構造，地すべり，Vol. 40，No. 5，pp. 53－57.

白山砂防直轄70周年記念事業実行委員会（1999）：白山砂防，未来への水脈，pp. 1－6.

Hoek, E., Kaiser, P. K. & Bawden, W. F. (1995) : Support of underground excavations in hard rock. Rotterdam : Balkema. 215p.

紺野義夫（1993）：石川県地質誌，北陸地質研究所，pp. 69－78.

紺野義夫（2001）：石川県地質誌・補遺，北陸地質研究所，194p.

国土交通省金沢工事事務所（2002a）：平成13年度甚之助谷地すべり調査作業報告書，139p.

国土交通省金沢工事事務所（2002b）：平成13年度甚之助谷地質ボーリング調査作業報告書，13p（コア写真と柱状図付き）.

松川正樹（2002）：石川県手取川上流域及び関連地域の手取層群，手取川流域中生代手取層群調査報告書，石川県白山自然保護センター，pp. 3－19.

守屋以智雄（1984）：白山の火山地形，金沢大学地理学報告，No. 1，pp. 130－139.

玉井敬泉（1958）：白山の歴史と伝説，石川県，pp. 1－4.

（原稿受付2004年２月12日，原稿受理2004年３月26日）

Igwe, G., K. Sassa, H. Fukuoka, F.W. Wang
(2006)

The undrained response of sands with different gradations
in a stress-controlled ring shear tests

Canadian Geotechnical Journal (submitted)

The undrained response of loose, medium and dense sands with varying grading

Ogbonnaya Igwe, Kyoji Sassa, Hiroshi Fukuoka and Fawu Wang
Research Centre on Landslides, Disaster Prevention Research Institute, Kyoto University, Japan.

Abstract: A series of tests undertaken to investigate the undrained shear behavior of sands with different grading is presented. The tests were conducted by means of a new ring shear apparatus at different relative densities and normal stresses. Silica sands constituted to various uniformity coefficients were classified as well graded (WG), intermediately graded (ING), narrowly graded (NAG) and gap graded (GAG). Osaka Formation specimens from a landslide site were used to verify some results of the investigation. Results of the investigation undertaken to clarify the influence of grading on the shear strength of sandy soils show that in medium and dense states the values of their peak strengths are ranked as WG> ING> NAG> GAG**.** However, their steady state strengths are in the order of NAG> ING>WG>GAG. Although the steady state strengths of WG, ING graded and NAG specimens in loose state are very low, only the steady strengths of NAG and ING specimens have steady state strengths of zero. The reduction of steady strength to zero after failure has been described in this paper as complete liquefaction. Results of the investigation on the factors initiating flow slides show that there is a threshold state demarcating sands that contract from those that dilate. The threshold state which is characterized by the equality of shear resistance and generated pore pressure at failure is independent of both initial confining stress and grading of specimens. When the threshold pore pressure is exceeded, specimens tend to collapse and flow-liquefy. When the contrary is the case, specimens show dilative behaviors.

Keywords: Flow liquefaction, threshold pore pressure, particle gradation, peak strength, steady-state strength, ring shear tests.

1. Introduction

1.1 Background and objectives

The conditions necessary for liquefaction and the mechanism underlying the liquefaction of saturated soils subject to dynamic or static loading have been discussed by a great deal of researchers, including Casagrande (1936, 1976), Terzaghi and Peck (1948), Seed (1966, 1979, 1981), Castro (1969, 1975), Seed and Idriss (1971), Whiteman (1971), Ambraseys (1973), Gilbert (1976), Poulos (1981), Kutter (1982), Poulos et al. (1985), Eckersley (1985), Gilbert and Marcuson (1988), Ishihara et al. (1990), Ishihara (1993), Marui (1996), Sassa (1996, 1997, 2000) Sassa et al. (1996, 1997, and 2003). It has been variously mentioned that the void ratio or relative density of the soil, the confining stress on the soil, the intensity and duration of ground shaking, are important factors determining the liquefaction susceptibility of a saturated soil.

While highlighting the importance of such factors as confining stress, initial shear stress, particle angularity, grain structure or fabric, over-consolidation ratio, previous strain history, intensity and duration of ground shaking in predicting the liquefaction susceptibility of a soil mass, researchers have also provided evidences that indicate liquefaction is associated, primarily, with loosely deposited, poorly graded sands and silts (Seed 1979; Castro and Poulos 1977; Seed 1981; Sassa 1985; Vaid and Chern 1985; Vaid et al. 1990; Kramer and Seed 1988; Sassa and Wang 2003; Yamamuro and Lade 1999; Yoshimine et al. 1999).

It is noted that while the factors mentioned above are valuable in understanding the mechanism of flow slides, they do not seem to be enough in predicting the liquefaction susceptibility of a mass of soil. Not all loose soils at a given effective normal stress, for instance, will collapse and liquefy when subject to sufficient amount of shearing stress. Since neither relative density nor initial stress condition can fully account for why

some soils liquefy and others do not, the authors have chosen to study the pore pressure changes associated with non-cohesive soils under stress. By investigating the pore pressure changes associated with the soils under stress, the authors hope to understand why some soils collapse and liquefy whereas others under identical initial stress conditions dilate and gain strength.

Furthermore, although liquefaction phenomenon has been the subject of a barrage of investigations and publications for decades now, not much is known about the influence of particle size distribution on the mechanical behavior of granular materials, despite the universal knowledge that whether a material slides or flows is closely tied to its nature. Greater emphasis, it seems, has been placed on the influence of such other factors as void ratio, confining stress, and rate of loading than on particle characteristics. It is the objective of this research to investigate the influence of grading on the shear behavior of sandy soils in loose, medium and dense states. This paper attempts to scrutinize the influence of grading on the peak and steady state strengths of soils categorized as narrowly graded, intermediately graded, well graded and gap graded. The concept of gap-graded soils has not been properly understood yet. Good knowledge of the underlying mechanism of failure in gap- graded soils may yield strong insight on liquefaction of soils.

Researchers including Hutchinson and Townsend (1961), Kirkpatrick (1965), Koerner (1969), Lee and Fitton (1969), Ross et al. (1969), Kishida (1969), Wong et al. (1975), and Vaid et al. (1990), Kokusho et al. (2004) have conducted tests using soils of varying grading, but they have done so using the triaxial cell apparatus which do not permit soils to be displaced for long distances. It stands to reason that if soils do not undergo sufficient displacement, making conclusions about their steady state strengths would be, at best, an inconclusive exercise. The ring shear apparatus, among other attributes, permits unlimited displacement of soils; and should be suitable for examining the post-failure behavior of granular materials.

1.2 Overview of related works

Although plenty of published works exists, with some of them predating Hutchinson and Townsed 1961, scarcity of conclusive laboratory evidences, irregularities arising from laboratory apparatuses ((Hutchinson and Townsed 1961; Kirkpatrick 1965)., narrow range of materials investigated, and sometimes, problems associated with difficulty distinguishing the effects of particle gradation from those of particle size have combined to limit what is presently known about the relationship between grading liquefaction. In spite of this, however, there are evidences relating liquefaction potential with gradation.

In their pulsating loading triaxial tests on saturated soil samples, Lee and Fitton (1969) compared soils tested at the same relative density and confining stress, and found that fine, silty sands were weaker than gravely ones. Lee and Fitton's conclusion were quite consistent with those of Wong et al. (1975), who had reported, in their evaluation of the liquefaction-susceptibility of gravely soils and sands, that the cyclic stresses required to cause a certain amount of strain of saturated samples of gravely sands were apparently higher than those causing similar strains in sands. Castro and Poulos (1977) had similarly noted that liquefaction was more likely in uniform, fine, clean sands than in wider graded sands.

While studying the resistance to liquefaction of three medium sands having linear grain-size-distribution curves, identical mean grain size and mineralogy, but different uniformity coefficients (1.5, 3.0, and 6.0), Vaid et al. (1990) found that at low relative densities, poorly graded, water-placed, sand had lower cyclic strength than well-graded sands at the same initial condition. They however found that the reverse trend was true at relative densities above 43 %. They observed that within a certain range of relative densities – from the loosest state to a relative density of about 43% - poorly graded sands deformed in a purely contractive manner without dilating, whereas well-graded ones, within the same range of relative densities, deformed in a dilative manner. They concluded, on these evidences, that gradation might control the occurrence of contractive behavior, and possibly, flow failure at low relative densities.

Some recent effort by Kokusho et al (2004) has also drawn some interesting conclusions. They found that while well-graded soil materials composed of non-crushable particles tended to have higher undrained monotonic strengths than poorly graded ones, well graded materials made up of crushable particles had lower undrained monotonic strength than poorly graded materials.

It may be important to note that the conclusions drawn from these laboratory tests appear similar to those drawn from field investigations including those by Ross et al. (1969) and Kishida (1969) who had in their separate investigations reported strong evidences of greater shear resistance to cyclic liquefaction by wider graded soils while investigating the bridge foundation displacements in the March 27, 1964 Alaska earthquake

which caused extensive damage to highway bridges, and the characteristics of liquefied sands during the Mino-Owari Tohnankai and Fukui earthquakes respectively. Ross et al. (1969) had specifically noted that there were no cases of bridge damage for those supported on gravely sands, whereas the bridges supported on sands suffered massive damage. Kishida (1969), too, had reported that liquefaction was limited to areas consisting of poorly graded soil, and that areas founded on well graded soils did not suffer liquefaction.

2. Apparatus and material

2.1 Apparatus

The results presented and discussed in this paper are from a new ring shear apparatus, hereafter referred to as DPRI-5, which is the fifth version of ring shear apparatuses available at Disaster Prevention Research Institute, Kyoto University, Japan. Designed, modified, and vastly improved by Sassa in 1996, DPRI-5 (Fig. 1) is reinforced with devices capable of sustaining undrain loading throughout the duration of a test. The apparatus is structured to eliminate some difficulties commonly encountered while studying the mechanism of landslide motion, and sufficiently equipped to allow speed-, and stress- controlled tests; and the measurement of very large shear displacement. Details of the structure and efficiency of the apparatus have been discussed comprehensively by Sassa et al. (2002), and Wang and Sassa (2001).

Fig.1 Picture of the ring shear apparatus

2.2 Specimen characteristics

Industrial sand materials composed of sub-angular to angular quartz and small amount of feldspar were reconstituted to three uniformity coefficients – 3.3, 4.5, 9.0 and 17.5 – referred to as narrowly graded (NAG), intermediately graded (ING), well graded (WG) and gap graded (GAG) The grain size distribution curves are shown in Fig. 2, while the physical properties of the reconstitutes are summarized in Table 1. The authors are aware of the importance of reconstituting sands with different uniformity coefficients but the same mean particle size. However, the mean particle sizes in Table 2 have slight differences.

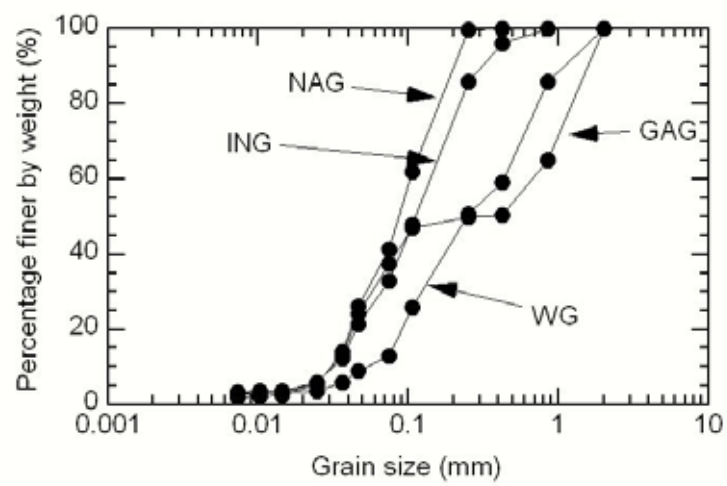

Fig.2 Grain size distribution curves of the four samples of silica sand

Table 1 Physical properties of test specimens

Specimen	Minimum dry density (g/cm^3)	Maximum dry density (g/cm^3)	Mean grain size (D_{50})	Effective grain size (D_{10})	Uniformity coefficient, Uc	Specific gravity
Well-graded (WG)	1.38	1.82	0.25	0.05	9.0	2.65
Intermediately graded(ING)	1.26	1.68	0.12	0.03	4.5	2.65
Narrowly graded(NAG)	1.24	1.66	0.09	0.03	3.3	2.65
Gap-graded(GAP)	1.25	1.67	0.50	0.03	17.5	2.65

Table 2 A summary of results of investigation on natural and artificially constituted sandy soils

Test No.	Material	Grading	*Dr* (%)	σ_i (kPa)	τ_p (kPa)	τ_{ss} (kPa)	I_B	Behavior	Test condition	B_D value
1	Silica	NAG	29.4	257	70	0	1.0	Purely contractive	Undrained	0.96
2	Silica	NAG	29.5	220	49	0	1.0	Purely contractive	Undrained	0.97
3	Silica	NAG	29.5	305	85	0	1.0	Purely contractive	Undrained	0.96
4	Silica	NAG	32.2	200	142	136		Large volume reduction	Drained	0.97
5	Silica	NAG	33.1	201	49	7	0.85	Purely contractive	Undrained	0.97
6	Silica	NAG	42.1	196	83	35	0.60	Contractive and dilative	Undrained	0.96
7	Silica	NAG	44.1	375	145	40	0.72	Contractive and dilative	Undrained	0.96
8	Silica	NAG	44.1	280	116	40	0.65	Contractive	Undrained	0.96

								and dilative		
9	Silica	NAG	44.2	196	93	40	0.57	Contractive and dilative	Undrained	0.96
10	Silica	Silica	NAG	44.3	360	144	40	Contractive and dilative	Undrained	0.96
11	Silica	NAG	48.2	196	100	45	0.54	Contractive and dilative	Undrained	0.97
12	Silica	NAG	50.5	196	120	48	0.60	Contractive and dilative	Undrained	0.96
13	Silica	NAG	52.3	196	130	56	0.57	Contractive and dilative	Undrained	0.96
14	Silica	NAG	53.3	196	137	52	0.54	Contractive and dilative	Undrained	0.97
15	Silica	NAG	42.5	196	81	36	0.55	**threshold pore pressure**	Undrained	0.96
16	Silica	NAG	55.2	290	134	40	0.70	**threshold pore pressure**	Undrained	0.96
17	Silica	NAG	56.2	196	154	70	0.49	Contractive and dilative	Undrained	0.96
18	Silica	NAG	60.0	196	168	65	0.58	Contractive and dilative	Undrained	0.96
19	Silica	NAG	62.1	196	196	84	0.57	Contractive and dilative	Undrained	0.97
20	Silica	NAG	64.5	196	200	84	0.58	Contractive and dilative	Undrained	0.96
21	Silica	NAG	74.1	196	243	100	0.59	Contractive and dilative	Undrained	0.97
22	Silica	ING	29.1	262	67	0	1.0	Purely contractive	Undrained	0.97
23	Silica	ING	29.2	202	54	5	0.91	Purely contractive	Undrained	0.96
24	Silica	ING	31.5	290	97	10	0.90	Purely contractive	Undrained	0.97
25	Silica	ING	44.3	196	81	32	0.60	Contractive and dilative	Undrained	0.96
26	Silica	ING	44.3	280	127	32	0.75	Contractive and dilative	Undrained	0.96
27	Silica	ING	44.1	374	161	32	0.80	Contractive and dilative	Undrained	0.96
28	Silica	ING	46.2	196	89	34	0.62	Contractive and dilative	Undrained	0.96
29	Silica	ING	53.3	196	145	55	0.62	Contractive and dilative	Undrained	0.96
30	Silica	ING	53.5	290	140	42	0.70	Contractive and dilative	Undrained	0.96
31	Silica	ING	56.5	196	165	56	0.66	Contractive and dilative	Undrained	0.96
32	Silica	ING	57.0	196	176	50	0.71	Contractive and dilative	Undrained	0.96
33	Silica	ING	60.2	196	188	62	0.67	Contractive	Undrained	0.96

								and dilative		
34	Silica	ING	62.2	196	199	70	0.64	Contractive and dilative	Undrained	0.97
35	Silica	ING	66.4	196	212	81	0.62	Contractive and dilative	Undrained	0.97
36	Silica	ING	66.5	290	235	70	0.70	Contractive and dilative	Undrained	0.97
37	Silica	ING	68.1	197	235	74	0.68	Contractive and dilative	Undrained	0.97
38	Silica	ING	74.3	196	246	86	0.65	Contractive and dilative	Undrained	0.96
39	Silica	ING	77.2	290	290	81	0.72	Contractive and dilative	Undrained	0.96
40	Silica	WG	29.5	250	80	13	0.84	Purely contractive	Undrained	0.96
41	Silica	WG	29.5	290	106	12	0.88	Purely contractive	Undrained	0.96
42	Silica	WG	29.5	196	60	12	0.80	Purely contractive	Undrained	0.96
43	Silica	WG	30.2	196	146	137		Large volume reduction	Drained	0.96
44	Silica	WG	39.5	105	47	13	0.72	**threshold pore pressure**	Undrained	0.97
45	Silica	WG	43.2	196	95	25	0.73	Contractive and dilative	Undrained	0.96
46	Silica	WG	44.1	235	122	23	0.81	Contractive and dilative	Undrained	0.96
47	Silica	WG	44.3	203	107	21	0.80	Contractive and dilative	Undrained	0.96
48	Silica	WG	44.3	366	198	23	0.88	Contractive and dilative	Undrained	0.96
49	Silica	WG	44.4	290	173	23	0.86	Contractive and dilative	Undrained	0.96
50	Silica	WG	45.1	196	115	30	0.74	Contractive and dilative	Undrained	0.97
51	Silica	WG	47.1	196	119	30	0.74	Contractive and dilative	Undrained	0.97
52	Silica	WG	48.5	196	128	31	0.75	Contractive and dilative	Undrained	0.96
53	Silica	WG	50.5	196	150	33	0.78	Contractive and dilative	Undrained	0.96
54	Silica	WG	53.2	200	166	35	0.79	Contractive and dilative	Undrained	0.96
55	Silica	WG	55.3	198	198	37	0.81	Contractive and dilative	Undrained	0.96
56	Silica	WG	57.1	196	209	29	0.81	Contractive and dilative	Undrained	0.96
57	Silica	WG	57.3	200	215	24	0.88	Contractive and dilative	Undrained	0.96
58	Silica	WG	64.1	198	230	57	0.75	Contractive	Undrained	0.96

								and dilative		
59	Silica	WG	66.5	196	238	52	0.78	Contractive and dilative	Undrained	0.97
60	Silica	WG	70.2	196	257	54	0.79	Contractive and dilative	Undrained	0.96
61	Silica	WG	72.1	200	287	56	0.80	Contractive and dilative	Undrained	0.96
62	Silica	WG	58.2	196	217	35	0.83	Contractive and dilative	Undrained	0.96
63	Silica	GAG	42.1	196	81	17	0.79	**threshold pore pressure**	Undrained	0.96
64	Silica	GAG	42.1	196	81	17	0.79	Contractive and dilative	Undrained	0.96
65	Silica	GAG	57.2	196	104	13	0.87	Contractive and dilative	Undrained	0.96
66	Silica	GAG	60.1	196	125	23	0.78	Contractive and dilative	Undrained	0.96
67	Silica	GAG	66.5	196	186	20	0.89	Contractive and dilative	Undrained	0.96
68	Silica	GAG	69.1	229	193	36	0.81	Contractive and dilative	Undrained	0.97
69	Silica	GAG	74.1	196	196	22	0.90	Contractive and dilative	Undrained	0.97
70	Silica	GAG	70.3	200	207	29	0.86	Contractive and dilative	Undrained	0.97
71	Silica	GAG	83.3	200	242	35	0.86	Contractive and dilative	Undrained	0.97
72	Osaka	Natural grading	40.8	105	45	17	0.62	**threshold pore pressure**	Undrained	0.96
73	Osaka	Natural grading	43.3	196	83	22	0.73	**threshold pore pressure**	Undrained	0.97
74	Osaka	Natural grading	56.5	290	123	30	0.76	**threshold pore pressure**	Undrained	0.96
75	Osaka	Natural grading	60.3	374	166	30	0.82	**threshold pore pressure**	Undrained	0.98

2.3 Sample preparation and testing procedure

Oven dried specimens having the desired uniformity coefficients were placed in the shear box by moist tamping method, a method chosen to decrease the possibility of particle segregation. Thereafter, test specimens were saturated with water. To achieve a B_D value of at least 0.95, which was the minimum acceptable value used in this study, carbon dioxide was first introduced into the samples, at a slow rate, for at least one hour, after which, de-aired water was introduced, again, at a slow rate, to ensure adequate saturation. B_D parameter – the ratio of change in pore pressure and change in normal stress ($\Delta u/\Delta\sigma$) over a specified period of time – was the standard parameter used in assessing the degree of saturation of the test samples (Sassa 1988).

Obtaining the B_D parameter involved a simple process of consolidating the samples at 49 kPa normal stress in drained condition, and increasing the normal stress to 98 kPa in undrained condition when a constant value of vertical displacement signaled the end of the consolidation process which lasts an average of 60 minutes. The resultant increase in pore pressure (from zero to a certain monitored value), Δu, divided by the corresponding increase in normal stress (from 49 kPa to 98 kPa), $\Delta\sigma$, is the B_D parameter. Specimens were considered fully saturated if the B_D was equal to or greater than 0.95. The objectives of the present research did not permit over-consolidation of specimens. In the light of this, all samples were normally consolidated and thereafter, shearing was performed by incremental loading of shear stress at the rate of 0.98 kPa/sec.

3. Test results

The test results are summarized in Table 2 .Two main behaviors were observed. Specimens in loose state responded to undrained shearing in a purely contractive manner while specimens in medium-dense to dense states responded in a dilative way. Grading affected the behaviors of the specimens as presented below.

3.1. Purely contractive behavior

Narrowly graded, intermediately graded and well-graded specimens in loose state all responded to undrained shearing in a purely contractive manner characterized by the attainment of peak strengths at small shear displacements and the rapid reduction of those strengths to very low values at steady state. This type of behavior has been referred to in this paper as mass-liquefaction (flow-liquefaction) in contrast to the sliding surface liquefaction introduced by Sassa (1996). Although all NAG, ING, and WG specimens in loose state exhibited purely contractive behaviors, there were still some obvious differences, arising from their differences in grading. These differences are expounded below.

A narrowly graded specimen consolidated at 220 kPa to a relative density of 29.5 % is presented in Fig. 3. It may be seen that soon after reaching a peak resistance of 49 kPa at 1.6 mm (point marked P), it underwent rapid loss of strength that saw its resistance decrease to about zero (point marked S) and remained so until shearing was terminated at 10 m shear displacement. By having its shear strength reduced to zero after failure, the specimen acquired a brittleness index of 1.0. The entire behaviour leading to zero or almost zero steady state strength has been termed complete liquefaction in this paper.

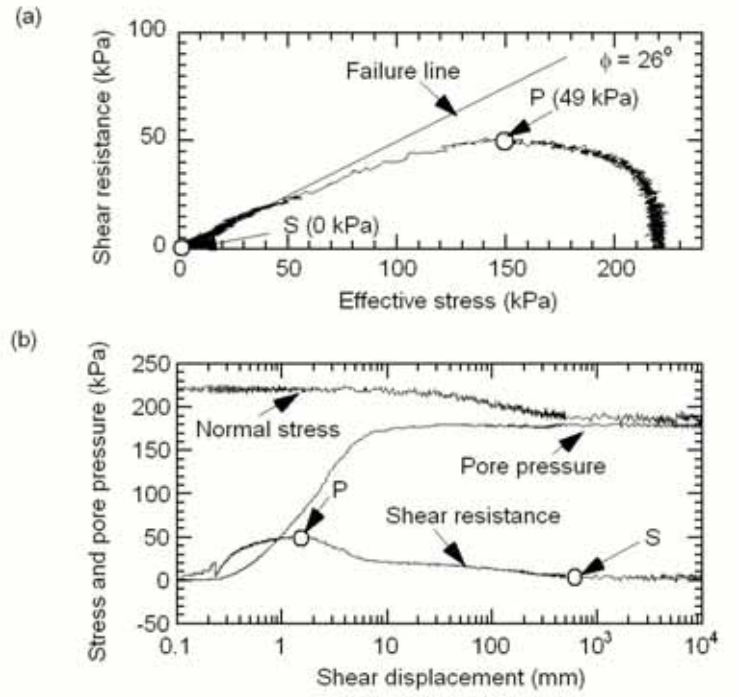

Fig. 3 Typical Complete liquefaction behavior of NAG specimen Dr = 29.5 %

A similar test on an intermediately graded specimen (ING) yielded a different result (Fig. 4). A specimen consolidated at 202 kPa and having a relative density of 29.2 % was loaded by incremental addition of shear stress at the rate of 0.98 kPa/sec. It could be observed that after the specimen reached its peak strength of 54 kPa at about 1 mm (point P in Fig 3b) its shear resistance suffered severe and rapid reduction until the resistance became 5 kPa at around 10 mm and remained so until the test was terminated at 1 m of shear displacement. For considerably losing its shear resistance, the specimen had a high brittleness index of 0.91. The corresponding pore pressure increase, within the period under consideration, is noted. By 10 mm shear displacement pore pressure had risen to a value as high as 187 kPa, which was about 93 % of the normal stress.

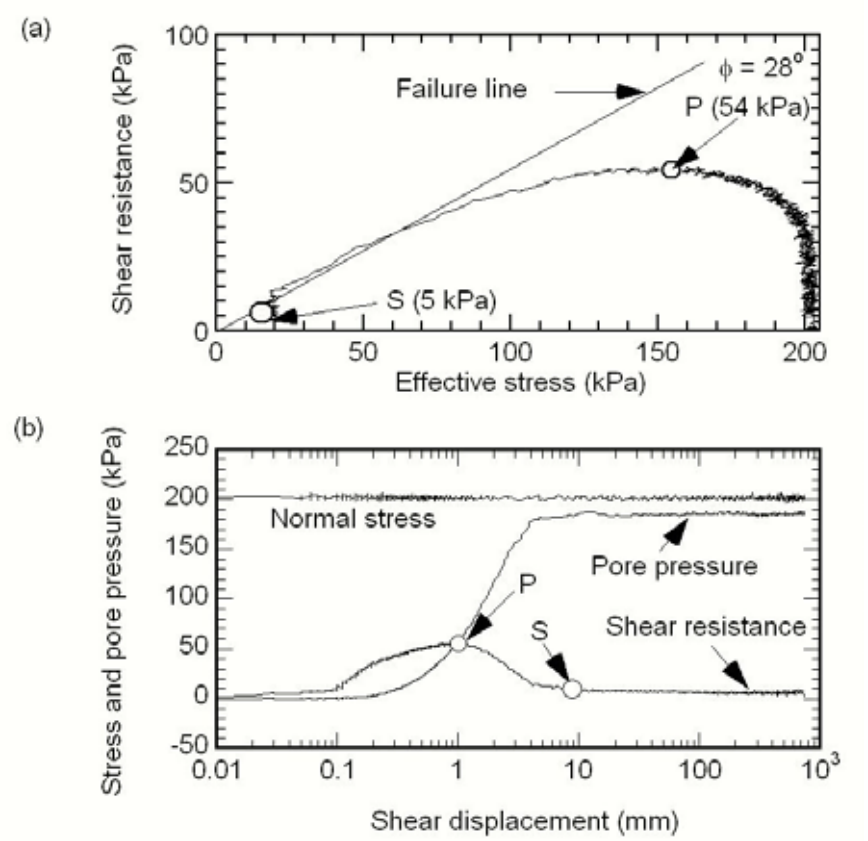

Fig. 4 Undrained response of ING specimen Dr = 29.2 %

The behaviour of a well graded specimen consolidated at 196 kPa to a relative density of 29. 5% is presented in Fig. 5. It may be seen from Fig. 5a that after the specimen reached peak shear strength of 60 kPa, the sample appeared to have collapsed and underwent rapid loss of resistance until it attained its steady state strength of about 12 kPa (point S bin Fig. 5) where deformation continued without further changes to both shear resistance and effective stress. As a result, the specimen acquired a high brittleness index of 0.80. Careful examination of the pore pressure changes within the period under consideration show that the specimen mobilized its peak strength (P) at 1.77 mm displacement; at which point pore pressure had risen to 60 kPa. Soon afterwards, the pore pressure rose further to 177. kPa (at point M in Fig. 5b), which amounted to a pore pressure ratio of 0.88, and remained constant until the experiment was terminated at 10 m. The sample is thought to have liquefied because of the high excess pore pressure built-up and the consequent low effective stress attained in the process.

Similar tests on loose specimens were carried out at different initial normal stresses. The brittleness index ($I_B = \frac{\tau_p - \tau_{ss}}{\tau_p}$)of the specimens plotted against normal stress is shown in Fig. 6. It may be seen from the

Figure that at every normal stress, the brittleness index of the narrowly graded specimens is unity. Among the specimens, the well graded specimens have the lowest brittleness index. Similarly, the plot of normalized peak and steady state strengths against uniformity coefficient (Fig. 7) show that the higher the uniformity coefficient, the higher the peak and steady state strengths. While the steady state strengths of the three narrowly graded specimens all plotted on zero, those of the well graded specimens plotted on values greater than zero. Of the three intermediately graded specimens, one liquefied completely and as a result its steady state strength plots on zero. Two others did not undergo complete liquefaction; Fig. 7 shows that their steady state strengths plot on values greater than zero.

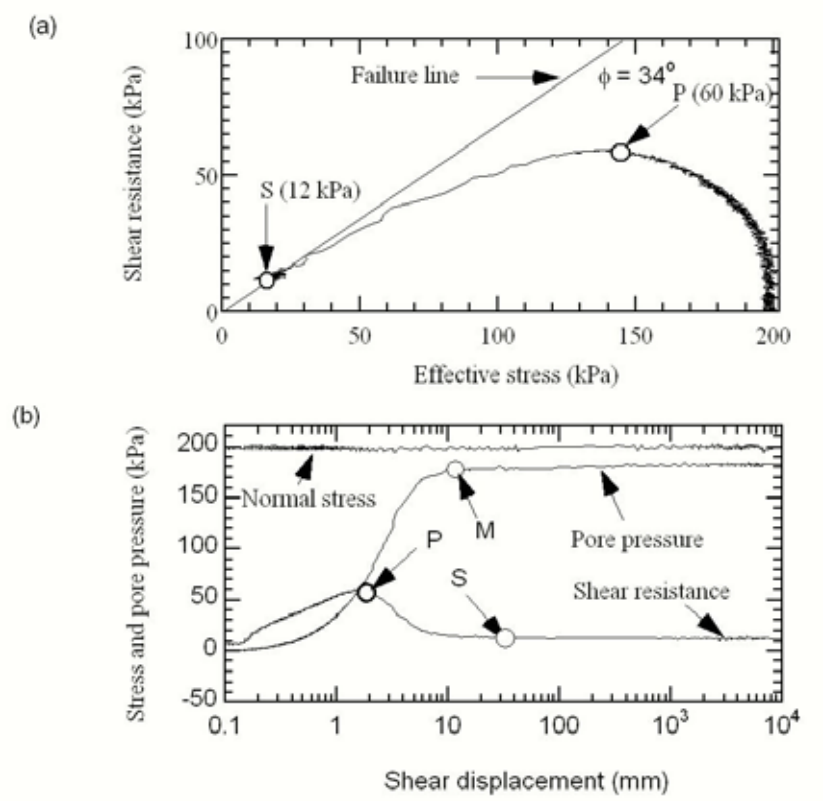

Fig. 5 Undrained response of WG specimen Dr = 29.5 %

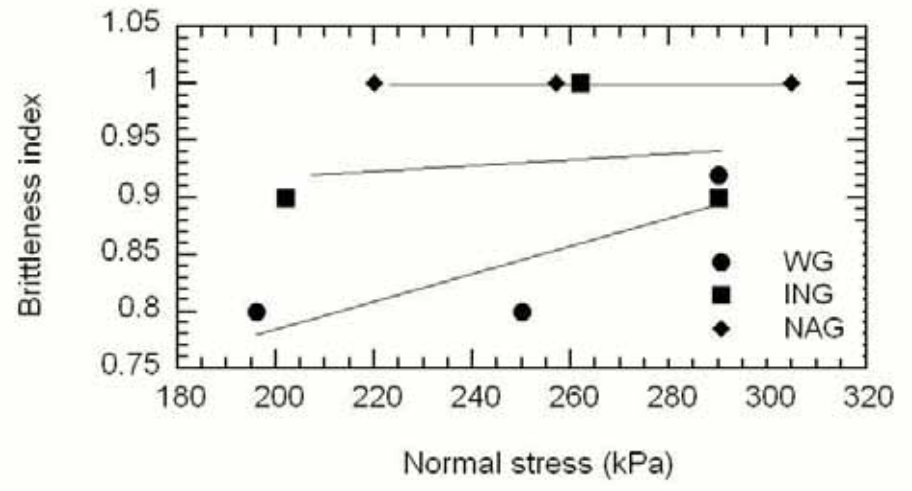

Fig. 6 The brittleness index of the loose specimens plotted against normal stress

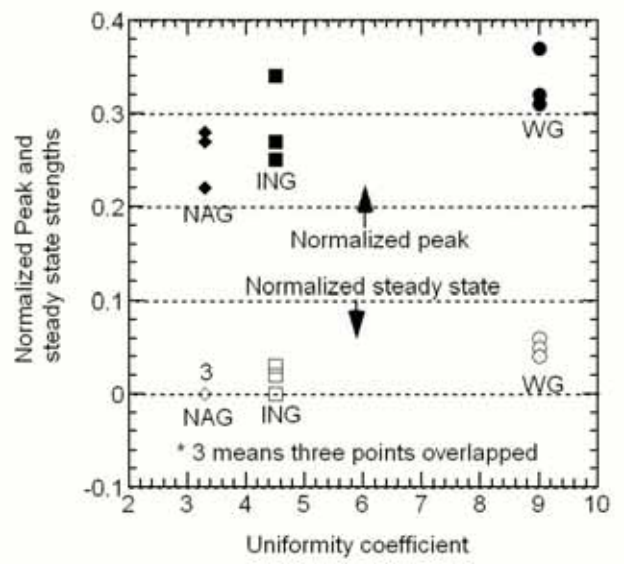

Fig. 7 Relationship between uniformity coefficient and normalized strengths of loose specimens

To investigate the volume changes associated with these loose sands, two drained tests were performed. Fig. 8 is the result of a drained test on a narrowly graded specimen. Close examination of the result of the test (Fig.8) of a specimen consolidated at 200 kPa to *Dr* = 32.2 %, shows that soon after shearing commenced, the specimen first suffered considerable volume reduction until around 30 mm from which point the sample underwent less volume reduction until the test was terminated at 10 m. Volume reduction before the peak (point P in Fig. 8) where the sliding surface is formed (Wafid et al., 2004) will be caused by the collapse of metastable structure. The major cause of volume reduction after the peak might be grain crushing along the sliding surface, especially after a certain shearing point (point M in Fig. 8), where the effect of collapse might not exist anymore.

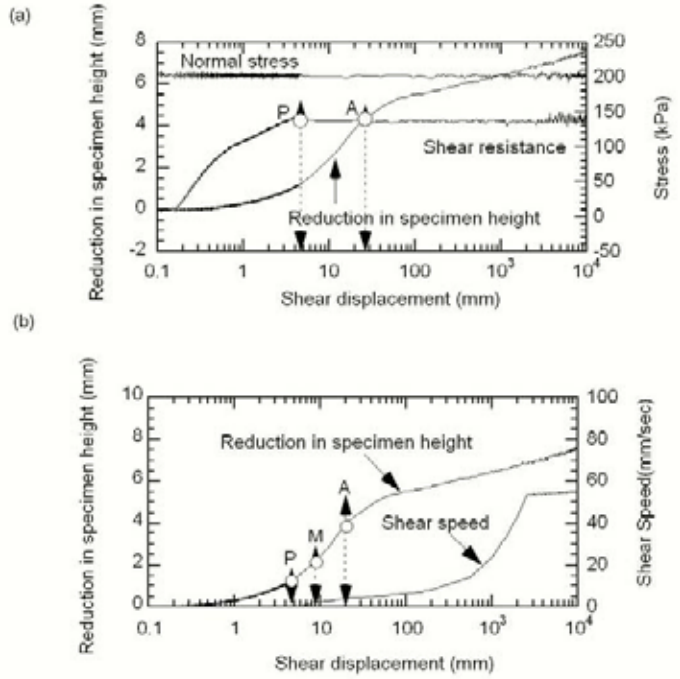

Fig. 8 Drained response of NAG specimen. Dr = 32.2 %

A similar drained test performed on a well graded specimen consolidated at 196 kPa to *Dr* = 30.2 % (Fig. 9) shows that soon after shearing commenced, the sample first suffered considerable volume reduction until about 30 mm from which point the sample underwent little volume reduction until the test was terminated at 10 m. A comparison of the two drained tests is attempted in Fig. 10. The Figure shows that the volume reduction in the NAG specimen is slightly higher than that of the WG specimen. It is difficult to imply that that the greater volume reduction in NAG specimen is due to grading from only two drained tests.

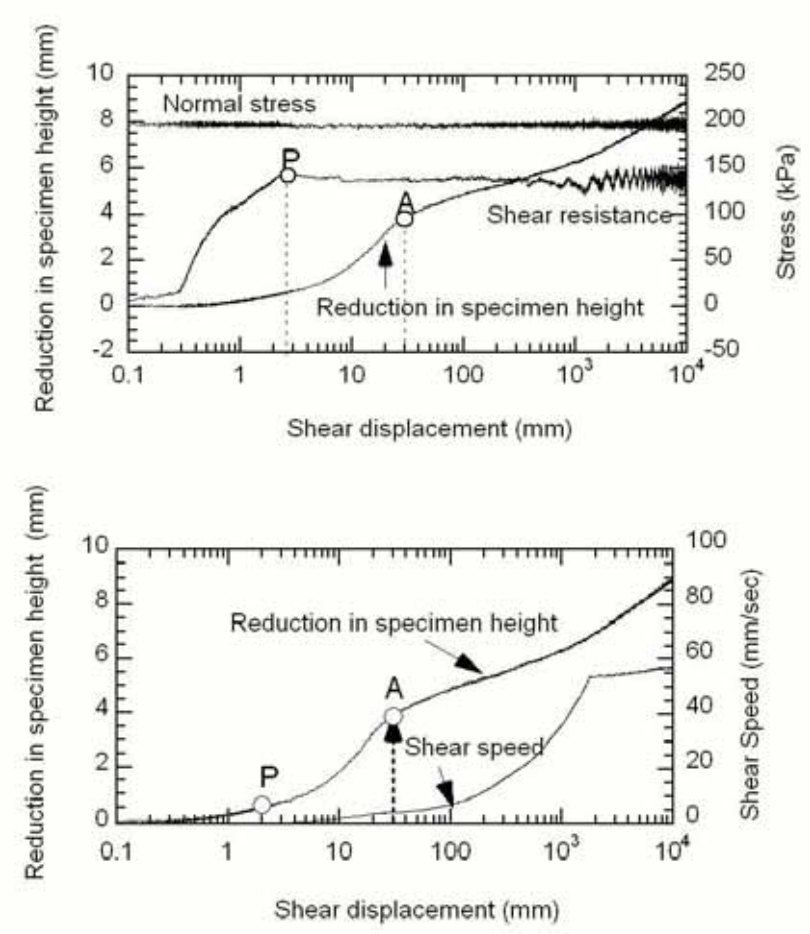

Fig. 9 Drained response of WG specimen. Dr = 30.2 %

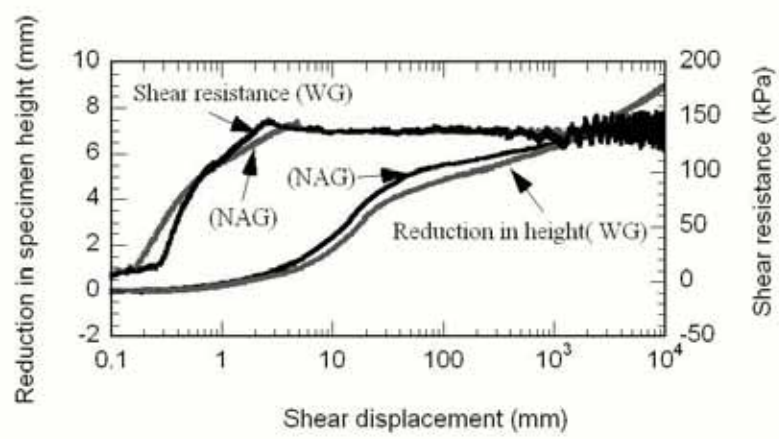

Fig. 10 Drained behavior of WG and NAG specimens compared

3.1.1 Influence of gradation on the collapse line

One of the objectives of the present study was to investigate the sensitivity of the position and slope of the collapse line to changes in uniformity coefficient in hopes of adding to what is already known about conditions necessary for liquefaction. Although research on the mechanism(s) controlling the initiation of liquefaction failure in loose, saturated, sands has been going on for decades now, not much is known about the conditions necessary for liquefaction and the characteristics of liquefiable materials.

Attempts at identifying points in a stress space diagram which could trigger flow liquefaction in granular materials have led to a number of beneficial concepts including the collapse line and the critical stress ratio concepts. Sladen et al. (1985) while proposing the concept of collapse surface observed that the peak strengths of a soil consolidated to the same void ratio at different initial confining stresses lay on a straight line passing through the steady-state point. On the basis of some strong evidences, they reported that the position of the line was a function of only void ratio. While Ishihara (1993) and Sasitharan et al. (1993, 1994) have made similar observations, there are other works where the position of the collapse line has been represented differently. Vaid and Chern, (1985) and Alarcon-Guzman, Leonards and Chemeau (1988) have reported that the critical stress ratio (CSR) line, a line which passes through the peak strengths of a soil at different initial confining stresses and which may be extrapolated through the origin of a given stress diagram was independent of initial void ratio. In the same vein, Vasquez-Herrera et al. (1988) and Negussey et al. (1988), Vaid et al. (1990), Konrad (1993), have not only reported the existence of the line which passes through peak strengths through the origin but have shown that any attempt by effective stress paths to cross this line could trigger flow liquefaction. A similar investigation by Mohamad and Dobry (1986) found that the stress ratio at which flow failure is triggered was independent of relative density and, as a consequence, that the critical stress ratio line or the collapse line extrapolates through the origin of a stress space diagram.

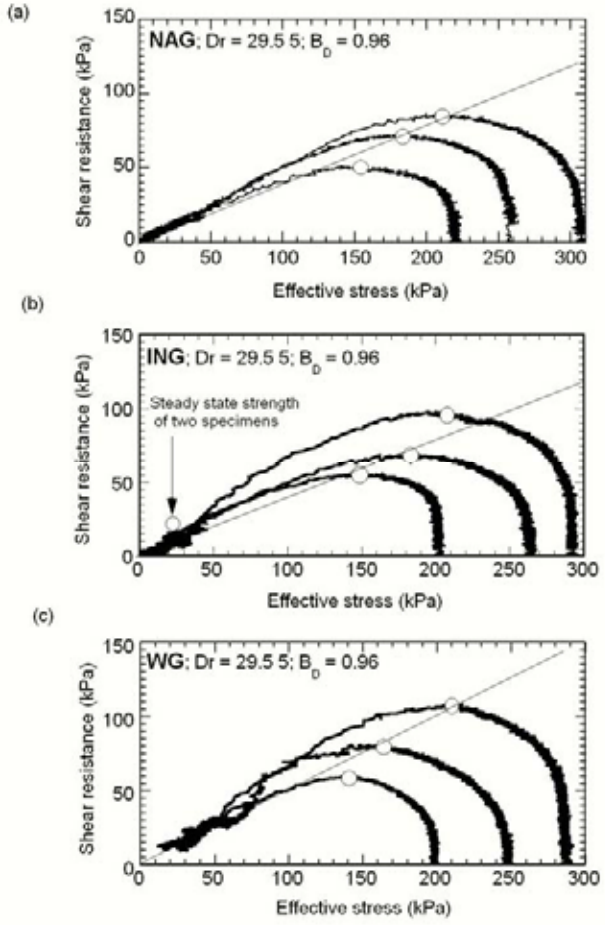

Fig. 11 Influence of gradation on the line collapse line

Figs. 11 a, b, c show that while the slope of a line that tends to pass through the peaks to the origin of the shear resistance-effective stress space diagrams appear to be greater in the well graded specimens (Fig. 11 c) than in the Intermediately and narrowly graded specimens (Fig. 11 a, b), there is no strong indication that grading affects the position of the line. It may be seen that the position of the line is essentially the same in the well-graded, intermediately graded, and narrowly graded materials with all the materials characterized by a collapse line extrapolating through the origin through the peak points.

4.2 Dilative behavior

4.2.1 Specimens in medium-dense state

Typical result in which dilative behaviour was observed in narrowly graded specimens is shown in Fig.12. It could be seen from Fig. 12, which represents the behaviour of a specimen with a relative density of 44.2 %, that the mechanical behaviour of a medium-dense narrowly graded specimen is clearly different from that of a narrowly graded specimen in loose state. Whereas narrowly graded specimens in loose state suffered complete liquefaction (because their steady state strengths were zero) the specimens in medium-dense state has relatively high steady state strength.

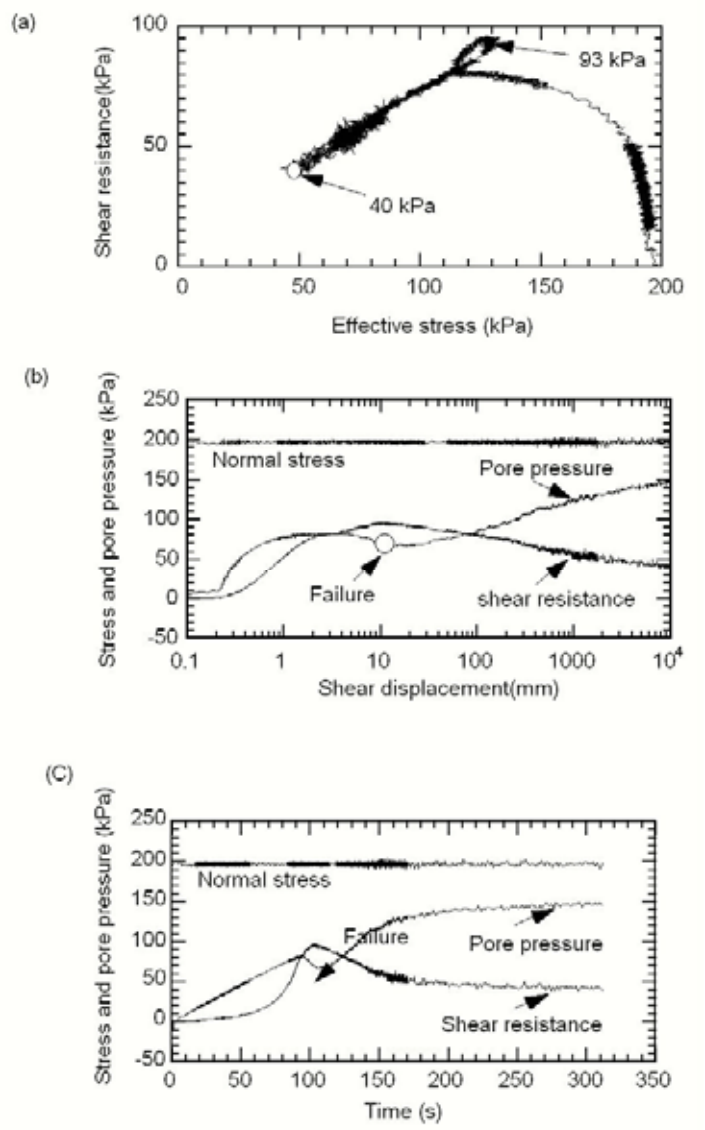

Fig. 12 Shear behavior of medium-dense NAG specimen. Dr = 44.2 %

The specimen under consideration attained peak resistance of 93 kPa after barely dilating, and subsequently mobilized steady-state strength of about 40 kPa after failure (Fig. 12a, b). Soon after failure, precisely at 10 mm corresponding to 102 seconds, the pore pressure had risen to 136 kPa, which was about 68% of the total normal stress (Fig. 12c). The peak strength may be relatively low, as we shall soon see, but its steady state strength is certainly high. Why such a reversal of fortune in medium-dense state? Why would a sample type that is prone to complete liquefaction in loose state turn around to have high steady state strength in medium-dense state? While seeking answer, tests were conducted at different normal stresses at the same relative density. Fig. 13 shows that although the narrowly graded specimens may have different peak strengths, their steady state strengths were always around 40 kPa.

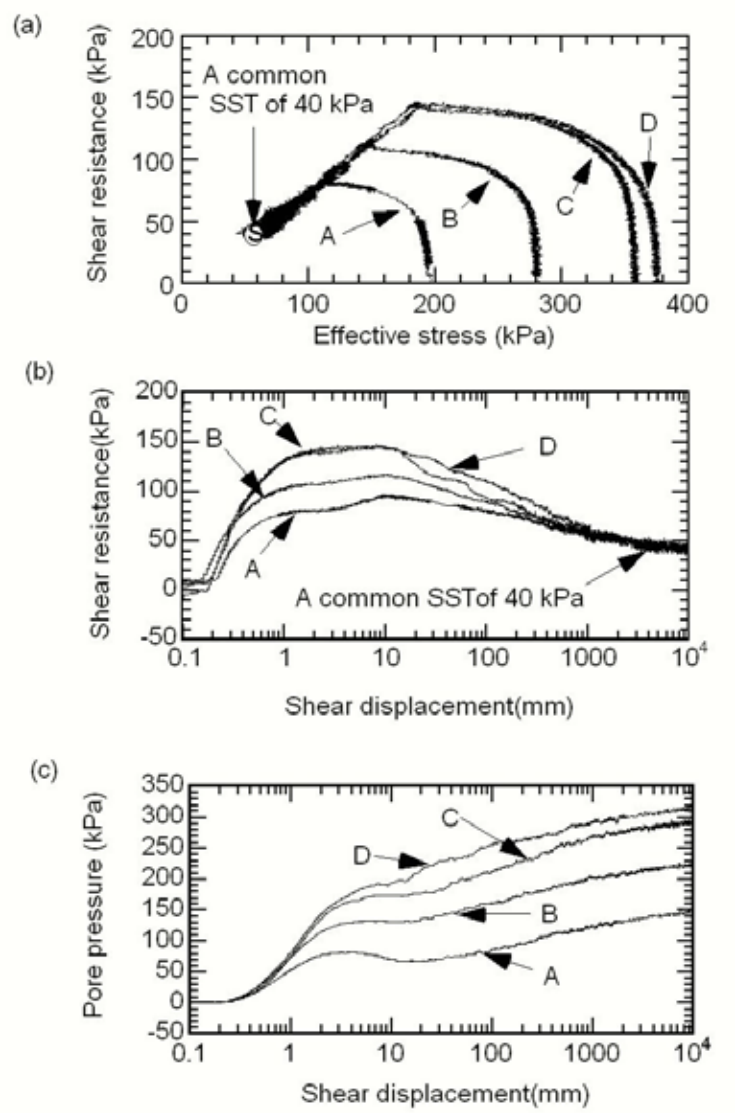

Fig. 13 Undrained response of medium-dense NAG specimens at about Dr = 44.2% at different effective normal stress

A specimen of the intermediately graded samples, having a relative density of 44.3% is shown in Fig. 14 It attained peak resistance of 81 kPa after dilation. Upon failure, its strength was reduced to a steady state value of about 32 kPa after 10 m of shear displacement. Tests were then conducted at different normal stress levels on specimens having the same relative density. Fig. 15 shows that although the normal stresses are different,

they all reached the same steady state strengths of about 32 kPa. It may be noticed from Figs 13 and 15 that with the exception of the specimen at a normal stress of 196 kPa, the peak strengths of the intermediately graded specimens are higher than those of the narrowly graded ones. But, the steady state strengths of the intermediately graded specimens are lower than those of the narrowly graded ones.

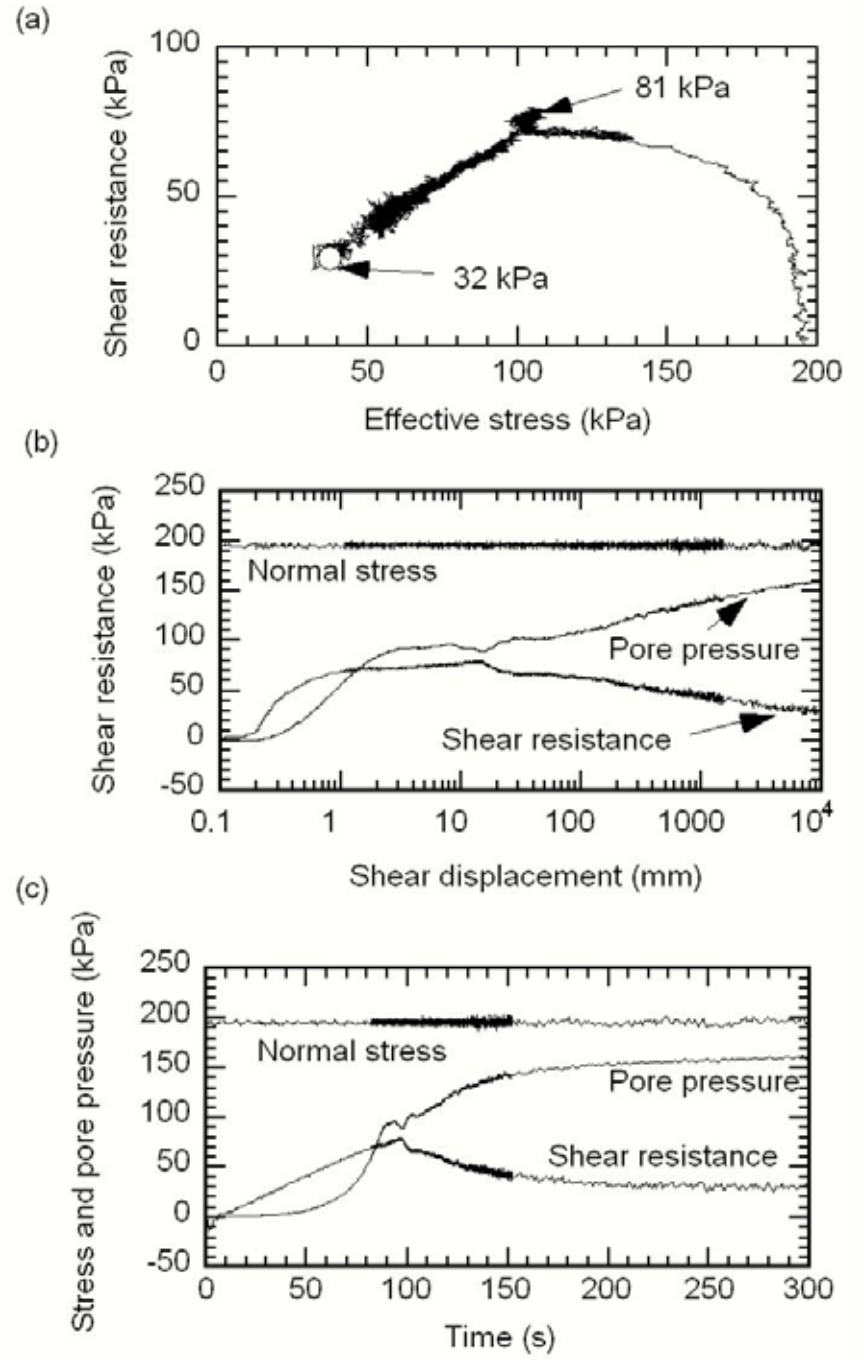

Fig. 14 Shear behavior of medium-dense ING specimen. Dr = 44.3 %

A stress path of a well-graded specimen, under effective normal stress of 202 kPa, which had a relative density of 44.3 %, is shown in Fig. 16a. Once the stress path reached point PT, it dilated and attained peak

strength of 107 kPa at 11 mm (shear displacement), after which, the specimen failed and had its resistance quickly reduced to a residual value of 23 kPa after 10 m of displacement. The rapid reduction of shear resistance after failure observed in the specimen under consideration might have resulted from particle crushing at the shear zone, and the consequent high pore pressure increase. The rapidity of pore pressure increase was such that at about 5 m shear displacement corresponding to 130 seconds, the pore pressure had risen to 177 kPa, which was about 88.5% of the normal stress imposed on the specimen (Fig. 16 b, c). The mode of behaviour after failure whereby the resistance of the specimen was rapidly reduced to a small residual value is especially typical of the WG specimens containing larger particle sizes. Tests were conducted at different normal stresses on specimens having the same relative density Fig. 17 shows that the WG at different normal stresses have different peak strengths (which are higher than those of both the ING and NAG specimens) but reach the same steady state strengths of about 23 kPa (which are lower than both the ING and NAG). It should be recalled that in loose state, well graded specimens had higher steady state strength. In medium-dense state however, the behaviour is reversed.

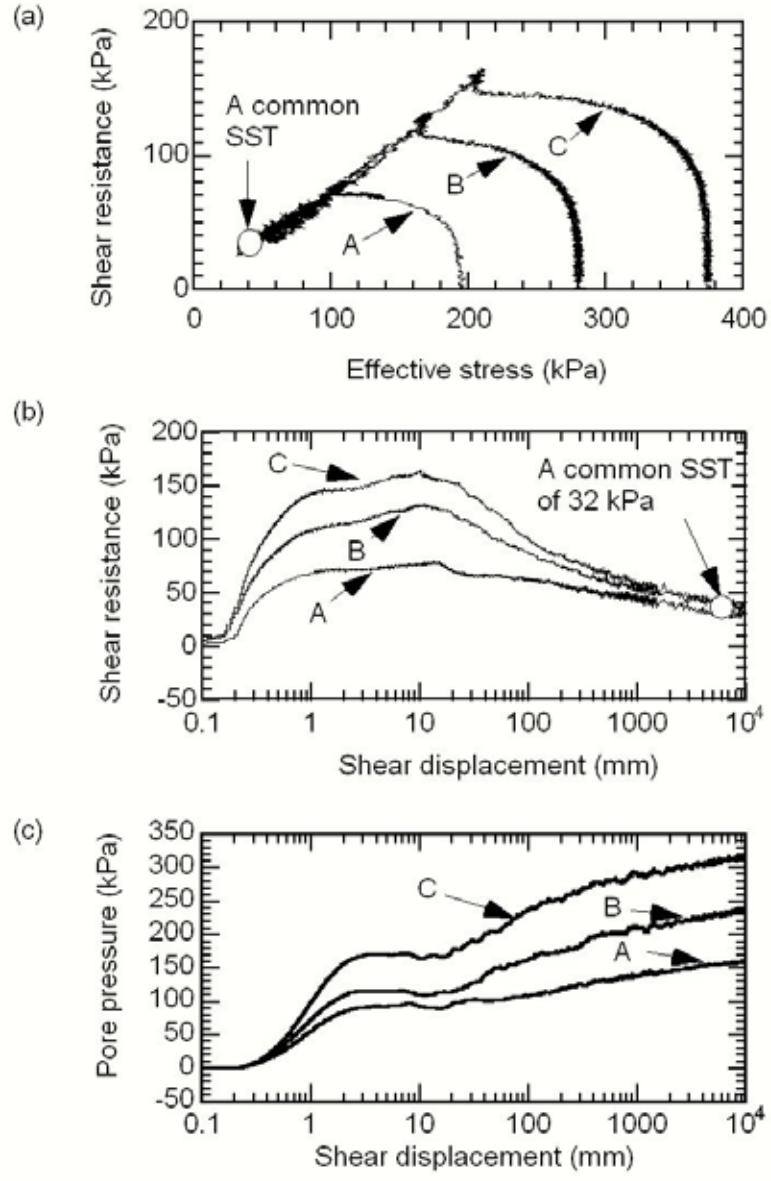

Fig. 15 Undrained response of medium dense ING specimens at Dr = 44% at different confining stress

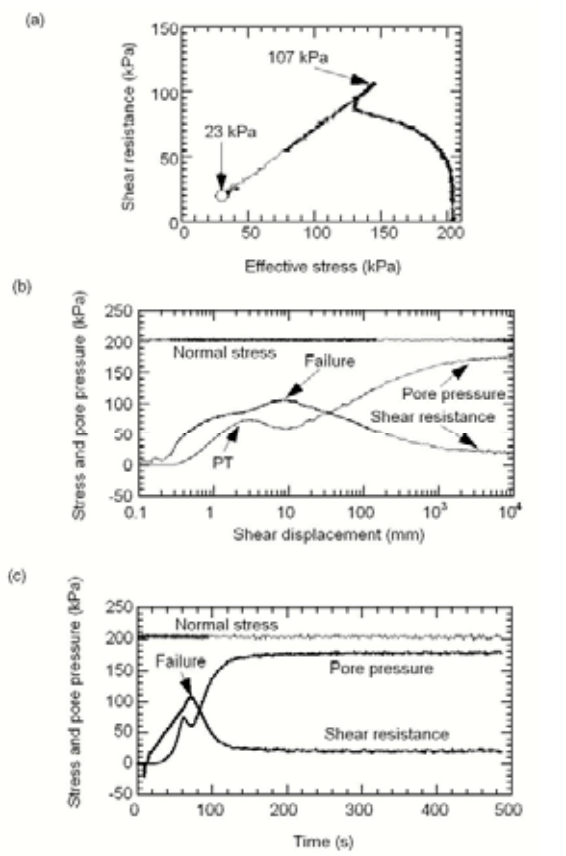

Fig. 16 Shear behavior of medium-dense WG specimen (a)stress path Dr = 44.3 %

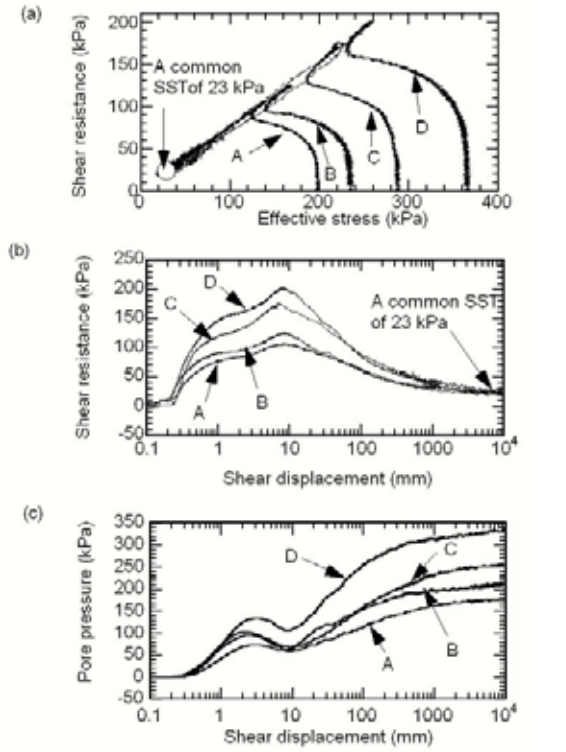

Fig. 17 Undrained response of medium-dense WG specimens at Dr = 44.3% different effective normal stress

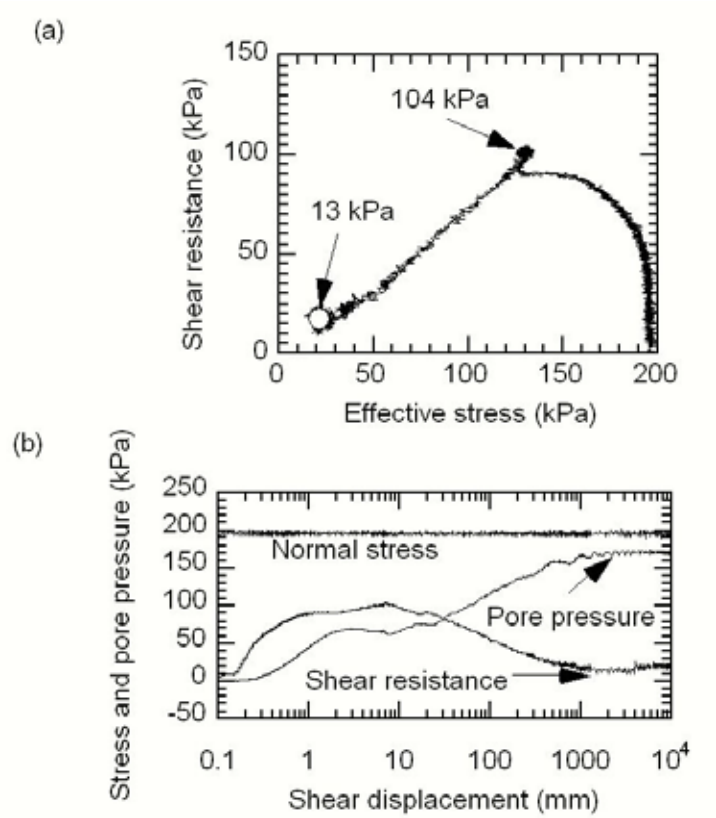

Fig. 18 Shear behavior of medium-dense GAG specimen Dr = 57.2 %

The result of a gap graded specimen is shown in Fig. 18. It may be observed from the Figure that even at a relative density of 57.2 %, the gap graded specimen has very low steady state strength.

3.2.2 Specimens in dense state

The specimens in dense states appear to follow the same pattern of behaviour observed for medium-dense specimens. Fig. 19 shows that a narrowly graded (NAG) specimen consolidated at 196 kPa to a relative density of 74.1 %, contracted first and then dilated to peak strength of 243 kPa. After failure, its strength was reduced to 100 kPa at 10 m of shear displacement. An intermediately graded (ING) specimen at the same initial conditions attained peak strength of 233 kPa and steady state strength of 86 kPa (Fig. 20). A well graded (WG) specimen having Dr = 66.5 %3(Fig. 21) attained peak strength of 235 kPa and a steady state of 52 kPa. A gap graded specimen having Dr = 74.1 % has a peak strength of 196 kPa and steady state strength of 22 kPa (Fig. 22).

The results of the tests conducted on medium-dense and dense specimens are summarized in Fig. 23. The Figure, which contains only data acquired at an initial effective normal stress of about 200 kPa, shows that there are significant differences between their peaks in medium and dense states; the differences appear to widen as density increases. This may imply that the effect of grading on their peak strengths may be significant for only densities above a certain limit. The proximity of peak strengths of narrowly and intermediately graded specimens may find explanation in the closeness of their uniformity coefficients. While the peak strengths of dense intermediately graded specimens approach those of dense narrowly graded ones, the well-graded specimens at the same state move away. On the basis of the results presented in Fig. 23 (a) it is evident that at the same relative density and effective normal stress, well-graded specimens have higher peak shear strengths than the other specimens.

In what may amount to a reversal of behavior, well graded specimens, which contain some quantity of relatively large particle sizes, can be observed in Fig. 23b to have lower steady state strength than the

intermediately and narrowly graded which are composed of only finer sizes. Test results seem to indicate that the degree of crushing or breakage is heavily dependent on the size of particles of which the specimens are composed (Marsal, 1967; Lee and Farhoomand, 1967; Hardin, 1985; Lade and Yamamuro, 1996; Wang, 1998).

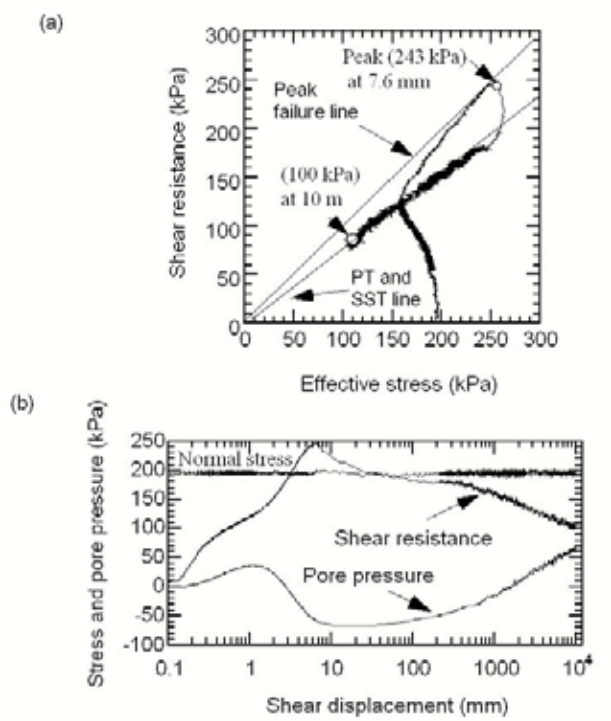

Fig. 19 Shear behavior of dense NAG specimen Dr = 74.1 %

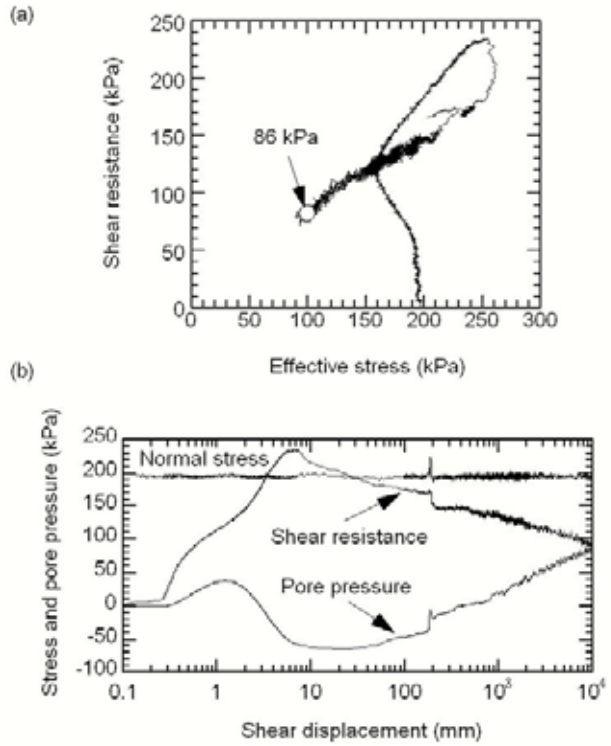

Fig. 20 Shear behavior of dense ING specimen Dr = 74.3 %

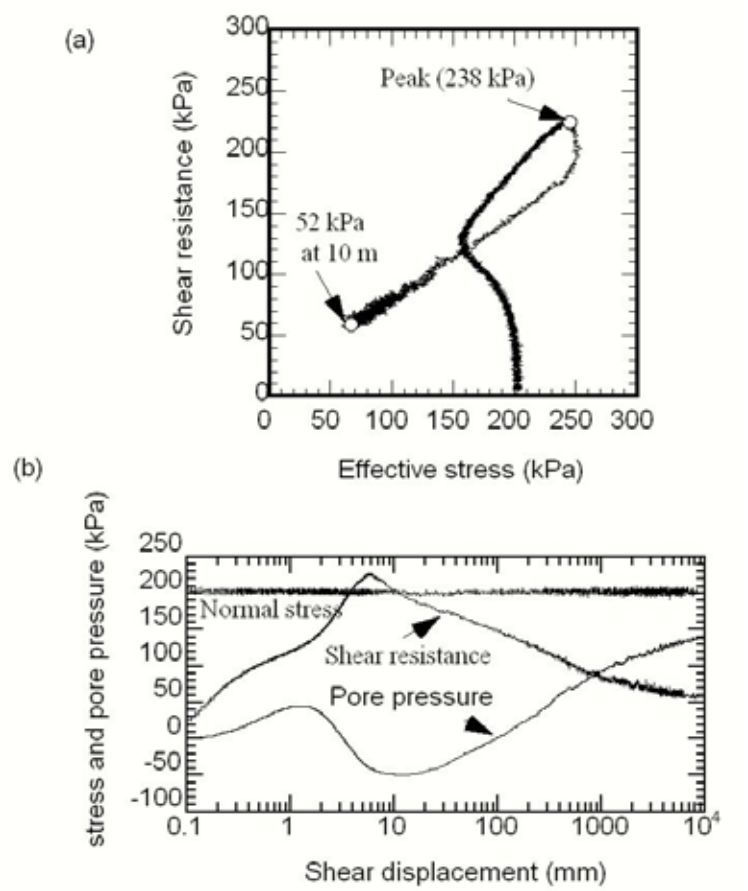

Fig. 21 Shear behavior of dense WG specimen Dr = 66.5 %

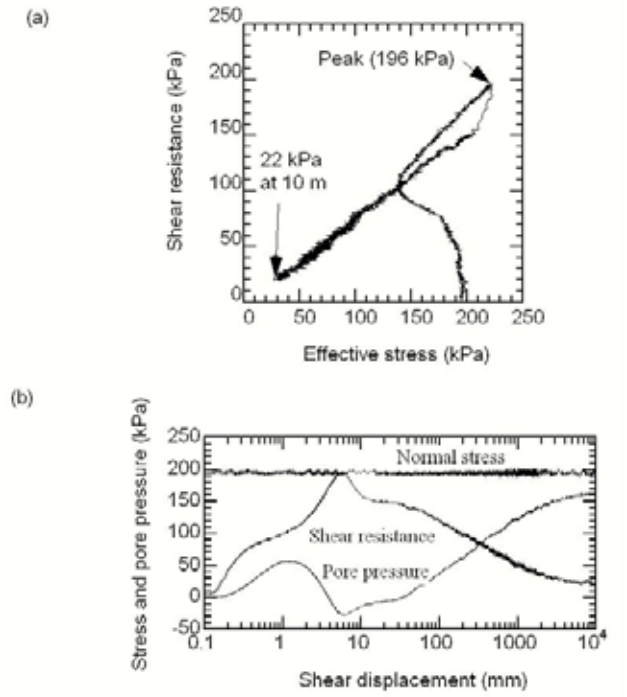

Fig. 22 Shear behavior of dense GAG specimen Dr = 74.1 %

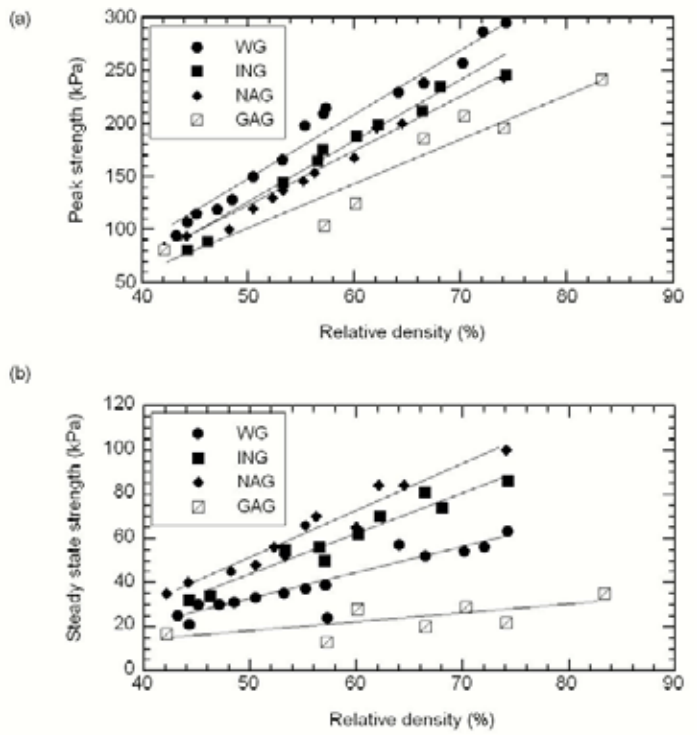

Fig. 23 The relationship between relative density and shear strength (all specimens at effective normal stress of about 200 kPa)

Analyses have shown that, at the same initial state, well-graded sands have higher peak strengths than poorly graded ones, the difference increasing as the sands become denser. In an interesting reversal however, it has been shown that in medium and dense states, the steady state strengths of well-graded materials are lower than those of the ING and NAG, the difference, again, increasing with relative density (Igwe et al., 2005b) From the view point of public safety, the better graded soils in medium and dense states are more dangerous after failure because of their potential for large post-failure travel distances than the NAG, and ING specimens.. Theses results may aid engineers when they make decisions on what soils to use for civil engineering works; or scientists when they assess slope stability, investigate landslides, or plan prevention methods (Igwe et al., 2004a; 2004b; 2005a; 2005b).

4.0 Undrained response at a fixed effective normal stress

4.1 When pore pressure parameter $A_{Df} = 1.0$ ($A_{Df} = \frac{\Delta u_f}{\Delta \tau_f}$)

One of the major outcomes of the present study was the observation that by carefully altering the relative density of a material of any grading at a given effective confining stress, that material could become dilative or purely contractive in behavior. Dilative specimens have distinct phase transformation and peak stress states (as may be seen in Fig. 19a and other Figures representing medium to dense specimens). Purely contractive specimens are defined by only distinct Mohr Coulomb failure line (as seen in Fig. 3a and all other Figures representing loose specimens).

However, in between these two fundamental behaviors is a relative density at which the phase transformation and peak stress states tend to coincide because excess pore pressure and shear resistance became equal at the phase transformation point and not only remained equal but essentially constant until failure, thus establishing a threshold state at a small shear displacement (Fig. 24a, b). The equality and subsequent constancy of excess pore pressure and shear resistance, which started at about 2 mm and continued until the sample failed at 10 mm

shear displacement, are typical characteristics of specimens that tend to form a transition region by demarcating the contractive from the dilative behavior. The specimen under consideration in Fig. 24 is normally consolidated silica sand (GAG) specimen with a relative density of 42.1 %.

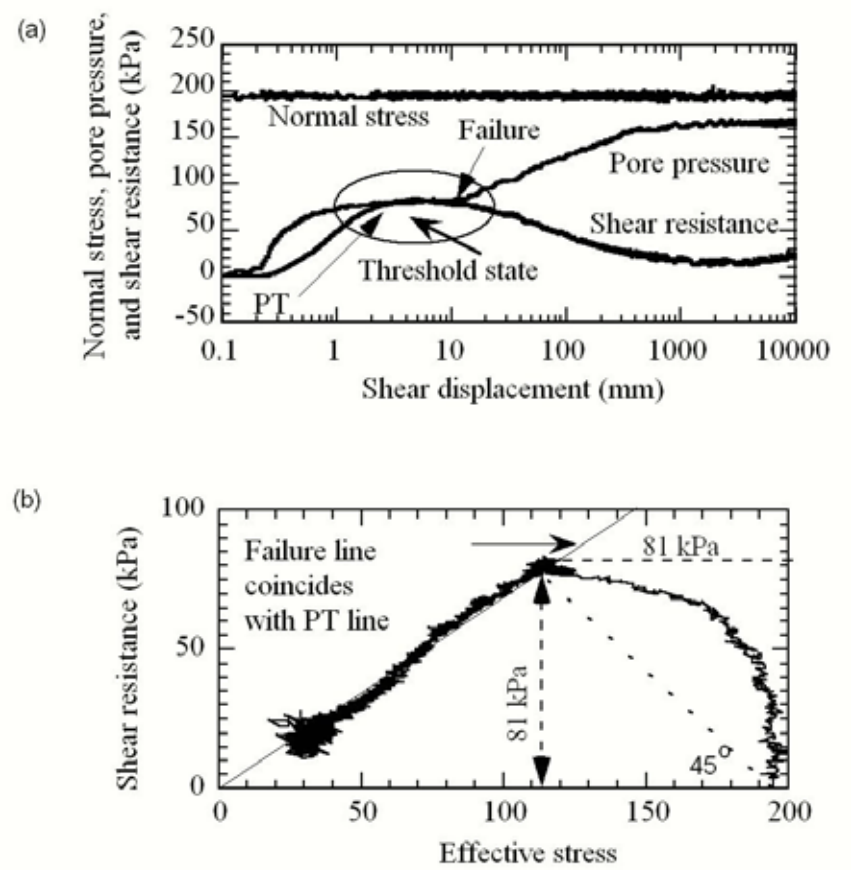

Fig. 24 Typical behavior of a sandy specimen when the ratio of change in shear resistance at failure and the corresponding change in effective stress is unity Dr = 42.1%;

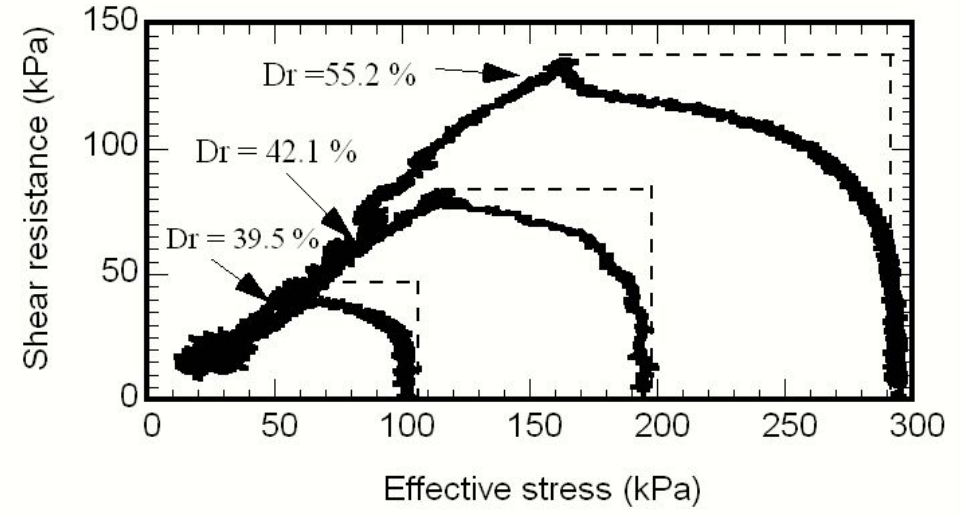

Fig. 25 Threshold stress paths of silica sands at different effective normal stresses

Further investigations at different effective normal stresses show that the behavior was not restricted to gap graded (GAG) sands as may be seen in Fig. 25 which displays the stress paths of a WG specimen consolidated at 105 kPa to a relative density of 39.5 %, a GAG specimen consolidated at 196 kPa to a relative density of 42.1 %, and a NAG consolidated at 290 kPa to a relative density of 55.2 %.

A sandy soil, known as Osaka Formation, from a landslide site was then studied under the same initial conditions as the silica sands. Results of the study show that the phenomenon of $\Delta u/\Delta\tau = 1$ at failure also occurred in the natural soils (Fig. 26). It may be seen from Figs 25 and 26 that. the higher the normal stress, the greater the relative density at which this threshold state is observed.

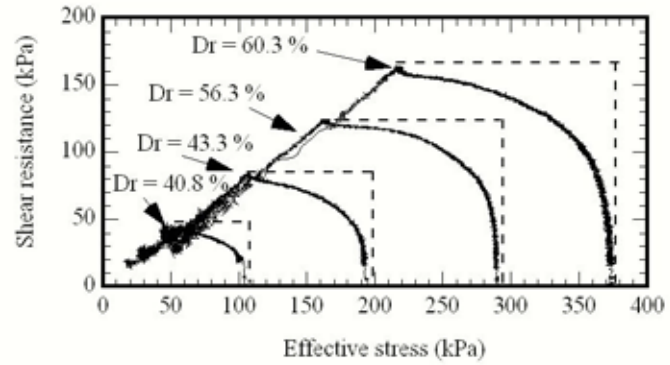

Fig. 26 Threshold stress paths of Osaka FM specimens at different effective normal stresses

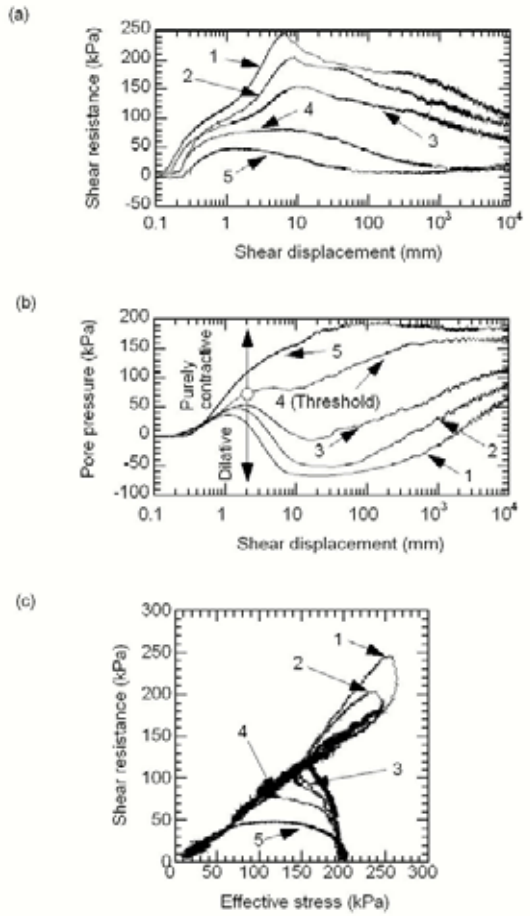

Fig. 27 The effect of relative density on the response of the NAG sands and the position of the threshold state
(1) Dr = 74.3 %, (2) Dr = 64.5 %, (3) Dr = 56.2 %, (4) Dr = 42.5 %, (5) Dr = 29.5 %

At any given effective normal stress these threshold states, characterized by the equality and subsequent constancy of pore pressure and resistance at failure appear to form a boundary between the purely contractive and dilative specimens. Fig. 27 shows the stress paths of NAG specimens at a fixed effective normal stress. Any specimen exceeding the threshold pore pressure at failure undergoes purely contractive behavior. Specimens having pore pressures lower than the threshold value dilate.

If increasing density leads to increasing difference between pore pressure and shear resistance at failure, then, the converse will also be true. A decrease in the density of a dilative specimen will decrease the difference between pore pressure and shear resistance at failure. As density is decreased further, a time reaches when the pore pressure and shear resistance at failure will become equal (Fig. 28a, b). This situation establishes a threshold state and appears to form a boundary between the dilative and the contractive specimens and in doing so. Define a transition condition for all specimens under the same effective normal stress. Specimens denser than that for which a threshold condition was defined would dilate, while those looser than the critical would collapse and show purely contractive behavior. In Fig. 29, similar interpretation may be drawn. Starting from dense, it may be seen in Fig. 29 that specimen A with Dr = 66.4 % has distinct peak failure and phase transformation lines. This is similar to specimen B with Dr = 66.2 %.

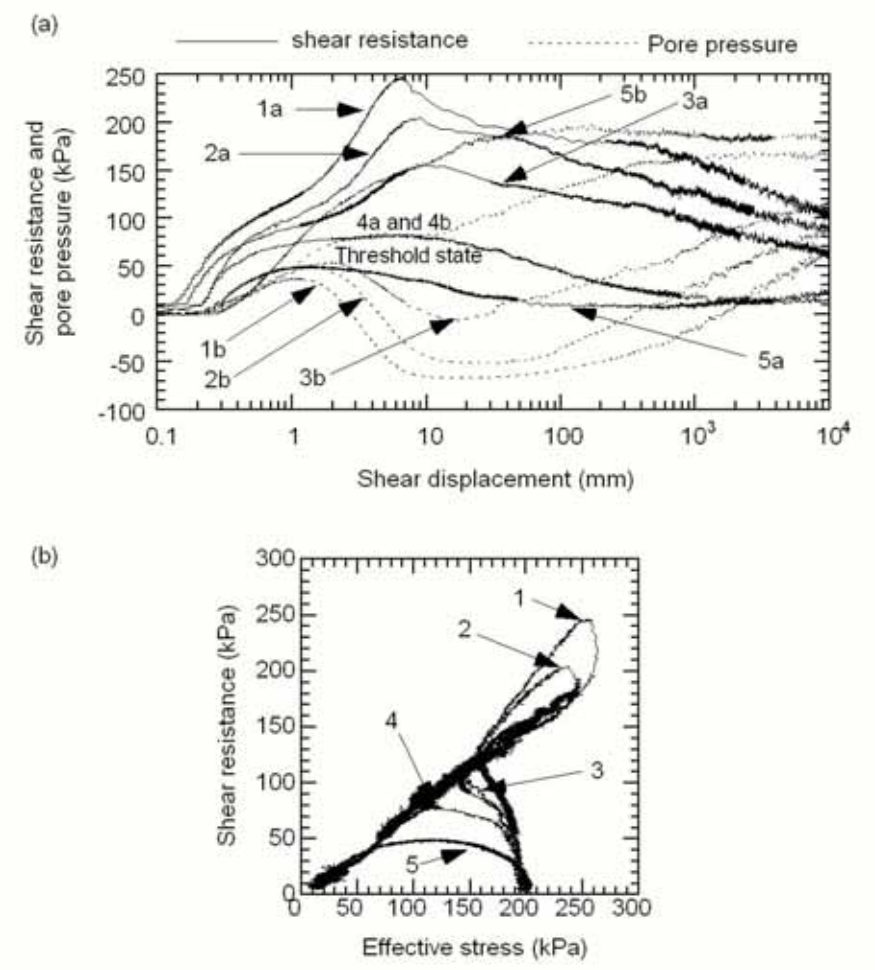

Fig. 28 The effect of relative density on the response of the NAG sands and the position of the threshold state (1) Dr = 74.3 %, (2) Dr = 64.5 %, (3) Dr = 56.2 %, (4) Dr = 42.5 %, (5) Dr = 29.5 %

As the sample is made looser, a point reaches when, as in specimen C, peak failure and phase transformation lines coincide because the sample experienced very little dilation. After this particular specimen, all other specimens can only posses a Mohr Coulomb failure line (or a steady state line) with a complete absence of a

phase transformation line. Although this will be treated in a different section, it may be important to note here that a line drawn through the phase transformation points of the specimens that first contracted and then dilated; and through the steady state of the purely contractive specimen, extrapolates through the origin of the shear resistance-effective stress diagram (Fig. 29).

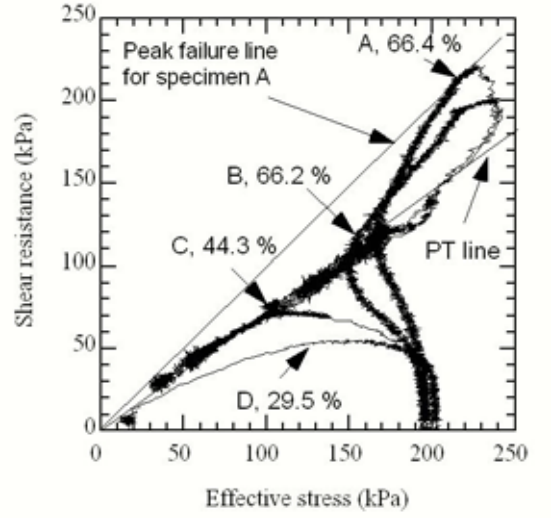

Fig. 29 The effect of relative density on the response of the ING sands

4.2 Hypothesis

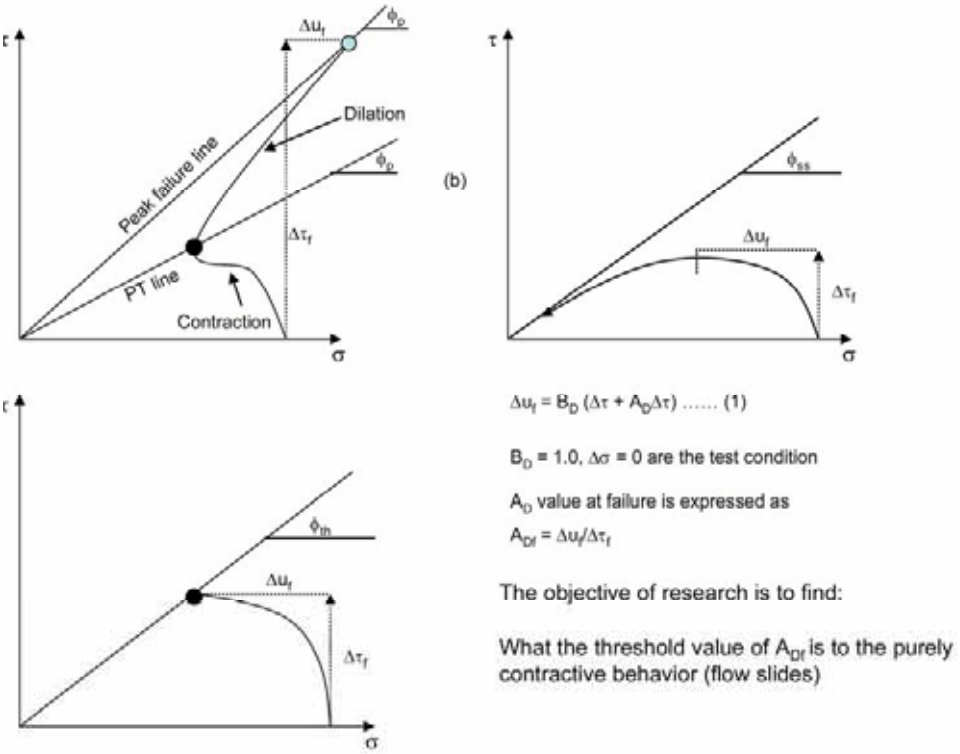

Fig. 30 The theory of threshold pore pressure

The hypothetic model used during the experimental investigation is presented in Fig. 30. Normally consolidated soils (Fig. 30 a, c) at same confining stresses will follow stress paths in Fig. 30 (a) and Fig. 30 (c) respectively depending on the material state of the samples. For these samples, the conditions at PT line are such that a dilation potential index, A_{Df}, ($A_{Df} = \Delta u_f/\Delta\tau_f$) are < and = 1 respectively. The conditions prevailing at Fig. 30 (c) are recognized in this paper as a threshold state. If however, the soil is made in such a way that ensures the stress path follows as in Fig. 30 b, the specimen may not go through the phase transformation stage because its A_{Df} would clearly be greater than one. The specimen may, instead, collapse and liquefy.

The present concept (of threshold pore pressure) underlines the fact that the magnitude of excess pore pressure from the outset of any undrained test determines whether or not a given specimen will pass through the phase transformation stage. The fate of specimens whose excess pore pressures are not big enough to induce outright flow liquefaction and avoid reaching the PT line, depends on the ratio $\Delta u/\Delta\tau$. If this ratio is unity, pore pressure and shear resistance should remain the same until failure occurs, meaning that the specimen neither dilated nor contracted until failure or that the specimen experience the least dilation possible at a given effective stress. The PT line of such a specimen may be approximately equal to its peak failure line because the state of stresses at the PT point approximately coincides with those at failure. This condition should define a threshold situation. All other stress paths above this threshold should dilate, while other stress paths below it should show purely contractive behavior.

It is reasoned that whenever the PT line coincides with the peak failure line of a specimen at a given effective normal stress, the specimen dilates the least. And the shear properties of such a material will define the boundary between two important soil behaviors: dilation and flow liquefaction. A possible merit of the new idea lies in the fact that the defining parameters considered threshold may be adequately represented in a stress-strain-void ratio space, and interpreted with references to some experimentally measurable quantities. Unlike abstract analogies, the reference parameters in the idea under consideration may be directly observed and measured. Such a quantitative analytical procedure may be easily verified by competent colleagues elsewhere.

Equally important is the fact that the threshold pore pressure (the pore pressure required at the phase transformation line to ensure that a specimen dilates the least) can be quickly but conditionally calculated with as small as one good laboratory test at a known effective stress. The conditions for a reliable calculation include: 1) the specimen must be fully saturated; 2) the test must be monotonically loaded undrained; 3) Mohr Coulomb failure criterion must be applied. If, and when these conditions are satisfied, threshold pore pressure, u_c, as used in this paper may be calculated from the following equation:

$$u_c = \sigma \tan\phi/(1+\tan\phi)$$

Where u_c is the threshold pore pressure, σ is the normal stress used in the undrained test, and ϕ is the friction angle of the material at a given normal stress σ. This is the amount of excess pore pressure that must be exceeded before flow liquefaction failure of the sands can be expected.

Fig. 31 shows the relationship between the ratio $\Delta u/\Delta\tau$ at failure and normal stress. It may be seen that the specimens with $\Delta u/\Delta\tau = 1$ forms a boundary between purely contractive specimens whose $\Delta u/\Delta\tau > 1$, and dilative specimens whose $\Delta u/\Delta\tau < 1$.

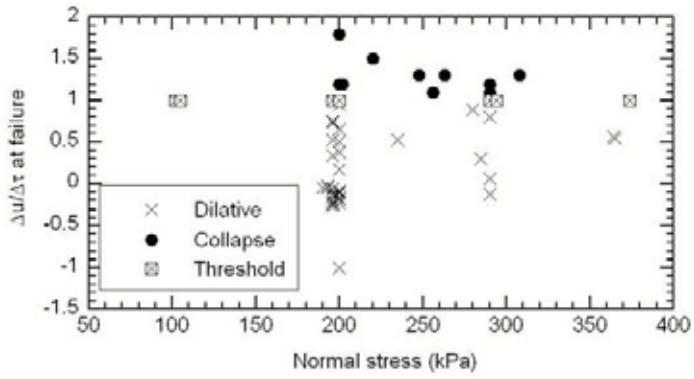

Fig. 31 Relationship between $\Delta u/\Delta t$ at failure and normal stress for all grading

On the basis of presented evidence, a transition model for the specimens is presented in Fig. 32. Starting from dense, Fig. 32a has a distinct peak failure and phase transformation lines. A systematic decrease in density will lead to a less dense specimen with the PT line and peak failure line getting closer to each other for every decrease in density as may be seen in Fig. 32 b. As density keeps reducing a time should come when peak failure line and PT will coincide; the specimen will experience the least dilation possible at the given effective normal stress as in Fig. 32c. The value of pore pressure (about 81 kPa) in Fig. 32c is known in this paper as threshold pore pressure. Attempts to exceed the threshold pore pressure should lead to collapse and flow behavior. Such soils will have only Mohr Coulomb failure line because there will be no phase transformation point. A direct transition from dilative behavior to a purely contractive behavior (a to c in Fig. 32) is thought to be incompatible with the present concept.

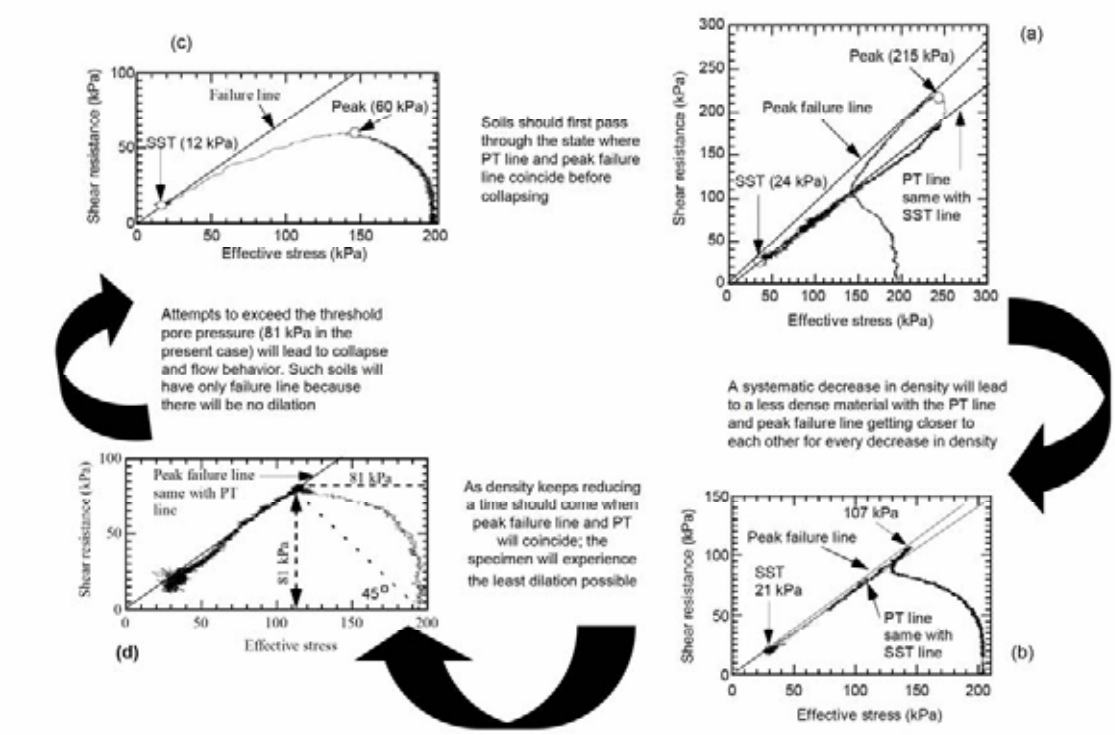

Fig. 32 Model of soil transition

5. Comparison of friction angles at various states

The friction angles at threshold, phase transformation, steady state, and peak are compared for the sands investigated (Figs. 33, 34, 36). Fig. 33(a) shows the relationship between friction angle at phase transformation (PT) and relative density. It may be seen from the figure that although the friction angle at phase transformation (PT) might be slightly affected by relative density, all data are within 36.2° ± 0.7°. Therefore, it can be approximated to be a constant at around 36.2° in practical usage. Fig. 33(b) shows the relationship between friction angle at threshold state and relative density; where the values are in the range of 36.1° ± 0.4°. Fig. 33(c) is the relationship between friction angles at steady state (SS) and relative density. The values appear to be independent of both grading and relative density. The range of values are within 36.2° ± 0.7̃° .

Fig. 34 is the relationship between friction angles at steady state, phase transformation, threshold state and relative density for all grading. All values of the three friction angles (ϕ at PT, ϕ at SS, ϕ at threshold) are close to one another and exist within 36.2° ± 0.7̃° The number of the friction angle at the threshold state is not enough. However, all plots fall in the distribution of friction angles at steady state. This is probably because grain crushing and the resulting change in grading do not affect the friction angle, which in turn might be because the minerals making up the samples are the same and angularity remains almost the same although the

sizes of grains and grading might change. The friction angles at phase transformation (before peak, where grain crushing is at minimum) fall in the same range of the friction angles at the threshold state and the steady state. This is also because grain crushing and the resulting change in grading have little or no effect on the angles. It can be said that under no positive or negative pore water generation state which may occur at the phase transformation point before failure, at failure point in the threshold state, at the steady state point (after failure) where all grain crushing has been completed, the mobilized friction angles are almost same even though grading are different.

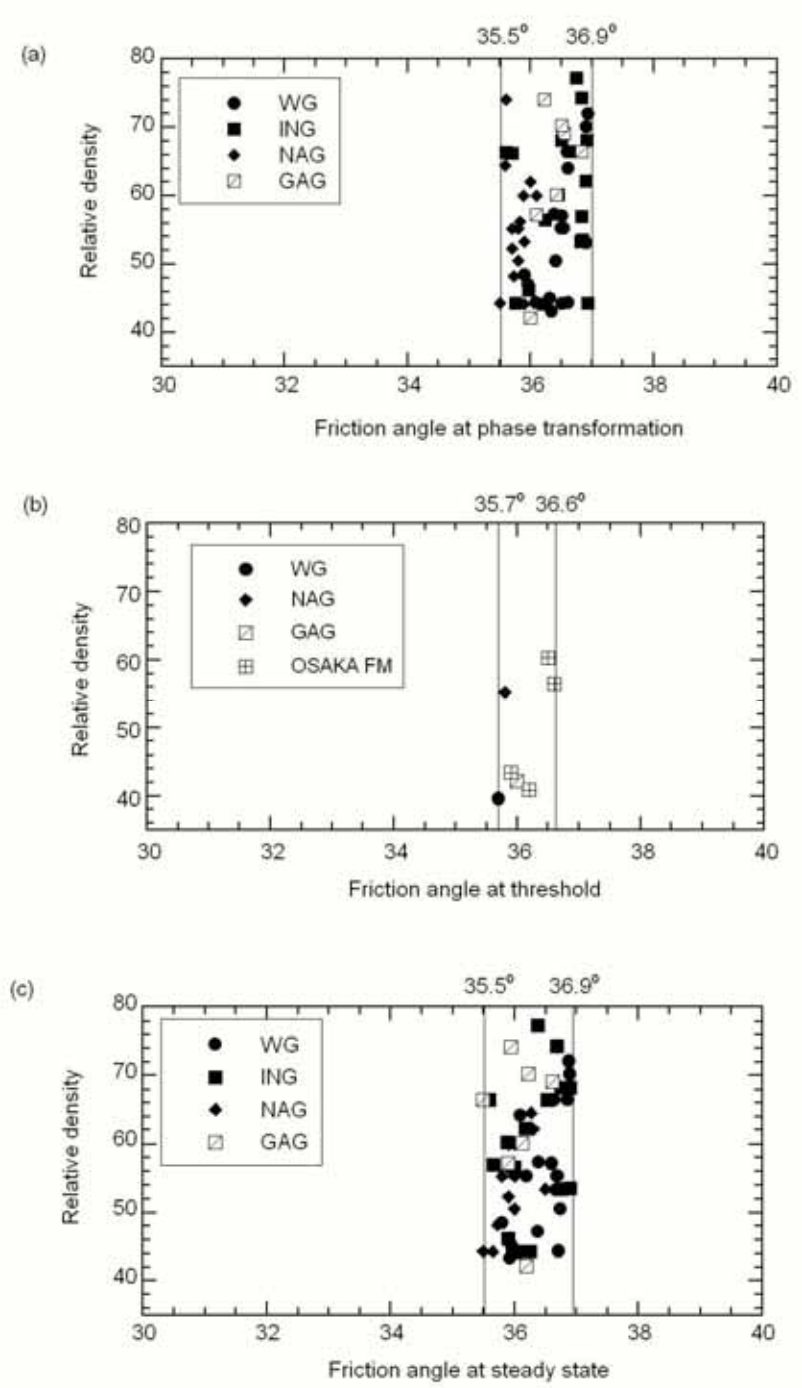

Fig. 33 Relationship between the friction angles at phase transformation, threshold state, steady state and relative density

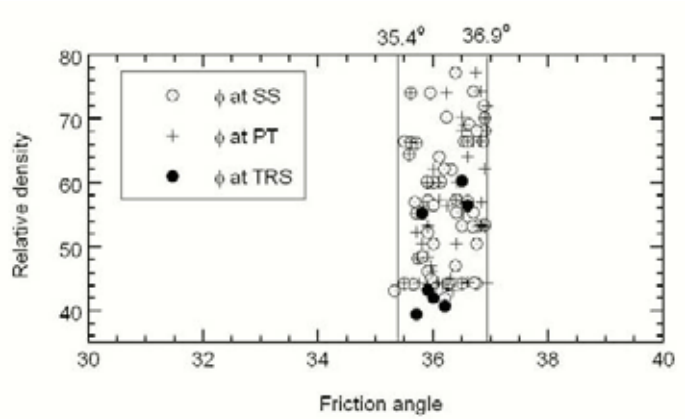

Fig. 34 Relationship between the friction angles at steady state, threshold state, phase transformation and relative density

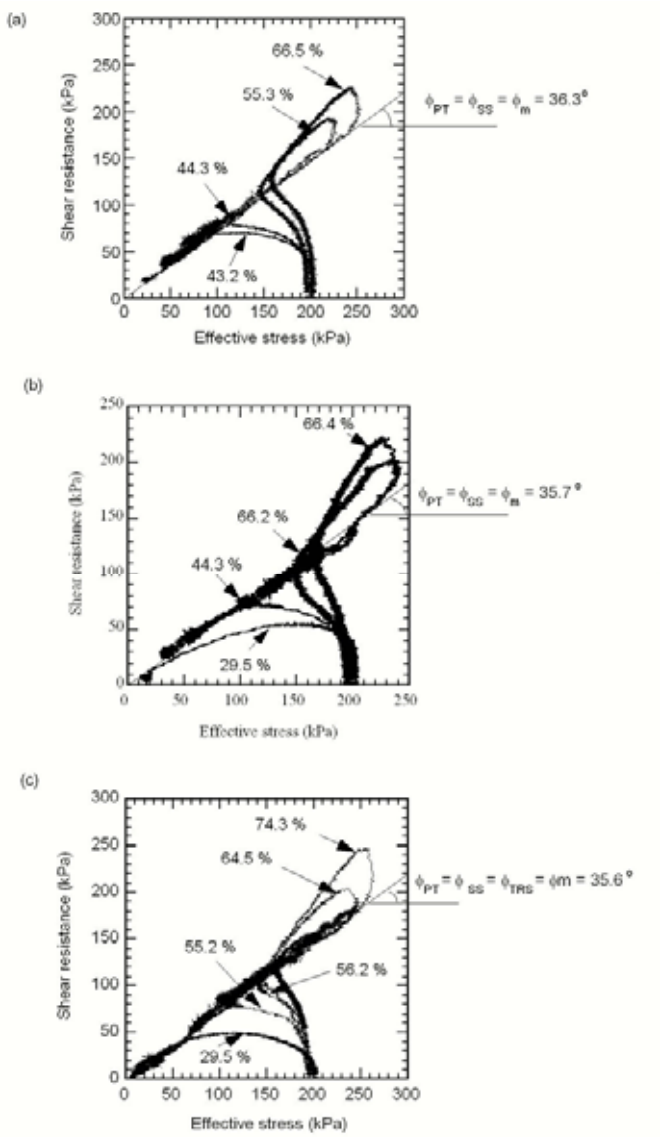

Fig. 35 Effective stress paths of (a) WG (b) ING (c) NAG specimens

Sassa (1988, 2000) proposed the friction angle during motion (ϕ_m) as the friction angle mobilized during motion of landslides. However, he did not mention that this value remains constant. This research shows (as shown in Fig. 35) that this friction angle during motion remains constant from the initial stage of movement to the steady state even though grain crushing and the resulting change in grading are associated with the movement. Fig. 35 shows the stress paths of WG, ING, and NAG specimens with various relative densities at a normal stress range of 196 kPa to 204 kPa. Fig. 32(a) shows that the friction angle at phase transformation state and steady state are approximately equal with a value of 36.3° Fig.32 (b) shows that the friction angles are approximately equal with a value of 35.7° Fig. 32 (c) the friction angles are also approximately equal with a value of 35.6°.

This finding may broaden the range of application of the friction angle during motion. The finding that the value of friction angle during motion is almost same with the friction angle at the threshold state, and practically same with the friction angle at phase transformation will provide a significant merit in the prediction of landslide mobility and hazard area because both friction angles at threshold state and phase transformation can be obtained by the conventional shear box test. Especially, the friction angle at phase transformation can be obtained by a single test by the shear box test; which will be a very convenient process.

The relationship between friction angle at peak and relative density is presented in Fig. 36. The friction angles at peak for all grading increase with relative density. This result is quite different from those obtained with the friction angles at steady state, phase transformation and threshold state.

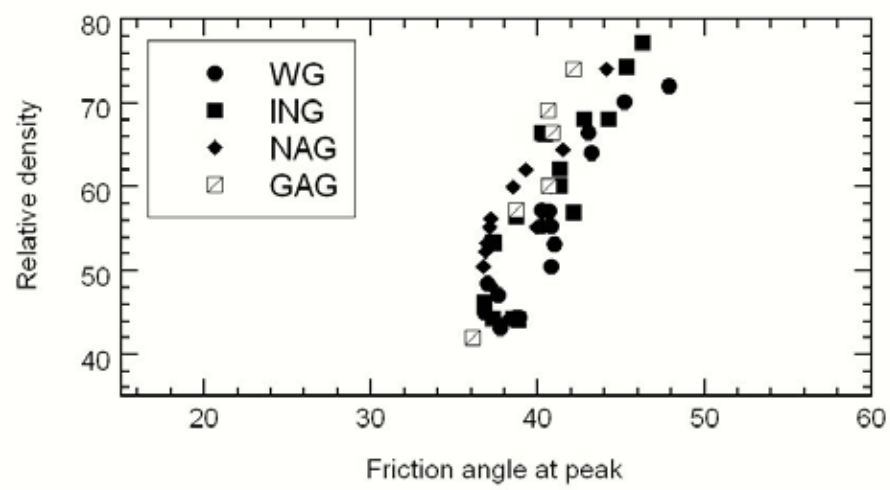

Fig. 36 Relationship between friction angle at peak and relative density

6. Conclusions

Based on the test results and their interpretation, the following conclusions are drawn:

1. There is a threshold state, which forms a transition region between sands that contract from those that dilate. The threshold state is characterized by the unity of the ratio $\Delta u/\Delta\tau$ at failure; and the ratio is independent of both initial confining stress and grading of specimens. The possibility of specimens exhibiting either contractive or dilative behaviours seems to depend on whether or not the threshold pore pressure is exceeded. When exceeded, specimens tend to collapse and liquefy. When the contrary is the case, specimens tend to dilate. The threshold pore pressure may be expressed as $u_c = (\sigma\tan\phi/1+\tan\phi)$ deduced from the relationship $\Delta u = \Delta\tau$ at failure, where u_c denotes the critical pore pressure, σ represents the total normal stress, and ϕ stands for the angle of internal friction.
2. Well-graded specimens in medium-dense to dense states have higher values of peak strength than the rest of the specimens at the same condition, with the difference appearing to increase with relative density The values are ranked as WG> ING>NAG>GAG. Better interlocking of particles at contacts achieved by mixing

a wide range of particle sizes in the well-graded specimens is thought to be responsible for the higher peak strength values associated with the well-graded specimens.

3. The steady state strengths of specimens in loose state showing collapse behavior are very small or almost zero The steady state strengths of specimens in medium to dense states have greater values in proportion to the relative densities. The values are affected by grading of sands and ranked as NAG>ING>WG>GAG. It is noted that whereas the steady state strengths are affected by grading, the friction angle at steady state is not affected by grading as stated in conclusion 8 below.
4. It is noted that widely graded specimens have greater peak shear strengths than poorly graded specimens of NG and ING. On the contrary, the steady state strengths of well graded specimens are smaller than those of poorly graded specimens. It may be interpreted as fine particles can exist within big pores of coarse particles in well graded specimens. So the packing of grains in well graded specimens is dense, it will increase difficulty of overriding of grains in shearing. Accordingly the peak shear resistance will be increased. Difficulty of overriding is likely to result in greater possibility of grain crushing during shearing. It may generate high excess pore water pressure and result in lower steady state shear strengths.
   The post-peak behaviors of these samples are important from the viewpoint of public safety. It is noted that although well-graded samples have higher peak strengths, their low steady-state strength may pose a serious safety concern because of their potential for long travel distances.
5. Gap graded specimens have the lowest peak and steady state strengths. The coarse and very fine grains in gap graded specimens may be packed in a way that permits the overriding of grains readily. The coarser grains are vulnerable to crushing, and as they crush or break, the finer particles tends to fall within the pores of coarse grains, making it denser but also resulting in a smaller steady state value due to high pore water pressure.
6. It is noted that specimens of a given grading at different initial normal stresses but having approximately the same relative density will all reach the same steady state strength
7. Friction at Phase transformation (PT) seems to be independent of grading. Similarly, the friction angle at the steady state (SS) appears to be independent of grading
8. All friction angles at phase transformation, threshold state, and steady state are almost equal independent of relative density
   Grain crushing will proceed after failure resulting in change of grading during the process. However, it has been found by this research that change of grading during motion does not affect the friction angle during motion which is equal to the friction angle at phase transformation, threshold state and steady state.
9. The friction angle at steady state (φ_{ss}) is the key parameter for predicting the velocity and travel distance of landslides. The finding that the friction angle at steady state is close to the friction angle of phase transformation and threshold state will provide a significant merit in the prediction of landslide mobility and hazard area because the friction angles at phase transformation and threshold state can be obtained by the conventional shear box test.

References

Alarcon-Guzman, A., Leonards, G. A., Chameau, J. L. (1988): Undrained monotonic and cyclic strength of sands. Journal of Geotechnical Engineering Division, Vol. 114, No.10, pp. 1089-1109.

Ambraseys, N. N. (1973): Dynamics and response of foundation materials in the epicentral regions of strong earthquakes. 5th World Conf. Earthquake Engineering Rome.

Casagrande, A. (1936): Characteristics of cohesionless soils affecting the stability of slopes and earth fills. Journal of the Boston Society of Civil Engineers, Vol. 23, No. 1, pp. 13-32.

Casagrande, A. (1976). Liquefaction and cyclic mobility of sands: a critical review. Harvard Soil Mechanics Series No.88, Harvard University, Cambridge, Mass.

Casagrande, A., Rendon, F. (1978): Gyratory shear apparatus design, testing procedures, and test results on undrained sand. Tech. Report S-78-15, U.S. Army Engineer Waterways Experiment Station, Vicksburg, Miss.

Castro, G. (1969): Liquefaction of sands. Ph.D. thesis, Harvard University, Cambridge, Mass.

Castro, G. (1975): Liquefaction and cyclic mobility of saturated sands. Journal of the Geotechnical Engineering Division, ASCE, Vol. 101, No. GT6, pp. 551-569.
Castro, G., Poulos, S. J. (1977): Factors affecting liquefaction and cyclic mobility. Journal of Geotechnical Engineering Division, ASCE, Vol. 103, No. GT6, pp. 501-516.
Eckersley, J. D. (1985): Instrumented Laboratory Flowslides. Geotechnique Vol. 40, No. 3, pp. 489-502.
Gilbert, P. A. (1976): Case histories of liquefaction failures. Misc. Paper S-76-4, U.S. Army Engineer Waterway Experiment Station, Vicksburg, Miss.
Gilbert, P. A., Marcuson, W. F. (1988): Density variation in specimens subjected to cyclic and monotonic loads. Journal of Geotechnical Engineering, Vol. 114, No. 1, pp. 1-20.
Hardin, B. O. (1985):'Crushing of soil particles. J. Geotch. Engrg., ASCE, 111(10), pp. 1177-1192.
Hardin, B. O., Drenevich, V. P. (1972): Shear Modulus and Damping in Soils: Design Equations and Curves. Journal of the Soil Mechanics and Foundation Division, ASCE, Vol. 98, No. SM7, Proc. Paper 9006, pp. 667-692.
Hutchinson, B., Townsend, D. (1961): Some grading-density relationships for sands. Proceedings, 5th International Conference on Soil Mechanics and Foundation Engineering, Vol. 1, pp. 159-163.
Igwe, O., Sassa, K., Fukuoka, H. (2004a): Liquefaction potential of granular materials using differently graded sandy soils. Annuals of Disas. Prev. Res. Inst., Kyoto Univ., No. 47B, pp. 893-902.
Igwe, O., Sassa, K., Fukuoka, H. (2004b): Experimental study on the potential for liquefaction of sands with varying gradations. Landslides: Evaluation and Stabilization (eds: Lacerda, Ehrich, Fontoura, & Sayao), Proceedings of the 9th International Symposium on Landslides, Rio de Janeiro, pp. 717-722.
Igwe, O., Sassa, K, Wang, F. W. (2005a): The Influence of Grading on the Shear Behavior of Loose Sands in Stress-controlled Ring Shear Tests. Landslides. Journal of the International Consortium on Landslides (in press).
Igwe, O., Sassa, K., Fukuoka, H., Wang, F. W. (2005b): Threshold pore pressure: a new perspective on the mechanisms of flowslides. Proc. Of 11th International Conference and Field Trips on Landslides, Norway, pp. 165-172.
Ishihara, K. (1993): Liquefaction and flow failure during earthquakes. Geotechnique, Vol. 47, No. 3, pp. 349-451.
Ishihara, K., Okusa, S., Oyagi, N., Ischuk, A. (1990): Liquefaction-induced flowslide in the collapsible loess deposit in Soviet Tajik. Soils and Foundations, Vol. 30, No. 4, pp. 73-89.
Koerner, R. M. (1969): Effect of particle characteristics on soil strength. Journal of Soil Mechanics and Foundations Division, Proceedings of the American Society of Civil Engineers, Vol. 96, No. SM4, pp. 1221-1232.
Kirkpatrick, W. M. (1965): Effects of grain size and grading on the shearing behavior of granular materials. Proceedings, 6th International Conference on Soil Mechanics and Foundation Engineering, Vol. 1, pp. 273-277
Kishida, H. (1969): Characteristics of liquefied sands during Mino-Owari, Tohnankai and Fukui earthquakes. Soil and Foundation, Vol. 10, No. 2, Tokyo, Japan.
Kokusho, T., Hara, T., Hiraoka, R. (2004): Undrained shear strength of granular soils with different particle gradations. Journal of Geotechnical and Geoenvironmental engineering, ASCE, Vol. 130, No.6, pp. 621-629.
Konrad, J. M. (1993): Undrained response of loosely compacted sands during monotonic and cyclic compression tests. Geotechnique 43, No1, 69-89.
Kramer, S. L., Seed, H. B. (1988): Initiation of soil liquefaction under static loading conditions. Journal of Geotechnical Engineering, Vol. 114, No. 4, pp. 412-430.
Kutter, B. L. (1982): Behavior of embankments under dynamic loading. Part of PhD thesis, University of Cambridge.
Lade, P. V., Pradel, D. (1990): Instability and plastic flow of soils. 1: Experimental observations. J. Engrg. Div., ASCE, 116(11), 2532-2500.
Lade, P. V., Yamamuro, J. A. (1996): Undrained sand behavior in axisymmetric tests at high pressures. J. Geotech. Engrg., ASCE, 122(2), pp. 120-129.
Lee, K. L., Farhoomand, I. (1967): Compressibility and crushing of granular soils in anisotropic triaxial compression. Can. Geotech. J., Ottawa, Canada, 4(1), pp. 68-86.

Lee, K. L., Fitton, J. A., (1969): Factors affecting the cyclic loading strength of soil: Vibration effects of earthquakes on soils and foundations, ASTM STP 450, American Society of Testing and Materials, pp. 71-95.

Marsal, R. J. (1967): Large scale testing of rockfill materials. J. Soil Mech. And Found. Div., ASCE, 93(2), PP. 27-43.

Marui, H. (1996): Preliminary report on the Gamahara torrent debris flow of 6 December 1996, Japan. Journal of Natural Disaster Science, Vol. 18, pp. 89-97.

Mohamad, R., Dobry, R. (1986): Undrained monotonic and cyclic triaxial strength of sand. ASCE Journal of Geotechnical Engineering, 112: pp. 941-958.

Negussey, D., Wijewickreme, W. K. D. and Vaid, Y. P. (1988): Constant-volume friction angle of granular materials. Can. Geotech. J. 25, 50-55.

Poulos, S. J. (1981): The steady state of deformation. Journal Geotech. Eng. Division, ASCE 107, No. GT5, pp. 553-562.

Poulos, S. J., Castro, G., France, J. W. (1985): Liquefaction evaluation procedure. Journal of Geotech. Eng. Division, ASCE 111, No. 6, pp. 772-792.

Ross, G. A., Seed, H. B., Migliaccio, R. R. (1969): Bridge foundation behavior in Alaska Earthquake. Journal of the Soil Mechanics and Foundation Division, ASCE, Vol. 95, No. SM4, Proc. Paper 6664, pp. 1007-1036.

Sasitharan, S., Robertson, P. K., Sego, D. C., Morgenstern, N. R. (1993): Collapse behavior of sand. Canadian Geotech. Journal, Vol. 30, pp. 569-577.

Sasitharan, S., Robertson, P. K., Sego, D. C., Morgenstern, N. R. (1994): State-boundary surface for very loose sand and its practical implications. Can. Geotech. Journal, Vol. 31, pp. 321-334.

Sassa, K. (1985): The mechanism of debris flow. In Proceedings of the 11th International Conference on Soil Mechanics and Foundation Engineering, San Francisco, Calif., Vol. 3, pp. 1173-1176.

Sassa, K. (1988): Geotechnical model for the motion of landslides. Special Lecture of the 5th International Symposium on Landslides, ''Landslides'', Vol. 1, Rotterdam: Balkema, pp. 37-55.

Sassa, K. (1996): Prediction of earthquake induced landslides. Special Lecture of the 7th International Symposium on ''Landslides'', Rotterdam: Balkema, Vol. 1, pp. 115-132.

Sassa, K., Fukuoka, H., Scarascia-Mugnozza, G., Evans, S. (1996): Earthquake-induced landslides: Distribution, motion, and mechanisms. Special Issue for the Great Hanshin Earthquake Disaster, Soils and Foundations, pp. 53-64.

Sassa, K., Fukuoka, H., Wang, F. W. (1997): Mechanism and risk assessment of landslide-triggered debris flows: Lessons from the 1996 Otari debris flow disaster, Nagano, Japan. Landslide Risk Assessment (ed. Cruden and Fell), Proceedings of the International Workshop on Landslide Risk Assessment, pp. 347-356.

Sassa, K. (1997): A new intelligent-type dynamic-loading ring shear apparatus. Landslide News no 10:33.

Sassa, K. (1998): Recent urban landslide disasters in Japan and their mechanisms. Proceedings of the 2nd International Conference on Environmental Management, ''Environmental Management'', Rotterdam: Balkema, Vol. 1, 47-58.

Sassa, K. (2000): Mechanism of flows in granular soils. Proceedings of the GeoEng2000, Melbourne, Vol. 1, pp. 1671-1702.

Sassa K, Wang G, Fukuoka H (2003): Performing undrained shear tests on saturated sands in a new intelligent-type of ring shear apparatus. Geotech. Test J. 26(3):257-265.

Seed, H. B. (1966): Landslides during earthquakes due to soil liquefaction. Journal of Soil Mechanics Foundations Division, ASCE, Vol. 94, No. 5, pp. 1055-1122.

Seed, H. B., Lee, K. L. (1966): Liquefaction of saturated sands during cyclic loading. Journal of Soil Mech. Fdn. Engng. Am. Soc. Civ. Engrs. Vol. 92, SM6, 105-134.

Seed, H. B., Idriss, I. M. (1969): Influence of Soil Conditions on Ground Motions During Earthquakes. Journal of the Soil Mechanics and Foundation Division, ASCE, Vol. 95, No. SM1, Proc. Paper 6347, pp. 99-137.

Seed, H. B., Idriss, I. M. (1971): Simplified procedures for evaluating soil liquefaction potential. Journal of Soil Mechanics Foundation Engineering Am. Soc. Civ. Engrs. Vol. 109, GT3, pp. 458-482.

Seed, H. B. (1979): Soil Liquefaction and cyclic mobility evaluation for level ground during earthquakes. Journal of Geotech. Engineering Division, ASCE, Vol. 105, pp. 201-255.
Seed, H B. (1981): Earthquake-Resistant Design of Earth Dams,'' International Conference on Recent Advances in Geotechnical Earthquake Engineering and Soil Dynamics, Vol. 3, St, Louis, Mo., pp. 1157-1173.
Sladen, J. A., D'Hollander, R. D., Krahn, J. (1985): The liquefaction of sands, a collapse surface approach. Can. Geotech. J. 22, pp. 564-578.
Terzaghi, K., Peck, R. B. (1948): Soil mechanics in engineering practice. 2nd edn., pp. 108. Chichester: Wiley.
Vaid, Y. P., Chern, J. C. (1985): Cyclic and monotonic undrained response of saturated sands. Advances in the Art of Testing Soils Under Cyclic Conditions, American Society of Civil Engineers Convention, Detroit, Mich., pp. 120-147.
Vaid, Y. P., Fisher, J. M., Kuerbis, R. H., Negussey, D. (1990): Particle gradation and liquefaction. Journal of Geotechnical Engineering, Vol. 116, No. 4, pp. 698-703.
Vasquez-Herrera, A., Dobry, R., Ng, T. T. (1988): Pore pressure build-up and liquefaction failure of anisotropically consolidated sand due to cyclic straining. Proceedings of conference on hydraulic fill structures, Fort Collins, pp. 346-366. New York: American Society of Engineers.
Wafid, M. A., Sassa, K, Fukuoka, H., Wang, G. (2004): Evolution of Shear-Zone in Undrained Ring Shear Tests. Landslides. Journal of the International Consortium on Landslides, 1:101-112.
Wang, F. W. (1998): An experimental study on grain crushing and excess pore pressure generation during shearing of sandy soils – a key factor for rapid landslide motion. PhD Thesis. Kyoto University, Japan.
Wang, G., Sassa K. (2000): Effects of grain size on sliding surface liquefaction behavior of sands based on ring shear tests. "Landslides in Research, Theory and Practice", Proceedings of 8th international Symposium on Landslides (edited by Eddie Bromhead, Neil Dixon and Maia-Laura Ibsen). Cardiff, Wales, UK, Vol. 3, pp.1539-1544.
Wang, G., Sassa, K. (2001): Factor affecting the rainfall-induced flowslides in laboratory flume tests. Geotechnique, Vol. 51, No. 7, pp. 587-599.
Wang, G., Sassa, K. (2002): Post-failure mobility of saturated sands in undrained load-controlled ring shear tests. Can. Geotech. J. Vol. 39, pp. 821-837.
Whiteman, R. V. (1971): Resistance of soil to liquefaction and settlement. Soils and Foundation, Vol. 11, No. 4, pp. 59-68.
Wong, R. T., Seed, B. H., Chan, C. K. (1975): Cyclic loading liquefaction of gravelly soils. J. Goetech. Engng. Div., ASCE, Vol. 101, No. GT6, pp. 571-583.
Yamamuro, J. A., Lade, P. V. (1999): Experiments and modeling of silty sands susceptible to static liquefaction. Mech. Of Cohesive-Frictional Mat., 4(6), pp. 545-564.
Yoshimine, M., Robertson, P. K., Wride, C. E. (1999): Undrained shear strength of clean sands to trigger flow liquefaction. Can. Geotech. J.36:891-906.

田中康博・汪发武・中村佳代・松本樹典
(2005)

金沢市山科町における長雨を誘因とする流動性地すべりの特徴と運動機構

日本地すべり学会誌，42(2) 34-43

Landslides - Journal of the Japan Landslide Society
Vol.42 No.2 (2005), July, pp.136-145, Original article

金沢市山科町における長雨を誘因とする流動性地すべりの特徴と運動機構

Feature and sliding mechanism of a flowslide triggered by continual rainfall in Yamashina area, Kanazawa City, Japan

田中康博[a)d)]・汪　発武[b)*]・中村佳代[c)]・松本樹典[a)]

Yasuhiro TANAKA, Fawu WANG, Kayo NAKAMURA and Tatsunori MATSUMOTO

Abstract

Due to a continual rainfall, a flowslide occurred in Yamashina area, Kanazawa City, Japan on November 8, 2002. The sliding mass was fully fluidized after slope failure and had deposited thickly in a bamboo area. The stratum around the landslide area was massive mudstone of Tertiary period. According to field investigation, the mudstone was classified into strongly weathered mudstone layer at top, densely cracked moderately weathered mudstone layer at middle and fresh mudstone layer at bottom. It is confirmed that the flowslide was initialized along the sliding surface between the densely cracked layer and the fresh layer, and the sliding mass moved in the strongly weathered mudstone layer. Based on the landslide motion simulation reproducing the Yamashina flowslide, the shear resistance at steady state in the strongly weathered mudstone area and the bamboo area were estimated as 10 kPa and 50 kPa respectively. It is concluded that the landslide with high mobility was caused by the low mobilization of shear resistance in the saturated strongly weathered mudstone with low permeability.

Key words : Tertiary mudstone formation, flowslide, continual rainfall, sliding mechanism, case study

和文要旨

2002年11月８日に金沢市山科町で長雨を誘因とする流動性地すべりが発生した。発生直後の地すべり土塊は完全に飽和されており，竹林の分布している範囲では地すべり土塊が厚く堆積していた。地すべり地は第三紀泥岩層（塚川層）からなり，現地調査より泥岩は下位から新鮮な泥岩，亀裂の発達した風化泥岩，粘土化した強風化泥岩の三層に分類され，風化泥岩と新鮮部との境界で地すべりが発生したことがわかった。また，運動機構を明らかにするために行った運動シミュレーションより，すべり面の定常状態でのせん断抵抗が強風化泥岩層では10kPa，竹林部では50kPa（竹林の土塊のせん断抵抗値ではなく，地すべり土塊中に含まれる竹の地すべり運動による衝突が地すべりを減速させる効果を表現した値）であることがわかり，竹林が分布している範囲に，地すべり運動を減速させる何らかの要因があった。山科地すべりの流動化した原因の一つとして，長雨によって飽和された低透水性の強風化泥岩が，地すべり土塊の後続荷重により，非排水せん断され，そのせん断抵抗が低くなり流動化したと考えられる。

キーワード：第三紀泥岩層，流動性地すべり，長雨，運動機構，事例研究

1．はじめに

流動性地すべり（flowslide）は高速長距離土砂流動現象の一つのタイプである。高速長距離土砂流動現象は，斜面崩壊，地すべり，土石流など，その状況によって種々の呼び方がなされているが，いずれにしても流動性の高い土砂移動現象である（佐々，2002）。流動性を表す指標として，見かけの摩擦角（土塊の運動中に発揮される平均の摩擦角：ϕ_m）が用いられている。佐々（2002）によれば，近年世界各地で発生した土砂災害の例では，そのほとんどが，見かけの摩擦角20度以下，特に10度前後のものが目立つ。このような流動性地すべりのほとんどはマサ化した花崗岩や火山砕屑物のような砂質土で発生していることが知られている（Cairo and Dente, 2003；Wang and Sassa, 2002）。また，リングせん断試験により，砂質土の粒子破砕性が流動性地すべりに重大な影響を与えていることが明らかになっている（Wang and Sassa, 2000）。

2002年11月８日に，石川県金沢市山科町で，源頭部の幅約60m，長さ100m，滑落崖の高さ約10m，移動距離約200mの流動化した山科地すべりが発生した（写真－１）。この地すべりの誘因は発生前13日間の連続降雨であると考えられる。この地すべりによって源頭部でりんご畑が崩壊し，末端付近で林道が抉られ，破壊された。地すべり発生後，地すべりによる土石流被害を防ぐための治山ダムが末端部に建設された。その後も滑落崖での

写真－１　2002年11月８日に発生した山科地すべり
Photo 1　The Yamashina flowslide occurred on 8 November, 2002

* 連絡著者／corresponding author
a) 金沢大学大学院自然科学研究科
Graduate School of Natural Science and Technology, Kanazawa University
b) 京都大学防災研究所斜面災害研究センター
Research Centre on Landslides, Disaster Prevention Research Institute, Kyoto University
〒611-0011　京都府宇治市五ヶ庄
Gokasho, Uji, Kyoto, 611-0011, Japan
c) 金沢大学工学部土木建設工学科
Dept. of Civil Engineering, Kanazawa University
d) 株式会社　日建技術
Nikken gijutsu Co., Ltd.

崩壊の拡大が続き，2003年12月31日には，再び流動性地すべりが発生した(汪他，2004a)。本論文では，2002年の流動性地すべりの特徴及び運動機構についてのみ論ずる。

本地すべり地の地質は第三紀の泥岩層からなり，金沢市周辺の丘陵地にも同様の地層が広く分布している。小出（1955）は第三紀層で発生した地すべりを第三紀層地すべりと呼んでいる。石川県ではほとんどの地すべりが第三紀層地すべりであり，且つ再活動地すべりが多い(図－1)。石川県の第三紀層地すべりは運動距離が短く，運動速度も10m/day以下のものがほとんどである。ゆえに，山科地すべりは第三紀層で発生しているが，現地での観察結果に基づけば少なくとも200m/day以上で運動したので，運動速度の相違より石川県の第三紀層地すべりとは明瞭に区別される。また，山科町は地すべり防止区域から外れ，これまで地すべりが発生した例は少ない。

金沢市は人口45万人の都市で，石川県の県庁所在地である。近年，地域開発が進み，住宅地が丘陵地の中腹にまで建設されている（図－2）。地すべり地の北側に流れる伏見川（二級河川）は山科町を通って犀川（二級河川）に流出する。伏見川の山林から住宅地への流出点付近には，第四紀更新世の大桑層の化石産地と瓢穴があり，天然記念物に指定されている。瓢穴とは，河底の硬い岩面にできる大きな円形状の穴のことである。山科地すべりはこの化石産地から約500m上流に位置している。また，山科町の北西には活断層である森本・富樫断層が位置している（図－1）。この断層帯付近での地震は約200年前に発生したのが最後であり，今後30年以内に最大5％の確率で，マグニチュード7.2程度の地震が発生する可能性があると考えられている（地震調査研究推進本部地震調査委員会，2001）。

したがって，斜面防災の観点から見ると，泥岩層での流動性地すべりの発生・運動機構を明らかにすることは急務であると考えられる。本論文では，泥岩層で発生した流動性地すべりの運動機構を，地表踏査，原位置試験，地すべり運動シミュレーションによって明らかにする。

2．山科地すべりの誘因

金沢市は年間を通して降水量が非常に多い都市である。山科地すべり発生前の1993年から2002年の降水量変化を図－3(a)に，年毎の月降水量変化を図－3(b)に，地すべりの発生した2002年11月8日から遡った1ヶ月間の日降水量を図－3(c)に示す（気象庁，2003）。金沢市の観測地点は金沢駅から北西1.5kmに位置する金沢駅西合同庁舎であり（北緯38度35.3分，東経136度38.0分），山科町とは約7km離れている。

地すべりの発生した2002年の年降水量は4795mmであり，ここ10年で最も多い（図－3(a)）。地すべりの発生した2002年の11月の月降水量は511mmであり，これに他年の11月の降水量よりもはるかに多く，梅雨時期の7月の降水量よりも多い（図－3(b)）。地すべり発生前の

図－1　山科地すべりの位置と石川県内の地すべり防止区域（鈴野，1993に加筆）

Fig. 1　Location of the Yamashina flowslide and landslide prevention zone in Ishikawa Prefecture (modified on Kaseno, 1993)

図－2　山科地すべり周辺の地形図（国土地理院25000分の1地形図「金沢」に加筆）

Fig. 2　Topographic map of the area around the Yamashina flowslide

最大日降水量は11月4日の79mmである（図－3(c)）。しかし，この日降水量は，過去の集中豪雨時ほど大きくない。過去の集中豪雨としては1996年6月25日の188mm，2000年9月10日の172mmが挙げられる。ところで，発生前13日間の総雨量は377mmであり，図－3(c)に示した期間の総雨量の77％に及ぶ。過去10年でこのような短

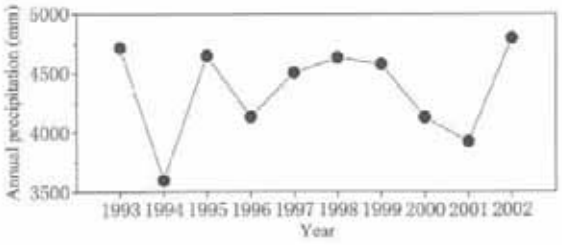

(a) Annual precipitation from 1993 to 2002

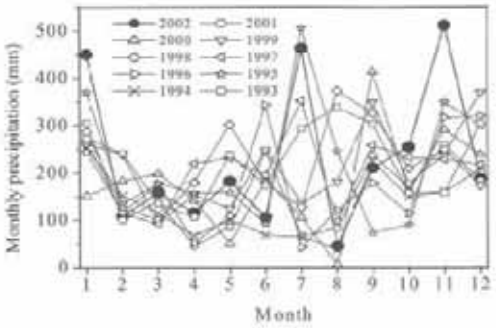

(b) Monthly precipitation from 1993 to 2002

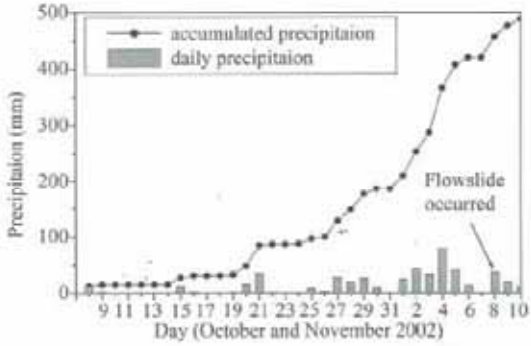

(c) Daily precipitation in Oct. and Nov. 2002

図－3　1993～2002年の金沢市の雨量状況

Fig. 3　Precipitation data in Kanazawa City from 1993 to 2002

期的な連続降雨は観測されていない。したがって10月27日から11月8日にかけての連続降雨が山科地すべりの誘因と考えられる。

3．山科地すべりの特徴と調査結果

3.1　山科地すべりの地形・地質概要

地すべり地周辺の地質は第三紀中新世の泥岩層（犀川層）である。舶野（1993），柳沢（1999）によれば，本層は大桑層に不整合に覆われ，下荒屋凝灰岩層を整合に覆う。また，山科地すべり地の東部では高位の段丘堆積物が犀川層を不整合に覆う。犀川層の岩相は塊状無層理の泥岩であり，層厚は約200mである。調査地から北西に向かうにつれて地層が新しくなる（図－4）。

地すべり地周辺は小起伏山地で，斜面は比較的緩やかに傾斜する。地すべりが発生する前は沢地形であり，斜面勾配は約13°であった。また，その沢は伏見川につながる。地すべり発生後は源頭部の両脇から湧水が見られ，小沢を形成している。

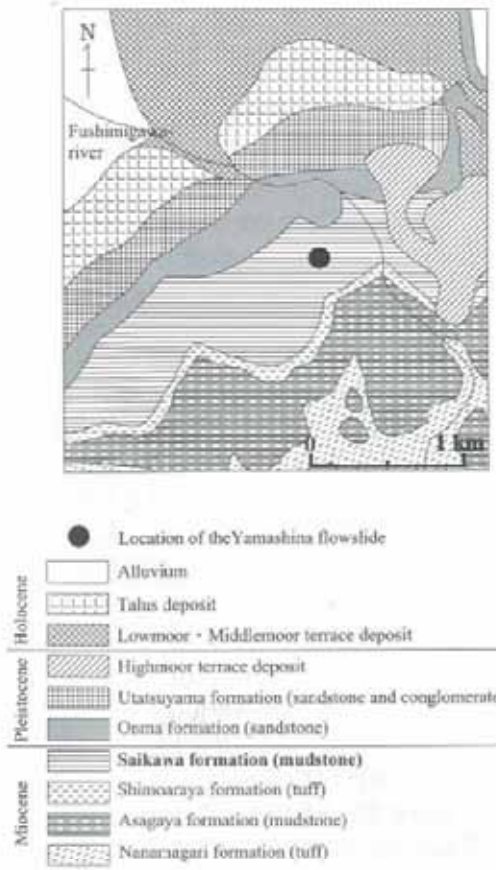

図－4　山科地すべり周辺の地質図（舶野，1993に加筆）

Fig. 4　Geological map of the area around the Yamashina flowslide(modified on Kaseno, 1993)

写真－2　山科地すべりの源頭部状況

Photo 2　Source area of the Yamashina flowslide

山科地すべり周辺の植生はほとんど竹林であるが，地すべり地の源頭部にはりんご畑が広がる。このりんご畑は過去の農地造成により造られた平地上にある。滑落崖に農地造成前の旧地表面と判断できる厚さ100mm程度の黒色の層が確認できた（写真－2）。この黒層の上位層は農地造成の際の盛土部分で，その下位層は風化泥岩であり，粘土化している。

3.2　地すべり土塊とすべり面の調査結果

図－5は，地すべり地内で行った調査位置図である。発生域（source area）は滑落崖に囲まれた範囲を，運

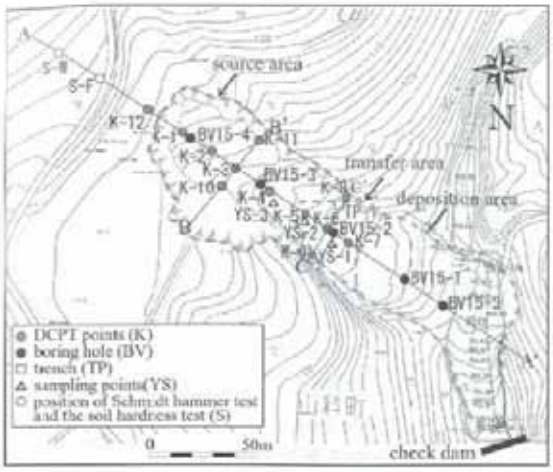

図－5　山科地すべりの調査位置
Fig. 5　Topographic plan of the Yamashina flowslide, together with site investigation points

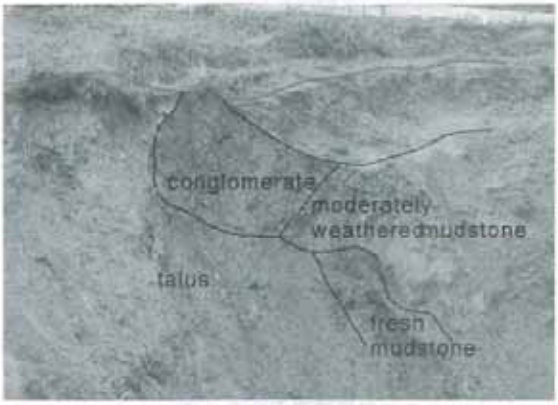

写真－3　滑落崖に分布する礫層と泥岩の関係
Photo 3　Relation between conglomerate and mudstone layer at main scarp

写真－4　堆積域の竹の状況
Photo 4　The bamboo in the deposition area

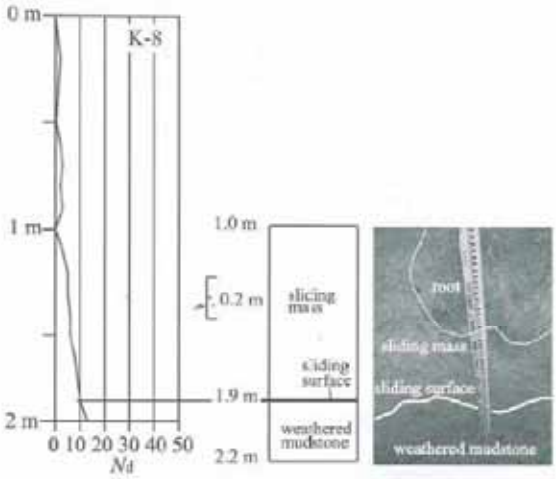

図－6　DCPT及びトレンチ調査結果
Fig. 6　Result of DCPT and trench excavation

動域（transfer area）は発生域と竹林が密集する場所の手前部分の範囲を，堆積域（deposition area）は竹林が密集する場所から末端までをそれぞれ示す。調査内容は，すべり面の位置を調べる目的で，地表踏査，簡易動的コーン貫入試験（以下DCPT；K－1～K－12），ボーリング調査（BV15－1～5，石川県実施）を行った。また，地すべり土塊の特徴を把握する目的でトレンチ調査（TP－1），試料採取（YS－1～YS－3）を，風化の程度を調べる目的で，シュミットハンマー試験（S），山中式土壌硬度計試験（S）を行った。さらに治山ダムから約100m下流のU字溝で雨量・流量観測も行った。

写真－2，3は源頭部での露頭の特徴を示している。地すべり土塊1は写真左の新鮮な泥岩に由来し，崩壊当時は青灰色であった。地すべり土塊2は写真奥の風化した泥岩に由来し，褐色で地すべり土塊1と明瞭に区別できた。堆積状況から地すべり土塊1の上位に地すべり土塊2が位置し，さざなみ状の地形が奥から手前に流れた様子を示していた。したがって，少なくとも2回の崩壊があったと判断できる。写真－3に礫層が風化泥岩層を不整合に覆っていることを示している。この礫層は最大層厚2m程度で，風化により褐色に変色し，水を通しやすい。この礫層は犀川層を不整合に覆う段丘堆積物であると判断できる。

堆積域では竹が密集しており，不動地盤上の竹に地すべり土塊中に含まれる竹が引っかかっているのが観察できた（写真－4）。写真右部分が不動地盤，写真左部分が地すべり土塊の竹である。ゆえに地すべり運動中は，土塊の抵抗だけでなく，不動地盤上の竹と地すべり土塊中に含まれる竹の衝突も抵抗要因となったと考えられる。

図－6にトレンチ調査とその付近で行ったDCPT（K－8）の結果を示す。DCPTは，地盤工学会基準（JGS 1433）に準拠して行った。トレンチ調査から深度1.90mまでは，軟弱な礫混じり粘土からなる地すべり土塊である。含有物として木根，腐敗したりんごの実が多く含まれる。1.90m以深は，粘土化した強風化泥岩であり，こ

れより下位ではスコップで掘削しにくくなる程度に土が硬くなる。また，地すべり土塊に多く含まれていた腐敗した木根やりんごの実などが全く含まれなくなることから，この深度がすべり面であると考えた。すべり面付近は旧地表面と考えられるような表土層が含まれず，特に粘土化が著しいことから，地すべり土塊は旧地表面を抉りながら運動したと判断できる。K－8地点ではN_d値が深さとともに，徐々に増加していく。トレンチ調査で確認できたすべり面付近の深度1.90mでは，N_d＝10前後であり，それ以深ではN_d値は増加していく。そのためN_d＝10を地すべり土塊と泥岩の境界値と判断した。

DCPTは，地すべり地内でK－1～K－11を，滑落崖の上でK－12を行った。図－7に代表的なDCPT結果を示す。地すべり地内では，K－3のように約N_d＝10まで脈状に増加していき，最深部で貫入不能により急増するタイプとK－6のような脈状に徐々に増加していき，N_d＞30になるタイプの二つがある。K－1，2，4，10，11はK－3タイプに，K－5，7，9は，K－6タイプに属する。K－3タイプを発生域のボーリングコア写真（BV15－3，石川県提供）と比較すると，N_d＜10の層は褐色の地すべり土塊に，それ以深は青灰色の新鮮な泥岩層に対比される（図－7）。同様にK－6タイプも比較すると，N_d＜10は褐色の地すべり土塊に，N_d値が10を超え，徐々にN_d値が増加する層は褐色の風化泥岩層にそれぞれ対比される。ゆえにN_d＝10を地すべり土塊と泥岩層の境界として用いることは妥当である。

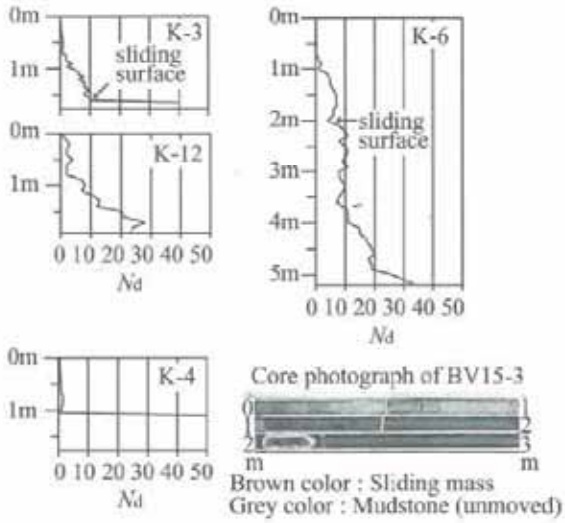

図－7　代表的なDCPT結果とBV15－3のコア写真
Fig. 7　Typical results of DCPT tests and the core photograph of borehole BV15－3

なお，K－6のすべり面を深度2mと判断した理由は，K－6のN_d値は深度2mまでは5前後，2～4mでは，10前後に集中し，それ以深では徐々に増加するという特徴を示す。すなわちN_d値深度分布の変換点は2箇所あり，試験区間内では強度から判断すると三層構造になっていると考えられる。ゆえに最上位層を地すべり土塊層，2層目（N_d＜10となる部分も含むが，強風化泥岩層に相当すると考える）を強風化層と考え，すべり面を深度2mと判断した。

滑落崖で行ったK－12は露頭の状況と比較すると深度1m前後まではりんご園の耕作土を含む表土で，それ以深が風化泥岩層である。風化泥岩層ではN_d値が深さとともに徐々に増加し，K－6タイプの風化泥岩層と同じ特徴を示す。

DCPT，ボーリング調査及びトレンチ調査結果から地質断面図（図－8）を推定した。地質断面図より，発生域では風化泥岩層すべてが崩壊した。そして運動域では地すべり土塊が，表層土すべてと強風化泥岩の一部を巻き込みながら移動したために高速運動になったと判断される。つまり，発生域でのすべり面は新鮮な泥岩面であるのに対し，運動域でのすべり面は粘土化した強風化泥岩層中の面である。堆積域では不動地盤上の竹と地すべり土塊中に含まれる竹の衝突により移動速度が低下したことが，堆積域での地すべり土塊が厚く堆積した原因の一つを担っていたと考えられる。

3.3　流量と地下水位関係

長期間の降雨により，流量は増加し，降雨後すぐに定常状態に戻るか，あるいは地下水位を上昇させしばらくの間高いままの状態を保つかの二つのパターンがあると考えられる。ここでは雨量と流量の関係を知ることで，降雨後にどれだけの速さで地下水位が低下するかを明ら

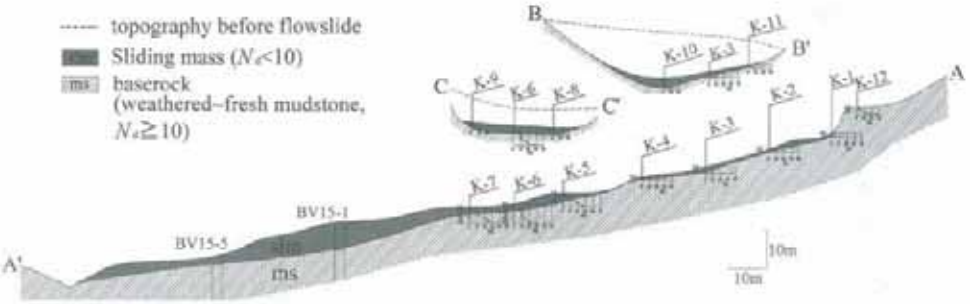

図－8　山科地すべりの地質推定断面図
Fig. 8　Geological longitudinal section of the Yamashina flowslide

かにすることを目的とする。なぜなら，山科地すべりは連続降雨を誘因としていたため，降雨後の地下水位の時間的変化を明らかにする必要があるからである。また，ボーリングをして地下水位を測らなくても，雨量と流量の関係から地下水位変動を推定することも可能であると考えられるためである。

降雨量と流量の関係を調べる目的で，雨量，流量観測を2003年７月13日～2003年９月30日まで行った。雨量観測は治山ダム付近の３地点で行い，その平均値を求めた。流量はU字溝内の流速を求め，この流速にU字溝中の水流の断面積を乗じて求めた。

雨量・流量観測結果を図－９(a)に示すが，比較として同時期の金沢市における気象庁の日降水量データ（図－９(b)）を併記した。図－９(a)と図－９(b)の日降水量は，大局的には類似し，地すべり発生前の降雨量データから地下水位変動を推定することは可能である。

図－９(a)より，一日に50mm以上の降雨があった翌日の流量は飛躍的に増大する。20mm以上の雨量の日は，U字溝は濁流であることが多く，上流で浸食されていると考えられる。降雨後の翌日に雨が降らなかった場合，流量は約1/3まで減少する。その後20mm以上の雨が降らなければ約１週間で流量は安定し，水も透明に戻る。ゆえに降雨量と流量には密接な関係があると判断できる。地下水位は降雨量と密接な関係があるので，降雨後地下水位は上昇し，約１週間で定常状態に戻るといえる。したがって降雨後２～３日は，地下水位も高く，地すべりが発生しやすい状態であると推定できる。

上記に基づくと，地すべり発生前の13日間（10/27～11/８）の地下水位変化は以下のように推定できる。図－３(c)より，10/27～29の降雨（総雨量86mm）で，地下水位が上昇する。10/30，31は20mm以上の雨量は観測されなかったが，２日間では地下水位は定常状態には戻らないので地下水位は高いままであった。11/１～５の降雨（234mm）で，地下水位は飛躍的に上昇し，地盤は飽和して斜面が臨界状態になったと考えられる。11/６，７の降雨は少なかったけれども，地下水に依然豊富に存在しており，地すべりが発生しやすい状態に保たれていたと推定できる。そして11/８の降雨が地すべりの誘因となった。

3.4　泥岩の風化特性

地すべり地内の泥岩の風化特性は，新鮮な青灰色の泥岩ではほとんど亀裂は分布していないのに対し（写真－２左側の露頭），風化した褐色の泥岩では亀裂が密に分布している（写真－５）。風化泥岩はぼろぼろと崩れやすく，亀裂の進行によりさらに風化すると粘土化する。粘土化した泥岩は風化泥岩の上位に位置する。したがって今回の調査地域における泥岩は風化度の違いにより３層に分類できる（図－10）。最下位の新鮮な泥岩層は亀裂が少ないため透水性は低い。中位の風化泥岩層は，亀裂が多いため透水性は高い。最上位の強風化泥岩は，完全に粘土化しており，透水性は低いと判断できる。

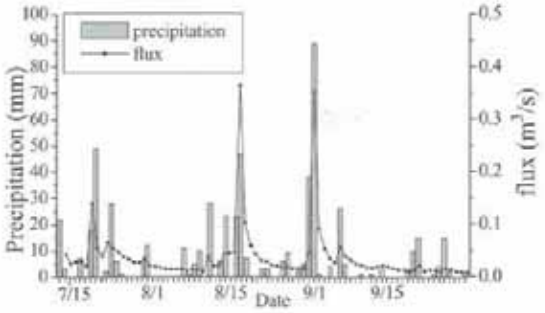

(a) Monitored flux from the flows.ide area and precipitations

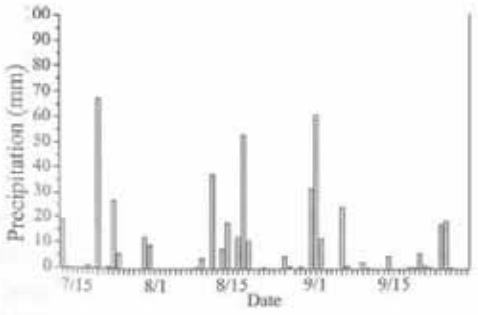

(b) Precipitation data from Japan Meteorological Agency

図－９　2003年７月13日～９月30日の日雨量と流量観測結果
Fig. 9　Daily precipitation and monitored flux from July 13 to September 30, 2003

写真－５　滑落崖での風化泥岩の亀裂状況
Photo 5　The crack situation of the moderately weathered mudstone at the main scarp

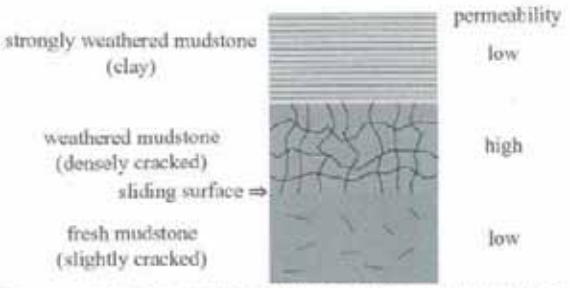

図－10　山科地すべり地域の泥岩の風化状態を表す模式柱状図
Fig. 10　Schematic column showing different weathered structures of mudstone in the Yamashina flow-slide area

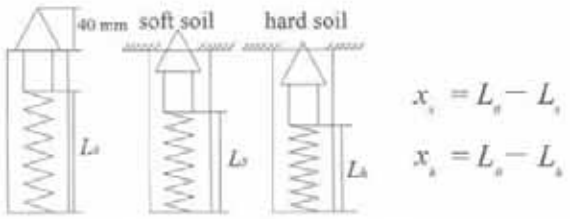

図－11　山中式土壌硬度計の概要図
Fig. 11　Illustration of the Yamanaka style soil hardness meter

次にシュミットハンマー試験と山中式土壌硬度計試験を用いて風化による泥岩の強度の変化を調べた。試験は新鮮な泥岩では地すべり地の滑落崖に露出する青灰色の部分で行い，風化泥岩では滑落崖の亀裂が密に分布した褐色の部分で行った（図－5に示すS－WとS－F）。シュミットハンマー試験は，シュミットハンマーのハンマー部を岩盤に叩きつけ，その反発力を測定し，反発値を求める原位置試験である。試験は一箇所につき約20回行った。その結果，新鮮部では5～21の範囲を示したのに対し，風化部では全く反発しなかった。菊地・斎藤（1976）によれば，CL～CM級岩盤の反発値は約9～20ぐらいであり，山科地すべりの新鮮な泥岩はこれに属すると判断できる。

山中式土壌硬度計試験は平らに削られた断面に垂直に長さ40mmのコーンを圧入し，土壌の反力（バネの縮み：x）を測定する試験であり，試験の概要図を図－11に示す。試験は一箇所につき10回行った。その結果，新鮮部では，バネの縮みがほとんど25mm以上（平均28.6mm）であるのに対し，風化部では25mm以下（平均17.6mm）であり，明瞭な違いが見られた（図－12）。また，山中式土壌硬度計から式(1)を用いて一軸圧縮強度q_s（kN/m^2）を概算することができる（大起理化工業株式会社，1979）。

$$q_s = \frac{10000x}{0.7952(40-x)^2} \quad \cdots\cdots(1)$$

ここに，x：バネの縮み（mm）。新鮮部と風化部のばねの縮み量の平均値を用いて，q_s（kPa）を算定すると，それぞれ2800kPaと460kPaとなり，一軸圧縮強度が明瞭に異なることが示せた。ゆえに風化が進行すると泥岩の強度が顕著に低下する傾向が明らかになった。

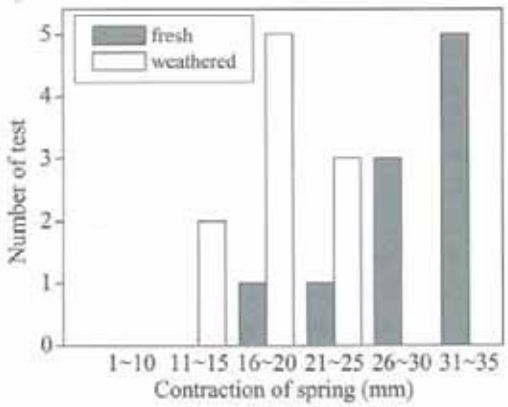

図－12　山中式土壌硬度計測定結果（ばねの縮みの頻度分布図）
Fig. 12　Test results of the Yamanaka style soil hardness meter tests (frequency distribution diagram of contraction of spring)

表－1　地すべり土塊の物理試験結果
Table 1　Physical properties of the sliding mass

	YS-1	YS-2	YS-3
wet density, ρ_t (t/m^3)	1.59	1.28	1.23
dry density, ρ_d (t/m^3)	0.98	0.82	0.79
water content, w (%)	61.9	55.9	55.7
soil particle density, ρ_s (t/m^3)	2.74	2.75	2.77
void ratio, e	1.79	2.34	2.51
degree of saturation, S_r (%)	94.8	65.6	61.5

3.5　地すべり土塊の特徴

地すべり発生直後の崩壊土砂は，軟弱で足を踏み入れることは不可能で，完全に飽和していた。試料採取と簡易的な水置換の現場密度試験を図－5に示す3ヶ所（YS－1～3）で行った。試験結果を表－1，図－13（粒径加積曲線）に示す。図－13よりYS－1は，細粒分に富み粘土質である。一方，YS－2，3は，粘土分が少ない砂質土である。ゆえに少なくとも崩壊土砂は2種類あることが確認された。さらにこれらは，表－1より湿潤密度も異なる。試料採取は地すべり発生から約6ヶ月経過した後に行ったので，難透水性の粘土試料であるYS－1の飽和度は94.8%であり，透水性のよい砂質土試料であるYS－2，3では飽和度が低かった（65.6%，61.5%）。

試料採取を行ったYS－1～3地点は近接しており，また土粒子密度が類似することから，同様の鉱物から構成されているといえ，周辺に露出する泥岩層から由来すると判断できる。これらの特徴からYS－1は，風化が進んで粘土化した泥岩と判断でき，YS－2，3は，滑落

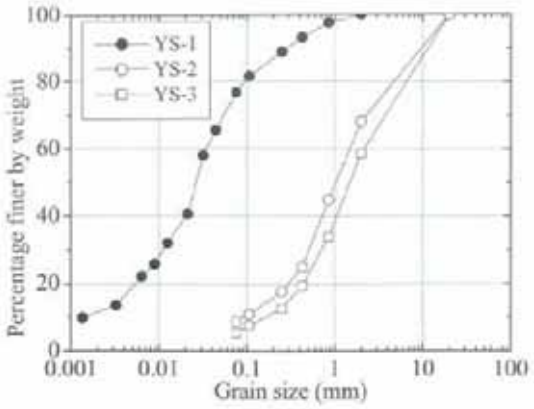

図－13　地すべり土塊の粒径加積曲線

Fig. 13　Grain size distribution curves of soils taken from sliding mass

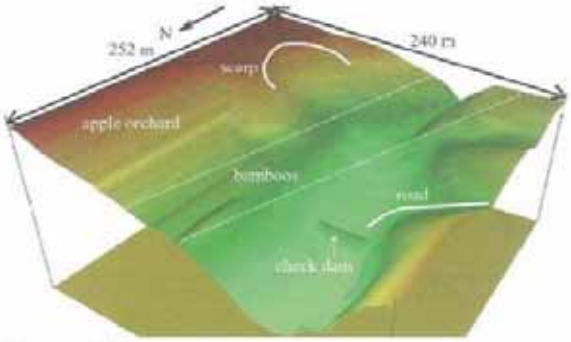

図－14　山科地すべりにおける地すべり運動シミュレーションの範囲

Fig. 14　Area of the landslide simulation before the landslide occurrence

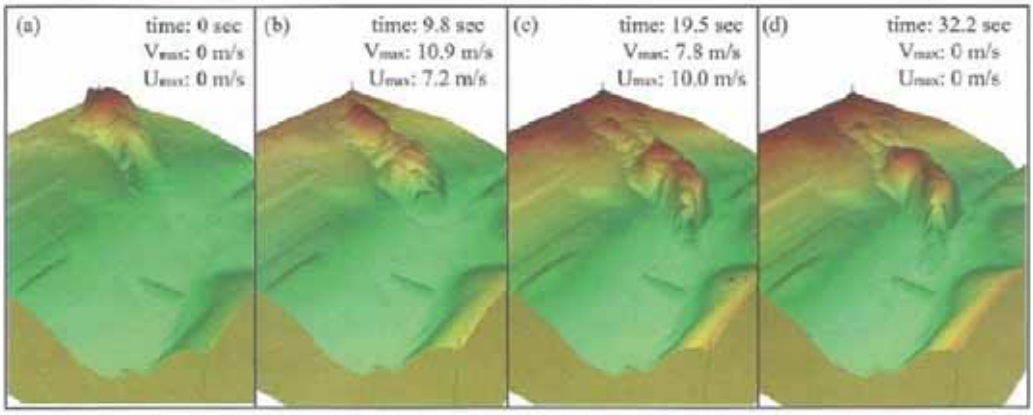

図－15　山科地すべりのシミュレーション結果（土塊厚さ：3倍に拡大表示）

Fig. 15　The simulation results of the Yamashina flowslide (Thickness of deposits is enlarged by 3 times)

崖に露出していたような風化泥岩が崩落の際に破砕した土であると判断できる。

4．山科地すべりの運動機構

山科地すべりの運動機構を明らかにするために，地すべり土塊の運動学的特性と連続性を考慮できる地すべり運動モデル（Sassa, 1988）にすべり面の見かけの摩擦係数項を改良したモデル（汪他，2004b）を導入した地すべり運動シミュレーションプログラムを用いて，山科地すべりの運動過程を再現し，すべり面のせん断抵抗変化挙動を考察する。

4.1　地すべり運動モデルの概要

Sassa（1988）は地すべり土塊に作用する力に基づいた運動方程式，及び運動中の体積変化が無いという前提条件の連続方程式をベースとした地すべり運動モデルを提案した。それに汪他（2004b）は地すべりはすべり面と運動土塊からなる二層構造を持つ特性から，(1)すべり面土は長距離せん断（300m:m程度）されると，定常状態に到達し，せん断抵抗が一定になる；(2)地すべり運動中，すべり土塊の厚さは徐々に薄くなる；(3)地すべり運動中は最初の加速過程を経て，減速運動となり，最終的に停止するという考え方に基づいて，すべり面の見かけ摩擦係数変化モデルを提案し，Sassa（1988）の地すべり運動モデルに導入した。

4.2　山科地すべり運動シミュレーション

シミュレーションを行った範囲は地すべり運動全体を把握できるように東西方向に240m（60メッシュ），南北方向252m（63メッシュ）とした（図－14）。図－14は運動シミュレーションを行った範囲と地すべり地周辺の植生状況などを示している。運動シミュレーションに用いた土質パラメータは，実際の堆積範囲に一致するように逆算法で定めた（表－2）。この内すべり土塊の単位体積重量は，室内試験より定めた。すべり面での定常状態でのせん断抵抗を竹林部とその他で分けた理由は，地すべり現場では，竹林が明らかにすべり土塊を厚く堆積させる役割を果たしており，その部分のせん断抵抗を高くすることは妥当であると考えたからである。発生直後の崩壊土砂は，完全に飽和しており，水溜りも多数見られ

表－2　地すべりシミュレーションに用いた土質パラメータ
Table 2　Soil parameters used in the landslide motion simulation

unit weight of sliding mass, γ_t (kN/m^3)	15.0
internal friction angle of sliding mass, ϕ'_m (deg.)	0
cohesion of sliding mass, c'_m (kPa)	40
horizontal earth pressure coefficient, K	0.6
shear resistance at the steady state of sliding surface	
bamboo area, τ_{ss1} (kPa)	50
the other area, τ_{ss2} (kPa)	10
effective friction angle of sliding surface, ϕ'_s (deg.)	35
possibility of excess pore pressure accumulation, B_m	0.99

たので，過剰間隙水圧蓄積率B_mは0.99とした。

図－15にt＝0，9.8，19.5，32.3secの運動シミュレーション結果を示す。運動土塊の動きを明確に示せるように，運動土塊の厚さを計算値の3倍にして表示した。シミュレーションによって求められた速度は東西方向の最大速度U_{max}と南北方向の最大速度V_{max}を示す。これらの速度は地すべり土塊のメッシュ間の移動速度である。地すべり土塊の最大移動速度は竹林到達前後で最も大きく10.9m/sであった。

運動シミュレーションにより，飽和している強風化泥岩の定常状態のせん断抵抗が10kPaと低いことが逆算された。このことは地すべりが流動化した原因であると判断できる。また，竹林部でのせん断抵抗が50kPaと逆算され，竹林部以外の部分に比べて，5倍のせん断抵抗であることがわかった。

4.3　山科地すべりの運動メカニズム

一般的に，第三紀泥岩層では再活動地すべりが多く，流動性地すべりはまれである。再活動地すべりが多く発生している原因は，すべり面が粘土状であり，その粘土がスメクタイトを多く含むことで，地すべりが繰り返し再活動しやすいと言われており，またスメクタイトの生成には凝灰岩が密接に関係している（守随，1999）。山科地すべり地の地質は泥岩であるが，スメクタイトの形成に重要な凝灰岩は調査地内には分布していないため，スメクタイトが含まれていないことが再活動地すべりに至らなかった原因の一つであると考えられる。

地すべりが流動化するには，運動中の過剰間隙水圧が高いままでなければならない。そしてせん断抵抗は過剰間隙水圧が増加することで低くなる。山科地すべりでは運動シミュレーションからせん断抵抗が低いことが明らかになっている。よって，13日間の長雨により地盤が飽和していたことと強風化泥岩の透水性が低いことが，地すべり運動中に発生した過剰間隙水圧が消散できずに，強風化泥岩の低せん断抵抗の原因となった。

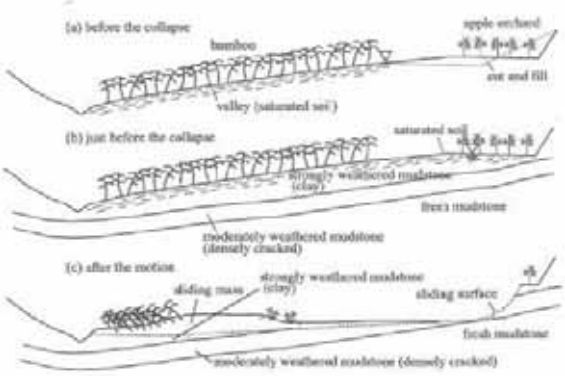

図－16　山科地すべりの斜面変化過程モデル
Fig. 16　Changing process of the Yamashina flowslide

山科地すべりの運動メカニズムをDCPT，ボーリング調査，雨量・流量観測及びトレンチ調査結果に基づき考察する。図－16は，山科地すべりの変形・崩壊・運動過程を示す。地すべり発生前（図－16(a)）は，谷地形であるため地盤は谷部では飽和していた。頭部では土地造成のための切土・盛土が行われ，斜面中～下部には竹が生えていた。地すべり直前（図－16(b)）では，強風化泥岩層が厚く分布していた。長雨により地盤は谷部だけでなく，その両側も飽和していた。斜面崩壊が発生すると（図－16(c)），地すべり土塊が表層と飽和した強風化泥岩を巻き込みながら移動した。その時，強風化泥岩は非排水状態で載荷されるので，透水性の低い飽和した強風化泥岩層のせん断抵抗は低くなる。よって，低せん断抵抗が保たれつづけたことが地すべりを流動化させた主な原因として考えられる。

5．結　論

山科地すべりでの現地調査，運動シミュレーションを通して，発生・運動機構について以下のことが明らかになった。

1）山科地すべりは連続降雨による地下水位の上昇によって発生した。

2）山科地すべりでの運動シミュレーションから，すべり面の定常状態のせん断抵抗が10kPa，竹林部は50kPa（竹林の土塊のせん断抵抗値ではなく，不動地盤上の竹と地すべり土塊中に含まれる竹の衝突が地すべりを減速させる効果を表現した値）と見積もられた。これにより強風化泥岩の定常状態でのせん断抵抗が低いこと，及び竹林の衝突が地すべり運動を減速させていたことが明らかになった。流動化の主な原因として，透水性の低い粘土化した強風化泥岩が飽和していたため，すべり面での過剰間隙水圧が消散しにくくなり，強風化泥岩が地すべり土塊により非排水載荷されるので，低いせん断抵抗が保たれ続けたことが考えられる。

謝　辞

石川県県央農林総合事務所の水道信二課長，縄大輔技師には地形図，ボーリングデータを提供していただいた。山科町生産組合の皆様には現場調査に関してご協力を頂いた。金沢大学の山上尚幸技官をはじめとする皆様には現場調査ならびに室内試験で協力を頂いた。以上の方々に感謝致します。

参考文献

Calvo, R. and Dente, G. (2003)：A flow slide in a pyroclastic soil fill, Proc. Fast Slope Movements Prediction and Prevention for Risk Mitigation, Napoli, Vol. 1, pp. 53－61.

地震調査研究推進本部地震調査委員会（2001）：森本・富樫断層の評価, http://www.jishin.go.jp/main/chousa/01dec_morimoto

給野義夫（1993）：新版石川県地質図(10万分の1)・石川県地質誌，北陸地質研究所，321p.

菊地宏吉・斎藤和雄（1976）：岩盤計測におけるコックシュミットハンマーの考案とその適用，電力土木，No. 145，pp. 47－53.

気象庁（2003）：http://www.data.kishou.go.jp

小出博（1955）：日本の地すべり－その予知と対策－，東洋経済新報社，259p.

Sassa, K. (1988)：Geotechnical model for the motion of landslides, Proc. 5th Int. Symp. on Landslides, Vol. 1, pp. 37－56.

佐々恭二（2002）：地震豪雨時の高速土砂流動現象メカニズムの解明　－大都市圏での災害とその防災－，都市域斜面防災の新世紀，地震豪雨時の高速長距離土砂流動現象の解明(APERIF)公開シンポジウム論文集，pp. 7－33.

守随治雄（1999）：第三紀層地すべり地におけるすべり面の発達過程とすべり面粘土の生成について，地すべり，Vol. 36，No. 2，pp. 13－23.

Wang, F.W. and Sassa, K. (2000)：Relationship between grain crushing and excess pore pressure generation by sandy soils in ring-shear tests, Journal of Natural Disaster Science, Vol. 22, No. 2, pp. 87－96.

Wang, F.W. and Sassa, K. (2002)：A modified geotechnical simulation model for the areal prediction of landslide motion, Proc. 1st European Conference on Landslides, Prague, pp. 735－740.

汪発武・田中康博・水道信二（2004a）：金沢市山科町における流動化地すべり，日本地すべり学会誌，Vol. 41，No. 1，pp. 70.

汪発武・佐々恭二・松本樹典・奥野哲志（2004b）：粒子破砕を考慮した地すべりの流動化メカニズムと運動範囲予測，日本地すべり学会誌，Vol. 40，No. 5，pp. 377－388.

大起理化工業株式会社（1979）：山中式土壌硬度計説明書，5 p.

柳沢幸夫（1999）：金沢市南部地域に分布する中新統の珪藻化石層序，地質調査所月報，Vol. 50，No. 1，pp. 49－65.

（原稿受付2004年4月12日，原稿受理2005年3月17日）

Wang, F.W., Wang, G., Sassa, K., Takeuchi, A., Araiba, K., Zhang, Y., Peng, X (2005)

Displacement monitoring and physical exploration on the Shuping Landslide reactivated by impoundment of the Three Gorge Reservoir, China

Landslides - Risk Analysis and Sustainable Disaster Management (ed. Sassa K, Fukuoka H, Wang G, Wang F), Springer Verlag, pp.313-319, 2005

Chapter 40

Displacement Monitoring and Physical Exploration on the Shuping Landslide Reactivated by Impoundment of the Three Gorges Reservoir, China

Fawu Wang* · Gonghui Wang · Kyoji Sassa · Atsuo Takeuchi · Kiminori Araiba · Yeming Zhang · Xuanming Peng

Abstract. The Three Gorges Dam construction on the Yangtze River in China is the largest hydro-electricity project in the world. After the first impoundment in June 2003, many landslides occurred or reactivated. Shuping landslide is one of the most active landslides among them. In this paper, the deformation of the Shuping landslide monitored by GPS, extensometers, and crack measurements are summarized. Also, for the investigation of the groundwater situation, 1 m depth ground temperature measurement was conducted, and the groundwater veins were estimated. Based on the monitoring data and exploration results, a deformation model of the landslide caused by impoundment of reservoir was proposed.

Keywords. Landslide, Three Gorges, impoundment, monitoring, groundwater

40.1 Introduction

The Three Gorges Dam construction on the Yangtze River in China is the largest hydro-electricity project in the world. The dam site is located at Sandouping Village near Maoping Town, the capital of Zigui County, Hubei Province. The designed final dam height is 185 m, the final length 2 309.5 m, and the designed final highest water level 175 m. When dam construction is finished, the Three-Gorge Reservoir will reach Chongqing City, about 660 km upstream from the dam. The first impoundment started from 95 m on 1 June 2003, and reached 135 m on 15 June 2003. As soon as the water level reached 135 m, many slopes began to deform and some landslides occurred (Wang et al. 2004). For example, in the early morning at 00:20 14 July 2003, Qianjiangping landslide occurred in Shazhenxi Town (Fig. 40.1) at the bank of Qinggan-he River, a tributary of the Yangtze River (Zhang et al. 2004).

Aiming to study the influence of impoundment on landslide deformation, we selected Shuping landslide, which is located at the main stream of the Yangtze River (Fig. 40.1) in Shazhenxi Town, just about 3.5 km from the Qianjiangping landslide, as our research and monitoring field. Figure 40.2 is an oblique photograph of the Shuping landslide, and Fig. 40.3 is the plane of the landslide. The landslide ranged its elevation from 65 m to 500 m. Its width was about 650 m, the estimated thickness of the sliding mass was 40 m to 70 m according to the bore hole data, and the total volume was estimated as 2.0×10^7 m^3. The toe part of the landslide was under the water level of the Yangtze River. The slope is gentle at the upper part and steep at the lower part with a slope angle of 22 degrees and 35 degrees respectively.

40.2 Features of the Shuping Landslide

The Shuping landslide is an old landslide which composed of two blocks. This can be confirmed in the photograph (Fig. 40.2). After the first impoundment of the Three Gorges Reservoir ended on 15 June 2003, obvious deformation phenomenon appeared at the slope, and it became intense from 8 February 2004. Also, the two blocks shows different deformation rate at slope surface. The serious de-

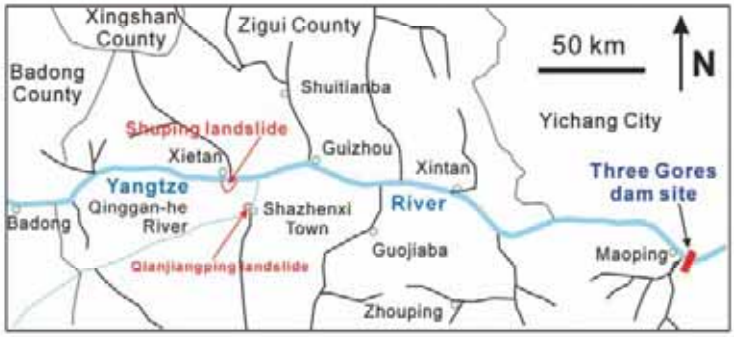

Fig. 40.1. Location map of the Shuping and Qianjiangping landslide in Three Gorge Water Reservoir area, Hubei Province

Fig. 40.2. Shuping landslide consisting of two blocks at the main stream of the Three Gorges Water Reservoir

Fig. 40.3. Plan of the Shuping landslide and locations of monitoring and measurement works (locations of extensometers and measurement area of 1 m depth ground temperature are shown)

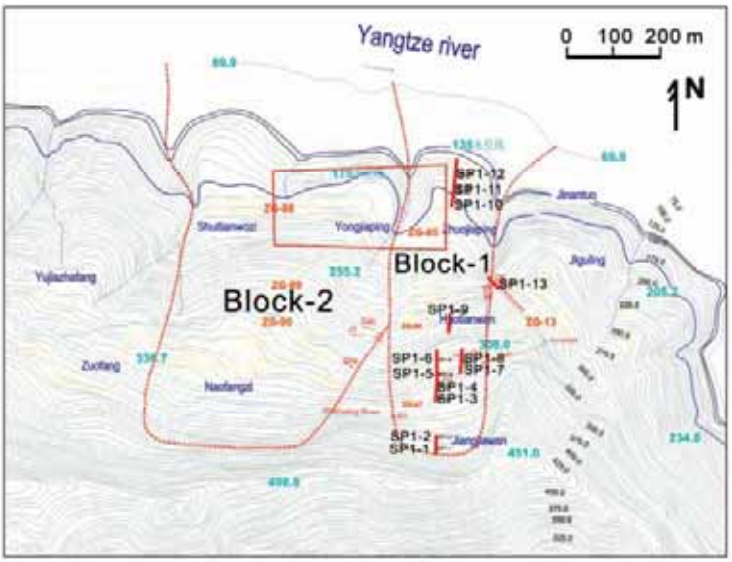

formation situation made 580 inhabitants and 163 houses in danger directly, and all of the inhabitants were asked to live in the disaster prevention tents which were provided by the central government. Until May 2004, most inhabitants moved their houses out of the landslide area.

Figure 40.4 shows a crack at the right boundary of block 1 outcropped at a local road. The right-hand side is the sliding mass consisting of red muddy debris of old landslide, and the left-hand side is bed-rock of sandy mudstone, muddy siltstone of Badong Formation of Triassic period (T3b).

Figure 40.5 shows muddy water coming from block 1. It appears at the river even at continual sunny days showing no relationship with surface water erosion, but the underground water erosion from the inner part of the landslide.

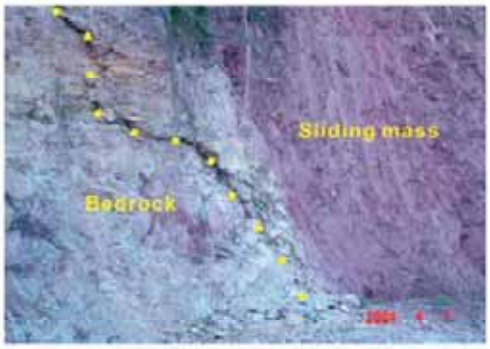

Fig. 40.4. Crack at the right boundary of block 1 outcropped at a roadside

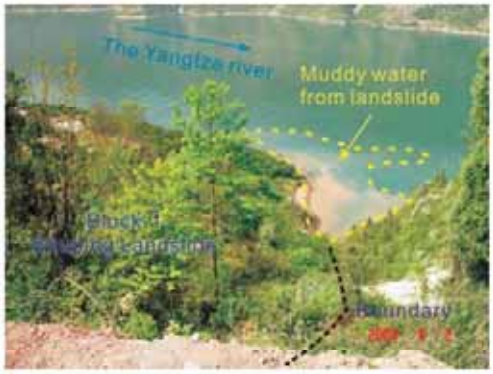

Fig. 40.5. Muddy water seeped out of the toe part of the Shuping landslide

40.3 Slope Deformation Characters of the Shuping Landslide

Because the landslide area is a densely populated area and its active deformation occurred just after the occurrence of the Qianjiangping landslide, the deformation situation was observed by the inhabitants and reported to the local government promptly. According to the urgent investigation report (Gan et al. 2004), the typical deformation behaviors were recorded as follows.

From the end of October to the beginning of November 2003: Cracks became obvious at the slope surface, especially at the upper part. These cracks were enlarged from January to February 2004.

On 5 January and 8 February 2004: The water at the toe part of the landslide became very muddy. From March, the muddy water appeared almost everyday. Figure 40.5 shows the muddy water situation in April 2004. This phenomenon is a very dangerous sign for slope deformation, because it may mean that the newly sheared soil at the sliding surface was eroded by underground water gradually.

On 25 January and 8 February 2004: Sharp noises coming from underground were heard by the inhabitants at night for two times. The noise is possibly caused by shearing at the sliding zone.

Because of the serious deformation situation, local government decided to monitor the cracks distributing in the slope from 12 February 2004. The inhabitants were asked to measure the width change of the cracks near their houses (see Fig. 40.3). For measurement, two small piles were set across a crack, and the distance between the two piles was measured three times one day. Figure 40.6 shows a part of the measured results of the cracks. However, because the inhabitants are moving out of this area, the measurement points are decreasing gradually.

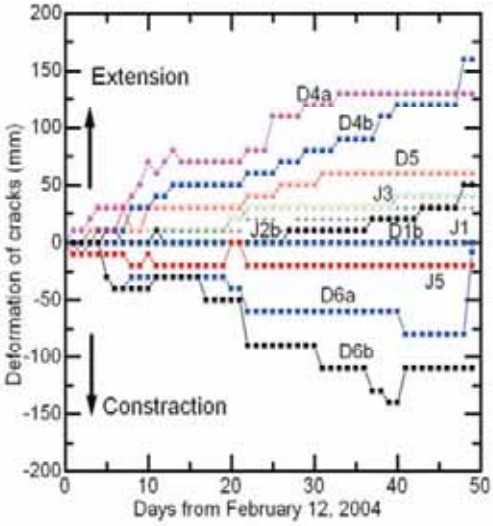

Fig. 40.6. Measured results of crack deformation in block I

Roughly, the measurement results of the crack deformation shows that the extension behavior occurred at the boundary and inside landslide, and contraction deformation occurred at the other parts in the landslide block. For the 50 days period from 24 February 2004, the maximum displacement including extension and contraction respectively reached about 140 mm, showing an active deformation.

40.4 GPS Monitoring Results

Two GPS monitoring lines were arranged at the central longitudinal section of the two blocks by China Geological Survey. Each monitoring line has three GPS monitoring points, i.e., ZG85, ZG86 and ZG87 from toe to upper part in block I, and ZG88, ZG89 and ZG90 from toe to upper part in block II (see Fig. 40.3). The monitoring started in July 2003, just one month after the first impoundment. The measurements were conducted one time each month by Rockfall and Landslide Research Institute of Hubei Province.

Figure 40.7 shows the monitored results of the GPS monitoring at the first six months after the impoundment. The displacement rate of block I increased rapidly after October 2003, and other two tendencies are also very clear. (1) The displacement at the lower part is larger than that at the upper part, this may be caused by water buoyant of the impoundment of the reservoir; (2) The displacement of block I is more active than block II, showing that the two blocks are independent from each other.

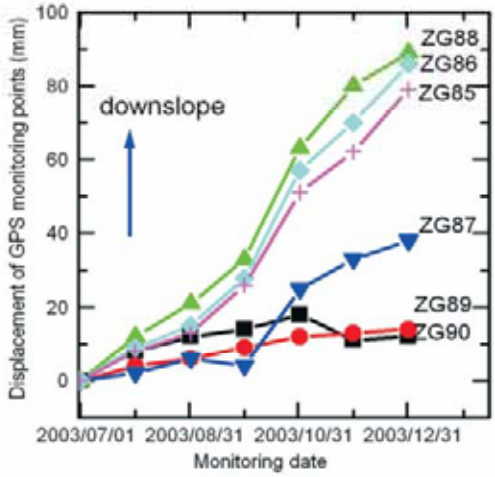

Fig. 40.7. GPS monitored results along the central section lines of block 1 and block 2

Fig. 40.8. Extensometer installed in Shuping landslide. The deformation is recorded on the rolled paper and also saved in a memory (visible in the right side)

40.5 Installation of Extensometer and the Monitoring Results

Until April 2004, the displacement monitoring of the Shuping landslides included crack measures conducted three times each day, and the GPS monitoring conducted one time each month. However, because of the evacuation of the inhabitants, the crack monitoring was interrupted gradually. Located at the main stream of the Yangtze River, it is not enough for the Shuping landslide to be monitored only with GPS when considering the safety of shipping along the Yangtze River. Although GPS monitoring has high precision, the time interval of measurement is too large. Facing this situation, two extensometers donated by Kowa Co. LTD., a Japanese company, were installed in the block I of the Shuping landslide in April 2004. The extensometer is Sakata Denki style. The monitoring can continue for one week or one month automatically. A warning system is also connected with the extensometer. When the displacement rate exceeds 2 mm h^{-1}, a warning will be announced.

The automatic monitoring with the extensometer was confirmed to be working well (Zhang et al. 2004). However, two extensometers are not enough for such a large landslide. In August 2004, another 11 extensometers were installed along the central line of the longitudinal section of block 1, with emphasizing on the serious deformation parts. Also because of the limit of funds, the extensometers cannot form a continual longitudinal section line.

Figure 40.8 shows the extensometer installed in Shuping landslide. The positions of all of the thirteen extensometers were shown in Fig. 40.3 as "SP1-x". Among them, SP1-1 and SP1-2 were set across the main scarp; SP1-3 to SP1-6 were set below the Shahuang road which has a high traffic. SP1-7 and SP1-8 were set almost parallel with SP1-5 and SP1-6. SP1-9 was set at the low part. Then, SP1-10, SP1-11, and SP1-12 were set near the Yangtze River at the toe part of the landslide. SP1-13 was set at the right boundary of block 1 shown in Fig. 40.4, because the crack extension is obvious.

Figure 40.9 is the monitoring results of all the thirteen extensometers from August 2004 to June 2005, companying with the water level in the Three Gorges at dam site showing at the bottom, and the rainfall records of this area showing at the top.

The monitoring results show some tendencies of the landslide displacement. (1) The SP1-1 and SP1-2 at the main scarp did not record obvious displacement. One

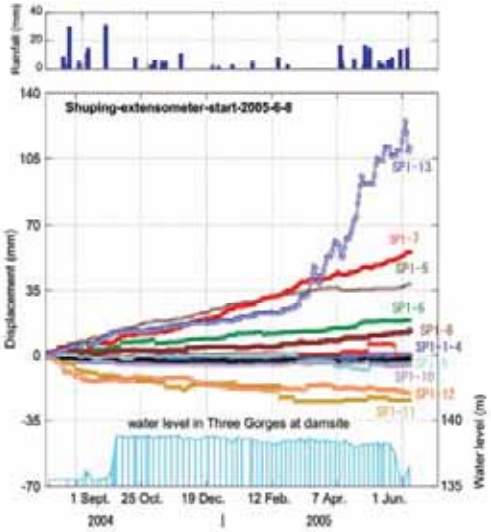

Fig. 40.9. Monitored results of the extensometers (*middle*), the precipitation data in Yichang City (*top*) and water level in the Three Gorges Dam site (*bottom*)

possible reason is that the setting positions of the two extensometers did not cross the main scarp. (2) The deformations at SP1-5, SP1-6, SP1-7 and SP1-8 were the most active ones showing extension. Because of local failure, the SP1-13 showed extremely great extension. (3) The toe part of the landslide showed compression behavior. Comparing with the largest displacement at the lower part by GPS monitoring in the first six months after the first impoundment, it may estimate that the toe part moved down faster at the first period and became silent now; the upper part moved slowly at the first stage, and now followed the movement of the lower part and compressed the lower part. An exact examination will be conducted with the comparison of the recent GPS monitoring data along the central longitudinal section, which is not open currently.

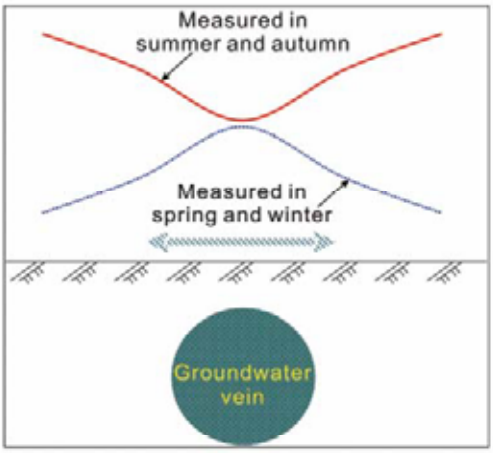

Fig. 40.10. Principle of the 1 m depth ground temperature measurement

Another important tendency was recorded in the monitoring results. In mid-September, the water level of the Three Gorges was raised for about 3 m, corresponding to this water level raising, the displacement velocity of SP1-5, SP1-6 and SP1-7 in-creased obviously, reflecting the influence of the impoundment on the slope deformation. Also, during the rainy season after April 2005, displacement acceleration tendency at some point (SP1-6, 7, 8) was monitored, showing the displacement of the landslide is also influenced by groundwater conditions.

40.6 One Meter Depth Ground Temperature Measurement for Groundwater Veins

Takeuchi (1972) developed a method for the investigation of groundwater veins through 1 m depth ground temperature measurement. This method is widely applied in the practice of groundwater exploration in landslide area, especially in Japan (Takeuchi 1996).

Figure 40.10 shows the principle of the 1 m depth ground temperature measurement for groundwater vein. Comparing with the ground without water, the ground with water always has a temperature similar to that of the groundwater. Generally, groundwater temperature does not change so much around a year. While, the temperature in the ground without water is controlled by the atmosphere temperature, which will be higher than groundwater in summer and autumn, and lower in spring and winter. Through measuring the temperature distribution in an area, the distribution situation of groundwater vein can be estimated.

One meter depth ground temperature measurement was conducted to detect the groundwater veins in the lower part of the Shuping landslide. The measured area was shown as a square in Fig. 40.3. Figure 40.11 is the

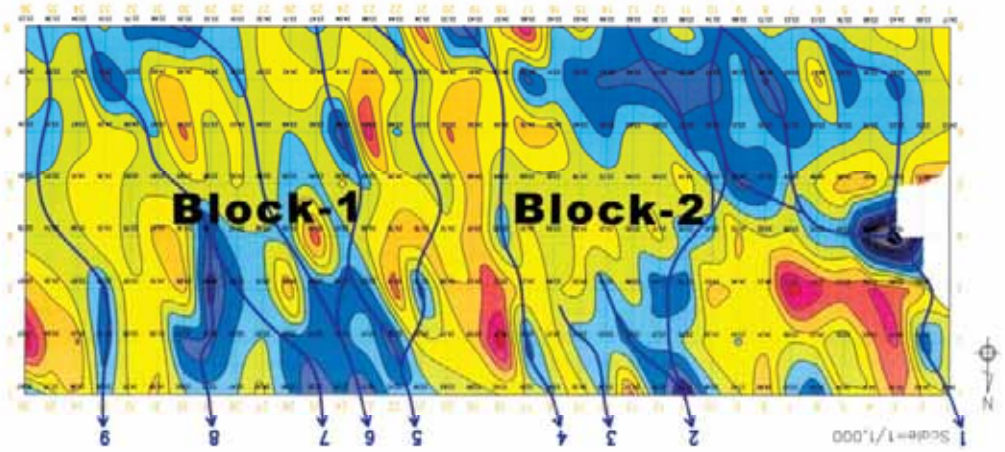

Fig. 40.11. Groundwater veins distribution estimated from 1 m ground temperature measurement

measured results. From the ground temperature distribution, two independent groundwater vein groups were estimated existing in block 1 and block 2. The exit of the groundwater vein in block 1 is lower that that in block 2. It is estimated that the groundwater veins no. 8 and no. 9 correspond to the muddy water seeped from block 1.

To confirm the above estimation, and to explore the sliding surface, a borehole drilling was conducted at SPZK-1, as shown in Fig. 40.11. Figure 40.12 is the column diagram of this borehole. The groundwater table was found at 8.8 m depth, and the sliding zone formed at the depth between 66.7 and 75.9 m. The sliding zone consisted of silty clay with 30% gravel. Scratches caused by sliding are rich in the zone.

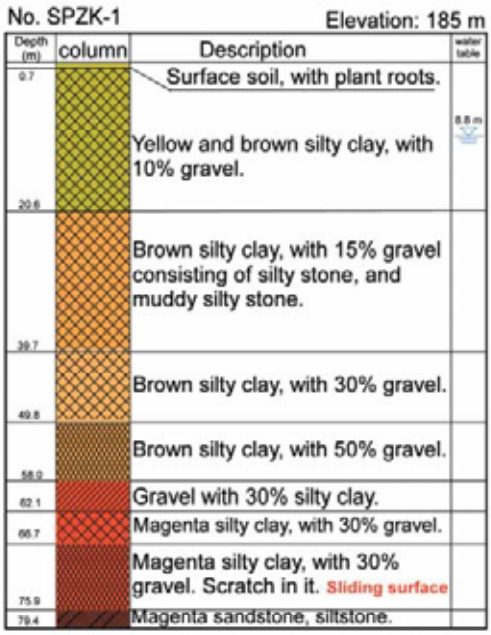

Fig. 40.12. Column diagram of borehole SPZK-1 in block 1 of Shuping landslide

40.7 Summaries and Conclusive Remarks

Through the GPS monitoring, crack displacement measurements, extensometer monitoring along the longitudinal section of block 1, the deformation style of the block 1 of Shuping landslide can be sketched as Fig. 40.13. Sooner after the impoundment of the water reservoir, the toe part displaced downward faster than the upper part. In the current stage, two years after the first impoundment, the slope deformation style changed. The displacement of the lower part almost terminated while the upper part displaced downward gradually, and compressed the toe part.

For the Shuping landslide, reactivating from an old landslide and with rich groundwater in it, the influencing factors on the slope deformation is complicated. From about one year monitoring with the extensometers, it is very clear that the slope displaced soon after the impoundment of the water reservoir. It is very important to keep the monitoring continued especially during the next stage of impoundment which will be conducted in June 2006 (water level will be raised from 139 m to 156 m).

Acknowledgments

Deep thanks are given to Mr. Masahiro NAGUMO in Kowa Co. LTD., Japan for donation of two extensometers. The local government of Shazhenxi supplied measurement results of the crack displacement. The research fund from Sabo Technical Center, Japan is highly appreciated.

Fig. 40.13. Longitudinal section of the Shuping landslide

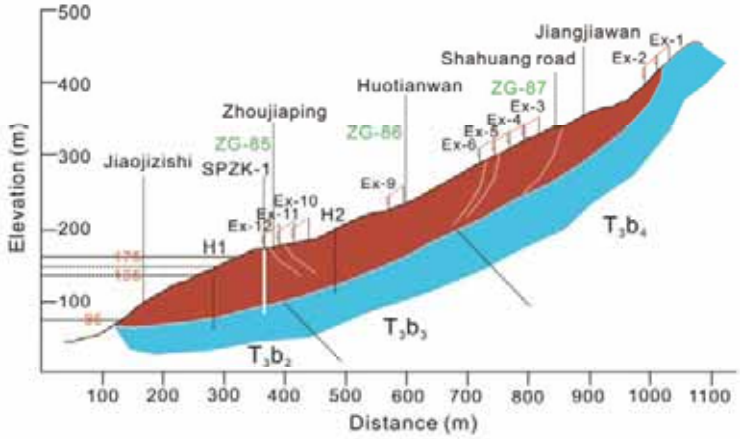

References

Gan YB, Sun RX, Zhong YQ, Liao SY (2004) Urgent investigation report on the Shuping landslide in Shazhenxi Town, Zigui County, Hubei Province. (in Chinese)

Takeuchi A (1972) Ground temperature measurement in landslide area. Journal of Japan Landslide Society 8(4):29–37 (in Japanese)

Takeuchi A (1994) Flowing groundwater investigation by temperature measurement. Kokon Syoin Press (in Japanese)

Wang FW, Zhang YM, Huo ZT, Matsumoto T, Huang BL (2004) The July 14, 2003 Qianjiangping landslide, Three Gorges Reservoir, China. Landslide 1(2):157–162

Zhang YM, Liu GR, Chang H, Huang BL, Pan W (2004) Tectonic analysis on the Qianjiangping landslide in Three Gorges Reservoir area and a revelation. Yangtze River 35(9):24–26 (in Chinese)

Zhang YM, Peng XM, Wang FW, Huo ZT, Huang BL (2004) Current status and challenge of landslide monitoring in Three Gorge Reservoir area, China. Proc. of Symp. on Application of realtime information in disaster management, JSCE, pp 165–170

F.W. Wang, Y.M. Zhang, Z.T. Huo, T. Matsumoto, B.L. Huang
(2004)

The July 14, 2003 Qianjiangping Landslide, Three Gorges Reservoir, China

Landslides: Journal of the International Consortium on Landslides, Vo.1, No.2, pp.157-162

Landslides (2004) 1:157–162
DOI 10.1007/s10346-004-0020-6
Received: 14 April 2004
Accepted: 2 May 2004
Published online: 23 June 2004

Fa-Wu Wang · Ye-Ming Zhang · Zhi-Tao Huo · Tatsunori Matsumoto · Bo-Lin Huang

The July 14, 2003 Qianjiangping landslide, Three Gorges Reservoir, China

Abstract The Qianjiangping landslide occurred after the first impoundment of the Three Gorges Reservoir in July 2003. Field investigation revealed that failure occurred when the reservoir reached 135 m, but the stability of the affected slope was already reduced by pre-existing bedding-plane shears, quarrying of mudstone from the landslide toe, and previous heavy rain. A possible explanation of the rapid and long runout mechanism of the landslide is that movement on a bedding-plane shear ruptured the calcite cement and rapidly reduced the sandstone strength to residual shear strength.

Introduction

The Three Gorges Dam construction on the Yangtze River in China is the largest hydro-electricity project in the World. The dam site is located at Sandouping village near Maoping, the capital of Zigui County, Hubei Province. The designed final dam height is 185 m, the final length 2,309.5 m, and the designed final highest water level 175 m. When dam construction is finished, the Three Gorges Reservoir will reach Chongqing City, about 660 km upstream from the dam. The first impoundment started from 95 m on June 1st, 2003, and reached 135 m on June 15th, 2003. Shortly after the water reached 135 m, many slopes began to deform and some landslides occurred.

In the early morning, at 00:20 July 14, 2003, the Qianjiangping landslide occurred at Shazhenxi Town (Fig. 1) beside Qinggan-he River, a tributary of the Yangtze. The Qianjiangping landslide was located on the western side of Qinggan-he River. On the opposite side of the river is the main street of Shazhenxi. The distance from the landslide to the junction of the Qinggan-he River with the Yangtze is about 3 km, and the distance along the Yangtze River from the junction to the Three Gorges Dam is about 50 km (the direct distance is about 40 km).

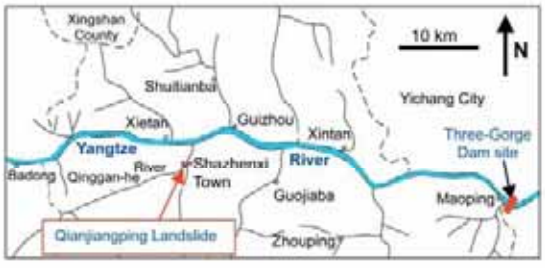

Fig. 1 Location map of the Qianjiangping landslide in the Three Gorges Reservoir area, Hubei Province, China

Features of the landslide

Figures 2 and 3 are photographs of the landslide taken from the upstream side and front of the landslide. The landslide had a tongue-shaped plan, with a length of 1,200 m, and a width of 1,000 m. It moved about 250 m in the main sliding direction of S45°E. The average thickness of the sliding mass was about 20 m, thinner in the upper part and thicker at the lower part. The total volume was estimated to be more than 20 million cubic meters. The elevation of the main scarp was 450 m, and the elevation of the Qinggan-he River water level was 135 m when the landslide occurred. The landslide release surface was along a bedding plane in the bedrock (Fig. 2). Factory buildings on the sliding mass still remained standing after sliding for about 250 m (Fig. 3). However, because serious cracks developed in the buildings, they could not be used again and were demolished and the building materials were recycled (compare with Fig. 2). Standing trees on the sliding mass in the middle of the landslide (Fig. 4) indicate that the angle of the sliding surface remained constant and no rotation occurred. The exposed sliding surface at the upper part was very planar, and sub-parallel to the sandstone bedrock strata (Fig. 5). All of these phenomena show that the sliding mass slid along a planar sliding surface. When the sliding mass entered Qinggan-he River, the dip direction of the strata was changed to N45°W, which is opposite to the original dip direction of S45°E. The dip angle is about 5° in the bed of Qinggan-he River (Fig. 6). The deposits at the distal landslide margin contain white gravel with clasts up to 100-mm-or-so in diameter. The dip angle of the sandstone bedding at the distal margin is steeper than 30° (Fig. 7).

Losses caused by the landslide

There was some loss of life and serious economic damage caused by the Qianjiangping landslide. It destroyed 346 houses and 70 ha of fields and rice paddy. Four factories on the lower part of the slope near Qinggan-he River (a brick factory, a metal and silica factory, a chemical fertilizer factory, and a food factory) were seriously damaged. Direct economic losses were about 7 million USD, and it reduced the asset value at Qianjiangping by 40%. Most of the workers became unemployed. In addition, 3 km of provincial roads and 20.5 km of electricity lines were cut. Twenty-two boats and ships were damaged and sunk in Qinggan-he River and the Yangtze River. Although a warning was given by the local government based on precursory deformation of the slope two hours before the final failure, 13 people on the slope, and 11 fishermen on boats in the nearby area were killed. The main reason for the deaths on the slope was that the people did not imagine that the landslide area would be so large, and believed their houses would be safe, because there was no ground deformation around them before the final failure of the slope. For the deaths on the river, the reason was just that it was not predicted that the landslide could move so rapidly. It was the wave caused

Fig. 2 View of the Qianjiangping landslide from the upstream side of Qinggan-he River (taken by FW Wang, March 15, 2004)

Fig. 3 Front-on view of the Qianjiangping landslide (taken by YM Zhang, July 15, 2003)

by the rapid sliding that killed the fishermen on their boats. A water trace left on the red bridge (shown in Fig. 2) detected after the landslide, indicated that the highest level of the wave was about 30 m above the water level of 135 m.

Geological conditions

The geological strata at the site are beds of quartzo-feldspathic sandstone, fine sandstone with carbonaceous siltstone, siltstone with mudstone, and silty mudstone of the Shazhenxi Group of Late Triassic age. Before the landslide occurred, the geology was thought to be very simple, and the slope was considered safe because no landslide trace on the slope was observed during the field investigation for the Three Gorges Dam construction. It looked like a simple slope with a dip structure. However, scratches (slickensides) on the sliding surface exposed after the sliding suggests a reasonable explanation for the sliding mechanism of the rapid, long-runout landslide (see below).

Scratches on the failure surface

Figure 8 show a sequence of two photographs of scratches on the sliding surface at the upper part of the landslide. Figure 8(a) shows the original situation, while in Fig. 8(b) a slice of sandstone has been stripped away from the plane to reveal more scratches. This shows that the scratches were present beneath the landslide sliding surface before the landslide occurred. The scratch strike direction is S15°W (red arrow). The sliding direction (S45°E) of the July 2003 event (blue arrow) is also shown by the water dribble trace in Fig. 8(b). The angle between the sliding direction and the scratches is about 60°. Comparison of the two photographs shows that the scratches were not formed by the event of July 2003. They must have formed earlier, probably in a much older geological event, because calcite veinstone is widely distributed along them. This site lies between the Zigui syncline and Baifulai-Liulaiguan anticline that were folded during the Cretaceous Period (Wang et al. 2002) and so the scratches can be interpreted as slickensides along bedding-plane shears.

Possible triggering factors and sliding mechanism

The high water level within the landslide toe caused by impounding of the Three Gorges Reservoir was naturally considered to be the trigger. Impoundment started from June 1st, 2003, and the reservoir water level reached 135 m on June 15th, 2003. The

Fig. 4 View of the unrotated trees on the sliding mass in the middle of the Qianjiangping landslide

Fig. 5 The exposed planar sliding surface, which is also a sandstone-bedding plane (there is a damaged rice paddy in front of the person)

first cracks due to the slope deformation, however, were observed on October 22nd, 2002 near the present main scarp. This means that the slope was in a critical state even before impoundment of the reservoir. With the slope in such a critical state, failure probably was triggered by the direct reduction in normal load within the toe of the slope caused by the rising water level.

According to local people, sandstone and mudstone were exposed in the Qinggan-he River bank before the reservoir was impounded. The dip angle of the sliding surface, which is also a bedding plane, was measured as 32° at the upper part. Zhang et al. (2004) observed two sets of large transversal cracks crossing the upper and middle parts of the slope. Although some rice paddies

Fig. 6 View of the reversed dip direction of the sandstone beside Qinggan-he River (taken by FW Wang, March 16, 2004)

Fig. 7 Gravels displaced from the bed of Qinggan-he River and deposited in the toe of the landslide deposit (*circled* in photograph). Note that the sandstone dip direction is reversed and the dip angle has become steeper compared with Figs. 4 and 5)

were located on the upper part of the landslide (Fig. 3), the associated high water table from irrigation should have been kept perched by the impervious weathered mudstone. The rice paddy was started ten years ago, and a pond for water supply was built near the paddy. So, for landslide stability analysis, the boundary conditions for the landslide are very clear. There was little volume of landslide in the uppermost part. The right lateral boundary was open, and so had no friction to resist sliding. As shown in Fig. 8, the sliding surface was a pre-existing structural shear-plane.

Precipitation is monitored in Yichang City (Fig. 1), about 70 km from the landslide site. Intense rain from June 21st to 26th, and rain from July 4th to July 9th (Fig. 9) may have saturated the sliding mass, and increased its unit weight. However, considering the high permeability of the slickensided sandstone, and the transverse cracks crossing the sliding mass, it is not likely that high pore pressure would have resulted.

The landslide toe had been eroded by the Qinggan-he River long ago, and offered little resistance to sliding. Only the left lateral boundary offered side friction and tension resistance from

Fig. 8 A pair of photographs at the same site showing the pre-existing scratches that underlie the sliding surface of the July 2003 event (*blue arrow* shows the sliding direction, *red arrows* show the strike direction of the pre-existing scratches). The scratches are inferred to be slickensides formed by bedding-plane shear during folding of the rocks in the Cretaceous Period

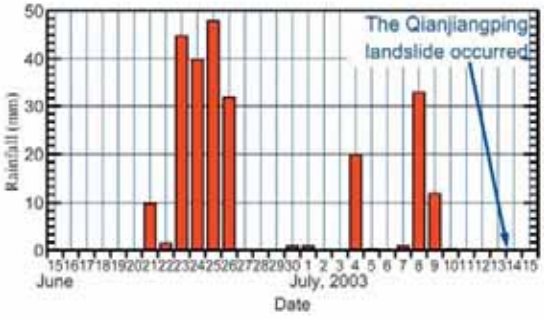

Fig. 9 Precipitation data monitored in Yichang City, 70 km from the landslide

the neighboring rock mass. For such a huge landslide, the mechanical model can be simplified as a two-dimensional longitudinal section as shown in Fig. 10(a). The situation of the landslide after failure is sketched in Fig. 10(b).

With the slope in a critical state (Fig. 10a), an increase in water level in the river would decrease the effective normal stress in the toe of the slope, and the shear resistance would decrease at the same time. These changes in the mechanical balance resulted in the slope failure.

For additional factors contributing to the failure, some attention should be paid to the factories on the lower slope before the landslide occurred. The brick factory had been quarrying mudstone in the lower part of the slope as raw material for brick making from 1997. Some 2–3 million bricks (each about 250x120x50 mm) had been produced during the six years. Such removal of mass from the toe of a landslide is a very dangerous action that leads to slope instability (but the presence of the landslide was unrecognized by experts until the cracks appeared in 2002).

When the existence of the widely distributed scratches on the sliding surface is considered, it is easy to assume that the shear strength between the sliding mass and the sliding surface was at residual strength. If this assumption were true, the rapid, long-runout sliding would be difficult to explain, because a rapid loss of shear strength is necessary to achieve the high rate of acceleration. As mentioned previously, the scratches probably were formed in the Cretaceous Period, and the beds on either side of the scratched surface were bonded together with calcite cement. After the occurrence of the landslide, Zhang et al. (2004) observed crushed crystalline calcite, some 20 to 30-mm thick, widely distributed on the exposed sliding surface on the upper part of the landslide. Figure 11 shows a sample of the calcite. Generally, failure of crystalline calcite is characterized by brittle fracture. After a certain small distance of shearing, the cement

Fig. 10a,b Structural model of the Qianjiangping slope (**a**) and a sketch of the landslide after failure (**b**)

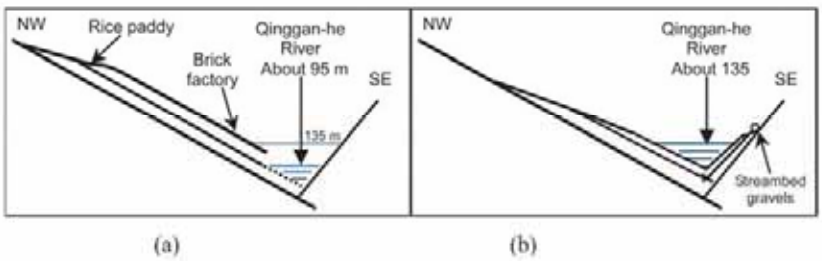

Fig. 11 Photograph of a crystalline calcite sample taken from the sliding surface at the upper part (the white color is crystalline calcite)

bonding would have been destroyed. The quick loss of adhesion of the crystalline calcite could be the main reason for the rapid landslide acceleration after the initial failure of the slope.

Conclusions

A detailed field investigation was made of the Qianjiangping landslide that occurred after the first impoundment of the Three Gorges Reservoir. The mechanisms of the landslide, especially the factors affecting slope failure were studied, and reasons for the rapid and long distance movement of the landslide were considered. Based on fieldwork and analyses, the following conclusions were reached:

1. The Qianjiangping landslide is a landslide with dip structure. The sliding surface was along a pre-existing structural plane of weakness (a bedding-plane shear).
2. Quarrying of mudstone for brick manufacture from the toe of the slope, and intense rainfall before the landslide put the slope in a critical state. This is not to assign blame for the landslide on the operators of the brick factory. Although quarrying of rock from the toe of a landslide is not good practice, there was no information to indicate that it was bad practice until the landslide was recognized. Prior to the cracks appearing, there appears to have been no reason to expect that the slope was unstable, and hence little reason to exercise caution.
3. The high water level in Qinggan-he River through impoundment of the reservoir was the trigger for the landslide occurrence.
4. Brittle fracture of crystalline calcite caused a quick loss of shear strength along the sliding surface, which is the main reason for the rapid movement of the landslide after the slope failure.
5. Because the landslide has a tectonic background, and there are many similar slopes in the nearby area, detailed evaluations for those slopes are very important for the future stability of the Three Gorges reservoir when it is raised to its final operating level.

Acknowledgements

The local government of Shazhenxi supplied useful information about the slope deformation and economic losses. Field investigation was partially supported by research grants (No. 15310127, Representative: F.W. Wang) from the Ministry of Education, Culture, Sports, Science, and Technology of Japan (MEXT), and IPL M2002-102 (Representative: T. Matsumoto) from the International Consortium on Landslides (ICL). Comments given by Mauri McSaveney were deeply appreciated.

References

Wang XF, Chen XH, Zhang RJ (2002) Protection of geological remains in the Yangtze Gorges area, China with the study of the Archean-Mesozoic multiple stratigraphic subdivision and sea-level change. Geological Publishing House, Beijing, 341 pp (in Chinese)

Zhang YM, Liu GR, Chang H, Huang BL, Pan W (2004) Tectonic analysis on the Qianjiangping landslide in Three Gorges Reservoir area and a revelation. Journal of Yangtze River (submitted, in Chinese)

F.-W. Wang (✉)
Disaster Prevention Research Institute,
Kyoto University,
Gokasho, 611-0011 Uji Kyoto, Japan
e-mail: wangfw@landslide.dpri.kyoto-u.ac.jp
Tel.: +81-774-384114
Fax: +81-774-384300

Y.-M. Zhang · Z.-T. Huo · B.-L. Huang
Environmental Geology Section,
Yichang Institute of Geology and Mineral Resources,
China Geological Survey,
Gangyao Road 37, 443003 Yichang, China

T. Matsumoto
Geotechnical Engineering Group,
Graduate School of Natural Science and Technology,
Kanazawa University,
Kodatsuno 2-40-20, 920-8667 Kanazawa, Japan

宮島昌克・奥野洋平・北浦　勝
(2006)

白山における地震時の斜面崩壊危険性の評価

日本海域研究，No.37, 15-21

白山における地震時の斜面崩壊危険性の評価

宮島昌克[1]・奥野洋平[2]・北浦　勝[1]

Estimation of Earthquake Induced Slope Failure Potential of Mt. Hakusan

Masakatsu MIYAJIMA[1], Yohei OKUNO[2] and Masaru KITAURA[1]

***Key Words*:** earthquake, hazard, Mt. Hakusan, slope failure

1. はじめに

石川県と岐阜県の県境に位置する白山は，急峻な地形，多雨・多雪の気象状況および軟弱な砂岩・頁岩互層からなる地質状況を有しており，古くから土砂災害が多発している．そのため 1912 年から石川県によって初めて治山事業が開始され，1927 年には国の直轄事業として本格的な砂防事業が開始、1962 年には地すべり防止区域に指定されている．土砂崩壊の起因としては降雨や雪解け水などが主たるものであるが，この他に内陸型の地震が考えられる．特に白山は周囲を複数の断層帯に囲まれており，地震が発生する可能性が高い地域にある．また，白山を源流とする手取川は，河床勾配が大きい急流河川であるため，通常の河川よりも短時間で土砂や洪水が下流の生活地域へ到達する危険性が高い．そのため地震が発生した場合，斜面崩壊によって発生した大量の土砂が手取川から流出し，下流の白峰地区などに甚大な被害をもたらす恐れがある．

本研究は，地震発生時に大規模な土砂の崩壊が起こる可能性やその規模を推定することを目的とする．これらは防災対策を考える上で，重要な資料となり得る．三霊山の１つである白山は，毎年約５万人の登山客が訪れている観光地でもある．したがって登山客の安全を考える上でも，本研究は重要である．

本研究では、まず過去の地震で土砂崩壊の生じた地点を全国の事例から抽出して距離減衰式を用いて最大加速度を計算し，土砂崩壊が発生しうる加速度を推測した．それを，過去に白山周辺で地震が発生した際の白峰観測所における推定最大加速度と比較して，過去の地震で白山で土砂崩壊が発生した可能性を検討した．また、過去の土砂崩壊の記録を用いて，土砂の崩壊量と崩壊地点の最大加速度の関係を，傾斜角や地質を考慮した上で検討した．こうして得られた結果を基に白山の地震による斜面崩壊危険性の評価を行った．

2. 白山周辺地域の特徴と災害史

2.1 白山の概要

図１に白山の位置を示す．白山は 2,703m の標高を有する独立峰であり，御前峰と剣ヶ峰，大汝峰の３つの峰が山頂部を形成している．白山には複数の地すべりブロックが存在しており，最も規模の大きいものが甚之助谷地すべりである．

[1] 金沢大学大学院自然科学研究科（Graduate School of Natural Science and Technology, Kanazawa University）
[2] 魚津市土木部（元　金沢大学学生）(Department of Civil Engineering, Uozu City Office)

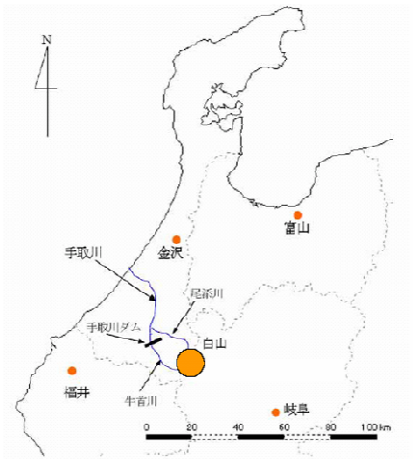

図１　白山の位置

図２　地すべり防止区域の航空写真 [1)]

この周辺は，御前峰から南の別山に伸びる稜線の西側直下の斜面であり，溶岩流の噴出によって形成された緩斜面である南龍ヶ馬場を除けば，斜面傾斜 30°を超える急峻な地形となっている．甚之助谷地すべりは標高 1,200m から 2,100m の区域に位置しており，全国でも極めてまれな高山地域にある大規模地すべりである．地すべり防止区域は御前峰を最高点とし，甚之助谷を中央に別当谷・柳谷・万才谷を含む区域である．図２に国土交通省によって撮影された地すべり防止区域の航空写真[1)]を示す．

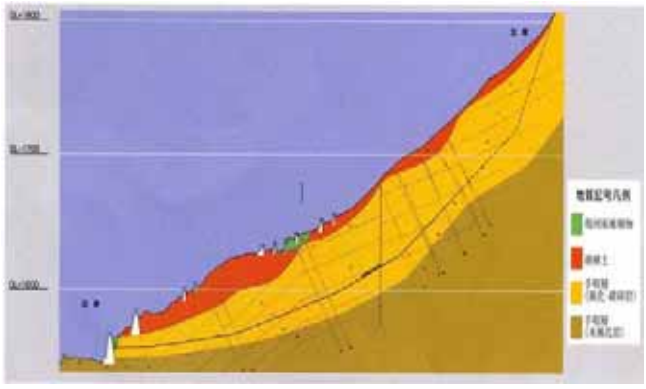

図３　甚之助谷地すべりの断面図 [1)]

図４　白山周辺の地質図 [1)]

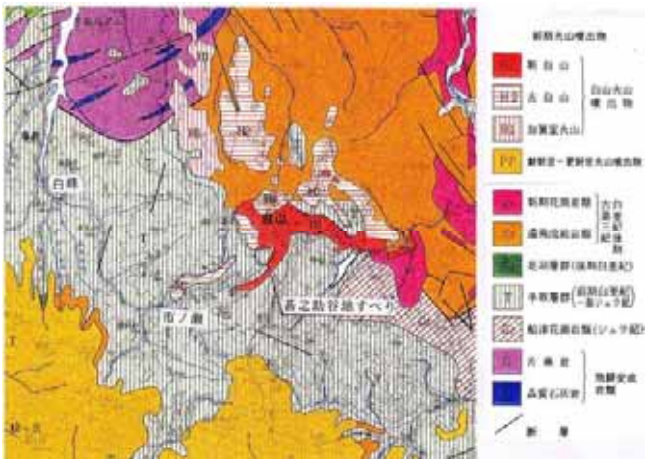

2.2 白山周辺の地質状況

国土交通省北陸地方整備局金沢河川国道事務所(2003)「甚之助谷地すべり」[1)]から転載した甚之助谷地すべりの断面図を図３に，甚之助谷地すべりとその周辺の地質図を図４に示す．白山の基盤岩は古生代の飛騨片麻岩であり，その上に中生代ジュラ紀～白亜紀前期の湖成堆積層である手取層群の頁岩・砂岩互層及び礫岩が広く分布している．手取層群の上を白亜紀の濃飛流紋岩，そして第四紀の古白山火山噴出物(10 万年前)，新白山火山噴出物(1 万年前)が覆っている．

白山を構成している地質のうち，手取層群は，構造運動による破砕と熱水変質あるいは温泉変質によって粘土化し，破砕と風化が著しくなっている．また断層の破砕帯が縦横に存在しているため，これらを伝わって豊富な地下水が被圧耐水層に流

入し，間隙水圧が増加しやすい状況となっていることから,地すべりが発生しやすい地質といえる.

2.3 白山における歴史的災害

白山の歴史時代の災害については，700 年代初めから 1600 年代中ごろまで周期的に噴火し,1659 年に最後の噴火活動を起こしたと文献に記録されている．706 年，1042 年及び 1554 年～1659 年の三回の活動期を統計的に見ると，噴火の活動周期は 100～150 年であり，1 つの活動期間を経て，約 300 年の休止期へと続いていることがわかる．この周期に従うと，現在白山は休止期の終わりから活動期の始めにあたるといえる．次の活動期に予想される新たな火山活動，溶岩流，火砕流及びそれによって生じる地震活動は地すべりの安定性に影響すると懸念されている.

これまでに白山で発生した斜面災害のうち，記録が残っている中で最も被害の大きかったものは 1934 年の別当崩れである．2 日間で約 466 ㎜を記録した激しい豪雨によって，別当谷の右側斜面の斜面崩壊が引き起こされた．崩壊土砂は土石流に発展し，手取川に沿って日本海まで流下し，112 名の命が失われ，240 戸の家屋が倒壊し，手取川下流の市ノ瀬村落が完全に壊滅した．現在でもその斜面崩壊跡が残っており，当時の災害の凄まじさを物語っている.

最近では，1999 年に別当谷で降雨によって斜面崩壊が引き起こされ,地すべりダムが形成された.この際，別当谷に監視カメラと警報システムがこの地すべりダムを監視するために設置されたが，その後地すべりダムはゆっくりと崩壊したため，大きな被害は発生していない．2001 年には推定崩壊土砂量 2 万㎥の斜面崩壊が別当谷左岸で発生している．2004 年 5 月 17 日には，豪雨によって別当谷で推定崩壊土砂量17万6千㎥の斜面崩壊が引き起こされ，別当出合に架けられていたつり橋が流出している.

3. 地震を起因とした土砂崩壊事例の検討

3.1 全国の土砂崩壊地点における最大加速度の推定

白山における地震時の斜面崩壊危険度の評価を行うに当たり，まず過去に全国で発生した土砂崩壊地点の推定最大加速度から，土砂の崩壊が発生する可能性を推測できるかを検討した．最大加速度の推測には，福島・田中が提案した以下の距離減衰式[2)]を用いた.

$$\log A_{\max} = 0.51M - \log\left(D+0.006\cdot 10^{0.51M}\right) - 0.0034D + 0.59$$

$A_{\max}$：基盤上での最大加速度(gal：cm/s^2)

M：気象庁マグニチュード

D：断層からの最短距離(km)

上式は，ほぼ硬質地盤における最大加速度の平均的な値を与える式である．そのため今回の計算は，対象とした地点がすべて硬質地盤であると仮定して行うこととした.

対象とした土砂崩壊は，建設省河川局砂防部(1995)「地震と土砂災害」[3)]に掲載されていた大規模土砂崩壊の事例から，本研究の条件に沿うものを抽出した．具体的な条件としては，内陸型地震を直接の誘因として発生したものとして，海溝型地震を誘因とした事例は考慮しないものとした.これは海洋型地震の震源は陸地から比較的離れている場合が多く，土砂崩壊の事例が少なかったからである．土砂崩壊の規模に関しては，記録が残されていた江戸時代以前は 100 万㎥以上のものを,明治時代以降は 1 万㎥以上の事例を中心に抽出した．その結果，条件に合う大規模土砂崩壊を引き起こした地震は 23 事例,抽出した大規模土砂崩壊は 53 箇所となった.これらの地点における最大加速度を福島･田中式を用いて算出した.

図５に算出した推定最大加速度と土砂崩壊発生件数の関係を示す．これより推定最大加速度が

300gal を超えると崩壊の発生件数が飛躍的に増加しているのが分かる．

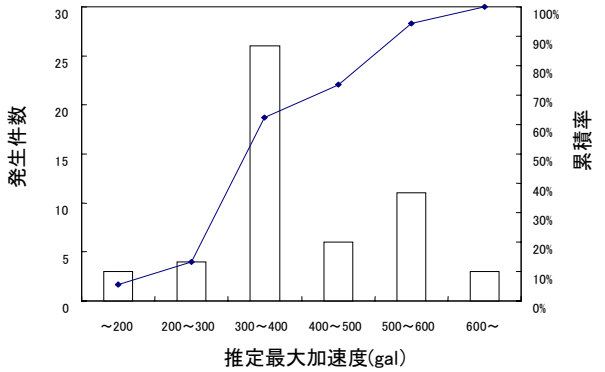

図５　推定最大加速度と土砂崩壊発生件数[3)]

3.2 推定最大加速度を用いた崩壊土砂量の予測

3.2.1 推定最大加速度と崩壊土砂量の関係

前節で算出した推定最大加速度の値から崩壊土砂の量を推測できるのかを検討した．まず推定最大加速度と崩壊土砂量の散布図を図６に示す．

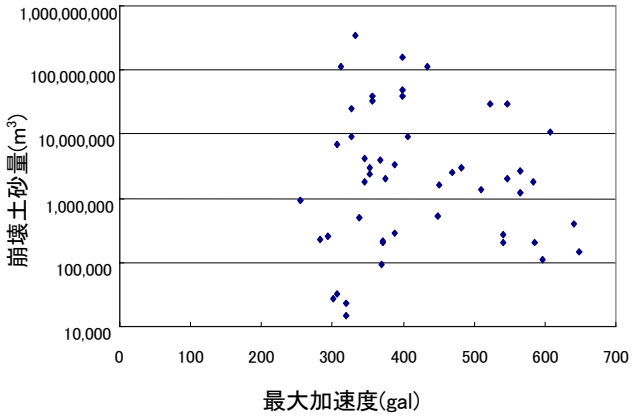

図６　推定最大加速度と崩壊土砂量の関係

同図から，推定最大加速度が 300gal～400gal の範囲内で最も規模の大きい４億㎥を超える崩壊が発生していること，600gal 以上の範囲では１千万㎥をかろうじて超える崩壊が１件発生しているだけであることがわかり，推定最大加速度と崩壊土砂量の相関を明確に読み取ることができなかった．これは推定最大加速度が 600gal を超える事例が少なかったことや崩壊地点の地質や斜面勾配などを考慮していなかったためであろう．そのため崩壊地点の地質や斜面勾配を考慮することとした．

3.2.2 地質による分類

まず，崩壊地点における地質を考慮する．図７に地質と土砂崩壊の発生件数及び崩壊土砂の量の関係を示す．

白山周辺に多く分布している火山岩噴出物の地域で土砂崩壊が多く発生しているのがわかる．またこの地域では100万㎥以上の規模の土砂崩壊が占める割合が多く，１億㎥を越える崩壊も発生していることがわかる．そのため火山噴出岩が分布する地域では大規模な土砂の崩壊が発生しやすいといえる．また，中・古成界が分布している地域では､火山噴出岩が分布する地域と比較すると､土砂崩壊の発生件数こそ少ないが崩壊土砂の量が100 万㎥を超える事例ばかりであった．このことから，土砂の崩壊は発生しにくいものの、一旦崩壊が起こると大規模な崩壊が起きる可能性が高い地質であるといえる．

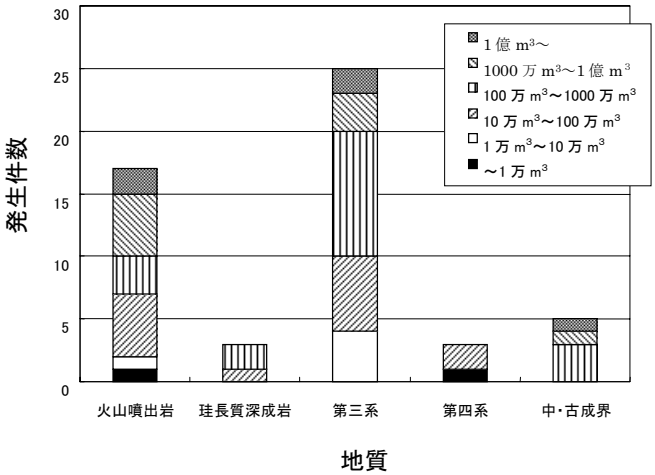

図７　地質と土砂崩壊発生の関係

つぎに，それぞれの地質における推定最大加速度と崩壊土砂量の関係を検討する．地質ごとの推

定最大加速度と崩壊土砂量の関係を図８に示す．このうち火山噴出岩が分布している地域では，推定最大加速度が 350gal～400gal の範囲で最も土砂の崩壊が発生していた．また崩壊土砂量の平均値は，約 1,920 万㎥であった．ただし崩壊土砂の量は 300gal～400gal の範囲内で分散していたため最大加速度と崩壊土砂の量の関係は読み取りにくい．この地質では，500gal を超える範囲で最大加速度が増加しているにも係わらず崩壊土砂の量が減少している傾向が見られた．このことから，火山噴出岩が分布する地域では最大加速度の大小によらず大規模な崩壊が起こりうるといえる．

中・古成界が分布する地域では，最大加速度にかかわらず崩壊土砂の量が 100 万㎥を超えていた．しかし，事例が少なかったため，最大加速度と崩壊土砂量の関係は明確ではない．また，事例が少ないものの崩壊土砂量の平均値は約 7,170 万㎥と非常に大規模であった．

火山噴出岩，中・古成界の両地質においてグラフの崩壊土砂量の値が分散しており，最大加速度と崩壊土砂量の関係が明確ではなかったので，加速度レンジごとの平均崩壊土砂量を考慮すること

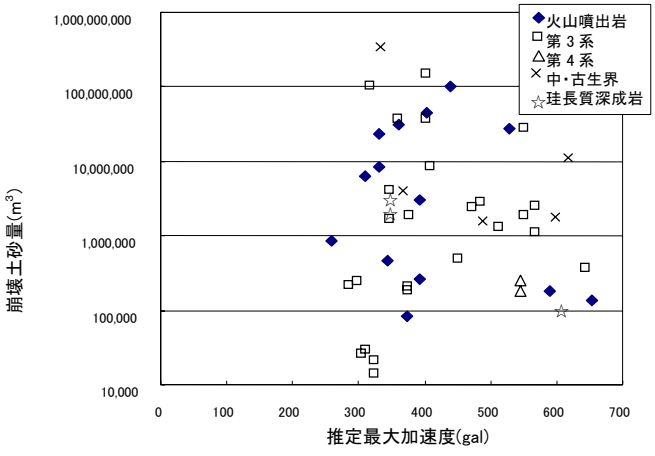

とする．

図８　地質ごとの推定最大加速度と崩壊土砂量の関係

図９に，最大加速度を 250gal から 500gal まで，50gal ごとの 5 つに分類した加速度レンジごとの平均崩壊土砂量を示す．同図より，火山噴出岩が分布している地域では，最大加速度の増加に伴って平均崩壊土砂量が増加していることがわかる．このため，最大加速度を計算することで，崩壊土砂量をある程度推測することは可能であると考えられる．しかし，中・古成界が分布している地域では事例が少なく，例外的な大規模崩壊事例を含んでいたためか，最大加速度と崩壊土砂量に負の相関が表れた．さらに，より多くの事例を収集し，最大加速度と崩壊土砂量の関係を検討にする必要がある．

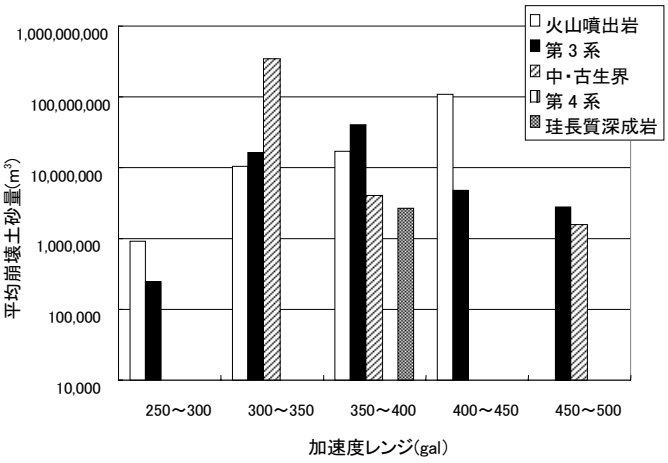

図９　加速度レンジごとの平均崩壊土砂量

3.2.3 斜面勾配による分類

崩壊地点の斜面勾配を考慮する．まず，図１０に全国 53 箇所の崩壊地点における斜面勾配と土砂崩壊発生件数関係を示す．同図より，斜面勾配が 30°～40°の斜面で集中して土砂崩壊が発生していることがわかる．40°を越える急斜面で土砂崩壊が少ない原因は，堅固な岩盤により構成され安定度が高いことや，急勾配斜面の数が少ないためと考えられる．

図１０　斜面勾配と土砂崩壊発生件数の関係

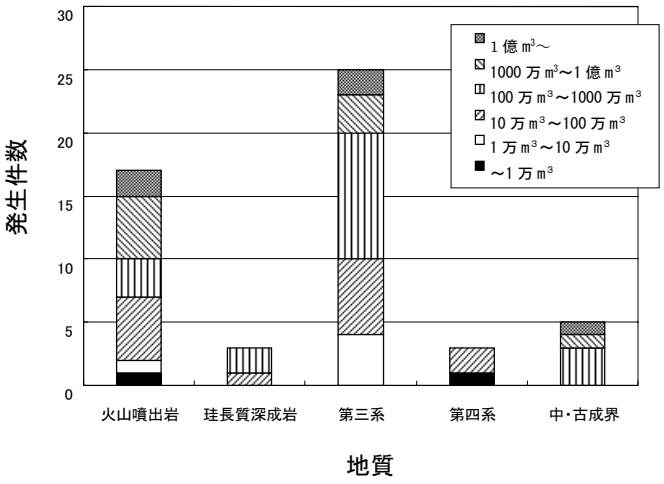

図１１　勾配ごとの推定最大加速度と崩壊土砂量の関係

つぎに，斜面勾配ごとの推定最大加速度と崩壊土砂量の関係を検討する．図１１に斜面勾配ごとの推定最大加速度と崩壊土砂量の関係を示す．同図より白山と同様の斜面勾配が 30°～40°の地点では，推定最大加速度が 350gal～400gal の範囲で最も土砂崩壊が発生していることがわかる．また 300gal～350gal，500～600gal の範囲でも多くの崩壊が発生しているのが読み取れる．斜面勾配が 30°～40°の範囲では，全体的に崩壊土砂の量が多かったためかその平均値は 4,650 万㎥であった．最大加速度と崩壊土砂量の関係は明確に現れなかったが，図からもわかるように，300gal～400gal の範囲では崩壊土砂量は広く分散していたが，500gal～600gal の範囲内では 100 万㎥を超える事例が多く，最大加速度の増加に伴い崩壊土砂量が増加傾向にあることを示しているといえる．しかし，斜面勾配が 30°～40°の地点では，300gal～400gal の地点の方が 500gal～600gal の地点よりも崩壊土砂量が多かった．これは 500gal を超える事例が少なかったこともあるが，小さい最大加速度でも大規模土砂崩壊が発生するということを示唆しているといえる．

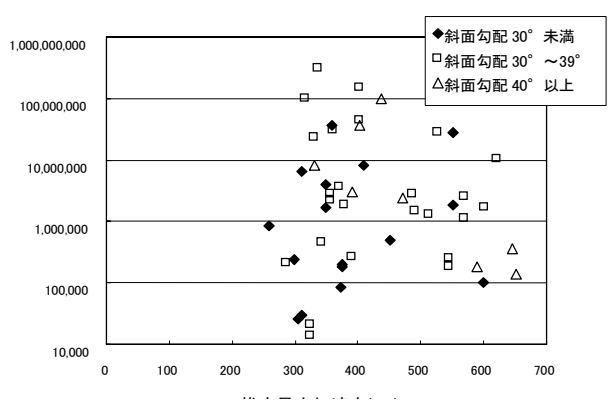

つぎに，地質と同様に加速度レンジごとの平均崩壊土砂量を検討する．加速度レンジは，地質と同様に最大加速度が 250gal から 500gal の範囲を 50gal ごとに分けて分類した．図１２に加速度レンジごとの平均崩壊土砂量の値を示す．

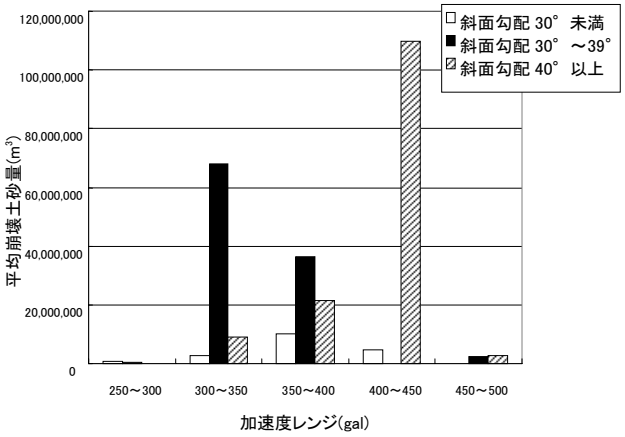

図１２　加速度レンジごとの平均崩壊土砂量

同図より，斜面勾配が 30°～40°の地点では，最大加速度と平均崩壊土砂量の間に負の相関が表れている．これは 300gal～350gal の範囲内で 1 億㎥を超える大崩壊が 2 件発生しており，300gal～350gal の地点よりも 350gal～400gal の地点の事例が多かったためである．

4.　白山における崩壊の発生可能性と崩壊土砂量の推測

4.1 白山周辺で発生した過去の地震時の最大加速度の推定

4.1.1 最大加速度の推定

白山周辺で過去に発生した地震時の白山における最大加速度を，福島・田中式を用いて推測した．白山の基盤岩である飛騨片麻岩は非常に強固な岩石であるため，ほぼ硬質地盤における最大加速度の平均的な値を与える福島・田中式を適用することが可能であるといえる．

計算に用いる地震は，白山から半径 150 km以内に震源が存在し，実際に大規模な土砂崩壊が発生したと記録が残っている，マグニチュード(以下、*M* と略記する)7.0～8.0 前後の内陸型地震の中から抽出した．これは白山の斜面崩壊危険性を評価するにあたって，将来発生する可能性が高い地震を評価する必要があるからである．白山周辺には活動度の高い断層が集中しており，*M*7.0 前後の地震の発生確率は数十年に 1 回程度である．また *M*8.0 前後の地震に関しても，1 つの断層帯では数千年に 1 回程度の発生確率だが，中部地方だけでこのような断層帯が 8 箇所分布しているため，白山周辺での発生確率は数百年に 1 回程度と考えられる．震源が半径 150 km以内にあったものを採用したのは，*M*8.0 前後の内陸型地震時には，被害を受ける範囲が震源から半径 70～150 km程度と考えられるからである．しかし海洋型地震に関しては，白山は内陸部に位置しているため，*M*8.0 以上の巨大地震が発生したとしても白山が受ける影響は少ないと思われるため，考慮しないこととした．

計算に用いた各地震の名称とその規模，発生年代及び起因となった断層帯と白山の最短距離をそれぞれ表 1 に示す．最大加速度を算出する地点は白山の白峰観測所とし，断層との最短距離は，過去の地震の起因と推測されている断層帯と白峰観測所との最短距離として算出した．

表 1　過去の地震の規模と断層から白山との距離 [3)]

発生年	地震名	*M*	白山との距離(km)
1586.1.18	天正地震	7.9	31.5
1662.6.16	琵琶湖西岸地震	7.6	92.3
1847.5.8	善光寺地震	7.4	152.5
1858.4.9	飛越地震	7.1	30.6
1891.10.28	濃尾地震	8.0	38.4
1948.6.28	福井地震	7.1	38.5
1961.8.19	北美濃地震	7.0	21.4
1984.9.14	長野県西部地震	6.8	97.2

計算結果を図１３に示す．このうち最大加速度が230galを超えた4つの地震発生時に白山で土砂の崩壊が発生したという記録が残っている．最大加速度が 230gal 程度で土砂の崩壊が発生する可能性が高いことより，全国の事例と比較して白山で崩壊が発生する危険性は高いといえる．

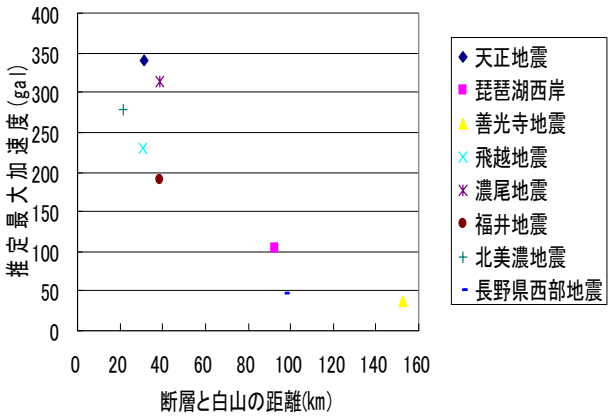

図１３　過去の地震時の白峰観測所における最大加速度

4.2 想定地震発生時の最大加速度の推定

白峰観測所における，周辺の断層帯を起因とする地震発生時の最大加速度を福島・田中式を用いて推測した．なお最大加速度を求める地点は，白峰観測所とし，断層からの距離も白峰観測所と各断層帯の最短距離として計算した．計算に用いる断層帯は，白山から半径 100 km以内に分布し，地震発生時に *M*7.0 前後と予想されているものから抽出した．いずれの断層帯も活動間隔は数百～数千年に一回程度であるが，最新の活動時期がず

れていることから，白山周辺で内陸型地震が発生する可能性は高いといえる．

計算に用いた断層名と予想される地震の規模，断層と白山の距離を表２に示す．

表２　白山周辺の断層の規模と白山からの距離 [3)]

断層帯名	*M*	白山との最短距離 (km)
庄川断層帯	7.9	46.9
跡津川断層帯	7.9	30.6
森本・富樫断層帯	7.2	33.3
福井平野東縁断層帯	7.6	29.4
砺波平野西縁断層帯	7.3	44.1
呉羽山断層帯	7.2	65.5
邑知潟断層帯	7.0	57.9
阿寺断層帯	（全体）7.9 （北部）6.9 （南部）7.8	（北部）54.3 （南部）54.8
長良川上流断層帯	7.3	30.0
濃尾断層帯	7.7	46.8
境峠・神谷断層帯	7.6	88.5

計算結果を図１４に示す．図より 7 つの断層帯が活動した場合に白峰観測所で最大加速度が 230gal を超える可能性があるとわかる．このうち 5 つの断層帯では，地震調査研究推進本部の長期評価[4)]より，今後 300 年以内に活動する可能性が 10^{-3}%未満と推測されているため危険性は低いといえる．しかし森本・富樫断層帯と福井平野東縁断層帯は，今後 30 年以内に活動する可能性が，それぞれ 0～5%，0.4%と高いため，白山で崩壊が発生しうる規模の地震が起きる可能性は高いといえる．また，前章で行った検討結果に基づくと，これらの断層帯が活動した際の推定最大加速度では 100 万～1 億㎥の規模の崩壊が発生する恐れがあるといえる．

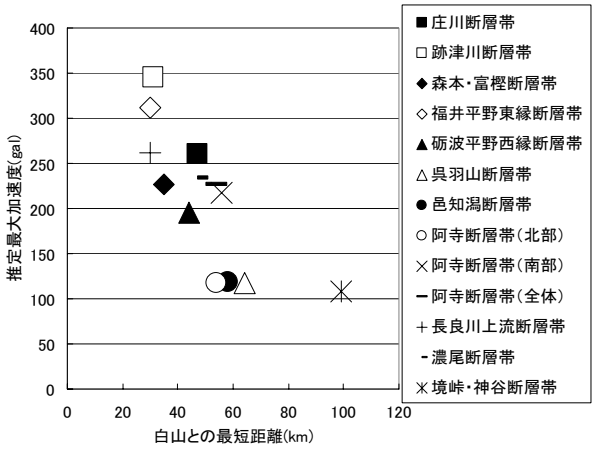

図１４　各断層帯が活動した際の白峰観測所における推定最大加速度

5.　結論

全国では最大加速度が 300gal を超えると崩壊の発生確率が高まるのに対し，白山では 230gal で崩壊が発生した事例がある．また白山周辺の森本・富樫断層帯や福井平野東縁断層帯は今後活動する可能性が高く，活動した際の白峰観測所における推定最大加速度が 230gal を超えることから，白山の斜面崩壊危険度は高いといえる．

またこれらの断層帯が活動した際の最大加速度の範囲では，全国の白山と同様の地質の地点で 100 万～1 億㎥の崩壊が発生しており，両断層帯が活動した際には同程度の規模の土砂が流出する恐れがあるといえる．

今後は、さらにより多くの過去の事例を収集し，最大加速度と崩壊土砂量の関係を明確にすることで，白山の斜面崩壊危険度をより正確に評価したい．

参考文献

1）国土交通省北陸地方整備局金沢河川国道事務所：

甚之助谷地すべり, pp.1-11, 2003.

2) Fukushima, Y. and Tanaka, T.： A new attenuation relation for peak horizontal acceleration of strong earthquake ground motion in Japan, *Bull. Seism. Soc. Am.*, Vol. 84, pp. 757-783, 1990.

3) 建設省河川局砂防部：地震と土砂災害,
砂防広報センター, pp.1-2, 1 , 1995.

4) 地震調査研究推進本部地震調査委員会：
http://www.jishin.go.jp/main/

Igwe, O., Sassa, K., Fukuoka, H. and Wang, F.W.
(2005)

Threshold pore pressure: a new perspective on the mechanisms of flowslides

Proc. of 11th International Conference and Field Trips on Landslides, Norway, September, 2005, pp.165-171

Threshold pore water pressure: a new perspective on the mechanism of flow slides

O. Igwe, K. Sassa, H. Fukuoka and F. W. Wang
Research Centre on Landslides, Disaster Prevention Research Institute, Kyoto University, Japan

Abstract: A model predicting the pore pressure change necessary for liquefaction failure of saturated soil masses in undrained condition is assessed. It is shown that a threshold pore pressure, u_c, derived from the Mohr Coulomb failure criterion when pore pressure at failure is equal to the corresponding shear resistance is enough to initiate liquefaction type of failure in sandy masses. Loading tests to failure on source-area sandy soils from a catastrophic landslide location, undertaken to verify the model, show that under definite conditions of loading, a threshold state, characterized by the equality and subsequent constancy of pore pressure and shear resistance from a few seconds after the commencement of shearing until failure, develops in the sands at a given density. Samples in which the threshold pore pressure was exceeded readily liquefied while those in which the pore pressure built-up was below the limit gained strength by tendencies to dilate. This paper demonstrates that while the stability of a slope founded on sandy soils may be breached when the pore pressure exceeds a certain limit, it is possible to make estimates of the limit. It is shown that where such estimates are accompanied with adequate field measurements of pore pressure, the efficiency of landslide prevention projects may be enhanced because only slopes whose stability is proven to constitute a real public threat are reinforced and reinforced adequately.

1 INTRODUCTION

1.1 *Background*

Landslides are vicious slope movements accounting for inestimable amount of loss, waste and damage in virtually every part of the world. Triggered by earthquake, volcanic eruption, intense rainfall, rapid snowmelt, changes in water level, and even by the activities of man himself, it is very difficult, if not impossible, to overestimate their threat to public safety. They are known to have frequently breached the peace of cities and towns, sacked communities and villages, buried the wealth of rural and urban dwellers, wrecked countless hopes and dreams, harshly punished some sloppy structure designing, defied some inadequate preventive measures, and produced endless catalogs of carnage. Landslides do not only destroy homes and hopes, they also deface and devalue historical, cultural, and entertainment facilities so dear to man. Taming their aggression and ruinous impacts, thereby rescuing the environment from a potential crisis, should, in point of fact, become a priority. Liquefaction of saturated soils, often regarded as the fundamental cause of flow slides, has been responsible for many of the tragedies resulting from slope failures. The intense mobility of liquefied soils, which permits movements that range from several tens of meters to several thousands of meters, almost always ensures that huge amount of resources is lost in the wake of a landslide disaster. Sound knowledge of the mechanism of liquefaction, the factors that influence the liquefaction potential of a mass of soil, and the characteristics of liquefiable soils, is a potent tool not only in landslide investigation and mitigation but also in the civil engineering industry. For indeed careful and rigorous assessment of the liquefaction potential of sands when selecting them for embankments, dams, foundations, and roads is a tradition of immense importance in the construction industry. And because a great deal of failures of earth structures, foundations, and slopes founded on sands have been attributed to the liquefaction of the sands, stakeholders in environmental protection and urban development seem to have elevated the importance of liquefaction-evaluation by placing it at the heart of their management policies. This elevation of importance has, in part, inspired intense research leading to, for instance, better knowledge of the factors and dynamics behind the failure of Fort Peck Dam in Montana in 1938, Calaveras Dam in California in 1920, the Lower Lan Norman Dam, the foundation failures induced by the 1964 earthquake in Alaska, USA, and Niigata, Japan, and the flow slides in the province of Zealand in Holland and Mississippi River. Ever since the

widespread destruction arising from the 1964 earthquakes in Alaska, U.S.A. and Niigata, Japan dramatically brought the subject of soil liquefaction to public awareness, considerable amount of research has been undertaken by several researchers, including Sassa, and colleagues at the Disaster Prevention Research Institute, Kyoto University, Japan, who have used one of the most refined ring shear apparatuses to simulate, as closely as possible, the stress-strain conditions that develop on a mass of soil when it is subject to conditions capable of triggering liquefaction.

1.2 *The problem*

Although liquefaction phenomenon has been the subject of a barrage of investigations and publications for decades now, its mechanism leading to large lateral displacements has yet to be fully understood. Questions such as – why do some soils collapse and liquefy whereas others, under identical stress conditions, dilate and gain some measure of strength; and what are the primary factors triggering liquefaction and flow failures, especially, in loose cohesionless soils, only serve to underscore the incompleteness of what researchers as yet know about soils liquefaction. Finding perfect answers has led to the emergence of a good number of beneficial concepts including Casagrande's critical voids ratio concept. In spite of the emergence of these concepts, questions still remain, especially as to effective ways of relating the critical state of soils with essential soil parameters, such as pore pressure and shear resistance; there does not seem to have been any previous attempt to relate collapse and liquefaction to an experimentally-verifiable limit or critical value of pore pressure, above which collapse occurs and below which it does not. In this paper, two new concepts – the concepts of least dilation, and critical pore pressure – are introduced to interpret the undrained shear behavior of granular soils at a threshold density. It is shown that the characteristics of the soils so interpreted tend to define the boundary between contraction in loose, and dilation in dense soils held under same effective normal stress. This paper also demonstrates that while the stability of slopes founded on sandy soils may be breached when the pore pressure exceeds a certain limit it is possible to estimate the limit. Where such estimates are accompanied with adequate field measurements the efficiency of landslide prevention projects may be enhanced because only slopes whose stability is proven to constitute a real public threat are reinforced and reinforced adequately.

1.3 *Liquefaction and limited liquefaction*

Since not all slope failures are due to liquefaction, establishing a standard that enhances the prediction and identification of flow-type failures in the field will not only shed more light on the mechanism of soil liquefaction but will also improve the efficiency of slope stability analysis. Literature is replete with studies, including that by Ishihara (1993), attempting to establish such a standard. Following a summary of a good number of field and laboratory data, Ishihara (1993) proposed a threshold SPT N-value to distinguish between flow-type and non-flow type failure. Although researchers have made quality efforts at drawing a boundary between liquefaction and non-liquefaction, they have yet to find a common ground over what behaviors of sand, as observed in the laboratory, should be recognized as an important mechanism determining the occurrence or otherwise of flow-type failures in the field. It may be important to note that even though beneficial concepts, hypotheses, and postulates explaining the undrained behaviors of sands whose voids ratio exceed or fall below the critical density exist in the literature, there has yet to be a distinctive behavior associated with sand at critical density. Determining how sand at a critical density behaves during undrained loading may be important in understanding more about soil liquefaction.

Three basic undrained behaviors of granular materials are very commonly referred to in geotechnical discourse: dilation, limited or partial liquefaction, and liquefaction, Fig. 1. The phase transformation line (PT line) as recognized by Ishihara 1993, is a line passing through points where contractive behaviors terminate and dilative behaviors begin, in specimens that first contract, and then dilate. Although the validity of limited liquefaction as a true soil behavior has been subjected to a considerable amount of doubt, debate and controversy, the three basic behaviors sketched above are not only a very useful means of characterizing granular soils but also an effective means of understanding the mechanism of slope failures. The occurrence of, and practical implication of the so-called limited liquefaction have been a contentious issue with two opposite views increasingly gaining currency. Sutter and Smith (1980) have reported that the occur-

rence of limited liquefaction is a function of how close the void ratio of a given material is to a critical void ratio. They have noted that whereas specimens with voids ratio considerably higher than the critical would almost certainly suffer complete liquefaction, those whose voids ratio are marginally higher or nearly equal to the critical would experience limited liquefaction. Sutter and Smith's results are supported by those of Castro and Poulos (1977), and Poulos et al. (1985) who, while assessing procedures for evaluating the undrained steady-state strength of sands with results of undrained triaxial tests, have reported that the undrained strength of sands was dependent on only in-situ void ratio; and independent of either soil fabrics or loading methods. They conclusively showed that sands whose voids ratio exceeded a certain threshold value suffered liquefaction instead of the so-called partial liquefaction.

Evidences from other works, however, seem to indicate that the occurrence of limited liquefaction does not depend wholly on the proximity of material density to the critical, but in part on the constraints offered by the testing apparatus, and test conditions (Mathew and John, 1991; Jude, 1998). It is this partial dependence on apparatus constraints that has compelled some (like Jude 1997, Love 2000) to question the validity of limited liquefaction as a true soil behavior. In their elaborate argument, doubts have been raised over the possibility of observing, in the field, a material flowing and at the same time undergoing hardening. Those who support limited liquefaction as a true soil behavior have, however, tried to make sense out of the frequency at which the behavior is observed. Relying heavily on the rate at which the behavior is observed on loose specimens during testing, they have vigorously demonstrated that the behavior is indeed a true characteristic associated with the deformation of granular materials in undrained shear. In spite of these divergent views, however, there seems to be a consensus that there exists a boundary between a purely dilative behavior and liquefaction, whether complete or limited liquefaction. But, that boundary has yet to be clearly assessed.

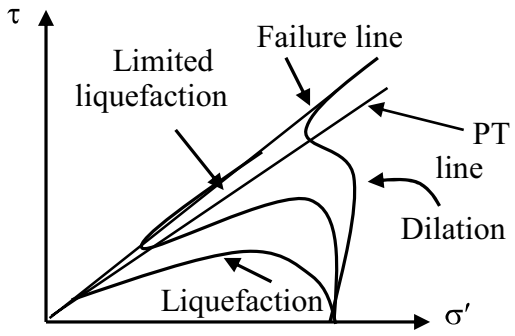

Fig.1 A sketch of the three basic behaviors of granular materials (after Castro 1969)

1.4 Objective and methodology

In the light of the above, it is possible then to ask whether or not there should be a boundary between dilation and liquefaction for material under same confining stress – limited liquefaction or complete liquefaction; and what the defining parameters of such a boundary should be. The approach employed in this paper was to carefully alter the void ratio of specimens held under same confining stress in attempts to identify stress paths whose peak strengths would nearly coincide with their strength values at the PT line. Any specimen whose peak strength equals its strength values at the PT line will be identified as the least dilating at a given normal stress because its phase transformation line will be the same as its failure line. The characters of such a specimen will then be used to define the boundary between dilation and liquefaction. Such a definition will permit adequate and logical interpretation of the behavior of soils as density is varied from dense to loose. It may instantly become obvious that if the density of a sand is gradually decreased, a density reaches where failure line and phase transformation line will coincide. Further decrease in density may lead to flow liquefaction behavior; with the ultimate consequence of having only a failure line as its prominent feature.

2 THE SOLUTION: HYPOTHESIS

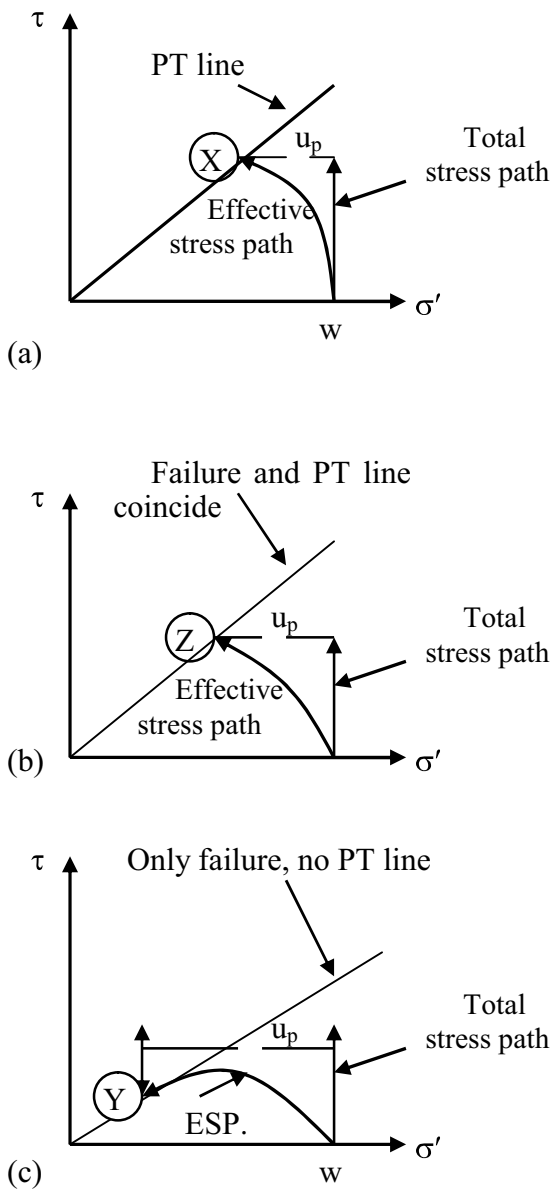

Fig 2 Schematic diagrams illustrating the concepts of least dilation and critical pore pressure **(a)** dilation **(b)** critical **(c)** liquefaction

Normally consolidated soils (Figure 2a, b) at same confining stresses will follow stress paths WX and WZ respectively depending on the material state of the samples. For these samples, the conditions at PT line are such that a dilation potential index, r_f, ($r_f = \Delta u_p / \Delta \tau_p$) are < and = 1 respectively. The conditions prevailing at 2b are recognized in this paper as critical. If however, the soil is made in such a way that ensures the stress path follows WY as in Fig. 2c, the specimen will not go through the phase transformation stage because its r_f would clearly be greater than one. The specimen will, instead, collapse and liquefy. It may be beneficial to note that a dilative specimen (Fig.2a) should have distinct phase transformation and peak stress states while contractive specimens (Fig. 2c) may be easily identified by just a distinct failure state. In between these two fundamental behaviors is a relative density at which the phase transformation and peak stress states should coincide to form a threshold state (Fig.2b). The present theory underlines the fact that the magnitude of excess pore pressure from the outset of any undrained test determines whether or not a given specimen will pass through the phase transformation stage. The fate of specimens whose excess pore

pressures are not big enough to induce outright liquefaction and avoid reaching the PT line, depends on the ratio $\Delta u_p/\Delta \tau_p$ at the phase transformation point. If this ratio is unity, pore pressure and shear resistance should remain the same until failure occurs, meaning that the sample will experience the least dilation possible at a given effective stress. The PT line of such a specimen will be approximately equal to its failure line because the state of stresses at the PT point approximately coincides with those at failure. This condition will define a critical situation. All other stress paths above this critical should dilate, while other stress paths below it should show contractive behavior. To enhance comprehension, the pore pressure at which this critical is observed will be called a critical pore pressure. If the ratio as seen above is less than one at the phase transformation line, the material will dilate significantly and its PT line will be different from its failure line.

2.1 Experimental verification

2.1.1 When failure and phase transformation lines coincide

Artificially constituted silica sands and natural samples taken from the 1995 Takarazuka landslide (Fig. 3) that killed 34 people in Kobe, Japan were used to verify the concepts. Both the artificial and natural samples have similar physical properties, and indeed have almost the same friction angle.

Fig. 3 Picture of the Takarazuka landslide that followed the Great Hanshin earthquake of 1995.

Figures 4a and b are stress path and stress versus shear displacement respectively of a normally consolidated gap graded silica sand material confined at 196 kPa with a void ratio of 0.89. The figures illustrate what happens whenever pore pressure at failure is equal to the corresponding shear resistance such that there is no distinction between the phase transformation stage and failure state because the specimen appeared to have experienced the least dilation possible at the given confining stress. Excess pore pressure and shear resistance became equal at the phase transformation point and not only remained equal but essentially constant until failure, thus establishing a threshold state at a small shear displacement (Fig. 4b). The equality and subsequent constancy of excess pore pressure and shear resistance, which started at about 2 mm and continued until the sample failed at 10 mm shear displacement, are typical characteristics of specimens that tend to form a transition region by demarcating the contractive from the dilative behavior.

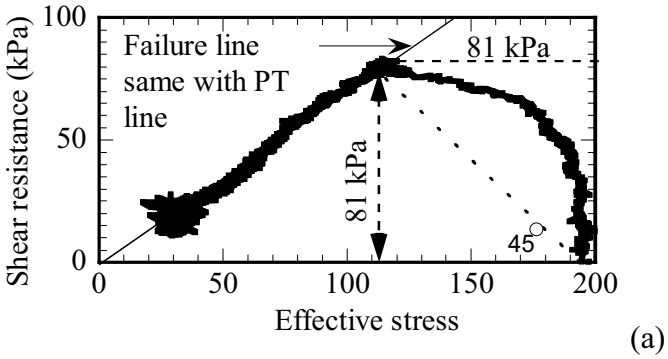

(a)

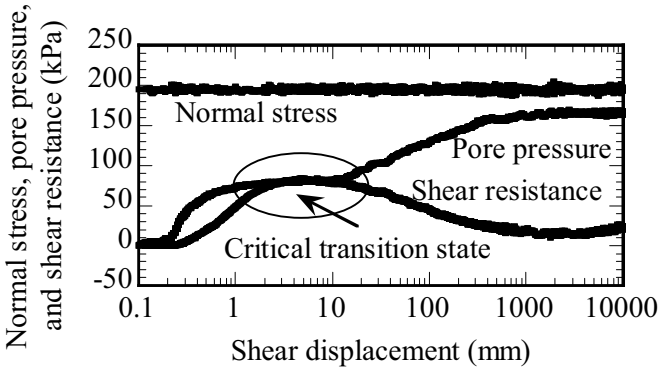

(b)

Fig. 4 (a) Stress path defining a critical condition (b) Pore pressure and shear resistance behavior

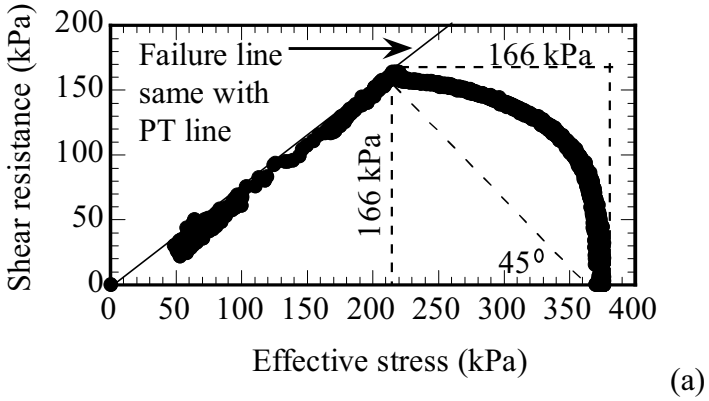

(a)

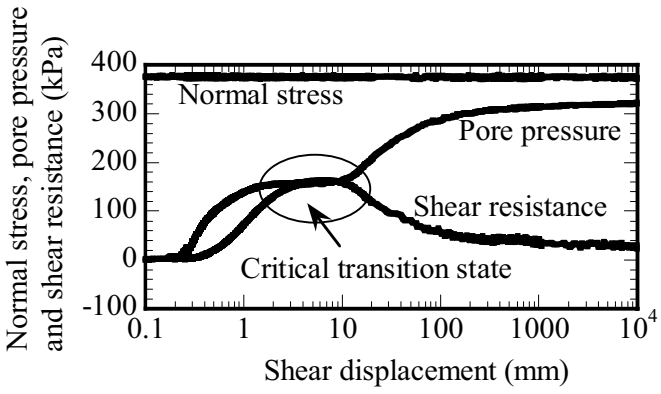

(b)

Fig. 5 (a) Stress path defining a critical condition (b) Pore pressure and shear resistance behavior as loading progressed.

Theoretically, it may be easy to see that any stress path below this critical will liquefy while any above will dilate. It may be noticed from Figure 4b that on becoming equal at the point that would have marked

the phase transformation, pore pressure and shear resistance remained the same value until failure because dilation was obviously suppressed. If the specimen had dilated significantly, pore pressure and shear resistance would not have remained same value until failure because while the former would have decreased, the latter would have increased making it impossible for the values to remain the same. The same behavior was found to be true in the Takarazuka specimens confined at 372 kPa and consolidated to a void ratio of 0.77, Fig. 5a and b.

2.1.2 When failure and phase transformation lines do not coincide

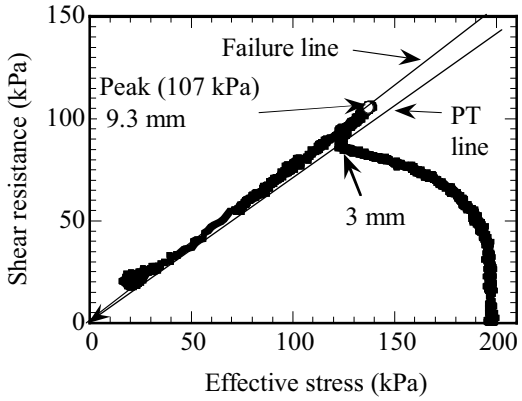

Fig. 6 (a) Typical stress path showing significant dilation because pore pressure and shear resistance at PT are not equal

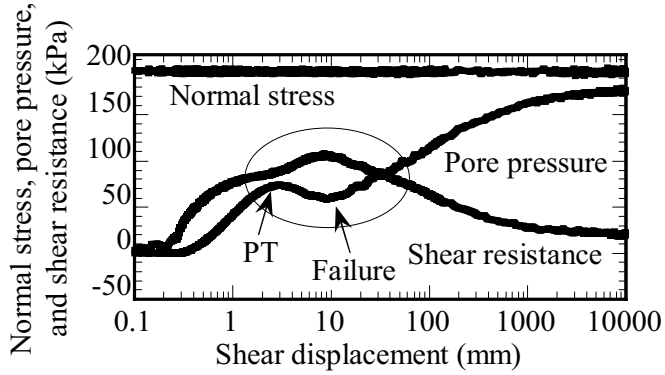

Fig. 6 (b) Stress versus shear displacement

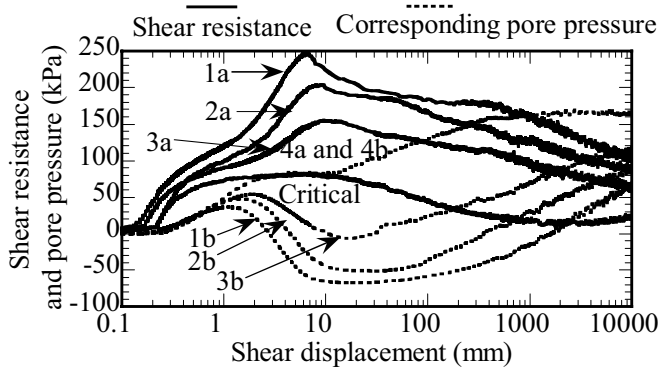

Fig. 7 Shear resistances and the corresponding pore pressures of some sands as density changes (specimens at 196kPa confining stress)

One case, among many cases, that typifies situations where pore pressure at the phase transformation stage is not equal to the corresponding shear resistance is illustrated in Fig. 8a and b. The consequence of this situation is that the specimens dilated and ensured that the phase transformation line remained different from the failure line. Fig. 6b illustrates the mechanism of dilation in a silica sand specimen consolidated to a void ratio of 0.82. The figure shows that because pore pressure at PT line is different from the corresponding shear resistance, the specimen dilated, expressed as a decrease in pore pressure and a corresponding increasing in shear resistance (highlighted in the circle). These changes continued until failure occurred. For a denser specimen, the changes would even be more remarkable although they follow the same pattern. Because the difference between pore pressure and shear resistance at the PT line would be greater in a denser specimen, the dilation would also be higher than in Fig. 6a and b. As density increases, the difference increases too. A decrease in the density of a material will decrease the difference between pore pressure and shear resistance at the PT point. As density is decreased further, a time reaches when the pore pressure and shear resistance at the PT point will have the same value; and will remain the same until failure takes place (Fig.7) This situation establishes a threshold state and unambiguously defines a transition condition for all specimens under the same confining stress. Liquefaction occurs in loose soils because pore pressures generated in them during static loading tend to exceed the critical. The critical pore pressure, u_c, as used in this paper may be calculated from the following equation:

$$u_c = \sigma \tan\phi /(1 + \tan\phi)$$

Where u_c is the critical pore pressure, σ is the normal stress used in the undrained test, and ϕ is the friction angle of the material at a given normal stress σ. This is the amount of excess pore pressure that must be generated before liquefaction failure of the sands can be expected.

3 CONCLUSIONS

1. Test results have shown that there is a critical or limit value of pore pressure, above which the sandy samples suffered sudden collapse and liquefaction, and below which they dilated and gained some measure of stability.
2 Any specimen whose pore pressure at the phase transformation point equals the corresponding shear resistance will dilate the least among other specimens held under the same confining stress.
3. Once pore pressure becomes equal with the corresponding shear resistance at the PT point, they remain the same until failure and ensure that the specimen dilates the least at a given confining stress.
4. One of the implications of these results is that some slopes are still sitting safe probably because a certain threshold pore pressure has yet to be exceeded. If such slopes must keep sitting safe, in situ pore pressure measurements followed with an adequate drainage regime should be a grave necessity.

REFERENCES

Ambrasseys, N. N. (1973): Dynamic and response of foundation materials in the epicentral regions of strong earthquakes. 5th World Conf. Earthquake Engineering Rome.

Casagrande, A. (1936): Characteristics of cohesionless soils affecting the stability of slopes and earth fills. Journal of the Boston Society of Civil Engineers, Vol. 23, No. 1, pp. 13-32.

Casagrande, A. (1976). Liquefaction and cyclic mobility of sands: a critical review. Harvard Soil Mechanics Series No.88, Harvard University, Cambridge, Mass.

Castro, G. (1969): Liquefaction of sands. PhD. Thesis, Harvard University, Cambridge, Mass.

Castro, G. (1975): Liquefaction and cyclic mobility of saturated sands. Journal of the Geotechnical Engineering Division, ASCE, Vol. 101, No. GT6, pp. 551-569.

Eckersley, J. D. (1985): Flowslides in stockpiled coal. Engineering Geology, Vol. 22, pp. 13-22.

Gilbert, P. A. (1976): Case histories of liquefaction failures. Misc. Paper S-76-4, U.S. Army Engineer Waterway Experiment Station, Vicksburg, Miss.

Gilbert, P. A., Marcuson, W. F. (1988): Density variation in specimens subjected to cyclic and monotonic loads. Journal of Geotechnical Engineering, Vol. 114, No. 1, pp. 1-20.

Ishihara, K. (1993): Liquefaction and flow failure during earthquakes. Geotechnique, Vol. 47, No. 3, pp. 349-451.
Ishihara, K., Okusa, S., Oyagi, N., and Ischuk, A. (1990): Liquefaction-induced flowslide in the collapsible loess deposit in Soviet Tajik. Soils and Foundations, Vol. 30, No. 4, pp. 73-89.
Kramer, S. L., and Seed, H. B. (1988): Initiation of soil liquefaction under static loading conditions. Journal of Geotechnical Engineering, Vol. 114, No. 4, pp. 412-430.
Kutter, B. L. (1982): Behavior of embankments under dynamic loading. Part of PhD thesis, University of Cambridge.
Marui, H. (1996): Preliminary report on the Gamahara torrent debris flow of 6 December 1996, Japan. Journal of Natural Disaster Science, Vol. 18, pp. 89-97.
McRoberts, E. C., and Sladen, J. A. (1992): Observations on static and cyclic sand-liquefaction methodologies. Canadian Geotechnical Journal, Vol. 29, pp. 650-665.
Poulos, S. J. (1981): The steady state of deformation. Journal Geotech. Eng. Division, ASCE 107, No. GT5, pp. 553-562.
Poulos, S. J., Castro, G., and France, J. W. (1985): Liquefaction evaluation procedure. Journal of Geotech. Eng. Division, ASCE 111, No. 6, pp. 772-792.
Sassa, K. (1996): Prediction of earthquake induced landslides. Special Lecture of the 7th International Symposium on ''Landslides'', Rotterdam: Balkema, Vol. 1, pp. 115-132.
Sassa, K., Fukuoka, H., Scarascia-Mugnozza, G., and Evans, S. (1996): Earthquake-induced landslides: Distribution, motion, and mechanisms. Special Issue for the Great Hanshin Earthquake Disaster, Soils and Foundations, pp. 53-64.
Sassa, K. (1997): A new intelligent type of dynamic loading ring shear apparatus. Landslide News. No. 10, pp. 33.
Sassa, K., Fukuoka, H., and Wang, F. W. (1997b): Mechanism and risk assessment of landslide-triggered debris flows: Lessons from the 1996 Otari debris flow disaster, Nagano, Japan. Landslide Risk Assessment (ed. Cruden and Fell), Proceedings of the International Workshop on Landslide Risk Assessment, pp. 347-356.
Sassa, K. (1998a): Recent urban landslide disasters in Japan and their mechanisms. Proceedings of the 2nd International Conference on Environmental Management, ''Environmental Management'', Rotterdam: Balkema, Vol. 1, 47-58.
Seed, H. B. (1966): Landslides during earthquakes due to soil liquefaction. Journal of Soil Mechanics Foundations Division, ASCE, Vol. 94, No. 5, pp. 1055-1122.
Seed, H. B. (1979): Soil Liquefaction and cyclic mobility evaluation for level ground during earthquakes. Journal of Geotech. Engineering Division, ASCE, Vol. 105, pp. 201-255.